Quantum-statistical approach to pressure broadening for Lyman lines from hydrogen and hydrogen-like plasmas

Kumulative Dissertation
zur
Erlangung des akademischen Grades
doctor rerum naturalium (Dr. rer. nat.)
der Mathematisch-Naturwissenschaftlichen Fakultät
der Universität Rostock

vorgelegt von
Dipl.-Phys. Sonja Lorenzen
geb. als Westermayer am 23.9.1982 in Tübingen
aus Bonn

Bonn, den 23.7.2014

urn:nbn:de:gbv:28-diss2015-0102-7

1. Gutachterin:	PD Dr. Heidi Reinholz Institut für Physik, Universität Rostock
2. Gutachterin:	Prof. Dr. Sibylle Günter Max-Planck-Institut für Plasmaphysik, Garching
Tag der Verteidigung:	11.12.2014

Adresse:	Universität Rostock Institut für Physik 18051 Rostock
Tel:	+49 381 498-6941
Fax:	+49 381 498-6942
Internet:	http://www.physik.uni-rostock.de

E-Mail der Autorin: Sonja.L@renzen.de

Abstract (English)

To apply spectroscopy as a diagnostic tool for dense plasmas, a theoretical approach to pressure broadening of spectral lines is indispensable. Plasma pressure broadening, i.e. the shift and broadening of spectral lines due to charged particles in the plasma, is well understood for ideal plasmas, where a semi-classical theory can be applied. Outside the ideal regime, some approximations are questionable. First of all, it is necessary to treat perturbers quantum-mechanically, too.

A quantum-statistical theory is used here to calculate full line profiles of Lyman lines of hydrogen (H) and H-like lithium (Li^{2+}). Since the no-coupling approximation is applied, effects due to electrons and ions are treated separately and in different approximations. Ionic perturbers are either treated quasi-statically or dynamically via frequency fluctuation model and model microfield method. The resulting line width from different ion-dynamics models can differ up to $\pm 30\%$ for H Lyman-α. This is of importance as soon as the theory is applied in diagnostics.

Electronic perturbers are treated in impact approximation with binary collisions. Strong electron emitter collisions are consistently taken into account with an effective two-particle T-matrix approach using scattering amplitudes. Convergent close coupling calculations produce the necessary scattering amplitudes including Debye screening for neutral emitters. For charged emitters, the effect of plasma screening is estimated with the help of the hydrogen results. A second order Born approximation with a cut-off $q_{\max}$ – adjusted to treat strong-collisions correctly – is used in the comparison with the T-matrix approach. The dependence of the T-matrix results on the magnetic quantum number m is shown to be important, whereas the dependence on the spin scattering channel S is weak and a spin-averaged self-energy can be used. Considered electron densities reach up to $n_e = 10^{27}$ m^{-3} for Li^{2+}. Plasma temperatures are between $T = (10^4 - 10^5)$ K.

The presented approaches and comparisons are an important contribution towards a reliable theory of pressure broadening which can be used as a precise tool in plasma diagnostics of dense plasmas.

Abstract (German)

Sobald Spektroskopie in der Diagnostik dichter Plasmen eingesetzt werden soll, ist ein zuverlässiger theoretischer Zugang zur Druckverbreiterung unverzichtbar. Plasma-Druckverbreiterung beschreibt die Verschiebung und Verbreiterung der Spektrallinien aufgrund geladener Teilchen im Plasma. Für ideale Plasmen kann eine semi-klassische Theorie angewendet werden. Außerhalb des idealen Bereiches sind einige Näherungen dieser Theorie jedoch fragwürdig. Insbesondere müssen dann auch die Störer quantenmechanisch behandelt werden.

In dieser Arbeit wird ein quantenstatistischer Zugang verwendet, um vollständige Linienprofile der Lymanlinien von Wasserstoff (H) und wasserstoffartigem Lithium (Li^{2+}) zu berechnen. Dabei werden Elektronen und Ionen in ihrer Wirkung auf den Strahler getrennt und in unterschiedlichen Näherungen betrachtet. Ionen werden entweder als statische Störer oder dynamisch behandelt. Für die Dynamik werden die Modell-Mikrofield-Methode und das Frequenz-Fluktuations-Modell verglichen, wobei sich die Linienbreiten beider Modelle um bis zu $\pm 30\%$ für H Lyman-α unterscheiden können. Diese Abweichung ist relevant für die Anwendung in der Plasmadiagnostik.

Effekte der Elektronen werden in binärer Elektronen-Strahler-Stoßnäherung betrachtet. Auch starke Elektronen-Stöße werden konsistent im verwendeten effektiven Zweiteilchen-T-Matrix Zugang berechnet. Für die dafür benötigten Streuamplituden wird auf Ergebnisse von "convergent close-coupling" Rechnungen zurückgegriffen, die für neutrale Strahler Debye-Abschirmung direkt im Stoßprozess berücksichtigen. Für geladene Strahler wird der Effekt der Abschirmung auf die Streuamplituden auf Grundlage der H-Rechnungen abgeschätzt. Zum Vergleich wird eine zweite Bornsche Näherung verwendet, die eine Abschneideprozedur zur Korrektur der starken Stöße enthält. Dabei wird deutlich, dass die Details der berechneten Linienprofile sich verändern, sobald die Abhängigkeit von der magnetischen Quantenzahl m des Strahlers berücksichtigt wird, was in der Bornschen Näherung nicht möglich ist. Die Abhängigkeit vom Spin-Kanal des Stoßprozesses ist allerdings gering, so dass eine Mittelung über die Spin-Kanäle in der Berechnung der elektronischen Selbstenergie gerechtfertigt ist. Die betrachteten freien Elektronendichten reichen bis $n_e = 10^{27}\ \mathrm{m}^{-3}$ für Li^{2+}. Die Plasmatemperaturen liegen zwischen $T = (10^4 - 10^5)$ K.

Die dargestellten Zugänge und Vergleiche sind ein wichtiger Beitrag dazu, eine zuverlässige Theorie der Druckverbreiterung für die Diagnostik dichter Plasmen mit Hilfe von Spektrallinienprofilen zu erhalten.

Contents

Abstract English and German I

Table of contents III

List of Figures V

1. Introduction 1

1.1. Motivation and Outline 2

1.2. Basics: Line emission in plasma surroundings 3

1.2.1. Plasma characterization 4

1.2.2. Spectral line measurements of H and Li plasmas 5

1.2.3. Photon emission and radiative transport 7

1.2.4. The shape of spectral lines 10

1.2.5. Recent progress in plasma pressure broadening 14

1.3. Quantum-statistical approach to spectral line profiles 16

1.3.1. Line absorption coefficients from the current-current correlation function 18

1.3.2. Effects due to ions 30

1.3.3. Effects due to free electrons 34

1.4. Overview over published results 37

1.4.1. Paper 1 - Li^{2+} Lyman lines in Born approximation without ion-dynamics 37

1.4.2. Paper 2, 3, 4 - testing an effective two-particle T-matrix approach for H Lyman-α 38

1.4.3. Paper 5 - Comparing two ion-dynamics models for H Lyman-α and Lyman-β 39

1.4.4. Paper 6 - Applying the effective two-particle T-matrix approach with static screening to H, He and Li^{2+} 39

1.5. Outlook 40

2. Publications **43**

2.1. List of own contributions in the publications 44

2.2. Peer-reviewed publications 45

1. Pressure Broadening of Lyman-Lines in Dense Li^{2+} Plasmas (2008) 45

2. Improved Self-Energy Calculations for Pressure Broadening of Spectral Lines in dense Plasmas (2009) 59

3. Quantum-statistical T-matrix approach to line broadening of hydrogen in dense plasmas (2010) 65

4. Quantum-statistical line shape calculation for Lyman-α lines in dense H plasmas (2012) 70

5. Comparative study on ion-dynamics for broadening of Lyman lines in dense hydrogen plasmas (2013) 75

6. Plasma pressure broadening for few-electron emitters including strong electron collisions within a quantum-statistical theory (2014) 82

A. Appendix **i**

A.1. About binary and correlated collisions i

A.2. Formal connection between dipole-dipole and current-current correlation functions iii

A.3. Correlation functions via Kubo scalar products vi

A.4. Matsubara summation: undressed and dressed case vi

A.5. Matrix element $M(\mathbf{k})$ vii

A.6. Sets of variables for two-particle propagator xi

A.7. Details for Eq. (1.70) xiii

A.8. Implementation of the frequency-fluctuation model (FFM) xiii

A.9. Self-energy calculation in Born approximation xiv

References **xvii**

Danksagung **xxvii**

Selbstständigkeitserklärung und CV **xxviii**

List of Figures

1.1. Plasma temperature-density plane 5
1.2. Basic radiative processes 8
1.3. Line broadening by self-absorption 10
1.4. Schematics of processes influencing the line shape 11
1.5. Density-density Green's functions (Doppler broadening) 20
1.6. Density-density Green's functions (Pressure broadening) 25
1.7. FWHM of Li^{2+} Lyman lines. 38

A.1. Validity range of binary collision approximation (electronic perturbers) ii
A.2. No-screening example with simultaneous collisions iv

1. Introduction

1.1. Motivation and Outline

Since the discovery of the dark lines in the spectrum of the sun by William Hyde Wollaston [1] in 1802 and independently by Joseph von Fraunhofer a decade later [2], spectral lines are known as a diagnostic tool. For this it does not matter, whether the emitting or absorbing matter is far away, e.g. like the sun or even more distant astrophysical objects, or close by, e.g. a plasma produced in an arc discharge or by laser light in the laboratory. The spectral lines can provide information about the emitting or absorbing atom or ion itself and about its surroundings. This thesis is concerned with the theory of plasma pressure broadening of spectral lines, i.e. the broadening and shift of a spectral line that is caused by the interaction of the emitter with the charged plasma particles, i.e. ions and electrons.

As Rostock has already a long tradition in quantum-statistical many-body spectral line shape theory, this thesis has a broad basis to start with. Some names have to be mentioned in this context. Already in 1986, Lothar Hitzschke and Gerd Röpke and others published a paper "Green's function approach to the electron shift and broadening of spectral lines in non-ideal plasmas" [3]. Details on the self-energy and the interference term for emitters with degenerate levels were worked out by Sibylle Günter, e.g. Ref. [4]. Many others followed in this field of research with different foci, e.g. on strong electron-emitter collisions (Axel Könies [5]), on H-like carbon plasmas (Stefan Sorge [6][1]), and on the expansion to two-electron emitters, i.e. helium, (Banaz Omar [7])[2].

Besides the motivation to carry on a traditional theory, I was challenged by the possibility to apply and adapt the theory to the emerging EUV technology, where the Lyman-α line of Li^{2+} at 13.5 nm was an ideal candidate[3]. Thus, this thesis follows the Latin motto of the university of Rostock, namely *traditio et innovatio* (tradition and innovation).

This cumulative thesis is structured as follows. In this first chapter, I briefly summarize the underlying theory and classify it in comparison to other approaches for plasma pressure broadening. Then, the quantum-statistical approach based on dipole-dipole correlation functions which is used in Rostock is connected to the more general

[1] His FORTRAN program to calculate line profiles has been used as a basis for this thesis.

[2] This list is not complete, e.g. there is another focus on the plasma shift of K-lines in the group of Heidi Reinholz (Andrea Sengebusch [8])

[3] In the mean time, tin plasmas are mainly used for the purpose to generate EUV radiation at 13.5 nm, i.e. in the NXE:3300B EUV lithography system of ASML [9].

current-current correlation functions which are even applicable when isolated emitters vanish in a dense plasma[4]. However, in the parameter range of my calculations, the dipole approximation can be applied. A second focus is on the importance of ion-dynamics. Ion-dynamics have been analyzed for a broad range of temperatures and densities for hydrogen Lyman lines within two different analytic models. Lastly, strong electron-emitter collisions were studied. They cannot be treated within a perturbative Born approximation. As an alternative to the dynamically screened T-matrix approach presented in [5], an effective two-particle T-matrix approach is used here. It utilizes scattering amplitudes from sophisticated convergent close-coupling calculations which can take Debye screening into account for neutral emitters. For Li^{2+}, the effect of plasma screening on the scattering amplitudes is only estimated. At the end of this chapter, the main results of this work are highlighted. They have already been published in Refs. [10–15]. In the second chapter, these publications are presented as part of this thesis and my personal contribution is outlined. In the appendix, more details on specific theoretical issues are given.

1.2. Basics: Line emission in plasma surroundings

Since the electronic states of an atom or ion are perturbed by its surroundings, line emission – i.e. the emission of photons during an electronic transition of an excited atom or ion from an upper state n to an energetically lower state n' – is dependent on the surroundings, too. For most partially ionized systems, the effect of charged perturbers is much stronger than the one of remaining neutral atoms. In Sec. 1.2.1, we will have a detailed look on the characteristics of the plasma surroundings with a focus on laboratory plasmas, which we use for a comparison with our theory. Then, electronic transitions in general and the basic mechanisms forming the line shape are presented in Secs. 1.2.3 and 1.2.4, respectively. Due to the dependence of the line shape on density and temperature, the shape can be used as a tool for plasma diagnostics. In Sec. 1.2.5, other theories to determine plasma pressure broadening are briefly reviewed.

[4] unpublished part of the thesis

1.2.1. Plasma characterization

Plasmas are many-body systems, where a large number of atoms is partially or fully ionized. Thus, a plasma consists of neutral atoms, different ion species i with charge Z_i, and electrons. Often quasi-neutrality is assumed in a plasma, i.e.

$$n_e = \sum_{i=1}^{i_{\max}} Z_i n_i \,, \tag{1.1}$$

where n_e and n_i are the particle number densities of electrons and ion species i, respectively, and $i_{\max} = Z$ is given by the atomic number of the considered element[5].

Plasmas can be characterized by different parameters. The mean degree of ionization

$$Z_{\text{mean}} = \sum_i Z_i n_i / \sum_i n_i \tag{1.2}$$

can be calculated for plasmas in thermodynamic equilibrium with the help of coupled Saha equations [16].

The coupling parameter Γ is a measure for the strength of the interaction between the plasma particles. A plasma is strongly or weakly coupled for $\Gamma > 1$ and $\Gamma < 1$, respectively. It is derived from the ratio of potential energy to kinetic energy. For ion-ion coupling, we have

$$\Gamma_{ii} = \frac{l}{d_i}, \quad \text{with} \quad l = \frac{Z_i^2 e^2}{4\pi\epsilon_0 k_{\text{B}} T}, \quad \text{and} \quad d_i = \left(\frac{3}{4\pi n_i}\right)^{\frac{1}{3}}, \tag{1.3}$$

where ϵ_0 and k_{B} are the electric and Boltzmann constant, respectively. Analogous to the ion-ion coupling Γ_{ii}, the electron-electron coupling Γ_{ee} and the electron-ion coupling Γ_{ei} can be defined with $Z_e = 1$, d_e, and $d_{\text{tot}} = (3/(4\pi(n_e + \sum_i n_i)))^{\frac{1}{3}}$. The degeneracy parameter

$$\Theta = \frac{k_{\text{B}} T}{E_{\text{F}}} \tag{1.4}$$

is defined by the ratio between thermal energy and Fermi energy E_{F}. For $\Theta < 1$, we have to take degeneracy into account and use Fermi and Bose statistics instead of Boltzmann statistics, respectively.

All plasma parameters depend on electron density and temperature. This dependence is depicted in Fig. 1.1, where astrophysical and laboratory plasmas are shown, as well as the electron-electron coupling Γ_{ee} and the electron degeneracy parameter Θ_e.

[5] If there is only one element in the plasma

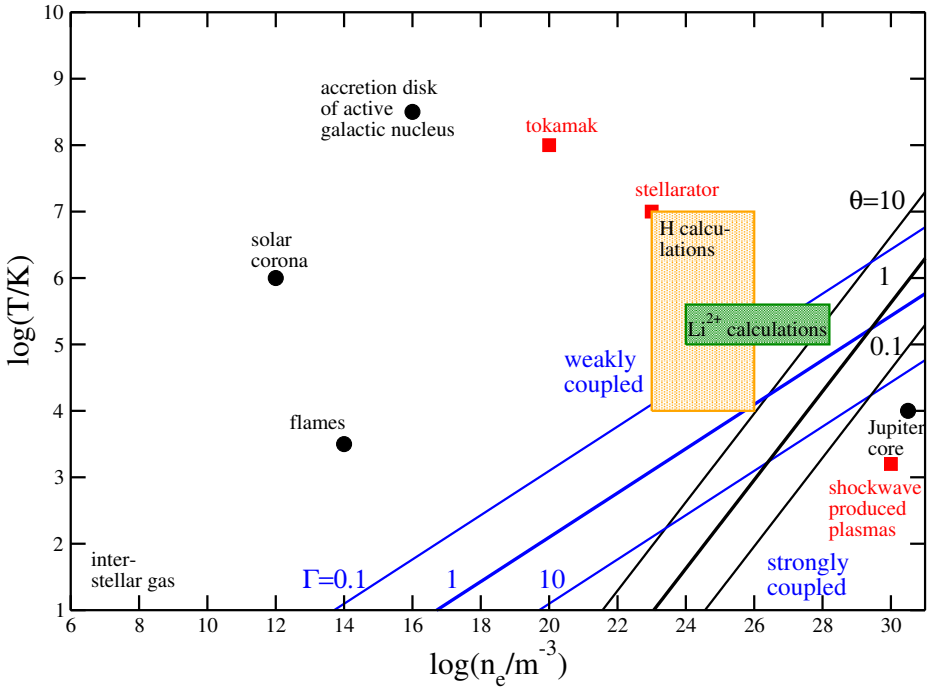

Figure 1.1.: Classification of ● natural and ■ artificially produced plasmas in the temperature-density plane. Relevant parameter regions for calculations of this thesis are marked in orange (H) and green (Li^{2+}).

1.2.2. Spectral line measurements of H and Li plasmas

To produce a dense plasma, i.e. a plasma with a high free electron density, solid or liquid matter has to be exposed to high amounts of energy. This energy is used to free the electrons from the binding potential of the nuclei. Within this thesis, two types of plasmas are used for comparisons with experimental data. For spectral line measurements of hydrogen, plasmas are produced in arc-discharges, see e.g. [17, 18]. Lithium plasmas are usually produced by laser irradiation [19–29]. This is due to the fact that higher energies have to be reached to ionize lithium, i.e. 13.6 eV for H^+ and (5.4+75.6) eV=81 eV for Li^{2+} [30, 31].

Hydrogen plasmas

Since H is mostly a testbed for our method, only a few comparisons to measured spectra have been carried out within this thesis. Although the correct calculation

of plasma pressure broadening for H Lyman lines is still under discussion [32][6], few measurements are available and none with up-to date equipment and resolution. We use the measurement of Grützmacher and Wende from 1977 [17] because it has well defined plasma parameters under rather dense conditions. In the experiment, a wall-stabilized argon arc source was used to create dense equilibrium plasmas with $n_e \sim 10^{23}$ m^{-3} at $T \sim 10^4$ K. Under these conditions, pressure broadening by electrons and Ar^+ ions dominates over the Doppler broadening of the Lyman-α line of H. With a hydrogen density of $n_H < 10^{19}$ m^{-3}, the plasma was optically thin and reabsorption could be avoided. The spectrometer bandwidth was stated to be better than $\lambda/\Delta\lambda = 30390$. The measured line profiles had already been compared to the unified theory in [17], and the remaining discrepancy had been resolved by Lee [33] with a perturbative method taking ion-dynamics into account. There, the importance of ion-dynamics for H Lyman-α had been emphasized for the first time.

Laser-induced lithium plasmas

Although there exist lithium plasma studies from the 1960s, which used strong electric currents through thin lithium wires to produce weakly ionized plasmas, we concentrate on the laser-produced plasmas from the last three decades. Due to the potential application as EUV light source a focus on the experiments was on the Li^{2+} Lyman-α line [19–27]. Several groups used different laser pulse durations, intensities, and wavelengths to obtain EUV radiation as intense as possible. Other groups studied Li^+ [28, 29]. Since a "cold" liquid or solid target is irradiated with one or more laser pulses, the produced plasma is not homogeneous and develops – expands and cools – with time. Since most measurements are space- and time-integrated, emission from areas with different plasma parameters contributes to the total spectrum. This fact has to be considered when the spectrum is analyzed to determine (mean) plasma parameters. Two measurements were able to avoid the time-integration. For Li^+, Doria *et al.* used a set-up which allowed for space and time resolution. These measurements have been analyzed by Omar [34] using a quantum-statistical approach for He-like emitters. For Li^{2+}, George *et al.* measured time-resolved Lyman lines [26, 27]. Unfortunately, these measurements were not suitable for a detailed line shape analysis due to an accidentally slightly rotated CCD-camera [35].

[6] Some of the discrepancies between MD simulations and analytical models could be resolved during the 2nd Spectral Line Shapes in Plasmas Workshop in Vienna 2013.

In the following, only those experiments which are referred to in the comparisons with our theory are discussed. For Li^{2+}, two measurements of Schriever *et al.* [20, 21] have been analyzed. In their experimental setup, a pulsed laser beam of a Nd:YAG laser (wavelength $\lambda = 1064$ nm) with a maximum energy of 1300 mJ per pulse was focused on the surface of a lithium target. Finding a spot size of 30 μm, intensities between 10^{10} and $1.1 \cdot 10^{13}$ W/cm^2 were realized by attenuating the laser beam. The pulse length was 13 ns. The emitted light has been detected in single pulse experiments at an angle of 45°. The emission time was measured to be as long as the laser pulse (13 ns). In [20], the line width of Lyman-α is determined in first and second diffraction order. The line profile is measured with a Rowland circle grazing-incidence spectrograph with the spectral resolution $\lambda/\Delta\lambda = 650$ in first order and $\lambda/\Delta\lambda = 1300$ in second order. With an intensity of $I_\mathrm{L} = 5.5 \cdot 10^{11}$ W/cm^2 of the laser, the plasma is assumed to have an average electron temperature of $k_\mathrm{B}T_e = 47$ eV. The electron density is expected to be above $n_e = 1 \cdot 10^{25}$ m^{-3} [20].

The Lyman-spectrum (α to γ) has been measured in [21] with a spectral resolution of $\lambda/\Delta\lambda = 300$. A laser intensity of $I_\mathrm{L} = 1.1 \cdot 10^{13}$ W/cm^2 was used to generate the plasma. The simultaneous measurement of different Lyman lines is suitable for plasma diagnostic, since temperature and mean electron density can both be deduced. The temperature is calculated under the assumption of a Boltzmann population of excited states from integrated line-intensity ratios. The mean electron density can be deduced from a comparison of measured and calculated spectral line profiles.

To discriminate between different line shape theories, plasma parameters have to be well known[7] and instrumental broadening has to be small. Unfortunately, none of these conditions applies for the spectrum in [21].

1.2.3. Photon emission and radiative transport

A hohlraum filled with a dense plasma in local thermal equilibrium can be seen as a blackbody radiator, thus, the emitted energy is given by Planck's law in the frequency domain. The following expressions are given in angular frequency domain with index ω, the notation follows [36]. The spectral radiance of a black body is given by

$$L_\omega^\mathrm{BB}(\omega; T) = \frac{\hbar\omega^3}{4\pi^3 c^2 (e^{\frac{\hbar\omega}{k_\mathrm{B}T}} - 1)}\,, \tag{1.5}$$

[7] Thus, temperature and density have to be determined from other measured data and not from the line spectrum.

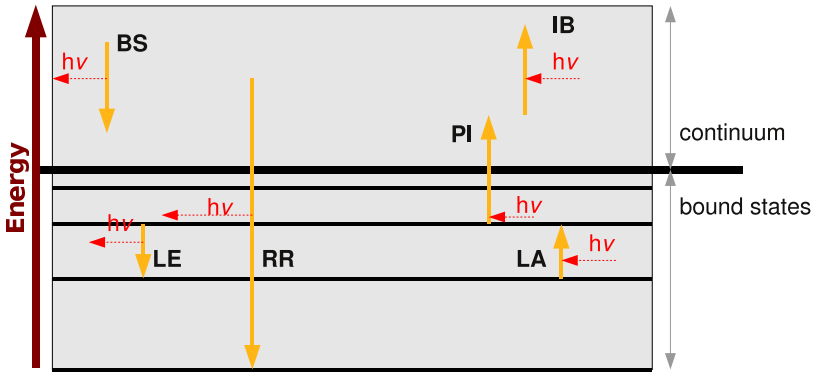

Figure 1.2.: Basic radiative processes. BS: bremsstrahlung, IB: inverse bremsstrahlung, RR: recombination radiation, PI: photo ionization, LE and LA: spectral line emission and absorption with photon energy $h\nu = \hbar\omega$.

where c is the speed of light. It is defined as the spectral power in an angular frequency interval, which is emitted from a small area into a small solid angle in the normal direction. Thus, it is the energy per time, angular frequency, area and solid angle with the unit $\mathrm{WHz^{-1}m^{-2}sr^{-1}}$.

In optically thin plasmas, the radiance is dominated by radiation from electron transitions in the electric field of the ions. The possible transitions are shown in Fig. 1.2: Electrons can change their state within the continuum and emit (bremsstrahlung) or absorb energy (inverse bremsstrahlung) in this free-free process. The second process is given by ionization and recombination, where a bound electron enters the continuum of free states and vice versa, respectively. The last possible electron transition leads to spectral line emission and absorption, respectively, and is caused by a transition from an upper bound state n to a lower bound state n' and vice versa.

Self-absorption

To connect the line emission with black body radiation, one has to consider self-absorption, i.e. the re-absorption and -emission of light which has been emitted by the plasma before, see e.g. [36, 37]. In thermal equilibrium, Kirchhoff's law can be applied

$$\epsilon_\omega(\omega;T) = L_\omega^{\mathrm{BB}}(\omega;T)\alpha'(\omega;T)\,. \tag{1.6}$$

It relates the spectral emission coefficient ϵ_ω to the effective absorption coefficient α'_ω via the black body radiance, Eq. (1.5). The spectral emission coefficient is given by the spontaneous emitted power per volume, angular frequency interval, and solid angle. The effective absorption coefficient consists of true absorption and the reduction of the absorption by induced emission. The effective absorption is given by

$$\alpha'(\omega;T) = \left(1 - e^{-\frac{\hbar\omega}{k_\mathrm{B}T}}\right) \alpha(\omega;T)\,. \tag{1.7}$$

For $k_B T \ll \hbar\omega$, the induced emission is negligible, thus $\alpha' = \alpha$.

Radiative transport

For a thin plasma layer in thermal equilibrium with a constant temperature and density, the equation of radiative transport can be treated in one dimension,

$$\frac{dL_\omega(\omega;x)}{dx} = \epsilon_\omega(\omega;x) - \alpha'(\omega;x)L_\omega(\omega;x)\,. \tag{1.8}$$

Taking a single layer of thickness d and temperature T, the equation can be solved and gives

$$L_\omega(\omega) = \left(1 - e^{-\alpha'(\omega)d}\right) L_\omega^{\mathrm{BB}}(\omega)\,. \tag{1.9}$$

For the solution, the optical depth $\tau(\omega;x) = \int_x^d dx'\alpha'(\omega;x')$ has been introduced and $L_\omega^{\mathrm{BB}}(\omega)$ has been used as source function, for details see [36].

Two limits can be considered: For $\alpha'(\omega)d \to \infty$, i.e. for great absorption coefficients or thick layers, the spectral radiance equals the black body radiance. In the limit of small absorption coefficients, the exponential function can be expanded, thus leading to $L_\omega(\omega) = \alpha'(\omega)dL_\omega^{\mathrm{BB}}(\omega) = \epsilon_\omega(\omega)d$, which corresponds to emitted spectral lines.

For intense lines, the radiative transport through the plasma layer limits the intensity in the line center to the Black body radiation, thus broadening the line. This can be seen in Fig. 1.3 for different optical depths τ.

Line emission

Every spectral line has an absorption profile $\alpha'(\omega)$. As the frequency interval over a spectral line is small, the transition strength $a'_{n'n}$ of the atom from level n' to level n can be used together with a normalized line profile $P(\omega)$. Then, the absorption profile is given by

$$\alpha'(\omega) = a'_{n'n}P(\omega)\,, \tag{1.10}$$

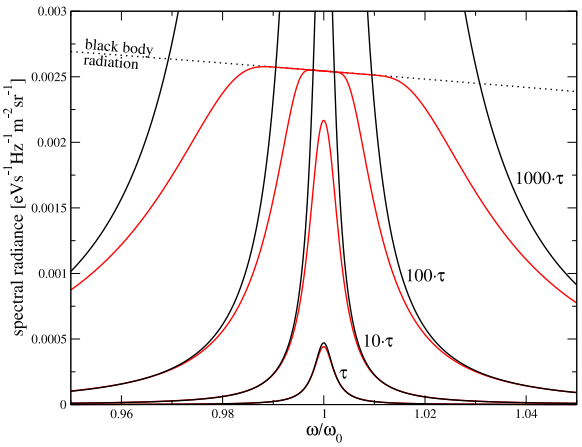

Figure 1.3.: Self-absorption on the example of Li^{2+} Lyman-α line with half width $\gamma_\omega = 7 \cdot 10^{13}$ Hz for a plasma with $k_B T = 22$ eV and density of ions in the ground state $n_{Li^{2+},0} = 10^{23}$ m^{-3}. The thickness of the plasma layer $d = (0.003; 0.03; 0.3; 3)$ cm is indicated by the corresponding optical thickness $(\tau; 10\tau; 100\tau; 1000\tau)$. Shown are black body radiation (dotted), line emission without (black) and with (red) self-absorption.

with the normalization $\int P(\omega) d\omega = 1$. Each coefficient of true absorption $a_{n'n}$ can be calculated with the help of the Einstein coefficient $B_{n'n}$ and the oscillator strength $f_{n'n}$, respectively, and the density $n_{n'}$ of atoms being in the lower level [36, 38],

$$a_{n'n} = \frac{\hbar\omega_{n'n}}{c} B_{n'n} n_{n'} = \frac{e^2}{4\varepsilon_0 m_e c} f_{n'n} n_{n'} \,. \tag{1.11}$$

The effective absorption coefficient $a'_{n'n}$ follows then from Eq. (1.7).

1.2.4. The shape of spectral lines

Even for an isolated emitter, the spectral line profile $P(\omega)$ is not a delta function at the transition frequency $\omega_{nn'} = \frac{1}{\hbar}(E_n - E_{n'})$, but has a natural line width. Instead of ω, we use sometimes $\Delta\omega = \omega - \omega_{nn'}$ as the variable for the line profile. Besides the natural line width, several effects influence the shape of a spectral line. They are depicted schematically for a Li^{2+} plasma in Fig. 1.4 and are discussed in the following paragraphs.

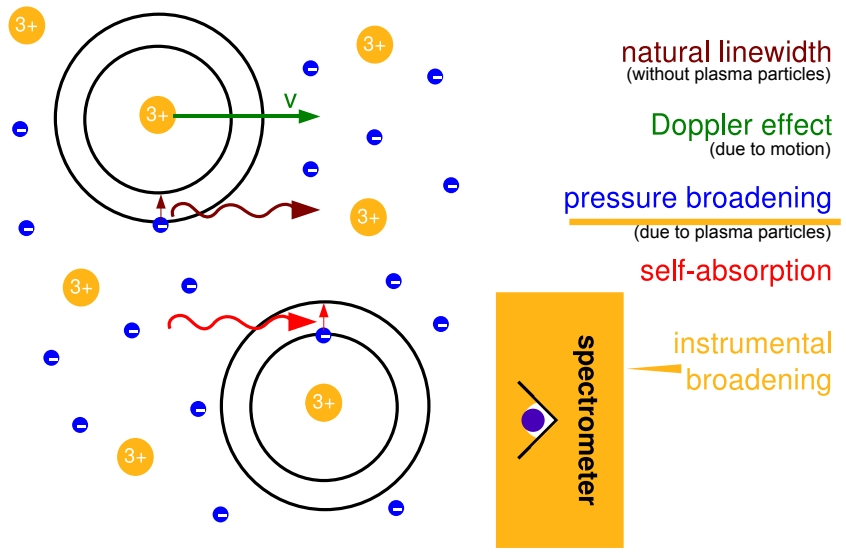

Figure 1.4.: Schematics of processes influencing the line shape. Natural linewidth arises already for isolated emitters. Doppler broadening is caused by the motion of the emitter. Plasma pressure broadening is due to the charged plasma particles. Self absorption sets in as soon as a plasma is not optical thin, i.e. other ions reabsorb the emitted photon. Instrumental broadening is due to the finite resolution of the spectrometer.

Natural line width

The natural line width is due to the final lifetime of the excited atomic state. The lifetime is restricted by the interaction with the photonic field. Emission and absorption change the state of the emitter. In the simplest approximation, the emitter is seen as a classical oscillator. Then, the natural line width stems from a damping of the oscillation due to the energy loss of an accelerated charge [38]. The resulting line profile is given by a Lorentzian

$$P(\Delta\omega) = \frac{1}{\pi} \frac{\frac{1}{2}\gamma_\omega}{\Delta\omega^2 + (\frac{1}{2}\gamma_\omega)^2}\,, \tag{1.12}$$

with γ_ω being the full width at half maximum (FWHM). In wavelength domain, the width is classically given by [38]

$$\gamma_\lambda = \frac{e^2}{3m_e c^2 \epsilon_0} = 1,18 \cdot 10^{-4}\,\text{Å}\,, \tag{1.13}$$

independent on the wavelength. The connection to the frequency domain is given by

$$\gamma_\omega = \frac{\omega_{nn'}^2}{2\pi c}\gamma_\lambda \,. \tag{1.14}$$

To improve the estimate of Eq. (1.13), we take quantum-mechanical effects into account via Einstein's coefficients of emission $A_{nn'}$. Then, the width is defined as [36]

$$\gamma_\omega = \sum_{k<n} A_{nk} + \sum_{k<n'} A_{n'k} \,, \tag{1.15}$$

where the energy levels k have to be lower than the upper level n and the lower level n', respectively. Thus, only levels are considered that can be reached by spontaneous emission. Einstein's coefficients of emission can be taken from a database [39] or calculated as

$$A_{nk} = \frac{4\omega_{nn'}^3}{3\hbar c^3} g_n |\langle n|\mathbf{r}|k\rangle|^2 \,, \tag{1.16}$$

with the degeneracy of the upper level g_n and the dipole matrix element $\langle n|\mathbf{r}|k\rangle$.

For Li^{2+} Lyman-α, the natural line width after Eqs. (1.14) and (1.15) is $\gamma_\lambda = 10^{-4}$ Å and thus comparable to the classical approach, see Eq. (1.13). In general, both equations give different natural line widths. In the examples in this thesis, the natural line width is always negligible compared to pressure and Doppler broadening.

Doppler broadening

Doppler broadening is caused by the thermal motion of the emitters. Following the description of [38], the velocity component of an emitter in the direction of sight is v_x. A statistical velocity distribution $W(v_x)$ has to be assumed for all emitters. For non-degenerate, non-relativistic plasmas in thermal equilibrium, a one dimensional Maxwell-Boltzmann distribution is suitable

$$W(v_x) = \sqrt{\frac{M}{2\pi k_\mathrm{B} T}} e^{-\frac{M v_x^2}{2k_\mathrm{B}T}} \,, \tag{1.17}$$

where M stands for the emitter's mass. Due to the Doppler effect, the observer measures the frequency

$$\omega = \omega_{nn'}\left(1 + \frac{v_x}{c}\right) \quad \Rightarrow \qquad \Delta\omega = \omega_{nn'}\frac{v_x}{c} \quad \Rightarrow \; dv_x = \frac{c}{\omega_{nn'}} d\Delta\omega \,. \tag{1.18}$$

This leads to the Gaussian line profile

$$P(\Delta\omega) = \frac{c}{\omega_{nn'}} \sqrt{\frac{M}{2\pi k_\mathrm{B} T}} e^{-\frac{M c^2 \Delta\omega^2}{2k_\mathrm{B} T \omega_{nn'}^2}} \,, \tag{1.19}$$

with the width (FWHM)

$$\gamma_\omega = \frac{2\omega_{nn'}}{c}\sqrt{\frac{2\ln 2 k_\mathrm{B} T}{M}}\,. \tag{1.20}$$

Thus, Doppler broadening is proportional to $\sqrt{T}$ for a non-degenerate plasma in thermal equilibrium. For a different velocity distribution, the Doppler broadening is non-Gaussian and can be calculated analogously. Depending on density and temperature, the Doppler broadening can be the dominating broadening mechanism of a spectral line.

Pressure broadening

Pressure broadening is caused by the surrounding medium, i.e. in our cases ions, electrons, and neutral atoms, affecting the energy levels of the emitter. First theoretical considerations have been developed by Lorentz for gases [40]. There, the emitter is treated as a classical oscillator with frequency $\omega_{nn'}$. When a perturber collides with the emitter, its oscillation is stopped. Averaging over all perturbers leads to a Lorentzian profile

$$P(\Delta\omega) = \frac{\gamma}{2\pi}\frac{1}{(\Delta\omega)^2 + (\frac{1}{2}\gamma)^2}\,. \tag{1.21}$$

Here, the width γ of the line is produced by perturber-emitter collisions. The theory has been advanced by Weisskopf. There, strong collisions which stop the oscillation completely, and weak collisions which alter only the phase of the oscillation are distinguished [41].

Pressure broadening is a general term for all density dependent broadening (and shift) mechanisms. For neutral perturbers, it is mainly given by Van-der-Waals interactions and for charged perturbers by Coulomb interactions. There exist several theories to describe pressure broadening. Besides the differentiation between perturber species (atoms, molecules, electrons, ions), the theories can be sorted by the way emitter and perturber are treated (classical or quantum-mechanical). Furthermore, the dynamics of the perturber can be neglected (static approach) or considered in a dynamic theory. In the plasma, it is justified by different time scales to treat the ions within a quasi-static theory, using their electric microfields, and the electrons within collision theory. During the time of emission $t_\mathrm{em} = \Delta\omega^{-1}$, every electron is likely to complete a full collision with the emitter. During the same time, the heavier ions are moving slowly, producing a quasi-static electric field at the emitter's site.

The collision time of an average perturber-emitter collision, can be approximated with the help of the collision parameter $\rho \approx n_{e/i}^{-\frac{1}{3}}$ and the thermal velocity of the perturber $v_{\text{therm}} = \sqrt{8k_{\text{B}}T/\pi m_{e/i}}$ [6, 42] as

$$t_{\text{coll}} = \frac{\rho}{v_{\text{therm}}} \approx \left(n_{e/i}^{\frac{1}{3}} \sqrt{\frac{8k_{\text{B}}T}{\pi m_{e/i}}} \right)^{-1} , \tag{1.22}$$

where T, $n_{e/i}$, and $m_{e/i}$ are temperature, density, and mass of perturbing electrons/ions, respectively.

The collision theory can be applied, if $t_{\text{coll}} \ll t_{\text{em}}$, and thus $|\Delta\omega| \ll \frac{v_{\text{therm}}}{\rho}$. This is always the case for the line center. The quasi-static approximation is applicable, if $t_{\text{coll}} \gg t_{\text{em}}$, leading to $|\Delta\omega| \gg \frac{v_{\text{therm}}}{\rho}$, i.e. in the line wings. Due to the different masses of electrons and ions, both theories have different ranges of validity for different perturber species. Furthermore, the validity range depends on the width of the line. E.g., if the collisional part in the line center corresponds to a small fraction of the line width, it is justified to calculate the whole profile in quasi-static approximation. In Sec. 1.2.5, different theories for plasma pressure broadening are presented briefly with a focus on recent developments.

Instrumental broadening

To compare theoretical results with measurements, the finite resolution of the spectrometer has to be taken into account, too. The instrumental resolution is assumed to have a distribution $W^I(\omega)$ (often approximated by a Gaussian). Then, the calculated line profile $P(\Delta\omega)$ has to be convolved with this distribution to account for instrumental broadening,

$$P^I(\Delta\omega) = \int_{-\infty}^{\infty} W^I(\omega') P(\Delta\omega - \omega') d\omega' . \tag{1.23}$$

1.2.5. Recent progress in plasma pressure broadening

As mentioned in the general description of pressure broadening in Sec. 1.2.3, one possibility to classify plasma pressure broadening theories is their treatment of the perturbers and emitters as classical or quantum objects. Probably the most used theory[8] is the semi-classical theory with binary collisions. It is inseparably connected

[8] known as standard theory

to the name Hans Griem, although others were involved in the development [42–44], too. Here, the electronic perturber moves as a classical particle on a straight (or hyperbolic) trajectory, while the emitter is treated quantum-mechanically and is affected by the interaction with the colliding electron and the quasi-static microfield of the surrounding ions [42, 43, 45]. Besides the classical view, this theory is limited by the applicability of the used approximations – namely, binary collisions for electrons and the quasi-static assumption for ions. To overcome these shortcomings, a smooth description from the collision approximation to the static approximation has been developed by Vidal *et al.* [46, 47] with the "unified theory". It allows for incomplete collisions. To go beyond the classical view, a full quantum-mechanical treatment of the perturbers has been developed by Baranger in [48]. Due to the increasing computer power during the last decades, computer simulations are widely used to calculate plasma pressure broadening, e.g. [49–52]. There, simulated electric fields are used as input to calculate the time-evolution of the emitter exposed to such a field. Since all these methods have already been reviewed in detail, e.g. in [53–55], here, only recent developments in plasma pressure broadening are discussed.

Briefly stated, the progress in simulations is mainly given by the possibility to put more particles in the simulation box and to include plasma-particle interactions due to increasing computer power and new sophisticated numerical methods. However, the main ideas and techniques behind the simulations are unchanged.

The problem to include ion-dynamics into a so far quasi-static theory, has been tackled again with the frequency-fluctuation model [56]. With this model, ion-dynamics can be taken into account for spectra which include many Stark-broadened components[9]. Of course, it can be used for less complex lines, too. A simplified implementation of the model [57] made it possible to easily take ion-dynamics into account starting from a line shape which had been calculated for static ions. The model has been applied in [14] of this thesis and will be discussed further in Sec. 1.3.2.

Since the effect of strong electron-emitter collisions is only estimated in the standard theory[10], in [58] the concept of "penetrating collisions"[11] has been developed using softened interaction potentials. This allows for a more sensible treatment of strong collisions within the semi-classical view. For the quantum-statistical approach,

[9] e.g. 50 upper states [56]

[10] Broadening due to strong collisions $\sim n_e v_{\mathrm{therm}} \rho_{\mathrm{min}}^2$ with Weisskopf's radius ρ_{min}.

[11] close electron-emitter collisions within the area where the wave function of the emitter has a substantial value

the treatment of strong collisions is also in the focus of this thesis, see Sec. 1.3.3.

The importance to go beyond the binary collision theory has been stated in [59, 60]. There, the unified theory was extended[12] to account for multiple collisions via a renormalization of the kinetic theory using the BBGKY hierarchy[13]. With this method weak correlated collisions are taken into account. To estimate the limits of this approach, parameters have been derived stating the importance of multiple weak and strong collisions, respectively. In App. A.1, these parameters are used in the discussion of the effect of correlated collisions for the lines calculated within this thesis, too. Weak correlated collisions can be taken into account in our quantum-statistical Born approach in a natural way via the dynamical screening. For the T-matrix approach, we could include the effect of correlated collisions with static Debye screening.

The most general extension has been derived in the "generalized theory" by Oks and his colleagues, it has been reviewed in [61]. There, the no-coupling approximation[14] which is used in most analytic approaches is circumvented. *Indirect* coupling via the interaction (and back interaction) with the emitter is considered as well as *direct* coupling, i.e. acceleration of electrons by the ionic field. Furthermore, the generalized theory provides an exact analytical result for ion-dynamical Stark broadening. The electron-ion coupling effect gives an important contribution for strongly coupled plasmas. Since the calculations in this thesis are not within the strongly coupled regime, electron-ion coupling and emitter-perturber back-reactions are not considered further here.

1.3. Quantum-statistical approach to spectral line profiles

After the brief overview over different methods to calculate plasma pressure broadening in the previous section, here, the quantum-statistical method which is used in this thesis is presented in more detail. The key formulas are derived starting from current-current correlation functions leading to the well-known dipole-dipole correlation functions. The treatment of ionic perturbers is discussed in quasi-static as well as

[12] UTPP for "unified theory++"
[13] Bogoliubov–Born–Green–Kirkwood–Yvon hierarchy
[14] independent treatment of ions and electrons

dynamic models. The broadening due to electrons is described within a perturbative Born approach as well as an effective two-particle T-matrix approach.

For a microscopic view on broadening and shift mechanisms, it is helpful to establish the connection between the transversal part of the dielectric function $\epsilon_{\mathrm{tr}}(\mathbf{k},\omega)$, depending on the transfer wave number $\mathbf{k}$, and the complex refraction index. We follow Ref. [62], where more details can be found. The long-wavelength limit ($\mathbf{k}\to 0$) is applied. This is justified as long as the wavelength of the spectral line is much greater than the atomic size of the emitter. This is true for optical as well as our considered EUV lines (10 nm $\gg a_0$). Starting from

$$n(\omega)+\imath\frac{c}{2\omega}\alpha(\omega)=\lim_{\mathbf{k}\to 0}\sqrt{\epsilon_{\mathrm{tr}}(\mathbf{k},\omega)}\,, \tag{1.24}$$

the absorption coefficient can be expressed as

$$\alpha(\omega)=\frac{\omega}{c\;n(\omega)}\lim_{\mathbf{k}\to 0}\mathrm{Im}\;\epsilon_{\mathrm{tr}}(\mathbf{k},\omega)\,, \tag{1.25}$$

and the (real) index of refraction as

$$n(\omega)=\frac{1}{\sqrt{2}}\lim_{\mathbf{k}\to 0}\sqrt{\mathrm{Re}\;\epsilon_{\mathrm{tr}}(\mathbf{k},\omega)+\sqrt{(\mathrm{Re}\;\epsilon_{\mathrm{tr}}(\mathbf{k},\omega))^2+(\mathrm{Im}\;\epsilon_{\mathrm{tr}}(\mathbf{k},\omega))^2}}\,. \tag{1.26}$$

Since the information about any direction is lost in the long wavelength limit, the transversal and the longitudinal part of the dielectric function become identical in this limit, see e.g. [63]. Thus, we concentrate in the following on the longitudinal part of the dielectric function, although a similar discussion can be carried out for the transversal part[15], see [64]. Following the definitions in Ref. [65], the longitudinal part of the dielectric function can be connected to the longitudinal part of the polarization function $\Pi_{\mathrm{l}}(\mathbf{k},\omega+\imath\delta)$ via

$$\epsilon_{\mathrm{l}}(\mathbf{k},\omega+\imath\delta)=1-\frac{1}{\epsilon_0 k^2}\Pi_{\mathrm{l}}(\mathbf{k},\omega+\imath\delta)\,. \tag{1.27}$$

Here and in the following, limit $\delta\to 0+$ is implied. Together with Eq. (1.25), we obtain for the absorption coefficient

$$\alpha(\omega)=-\frac{\omega}{cn(\omega)}\lim_{\mathbf{k}\to 0}\frac{1}{\epsilon_0 k^2}\mathrm{Im}\;\Pi_{\mathrm{l}}(\mathbf{k},\omega+\imath\delta)\,. \tag{1.28}$$

[15] which is directly connected to electro-magnetic fields and thus to radiation

In the chemical picture, the polarization function $\Pi(\mathbf{k}, \omega+\imath\delta)$ can be split into different parts including bound-bound, free-bound, and free-free electronic features in a cluster expansion [62]

$$\Pi = \Pi_{\text{free-free}} + \Pi_{\text{free-bound}} + \Pi_{\text{bound-bound}} + \text{higher orders}\,. \tag{1.29}$$

This work is only concerned with the polarization function for bound-bound electronic transitions, leading to spectral lines. The free-free and free-bound contributions are connected to bremsstrahlung and continuum edges, respectively, see Fig. 1.2. We will have a closer look at the resulting line absorption coefficient in the next section.

1.3.1. Line absorption coefficients from the current-current correlation function

Previously, the calculation of spectral line shapes was usually based on the chemical picture of partially ionized plasmas with well defined atoms, which allows us to consider directly dipole-dipole correlations to obtain the polarization function. This has been elaborated in Refs. [3, 54, 62]. Here, a slightly different way is presented. It has the advantage to start from current-current correlations instead. This is useful as soon as the chemical picture with well defined atoms or ions as emitters breaks down due to overlapping wave functions of neighboring emitters. A formal connection between currents and dipoles can be found in App. A.2. For the line shape calculations in this thesis, we can use the dipole-dipole description. However, this is only possible as long as collective effects do not play a role.

To obtain the polarization function via current-current correlations, linear response theory [66] and the Zubarev formalism [67, 68] are applied. Then, the polarization function can be calculated from equilibrium correlation functions. The connection to the irreducible[16] current-current correlation function is given by [65],

$$\Pi_{\text{l}}(\mathbf{k}, \omega) = -\frac{\imath k^2 \beta \Omega}{\omega} \langle j_{\mathbf{k}}^{\text{long}}; j_{\mathbf{k}}^{\text{long}} \rangle_{\omega+\imath\delta}^{\text{irred}}\,, \tag{1.30}$$

with the longitudinal parts of the canonical current density, generally defined as [65]

$$\mathbf{j}_{\mathbf{k}} = \sum_c \mathbf{j}_{\mathbf{k}}^c = \frac{1}{\Omega} \sum_{c,\mathbf{p}} \frac{e_c}{m_c} \hbar \mathbf{p} n_{\mathbf{p},\mathbf{k}}^c\,. \tag{1.31}$$

[16] This means that the diagram cannot be separated into two diagrams by cutting one interaction line. In this way, double counting of diagrams is avoided.

Here, the index c corresponds to the different spins and sorts, i.e. electrons and ions in the plasma, and the number density is $n^c_{\mathbf{p},\mathbf{k}} = a^\dagger_{\mathbf{p}-\mathbf{k}/2,c} a_{\mathbf{p}+\mathbf{k}/2,c}$[17]. Thus, the complete expression for the absorption coefficient in terms of the longitudinal current-current correlation function is

$$\alpha(\omega) = \frac{\omega}{cn(\omega)} \lim_{\mathbf{k}\to 0} \frac{1}{\epsilon_0 k^2} \mathrm{Im} \left(\frac{\imath k^2 \beta \Omega}{\omega} \langle j^{\mathrm{long}}_{\mathbf{k}}; j^{\mathrm{long}}_{\mathbf{k}} \rangle^{\mathrm{irred}}_{\omega+\imath\delta} \right) \tag{1.32}$$

$$= \frac{\beta\Omega}{cn(\omega)\epsilon_0} \lim_{\mathbf{k}\to 0} \mathrm{Re} \left(\langle j^{\mathrm{long}}_{\mathbf{k}}; j^{\mathrm{long}}_{\mathbf{k}} \rangle^{\mathrm{irred}}_{\omega+\imath\delta} \right) . \tag{1.33}$$

A definition of the correlation functions via Kubo scalar products and thermodynamic Green's functions can be found in Appendix A.3. In Ref. [65], further details on current-current correlation functions and the application for unbound particles are given. From Eq. (1.31) follows that the current-current correlation can be expressed by a density-density correlation

$$\langle \mathbf{j}^c_{\mathbf{k}}; \mathbf{j}^{c'}_{\mathbf{k}} \rangle_{\omega+\imath\delta} = \left(\frac{\hbar}{\Omega} \right)^2 \sum_{\mathbf{p}\mathbf{p}'} \frac{e_c e_{c'}}{m_c m_{c'}} \mathbf{p}\cdot\mathbf{p}' \langle n^c_{\mathbf{p},\mathbf{k}}; n^{c'}_{\mathbf{p}',\mathbf{k}} \rangle_{\omega+\imath\delta} . \tag{1.34}$$

For the longitudinal part[18], we take $\mathbf{k} = k\mathbf{e}_z$ and obtain

$$\langle j^{c,\mathrm{long}}_{\mathbf{k}}; j^{c',\mathrm{long}}_{\mathbf{k}} \rangle_{\omega+\imath\delta} = \frac{\hbar^2}{\Omega^2} \sum_{cc'} \sum_{\mathbf{p}\mathbf{p}'} \frac{e_c e_{c'}}{m_c m_{c'}} p_z p'_z \langle n^c_{\mathbf{p}\mathbf{k}}; n^{c'}_{\mathbf{p}'\mathbf{k}} \rangle_{\omega+\imath\delta} . \tag{1.35}$$

The density-density correlation function is given by the density-density Green's function, see Eq. (A.23),

$$\langle n^c_{\mathbf{p},\mathbf{k}}; n^{c'}_{\mathbf{p}',\mathbf{k}} \rangle_z = \frac{\imath}{\beta} \int_{-\infty}^{\infty} \frac{\mathrm{d}\omega}{\pi} \frac{1}{z-\omega} \frac{1}{\omega} \mathrm{Im}\, G_{n^c_{\mathbf{p},\mathbf{k}} n^{c'\dagger}_{\mathbf{p}',\mathbf{k}}}(z) . \tag{1.36}$$

$G_{n^c_{\mathbf{p},\mathbf{k}} n^{c'\dagger}_{\mathbf{p}',\mathbf{k}}}(\omega + \imath\delta)$ is in lowest order given by the product of two free single particle Green's functions, where the free single particle Green's function is [69]

$$G^{(0)}_1(\mathbf{p},\mathbf{p}';z_\nu) = \frac{\delta_{\mathbf{p}\mathbf{p}'}}{\hbar z_\nu - \epsilon^c_{\mathbf{p}}} , \tag{1.37}$$

with $\epsilon^c_{\mathbf{p}} = E_{\mathbf{p}} - \mu_c = \frac{\hbar^2 p^2}{2m} - \mu_c$ and the Matsubara frequency $z_\nu = \frac{\pi\nu}{\imath\beta\hbar}$ with $\nu = \pm 1; \pm 3; \ldots$ for fermions and $\nu = 0; \pm 2; \pm 4; \ldots$ for bosons. Here, μ_c is the chemical potential of the particle sort c. The calculation for free particles can be found in Ref. [65] leading to the random phase approximation (RPA) result for the dielectric function.

[17] defined in terms of creation and annihilation operators

[18] longitudinal current in z-direction

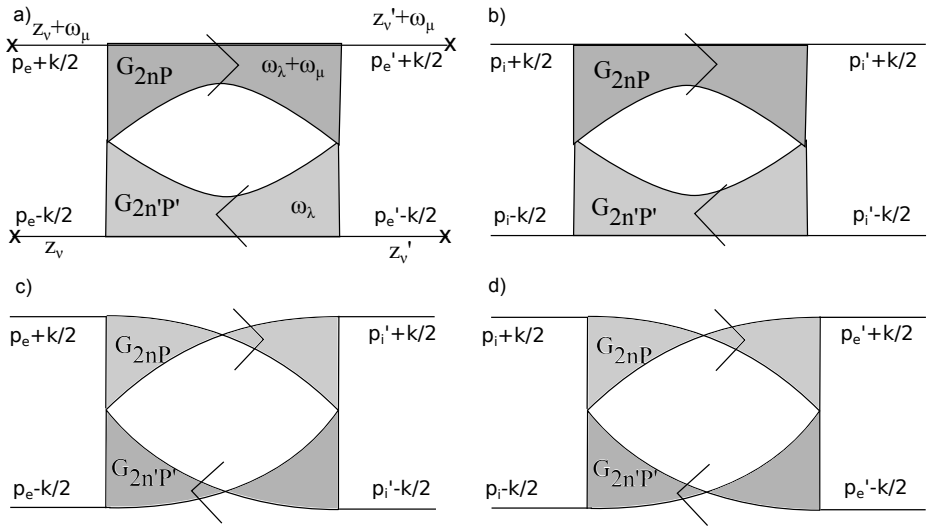

Figure 1.5.: Diagrams to calculate the density-density Green's functions. a) electron-electron G_{n^e,n^e}, b) ion-ion G_{n^i,n^i}, c) and d) electron-ion G_{n^e,n^i} and G_{n^i,n^e}. Matsubara frequencies are only included in Fig. a): z and ω for fermionic and bosonic propagators, respectively. The incoming and outgoing propagators are cut. For coupling to an interaction, incoming and outgoing arguments are $\mathbf{k}$ and ω_μ. Bound two-particle propagators $G_2(nP)$ are shaded for clarity.

Bound states

To consider spectral lines, we have to take bound states into account. For this reason the Green's function $G_{nn} = G_{n^c_{\mathbf{p},\mathbf{k}} n^{c'\dagger}_{\mathbf{p}',\mathbf{k}}}(\omega + \imath\delta)$ has to be evaluated to higher orders. A first step to go beyond RPA would be to "dress" the free electron propagators by self-energies. However, this does not lead to bound states in finite order of perturbation theory. For spectral lines, ladder-like coupling has to be considered between electronic and ionic propagators. Then, a bound state can be described by an infinite sum of interactions (T-matrix), leading to the free two-particle propagator $G_2^{(0)}$. In general, we have to consider four different diagrams for the density-density Green's function, see Fig. 1.5. However, in the following we use the electron-electron diagram as an example, i.e. set $c = c' = \mathrm{e}$. The results of the other terms can be obtained analogously and will be added at the end.

The density-density correlation functions are expressed via the imaginary part of

the Green's functions $G_{nn'}$, see Eq. (1.36). We calculate $G_{n^e n^e}$ as

$$G_{n^e n^e}(\mathbf{p}_e - \frac{\mathbf{k}}{2}, \mathbf{p}_e + \frac{\mathbf{k}}{2}; \mathbf{p}'_e - \frac{\mathbf{k}}{2}, \mathbf{p}'_e + \frac{\mathbf{k}}{2}; \omega_\mu) = -\frac{1}{\beta} \sum_{\omega_\lambda} \sum_{\mathbf{p}_i \mathbf{p}'_i} (2s_i + 1)$$
$$\times G_2(\mathbf{p}_e + \frac{\mathbf{k}}{2}, \mathbf{p}_i; \mathbf{p}'_e + \frac{\mathbf{k}}{2}, \mathbf{p}'_i; \omega_\mu + \omega_\lambda) G_2(\mathbf{p}'_e - \frac{\mathbf{k}}{2}, \mathbf{p}'_i; \mathbf{p}_e - \frac{\mathbf{k}}{2}, \mathbf{p}_i; \omega_\lambda)\,, \quad (1.38)$$

where the spin-factor $(2s_i + 1) = 2$ is due to the closed ion-propagator loop. Here, we use for the two-particle function the result of a ladder summation[19] [69]

$$G_2^{(0)}(\mathbf{p}_1, \mathbf{p}_2; \mathbf{p}'_1, \mathbf{p}'_2; z) = \sum_{n\mathbf{P}} \Psi_{n\mathbf{P}}(\mathbf{p}_1, \mathbf{p}_2) \frac{1}{\hbar z - E_{n\mathbf{P}} + \mu_{1'2'}} \Psi^*_{n\mathbf{P}}(\mathbf{p}'_1, \mathbf{p}'_2) \delta_{\mathbf{P}, \mathbf{p}_1 + \mathbf{p}_2} \delta_{\mathbf{P}, \mathbf{p}'_1 + \mathbf{p}'_2}\,, \quad (1.39)$$

where $\mu_{12} = \mu_1 + \mu_2$ is the total chemical potential, n stands for the quantum numbers of inner excitation, and $\mathbf{P}$ is the total momentum, i.e. $\mathbf{P} = \mathbf{p}_1 + \mathbf{p}_2 = \mathbf{p}'_1 + \mathbf{p}'_2$. The wave functions $\Psi_{n\mathbf{P}}(\mathbf{p}_1, \mathbf{p}_2)$ and the corresponding energies $E_{n\mathbf{P}}$ are the solutions and eigenvalues of Schrödinger's equation of the unperturbed emitter system, respectively. The δ-functions guarantee momentum conservation. Substituting $\epsilon^{ei}_{n\mathbf{P}} = E_{n\mathbf{P}} - \mu_{\mathrm{ei}}$[20], we get

$$G_{n^e n^e}(\mathbf{p}_e - \frac{\mathbf{k}}{2}, \mathbf{p}_e + \frac{\mathbf{k}}{2}; \mathbf{p}'_e - \frac{\mathbf{k}}{2}, \mathbf{p}'_e + \frac{\mathbf{k}}{2}; \omega_\mu) = -\frac{2}{\beta} \sum_{\omega_\lambda} \sum_{\mathbf{p}_i \mathbf{p}'_i}$$
$$\times \sum_{n\mathbf{P}} \Psi_{n\mathbf{P}}(\mathbf{p}_e + \frac{\mathbf{k}}{2}, \mathbf{p}_i) \frac{1}{\hbar\omega_\lambda + \hbar\omega_\mu - \epsilon_{n\mathbf{P}}} \Psi^*_{n\mathbf{P}}(\mathbf{p}'_e + \frac{\mathbf{k}}{2}, \mathbf{p}'_i) \delta_{\mathbf{P}, \mathbf{p}_e + \frac{\mathbf{k}}{2} + \mathbf{p}_i} \delta_{\mathbf{P}, \mathbf{p}'_e + \frac{\mathbf{k}}{2} + \mathbf{p}'_i}$$
$$\times \sum_{n'\mathbf{P}'} \Psi_{n'\mathbf{P}'}(\mathbf{p}'_e - \frac{\mathbf{k}}{2}, \mathbf{p}'_i) \frac{1}{\hbar\omega_\lambda - \epsilon_{n'\mathbf{P}'}} \Psi^*_{n'\mathbf{P}'}(\mathbf{p}_e - \frac{\mathbf{k}}{2}, \mathbf{p}_i) \delta_{\mathbf{P}', \mathbf{p}'_e - \frac{\mathbf{k}}{2} + \mathbf{p}'_i} \delta_{\mathbf{P}', \mathbf{p}_e - \frac{\mathbf{k}}{2} + \mathbf{p}_i}\,, \quad (1.40)$$

for the density-density Green's function. The δ-functions lead to the replacements

$$\mathbf{P}' = \mathbf{P} - \mathbf{k}\,, \quad \mathbf{p}_i = \mathbf{P} - \mathbf{p}_e - \frac{\mathbf{k}}{2}\,, \quad \mathbf{p}'_i = \mathbf{P} - \mathbf{p}'_e - \frac{\mathbf{k}}{2}\,. \quad (1.41)$$

The summation over even Matsubara-frequencies can be carried out, see Appendix A.4,

$$\sum_{\omega_\lambda} \frac{1}{\hbar\omega_\lambda + \hbar\omega_\mu - \epsilon_{n\mathbf{P}}} \frac{1}{\hbar\omega_\lambda - \epsilon_{n'\mathbf{P}-\mathbf{k}}} = \frac{\beta}{E_{n'\mathbf{P}-\mathbf{k}} - E_{n\mathbf{P}} + \hbar\omega_\mu} \left(g\left(\epsilon_{n'\mathbf{P}-\mathbf{k}}\right) - g\left(\epsilon_{n\mathbf{P}}\right) \right)\,, \quad (1.42)$$

[19] This is the "free" bound two-particle function in ladder summation, leading to Doppler broadening. To include plasma effects, we have to consider the "dressed" bound two-particle function including self-energies and coupling corrections due to the medium, which is treated afterwards.

[20] $\mu_{\mathrm{ei}} = \mu_{\mathrm{e}} + \mu_{\mathrm{i}}$.

with the Bose function $g(x) = (e^{\beta x} - 1)^{-1}$, and the total energies $E_{n\mathbf{P}} = E_n + \hbar^2 P^2/2M$, consisting of a bound part E_n and the center of mass translational energy with the total mass $M = m_e + m_i$. The relative momentum is given as

$$\mathbf{p}_{\rm rel}(\mathbf{p}_e, \mathbf{p}_i) = \frac{m_i}{M}\mathbf{p}_e - \frac{m_e}{M}\mathbf{p}_i \,. \tag{1.43}$$

When the center of mass motion is separated, the two-particle wave function $\Psi(\mathbf{p}_e, \mathbf{p}_i)$ can be written as a one-particle function depending on the relative momentum $\Psi^{ei}_{nP}(p_{\rm rel})$. Thus, we can write

$$\begin{aligned} &G_{n^e n^e}(\mathbf{p}_e - \frac{\mathbf{k}}{2}, \mathbf{p}_e + \frac{\mathbf{k}}{2}; \mathbf{p}'_e - \frac{\mathbf{k}}{2}, \mathbf{p}'_e + \frac{\mathbf{k}}{2}; \omega_\mu) \\ &\quad = -2\sum_{n'n}\sum_{\mathbf{P}} \frac{g(\epsilon_{n'\mathbf{P}-\mathbf{k}}) - g(\epsilon_{n\mathbf{P}})}{E_{n'\mathbf{P}-\mathbf{k}} - E_{n\mathbf{P}} + \hbar\omega_\mu} \xi_{nn'\mathbf{P}}(\mathbf{p}_e, \mathbf{p}'_e, \mathbf{k}) \,, \end{aligned} \tag{1.44}$$

where the wave functions have been abbreviated by

$$\begin{aligned} \xi_{nn'\mathbf{P}}(\mathbf{p}_e, \mathbf{p}'_e, \mathbf{k}) &= \Psi_{n\mathbf{P}}\left(\mathbf{p}_{\rm rel}(\mathbf{p}_e, \mathbf{P} - \mathbf{p}_e - \frac{\mathbf{k}}{2}) + \frac{m_i}{M}\frac{\mathbf{k}}{2}\right) \\ &\times \Psi^*_{n'\mathbf{P}-\mathbf{k}}\left(\mathbf{p}_{\rm rel}(\mathbf{p}_e, \mathbf{P} - \mathbf{p}_e - \frac{\mathbf{k}}{2}) - \frac{m_i}{M}\frac{\mathbf{k}}{2}\right) \Psi_{n'\mathbf{P}-\mathbf{k}}\left(\mathbf{p}_{\rm rel}(\mathbf{p}'_e, \mathbf{P} - \mathbf{p}'_e - \frac{\mathbf{k}}{2}) - \frac{m_i}{M}\frac{\mathbf{k}}{2}\right) \\ &\times \Psi^*_{n\mathbf{P}}\left(\mathbf{p}_{\rm rel}(\mathbf{p}'_e, \mathbf{P} - \mathbf{p}'_e - \frac{\mathbf{k}}{2})' + \frac{m_i}{M}\frac{\mathbf{k}}{2}\right) \,. \end{aligned} \tag{1.45}$$

To evaluate $\langle n^e; n^e\rangle$, we need only the imaginary part of $G_{n^e n^e}$. For this reason, we take the analytic continuation $\omega_\mu = \omega' + \imath\delta$ and apply Dirac's identity

$$\lim_{\delta\to 0}\frac{1}{x \pm \imath\delta} = \wp\frac{1}{x} \mp \imath\pi\delta(x) \,, \tag{1.46}$$

where $\wp$ stands for the principal value. With the definition $\Delta E_{nn',\mathbf{PP}-\mathbf{k}} = E_{n\mathbf{P}} - E_{n'\mathbf{P}-\mathbf{k}}$ and Eqs. (1.36) and (1.34) the current-current correlation can be derived as

$$\langle j^{e,\rm long}_k; j^{e,\rm long}_k\rangle_{\omega+\imath\delta} = \frac{\hbar^2}{\Omega^2}(2s_e+1)\sum_{\mathbf{pp}'}\frac{e^2}{m_e^2}p_z p'_z\langle n^e_{\mathbf{pk}}; n^e_{\mathbf{p}'\mathbf{k}}\rangle_{\omega+\imath\delta} \tag{1.47}$$

$$\begin{aligned} &= \frac{\imath 4\hbar^3}{\beta\Omega^2}\frac{e^2}{m_e^2}\sum_{n'n}\sum_{\mathbf{P}}\frac{1}{\hbar(\omega+\imath\delta) - \Delta E_{nn',\mathbf{PP}-\mathbf{k}}}\frac{g(\epsilon_{n'\mathbf{P}-\mathbf{k}}) - g(\epsilon_{n\mathbf{P}})}{\Delta E_{nn',\mathbf{PP}-\mathbf{k}}} \\ &\times \sum_{\mathbf{p}_e,\mathbf{p}'_e} p_{{\rm rel},z}(\mathbf{p}_e, \mathbf{P} - \mathbf{p}_e - \frac{\mathbf{k}}{2}) p'_{{\rm rel},z}(\mathbf{p}'_e, \mathbf{P} - \mathbf{p}'_e - \frac{\mathbf{k}}{2}) \xi_{nn'\mathbf{P}}(\mathbf{p}_e, \mathbf{p}'_e, \mathbf{k}) \,, \end{aligned} \tag{1.48}$$

where we keep in mind, that $\mathbf{p}_{\rm rel}$ and $\mathbf{P}$ are functions of $\mathbf{p}_e$ and $\mathbf{p}_i$. In the adiabatic limit $\frac{m_e}{M} = 0$, the relative momentum is given by $\mathbf{p}_{\rm rel} = \mathbf{p}_e$ and the center of mass

momentum is $\mathbf{P} = \mathbf{p}_i$. With the factor $(2s_e + 1) = 2$, we take the electron spin into account. Furthermore, to calculate the absorption coefficient from Eq. (1.33), we need only the long wavelength limit $k \to 0$, and obtain

$$\alpha(\omega) = \frac{\beta\Omega}{cn(\omega)\epsilon_0} \lim_{\mathbf{k}\to 0} \mathrm{Re}\left(\langle j_k^{\mathrm{long}}; j_k^{\mathrm{long}}\rangle_{\omega+\imath\delta}^{\mathrm{irred}}\right) \tag{1.49}$$

$$= \frac{4\hbar^3 e^2\pi}{cn(\omega)\epsilon_0 m_e^2\Omega} \lim_{\mathbf{k}\to 0}\left(\sum_{n'n}\sum_{\mathbf{P}} \delta\left(\hbar\omega - \Delta E_{nn',\mathbf{PP-k}}\right) \frac{g(\epsilon_{n'\mathbf{P-k}}) - g(\epsilon_{n\mathbf{P}})}{\Delta E_{nn',\mathbf{PP-k}}} \right.$$

$$\left. \times \sum_{\mathbf{p}_{\mathrm{rel}}\mathbf{p}'_{\mathrm{rel}}} p_{\mathrm{rel},z} p'_{\mathrm{rel},z} \xi_{nn'\mathbf{P}}(\mathbf{p}_{\mathrm{rel}}, \mathbf{p}'_{\mathrm{rel}}, \mathbf{k})\right) . \tag{1.50}$$

For the P-integration, we substitute $\mathbf{P} \to \mathbf{P} + \frac{1}{2}\mathbf{k}$. With $\mathbf{k} = k\mathbf{e}_z$, the energy difference is given by

$$\Delta E_{nn',\mathbf{PP-k}} = \Delta E_{nn',\mathbf{P}+\frac{1}{2}\mathbf{k}\mathbf{P}-\frac{1}{2}\mathbf{k}} \tag{1.51}$$

$$= E_n - E'_n + \frac{\hbar^2}{2M}\left(P_x^2 + P_y^2 + (P_z + \frac{k}{2})^2 - P_x^2 - P_y^2 - (P_z - \frac{k}{2})^2\right) \tag{1.52}$$

$$= \hbar\omega_{nn'} + \frac{\hbar^2}{M} P_z k\,. \tag{1.53}$$

For non-degenerate plasmas, it is legitimate to approximate the Bose functions by Boltzmann distributions, i.e.

$$g(E_n + E_{\mathbf{P}} - \mu_{\mathrm{ei}}) \approx \frac{1}{4} n_{\mathrm{a}} \Lambda_{ei}^3 e^{-\beta E_n} e^{-\beta E_{\mathbf{P}}}\,, \tag{1.54}$$

with the thermal wavelength $\Lambda_{ei} = \sqrt{2\pi\hbar^2\beta/M}$ and the number density of emitters n_{a}[21]. Using $g(\epsilon_{n\mathbf{P}}) = g(\epsilon_{n'\mathbf{P-k}} + \Delta E_{nn',\mathbf{PP-k}})$, we get

$$g(\epsilon_{n'\mathbf{P-k}}) - g(\epsilon_{n\mathbf{P}}) = \frac{1}{4} n_{\mathrm{a}} \Lambda_{ei}^3 e^{-\beta E'_n} e^{-\beta\frac{\hbar^2}{2M}(P_x^2 + P_y^2 + (P_z - \frac{k}{2})^2)} \left(1 - e^{-\beta\Delta E_{nn',\mathbf{PP-k}}}\right) \tag{1.55}$$

$$= \frac{1}{4} n_{\mathrm{a}} \Lambda_{ei}^3 e^{-\beta E'_n} e^{-\beta\frac{\hbar^2}{2M}(P_x^2 + P_y^2 + (P_z - \frac{k}{2})^2)} \left(1 - e^{-\beta(\hbar\omega_{nn'} + \frac{\hbar^2}{M} P_z k)}\right) . \tag{1.56}$$

With $\sum_{\mathbf{P}} \to \Omega \frac{1}{(2\pi)^3} \int_{-\infty}^{\infty} \mathrm{d}P_x \int_{-\infty}^{\infty} \mathrm{d}P_y \int_{-\infty}^{\infty} \mathrm{d}P_z$, the integration over P_x and P_y are of the form $\int_{-\infty}^{\infty} \mathrm{d}x e^{-ax^2} = \sqrt{\frac{\pi}{a}}$. Thus, the absorption is given by

$$\alpha(\omega) = \frac{\hbar^3 e^2 \pi \Lambda_{ei}^3}{cn(\omega)\epsilon_0 m_e^2 8\pi^3} \left[\sum_{n'n}\sum_{\mathbf{p}_{\mathrm{rel}}\mathbf{p}'_{\mathrm{rel}}} p_{\mathrm{rel},z} p'_{\mathrm{rel},z} \xi_{nn'\mathbf{P}}(\mathbf{p}_{\mathrm{rel}}, \mathbf{p}'_{\mathrm{rel}}, 0) n_{\mathrm{a}} e^{-\beta E'_n} \frac{2\pi M}{\beta\hbar^2} \right.$$

$$\left. \times \int \mathrm{d}P_z e^{-\beta\frac{\hbar^2}{2M}P_z^2} \delta\left(\hbar(\omega - \omega_{nn'}) - \frac{\hbar^2}{M} P_z \frac{\omega_{nn'}}{c}\right) \frac{1 - e^{-\beta\hbar\omega_{nn'}}}{\hbar\omega_{nn'}}\right] . \tag{1.57}$$

[21] The factor 1/4 is due to the spins of the ion and electron of the bound system $s_i = s_e = 1/2$.

Here, we performed the long-wavelength limit after we used Bohr's energy relation ($\omega_{nn'} = kc$) [70] in the argument of the δ-function. When we replace the thermal wavelength $\Lambda_{ei} = \sqrt{2\pi\hbar^2\beta/M}$, the Gaussian form of Doppler broadening can be recovered. Using the velocity form of the dipole-moment, see Eq. (A.17),

$$|D^z_{nn'}|^2 = \frac{e^2\hbar^2}{m_e^2\omega^2_{nn'}} \sum_{p_{\rm rel}p'_{\rm rel}} p_{{\rm rel}z}p'_{{\rm rel}z}\xi_{nn'\mathbf{P}}(\mathbf{p}_{\rm rel},\mathbf{p}'_{\rm rel},0)\,, \tag{1.58}$$

and the oscillator strength for one polarization direction [70]

$$f_{nn'} = \frac{2m_e}{\hbar e^2}\omega_{nn'}|D^z_{nn'}|^2\,, \tag{1.59}$$

we obtain

$$\alpha(\omega) = \sum_{n'n} \frac{2\pi}{n(\omega)}\frac{e^2}{4\epsilon_0 c m_e} f_{nn'} n_{\rm a} e^{-\beta E'_n}\left(1-e^{-\beta\hbar\omega_{nn'}}\right) P_D(\omega)\,, \tag{1.60}$$

with the expected Gaussian Doppler profile

$$P_D(\omega) = \frac{c\sqrt{M\beta}}{\sqrt{2\pi}\omega_{nn'}} e^{-\beta\frac{1}{2}\frac{Mc^2}{\omega^2_{nn'}}(\omega-\omega_{nn'})^2}\,, \tag{1.61}$$

centered around $\omega_{nn'}$. The other factors are the density of the lower level $n_{n'} = n_{\rm a}e^{-\beta E_{n'}}$, a factor to account for the reduction of absorption by emission $\left(1-e^{-\beta\hbar\omega_{nn'}}\right)$ and the strength of each absorption line given by the expected factor $\frac{e^2}{4\epsilon_0 c m_e n(\omega)} f_{nn'}$, see Eq. (1.11).

When the other diagrams $e-i$ and $i-i$ are considered as well, the matrix element $D^z_{nn'}/e$ can be replaced by the more general definition of the empty vertex

$$M^0_{nn'}(\mathbf{k}) = \imath\int\frac{d\mathbf{p}}{(2\pi)^3}\Big[Z\Psi^*_n(\mathbf{p}+\frac{m_e}{2M}\mathbf{k})\Psi_{n'}(\mathbf{p}-\frac{m_e}{2M}\mathbf{k}) - \Psi^*_n(\mathbf{p}-\frac{m_i}{2M}\mathbf{k})\Psi_{n'}(\mathbf{p}+\frac{m_i}{2M}\mathbf{k})\Big]\,, \tag{1.62}$$

which has been considered in the quantum-statistical approach so far [54]. Writing out the absolute square of $M^0_{nn'}(\mathbf{k})$ leads to four terms, which correspond to the four diagrams in Fig. 1.5. More information about the relation between this definition of the k-dependent empty vertex and the dipole moment can be found for the long-wavelength limit in Appendix A.5. Furthermore, a comparative calculation is included in Appendix A.1.

Thus, the expected Doppler broadening can be obtained for undressed bound-bound transitions starting from a current-current correlation function.

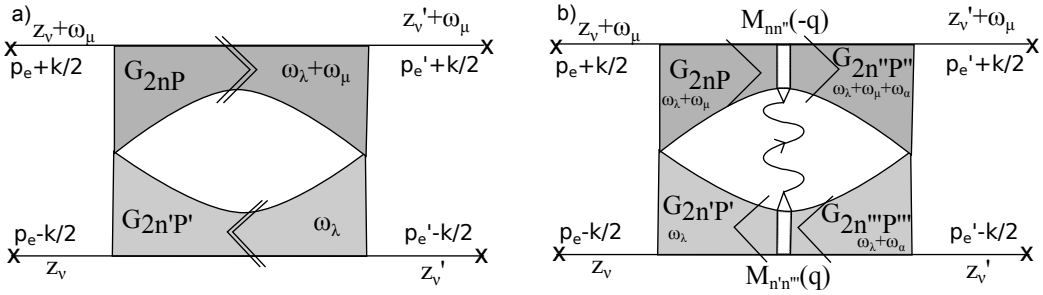

Figure 1.6.: To consider pressure broadening two types of corrections have to be taken into account in diagrams to calculate the e-e density-density Green's function. a) dressed two particle propagators (double arrow), b) coupling between both emitter states by a dynamically screened interaction (wiggly line) with empty vertices $M(\mathbf{q})$, see Eq. (1.62). The full complexity can be obtained by diagrams combining dressed propagators and coupling effects (not shown here).

Plasma effects via dressed two-particle functions

To include the effect of the plasma surroundings, we have to take the perturbation expansion to a higher level. At this level, we have diagrams with dressed bound two-particle Green's functions as well as a coupling diagram which leads to the vertex term, see Fig. 1.6. When we evaluate Fig. 1.6 a), we need the dressed two-particle Green's function. It can be described via its spectral function $A_2(n, \mathbf{P}, \omega)$ [62, 69]

$$G_2^1(n, n', \mathbf{P}, \mathbf{P}', z) = G_2(n, \mathbf{P}, z)\delta_{nn'}\delta_{\mathbf{P}\mathbf{P}'}\,, \tag{1.63}$$

$$G_2(n, \mathbf{P}, z) = -\int_{-\infty}^{\infty} \frac{\mathrm{d}\omega}{2\pi} \frac{A(n, \mathbf{P}, \omega)}{\omega - z}\,, \tag{1.64}$$

$$A(n, \mathbf{P}, \omega) = -2\imath \frac{\operatorname{Im}\Sigma_{n\mathbf{P}}(\omega)}{\left(\epsilon_{n\mathbf{P}} - \hbar\omega + \operatorname{Re}\Sigma_{n\mathbf{P}}(\omega)\right)^2 + \left(\operatorname{Im}\Sigma_{n\mathbf{P}}(\omega)\right)^2}\,. \tag{1.65}$$

Here, $\Sigma_{n\mathbf{P}}(\omega)$ is the frequency-dependent self-energy of the emitter in state n with center of mass momentum $\mathbf{P}$, i.e. quasi-particle shift and damping. The evaluation of the self-energies will be discussed in Secs. 1.3.2 and 1.3.3 for ions and electrons separately. The electronic self-energy is assumed to be diagonal in n,n'.

For the evaluation of the density-density Green's function, we need a connection between different types of two-particle Green's functions, given in Appendix A.6.

With this we obtain from Eq. (1.38)

$$G_{n^e n^e}(\mathbf{p}_e - \frac{\mathbf{k}}{2}, \mathbf{p}_e + \frac{\mathbf{k}}{2}; \mathbf{p}'_e - \frac{\mathbf{k}}{2}, \mathbf{p}'_e + \frac{\mathbf{k}}{2}; \omega_\mu) = -\frac{2s_i+1}{\beta} \sum_{\omega_\lambda} \sum_{\mathbf{p}_i \mathbf{p}'_i}$$
$$G_2(\mathbf{p}_e + \frac{\mathbf{k}}{2}, \mathbf{p}_i; \mathbf{p}'_e + \frac{\mathbf{k}}{2}, \mathbf{p}'_i; \omega_\mu + \omega_\lambda) G_2(\mathbf{p}'_e - \frac{\mathbf{k}}{2}, \mathbf{p}'_i; \mathbf{p}_e - \frac{\mathbf{k}}{2}, \mathbf{p}_i; \omega_\lambda) \tag{1.66}$$
$$= -\frac{2}{\beta} \sum_{\omega_\lambda} \sum_{\mathbf{p}_i \mathbf{p}'_i} \sum_{nn'\mathbf{P}\mathbf{P}'} G_2(n, \mathbf{P}, \omega_\mu + \omega_\lambda) G_2(n', \mathbf{P}', \omega_\lambda)$$
$$\times \xi_{nn'\mathbf{P}}(\mathbf{p}_e, \mathbf{p}'_e, \mathbf{k}) \delta_{\mathbf{P}, \mathbf{p}_e + \frac{\mathbf{k}}{2} + \mathbf{p}_i} \delta_{\mathbf{P}, \mathbf{p}'_i + \mathbf{p}'_e + \frac{\mathbf{k}}{2}} \delta_{\mathbf{P}', \mathbf{p}'_e - \frac{\mathbf{k}}{2} + \mathbf{p}'_i} \delta_{\mathbf{P}', \mathbf{p}_i + \mathbf{p}_e - \frac{\mathbf{k}}{2}} \,. \tag{1.67}$$

The Kronecker's δ-symbols and hence the wave functions $\xi_{nn'\mathbf{P}}(\mathbf{p}_e, \mathbf{p}'_e, \mathbf{k})$ are the same as in the undressed case. The central term is given as

$$\frac{1}{\beta} \sum_{\omega_\lambda} G_2(n, \mathbf{P}, \omega_\mu + \omega_\lambda) G_2(n', \mathbf{P}', \omega_\lambda)$$
$$= \hbar^2 \int_{-\infty}^{\infty} \frac{\mathrm{d}\omega_1}{2\pi} \int_{-\infty}^{\infty} \frac{\mathrm{d}\omega_2}{2\pi} \frac{A(n, \mathbf{P}, \omega_1) A(n', \mathbf{P}', \omega_2)}{\hbar(\omega_\mu - \omega_1 + \omega_2)} \left(g(\hbar\omega_1) - g(\hbar\omega_2) \right) \,, \tag{1.68}$$

see App. A.4 for details. It is not possible to evaluate both remaining integrals analytically. However, we assume a Lorentzian structure of the spectral functions and make the self-energies ω-independent. Then, it is legitimate to simplify the dependence on ω_1 and ω_2 by evaluating the Bose functions at the peak of the spectral functions, i.e. at $\hbar\omega_1 = \epsilon_{n\mathbf{P}} + \mathrm{Re}\,\Sigma_{n\mathbf{P}}(\epsilon_{n\mathbf{P}})$ and $\hbar\omega_2 = \epsilon_{n'\mathbf{P}'} + \mathrm{Re}\,\Sigma_{n'\mathbf{P}'}(\epsilon_{n'\mathbf{P}'})$. The self-energies are evaluated at the unperturbed energies. Thus, $\Sigma_{n\mathbf{P}}(\omega) = \Sigma_{n\mathbf{P}}(\epsilon_{n\mathbf{P}}) = \Sigma_{n\mathbf{P}}$. Then, we have

$$\frac{1}{\beta} \sum_{\omega_\lambda} G_2(n, \mathbf{P}, \omega_\mu + \omega_\lambda) G_2(n', \mathbf{P}', \omega_\lambda)$$
$$= 4\hbar^2 \mathrm{Im}\,\Sigma_{n\mathbf{P}} \mathrm{Im}\,\Sigma_{n'\mathbf{P}'} \left(g(\epsilon_{n\mathbf{P}} + \mathrm{Re}\,\Sigma_{n\mathbf{P}}) - g(\epsilon_{n'\mathbf{P}'} + \mathrm{Re}\,\Sigma_{n'\mathbf{P}'}) \right)$$
$$\times \int_{-\infty}^{\infty} \frac{\mathrm{d}\omega_1}{2\pi} \int_{-\infty}^{\infty} \frac{\mathrm{d}\omega_2}{2\pi} \frac{1}{\hbar(\omega_\mu - \omega_1 + \omega_2)} \frac{1}{\left(\epsilon_{n\mathbf{P}} - \hbar\omega_1 + \mathrm{Re}\,\Sigma_{n\mathbf{P}}\right)^2 + \left(\mathrm{Im}\,\Sigma_{n\mathbf{P}}\right)^2}$$
$$\times \frac{1}{\left(\epsilon_{n'\mathbf{P}'} - \hbar\omega_2 + \mathrm{Re}\,\Sigma_{n'\mathbf{P}'}\right)^2 + \left(\mathrm{Im}\,\Sigma_{n'\mathbf{P}'}\right)^2} \,. \tag{1.69}$$

Since we are interested in the imaginary part of G_{n_e, n_e}, we use analytic continuation and Dirac's identity to evaluate the expression further, see Appendix A.7 and obtain

$$\mathrm{Im}\,(\frac{1}{\beta} \sum_{\omega_\lambda} G_2(n, \mathbf{P}, \omega + \imath\delta + \omega_\lambda) G_2(n', \mathbf{P}', \omega_\lambda))$$
$$= \mathrm{Im} \left(\frac{g(\epsilon_{n\mathbf{P}} + \mathrm{Re}\,\Sigma_{n\mathbf{P}}) - g(\epsilon_{n'\mathbf{P}'} + \mathrm{Re}\,\Sigma_{n'\mathbf{P}'})}{\hbar\omega - \epsilon_{n\mathbf{P}} + \epsilon_{n'\mathbf{P}'} - \mathrm{Re}\,\Sigma_{n\mathbf{P}} + \mathrm{Re}\,\Sigma_{n'\mathbf{P}'} + \imath\left(\mathrm{Im}\,\Sigma_{n'\mathbf{P}'} + \mathrm{Im}\,\Sigma_{n\mathbf{P}}\right)} \right) \,. \tag{1.70}$$

Using this result in Eq. (1.67) and going into the reference frame of the center of mass motion, we obtain for the imaginary part of the density-density Green's function

$$\begin{aligned}\operatorname{Im} G_{n^e n^e}(\mathbf{p}_e - \frac{\mathbf{k}}{2}, \mathbf{p}_e + \frac{\mathbf{k}}{2}; \mathbf{p}'_e - \frac{k}{2}, \mathbf{p}'_e + \frac{\mathbf{k}}{2}; \omega' + \imath\delta) = -2 \sum_{nn'\mathbf{P}} \xi_{nn'\mathbf{P}}(\mathbf{p}_e, \mathbf{p}'_e, \mathbf{k}) \\ \times \operatorname{Im}\left(\frac{g(\epsilon_{n\mathbf{P}} + \operatorname{Re}\Sigma_{n\mathbf{P}}) - g(\epsilon_{n'\mathbf{P}-\mathbf{k}} + \operatorname{Re}\Sigma_{n'\mathbf{P}-\mathbf{k}})}{\hbar\omega - \epsilon_{n\mathbf{P}} + \epsilon_{n'\mathbf{P}-\mathbf{k}} - \operatorname{Re}\Sigma_{n\mathbf{P}} + \operatorname{Re}\Sigma_{n'\mathbf{P}-\mathbf{k}} + \imath\left(\operatorname{Im}\Sigma_{n'\mathbf{P}-\mathbf{k}} + \operatorname{Im}\Sigma_{n\mathbf{P}}\right)} \right) \end{aligned} \tag{1.71}$$

$$= -2 \sum_{nn'\mathbf{P}} \xi_{nn'\mathbf{P}}(\mathbf{p}_e, \mathbf{p}'_e, \mathbf{k}) \operatorname{Im}\left(\frac{B_{nn'\mathbf{Pk}}}{\hbar\omega - R^S_{nn'\mathbf{Pk}} + \imath I^S_{nn'\mathbf{Pk}}} \right), \tag{1.72}$$

where the expression was simplified by several abbreviations: The difference of the Bose distributions

$$B_{nn'\mathbf{Pk}} = g(\epsilon_{n\mathbf{P}} + \operatorname{Re}\Sigma_{n\mathbf{P}}) - g(\epsilon_{n'\mathbf{P}-\mathbf{k}} + \operatorname{Re}\Sigma_{n'\mathbf{P}-\mathbf{k}}), \tag{1.73}$$

and the real and imaginary parts in the denominator, respectively,

$$R^S_{nn'\mathbf{Pk}} = \epsilon_{n\mathbf{P}} - \epsilon_{n'\mathbf{P}-\mathbf{k}} + \operatorname{Re}\Sigma_{n\mathbf{P}} - \operatorname{Re}\Sigma_{n'\mathbf{P}-\mathbf{k}}, \tag{1.74}$$

$$I^S_{nn'\mathbf{Pk}} = \operatorname{Im}\Sigma_{n'\mathbf{P}-\mathbf{k}} + \operatorname{Im}\Sigma_{n\mathbf{P}}. \tag{1.75}$$

The density-density correlation after Eq. (1.36) is then

$$\begin{aligned}\langle n^e_{\mathbf{pk}}; n^e_{\mathbf{p'k}} \rangle_{\omega+\imath\delta} =& \frac{2}{\imath\hbar\beta} \sum_{nn'\mathbf{P}} \xi_{nn'\mathbf{P}}(\mathbf{p}_e, \mathbf{p}'_e, \mathbf{k}) \\ & \times \int_{-\infty}^{\infty} \frac{\mathrm{d}\omega'}{\pi} \frac{1}{\omega + \imath\delta - \omega'} \frac{1}{\omega'} \operatorname{Im}\left(\frac{B_{nn'\mathbf{Pk}}}{\omega' - \frac{1}{\hbar} R^S_{nn'\mathbf{Pk}} + \imath\frac{1}{\hbar} I^S_{nn'\mathbf{Pk}}} \right) \end{aligned} \tag{1.76}$$

$$\begin{aligned} =& \frac{2\imath}{\hbar^2\beta} \sum_{nn'\mathbf{P}} \xi_{nn'\mathbf{P}}(\mathbf{p}_e, \mathbf{p}'_e, \mathbf{k}) B_{nn'\mathbf{Pk}} I^S_{nn'\mathbf{Pk}} \\ & \times \int_{-\infty}^{\infty} \frac{\mathrm{d}\omega'}{\pi} \frac{1}{\omega + \imath\delta - \omega'} \frac{1}{\omega'} \frac{1}{(\omega' - \frac{1}{\hbar} R^S_{nn'\mathbf{Pk}})^2 + (\frac{1}{\hbar} I^S_{nn'\mathbf{Pk}})^2}. \end{aligned} \tag{1.77}$$

Thus, we have a Lorentzian instead of a δ-function under the integral. Via Dirac's identity, we obtain the real part of the density-density correlation function

$$\operatorname{Re}\left[\langle n^e_{\mathbf{pk}}; n^e_{\mathbf{p'k}} \rangle_{\omega+\imath\delta}\right] = \frac{2}{\hbar^2\beta} \sum_{nn'\mathbf{P}} \int_{-\infty}^{\infty} \mathrm{d}\omega' \delta(\omega - \omega') \frac{1}{\omega'} \frac{\xi_{nn'\mathbf{P}}(\mathbf{p}_e, \mathbf{p}'_e, \mathbf{k}) B_{nn'\mathbf{Pk}} I^S_{nn'\mathbf{Pk}}}{(\omega' - \frac{1}{\hbar} R^S_{nn'\mathbf{Pk}})^2 + (\frac{1}{\hbar} I^S_{nn'\mathbf{Pk}})^2} \tag{1.78}$$

$$= \frac{2}{\hbar^2\beta} \sum_{nn'\mathbf{P}} \frac{1}{\omega} \frac{\xi_{nn'\mathbf{P}}(\mathbf{p}_e, \mathbf{p}'_e, \mathbf{k}) B_{nn'\mathbf{Pk}} I^S_{nn'\mathbf{Pk}}}{(\omega - \frac{1}{\hbar} R^S_{nn'\mathbf{Pk}})^2 + (\frac{1}{\hbar} I^S_{nn'\mathbf{Pk}})^2}. \tag{1.79}$$

The absorption coefficient in adiabatic limit is given with Eqs. (1.33) and (1.34) as

$$\alpha(\omega) = \frac{2\beta\Omega\hbar^2 e^2}{cn(\omega)\epsilon_0\Omega^2 m_e^2} \lim_{\mathbf{k}\to 0} \left((2s_e+1) \sum_{\mathbf{p}_e\mathbf{p}'_e} p_{e,z} p'_{e,z} \mathrm{Re}\left[\langle n_{\mathbf{p}_e\mathbf{k}}; n_{\mathbf{p}'_e\mathbf{k}} \rangle_{\omega+\imath\delta} \right] \right) \tag{1.80}$$

$$= \sum_{nn'} \frac{4e^2}{cn(\omega)\epsilon_0\Omega m_e^2} \lim_{\mathbf{k}\to 0} \left(\sum_{\mathbf{p}_e\mathbf{p}'_e} p_{e,z} p'_{e,z} \sum_{\mathbf{P}} \frac{1}{\omega} \frac{\xi_{nn'\mathbf{P}}(\mathbf{p}_e, \mathbf{p}'_e, \mathbf{k}) B_{nn'\mathbf{Pk}} I^S_{nn'\mathbf{Pk}}}{(\omega - \frac{1}{\hbar} R^S_{nn'\mathbf{Pk}})^2 + (\frac{1}{\hbar} I^S_{nn'\mathbf{Pk}})^2} \right) . \tag{1.81}$$

Here, Doppler broadening and pressure broadening are coupled. Assuming, they can be uncoupled, we firstly consider pure pressure broadening[22] by setting the ion momentum $\mathbf{P} = 0$. Carrying out the long-wavelength limit and identifying again the dipole-moments, we have

$$\alpha(\omega) = \sum_{nn'} \frac{4\omega^2_{nn'}}{cn(\omega)\epsilon_0\hbar^2\Omega} |D_{nn'}|^2 \frac{1}{\omega} \frac{B_{nn'00} I^S_{nn'00}}{(\omega - \frac{1}{\hbar} R^S_{nn'00})^2 + (\frac{1}{\hbar} I^S_{nn'00})^2} . \tag{1.82}$$

We neglect the energy shift in the Bose distributions, recall the abbreviations

$$B_{nn'00} = g(\epsilon_{n0}) - g(\epsilon_{n'0}) = \frac{1}{4} n_\mathrm{a} \Lambda^3_{ei} e^{-\beta E_{n'}} (e^{-\beta\hbar\omega_{nn'}} - 1) , \tag{1.83}$$

$$R^S_{nn'00} = \hbar\omega_{nn'} + \mathrm{Re}\,\Sigma_n - \mathrm{Re}\,\Sigma_{n'} , \tag{1.84}$$

$$I^S_{nn'00} = \mathrm{Im}\,\Sigma_{n'} + \mathrm{Im}\,\Sigma_n , \tag{1.85}$$

and arrive at our final expression

$$\alpha(\omega) = \sum_{nn'} \frac{2\pi}{n(\omega)} \frac{\omega_{nn'}}{\omega} \frac{\Lambda^3_{ei}}{\Omega} \frac{e^2}{4c\epsilon_0 m_e} f_{nn'} \left(n_\mathrm{a} e^{-\beta E_{n'}} (e^{-\beta\hbar\omega_{nn'}} - 1) \right) P_{L,nn'}(\omega) . \tag{1.86}$$

Here, the prefactors are mainly the same as in Eq. (1.60). The factor $\frac{\omega_{nn'}}{\omega} \approx 1$ is almost constant over the center of the line and the ratio between thermal and normalization volume $\frac{\Lambda^3_{ei}}{\Omega}$ stems from setting $\mathbf{P} = 0$. In Eq. (1.86), pressure broadening is given by a Lorentzian with the maximum at the transition frequency $\omega_{nn'}$ shifted by the difference of the real parts of the self energies of upper and lower energy level. The width of the Lorentzian is determined by the sum of the imaginary parts of both energy levels,

$$P_{L,nn'}(\omega) = \frac{\hbar}{\pi} \frac{\mathrm{Im}\,\Sigma_{n'} + \mathrm{Im}\,\Sigma_n}{\left[\hbar(\omega - \omega_{nn'}) - (\mathrm{Re}\,\Sigma_n - \mathrm{Re}\,\Sigma_{n'})\right]^2 + \left[\mathrm{Im}\,\Sigma_{n'} + \mathrm{Im}\,\Sigma_n\right]^2} . \tag{1.87}$$

[22] Doppler broadening can be considered by a convolution with the Gaussian profile afterwards.

However, this derivation does not take the coupling contribution into account, which compensates mainly some fraction of the width but can also have a real part. The coupling contribution – also called vertex or interference term – can be derived when an additional diagram with an interaction between both two-particle propagators in the polarization function is considered, see Fig. 1.6. The derivation of the coupling contribution for systems with degenerate energy levels can be found in [54]. When this contribution is taken into account as well, the normalized Lorentzian line shape function is

$$P_{L,nn'}(\omega) = \frac{\frac{\hbar}{\pi}(\operatorname{Im}\Sigma_{n'} + \operatorname{Im}\Sigma_n + \operatorname{Im}\Gamma^{\mathrm{V}}_{nn'})}{[\hbar(\omega-\omega_{nn'}) - (\operatorname{Re}\Sigma_n - \operatorname{Re}\Sigma_{n'} + \operatorname{Re}\Gamma^{\mathrm{V}}_{nn'})]^2 + [\operatorname{Im}\Sigma_{n'} + \operatorname{Im}\Sigma_n + \operatorname{Im}\Gamma^{\mathrm{V}}_{nn'}]^2} \tag{1.88}$$

$$= -\frac{\hbar}{\pi}\operatorname{Im}\left[\{L_{nn'}(\omega)\}^{-1}\right], \tag{1.89}$$

where the line profile operator

$$L_{nn'}(\omega) = \hbar(\omega-\omega_{nn'}) - (\operatorname{Re}\Sigma_n - \operatorname{Re}\Sigma_{n'} + \operatorname{Re}\Gamma^{\mathrm{V}}_{nn'}) + \imath\left(\operatorname{Im}\Sigma_{n'} + \operatorname{Im}\Sigma_n + \operatorname{Im}\Gamma^{\mathrm{V}}_{nn'}\right) \tag{1.90}$$

has been defined. The detailed calculation of the self-energies and the vertex term will be discussed in the following.

For the comparison with measurements, we usually need the emission coefficient and use Kirchhoff's Law, Eq. (1.6). However, in the following, we concentrate on the shape of the line profile and neglect all prefactors for absorption/emission. As has been discussed in Sec. 1.2.4, the influence of surrounding electrons and ions on the emitter can be considered separately due to different interaction time scales. The surrounding ions are treated as quasi-static perturbers or within an ion-dynamics model, see Sec. 1.3.2, whereas binary collision approximation is applied for the free electrons, see Sec. 1.3.3. The total self-energy is split into an ionic part depending on the ionic microfield and a frequency-dependent electronic part[23]

$$\Sigma_{\nu\nu'}(E,\Delta\omega) = \Sigma^{\mathrm{i}}_{\nu\nu'}(E) + \Sigma^{\mathrm{e}}_{\nu}(\Delta\omega)\delta_{\nu\nu'}\,. \tag{1.91}$$

Here, $\nu = \{i, f\}$ can be the initial or final state and $\nu' = \{i', f'\}$ are their degenerate states. In Eq. (1.91), we take the electronic part of the self-energy to be diagonal, whereas for the ionic part non-diagonal elements are considered as well. Only

[23] Self-energies due to electrons are considered to be diagonal, while ions contribute to off-diagonal matrix elements, too.

electronic contributions are considered for the vertex term. Then, the normalized intensity profile at $\Delta\omega = \omega - \omega_0$ near the unperturbed transition frequency ω_0 is described by

$$I(\Delta\omega) = \frac{1}{N}\mathrm{Im}\left[\sum_{ii'ff'}\left\{\langle i|\mathbf{r}|f\rangle\langle f'|\mathbf{r}|i'\rangle\langle i|\langle f| < U(\Delta\omega) > |f'\rangle|i'\rangle\right\}\right], \tag{1.92}$$

with the normalization constant N that is chosen to obtain $\int \mathrm{d}\omega I(\Delta\omega) = 1$.
$< U(\Delta\omega) >$ is the time evolution operator which is closely connected to the line profile operator from Eq. (1.90). The relation depends on the considered model for ion-dynamics. The sum runs over all initial i and final f emitter states. The double sum is due to the degeneracy of H-like emitters. In the previous discussion, we had $n' = \{i, i'\}$ and $n = \{f, f'\}$ (for absorption). The contributions to the line profile are weighted with the transition probability, which is given by the dipole matrix elements $\langle i|\mathbf{r}|f\rangle$. They are connected to $M^0(\mathbf{k})$, see Appendix A.5, and to the previously used form $D^z_{fi} = \frac{1}{\sqrt{3}}e\langle i|\mathbf{r}|f\rangle$ assuming unpolarized light.

1.3.2. Effects due to ions

Stark effect and quadrupole effect

The perturbation of the emitter by the plasma ions is mainly given by the linear and quadratic Stark effect, i.e. the shift of an energy level caused by an outer electric field $\mathbf{E}_{\mathrm{ext}}$. Considering the dipole perturbation of the Hamiltonian, i.e., $H' = \mathbf{r}\cdot\mathbf{E}_{ext}$, it is possible to derive the linear and quadratic Stark effect for hydrogen or a H-like emitter in parabolic coordinates [71],

$$\Delta E^{(1)}_{n_1,n_2,m}(E_{\mathrm{ext}}) = \frac{3}{2}\frac{n(n_1-n_2)ea_0}{Z}E_{\mathrm{ext}}\,, \tag{1.93}$$

$$\Delta E^{(2)}_{n_1,n_2,m}(E_{\mathrm{ext}}) = -\frac{4\pi\epsilon_0 a_0^3}{Z^4}\frac{1}{16}n^4\left(17n^2 - 3(n_1-n_2)^2 - 9m^2 + 19\right)E^2_{\mathrm{ext}}\,. \tag{1.94}$$

Here, n_1, n_2 and m are the parabolic quantum numbers and the "usual" main quantum number is given by $n = n_1 + n_2 + |m| + 1$. The linear Stark effect is only present for emitters with degenerate energy levels.

Besides the effect of the external electric field, the field gradient has an influence on the energy levels, too. This effect is known as quadrupole interaction [72] and can be calculated starting from a further perturbation of the Hamiltonian $H'' =$

$-\frac{1}{6}\sum_{ij} Q_{ij} E_{ij,\mathrm{ext}} + \frac{1}{6} e\, r^2 \bigtriangledown \cdot \mathbf{E}_{\mathrm{ext}}$. Following [6] and [54], it leads to the energy shift

$$\Delta E^{(3)}_{n,n'}(E_{\mathrm{ext}}) = -\frac{5}{2\sqrt{32\pi}} \frac{eE_0}{d_i} B_a \left(\frac{E_{\mathrm{ext}}}{E_0}\right) \langle n|3z^2 - r^2|n'\rangle \,. \tag{1.95}$$

The mean field gradient $B_a(\frac{E_{\mathrm{ext}}}{E_0})$ is tabulated [72] and the parameters a and E_0 are defined as $a = d_i/\lambda_D$ (Hooper's parameter) and $E_0 = Ze/4\pi\epsilon_0 d_i^2$ (Holtsmark field strength), with the ion distance d_i and the Debye length λ_D.

Quasi-static treatment and microfield distributions

If the ions are considered to be static during the emission time, the normalized line shape with normalization constant N is determined by an averaging over the static microfield,

$$I_s(\Delta\omega) = \frac{1}{N}\mathrm{Im}\left[\sum_{ii'ff'} \langle i|\mathbf{r}|f\rangle\langle f'|\mathbf{r}|i'\rangle \int W(E)\langle i|\langle f|\{L_{if}(\Delta\omega, E)\}^{-1}|f'\rangle|i'\rangle \,\mathrm{d}E\right] . \tag{1.96}$$

Therefore, we need the microfield distribution, i.e. the isotropic probability distribution $W(E)$ to find the field strength E at the site of the emitter. For non-interacting ions, this distribution was derived by Holtsmark [73, 74]

$$W(E) = \frac{E^2}{\pi} \int_0^\infty \frac{k^2}{kE} \sin(kE) e^{-(kE_0)^{3/2}} dk \,. \tag{1.97}$$

For weakly coupled plasmas, Hooper [75, 76] and Baranger and Mozer [77] improved the distribution with the help of a cluster expansion of the many-body correlations. This approach can only be used as long as $a = d_i/\lambda_D < 0.8$. Since Hooper's low frequency tables are only available for neutral emitters and emitters with $Z = 1$, we use a different approach for Li^{2+}. Here, APEX [78, 79] based on Debye-Hückel pair correlations is used. For stronger coupling, we use the method of Potekhin *et al.* [80]. They developed a fit formula for $W(E)$ on the basis of Monte Carlo simulated microfield distributions. Then the microfield distribution is easily calculated for neutral and charged emitters, respectively.

Ion-dynamics

Now, we want to consider the effect of ion-dynamics. Qualitatively, line wings can be treated statically and the line center is affected by ion-dynamics. This can be seen

from the fact that the inverse of the excited emitter state lifetime τ is of the same order as the resulting line shift $\Delta\omega$, $\tau \sim \Delta\omega^{-1}$. Hence, in the center, $\tau \gg t_{\text{coll}}$, where t_{coll} is the duration of perturber-emitter collisions. Thus, perturber and emitter can complete a full collision during the emission time. Here, dynamics are important and the collision approximation does apply. In the line wings, the opposite is true, $\tau \ll t_{\text{coll}}$, i.e. the perturber is almost static during the emission time. Then, the quasi-static approximation is well justified. Depending on the plasma parameters, either of the approximations can be dominant for the line profile. Both regimes can be bridged by the unified theory [81, 82]. However, as the unified theory implies binary collisions, it can only be applied for ions in low density plasmas, see e.g. [83]. Thus, we follow two other ideas to include ion-dynamics into the line profile calculation, namely the model microfield method [84, 85] and the reformulation of the frequency fluctuation model [57]. They are both closely connected to the static approximation based on microfield distributions.

Model microfield method (MMM): The MMM considers the microfield dynamics as a stochastic process, where the electric field at the site of the emitter changes with a certain jump-frequency $\Omega(E)$ from one constant value E_1 to another random constant value E_2 and so on. Thus, the change of the electric field models the movement of the surrounding ions. In this process, E_2 does not depend on E_1 and the system has no memory. The time dependence can be worked out analytically [84, 85], if the jumps in the electric field are described by a kangaroo process. Then, the jump-frequency is chosen in such a way, that the static properties, i.e. $W(E)$, and the dynamic properties, i.e. the second moment of the microfield are preserved [86]. MMM is only applicable for neutral emitters[24].

To include the MMM into the line profile calculation, the time evolution operator has the following form [54]

$$U(\Delta\omega) = < L^{-1}_{\text{MMM}}(\Delta\omega, E) >_{\text{s}} + \frac{< \hbar\Omega(E) L^{-1}_{\text{MMM,if}}(\Delta\omega, E) >^2_{\text{s}}}{< \hbar\Omega(E) >_{\text{s}} - < \hbar^2\Omega^2(E) L^{-1}_{\text{MMM,if}}(\Delta\omega, E)) >_{\text{s}}}\,, \tag{1.98}$$

with the extended line profile operator based on $L_{if}(\omega)$, see Eq. (1.90),

$$L_{\text{MMM,if}}(\Delta\omega, E) = L_{if}(\Delta\omega, E) + \imath\hbar\Omega(E)\,. \tag{1.99}$$

In Eq. (1.98), the average $< \cdots >_{\text{s}}$ is over the static ion microfield distribution

[24] For charged emitters, BID can be applied [87] instead.

function $W(E)$ as in Eq. (1.96). In the limit $\Omega(E) \to 0$, the second terms on the right hand sides of Eqs. (1.98) and (1.99) vanish and the quasi-static approximation, Eq. (1.96), is recovered.

Frequency fluctuation model (FFM): The main ideas behind the FFM are that microfield-fluctuations produce frequency fluctuations and that the emitting system perturbed by the microfield can be described by a set of dressed two level transitions each with a certain frequency, amplitude and width [88]. As has been discussed in the publication of the first version of FFM [56], the model has been developed to calculate complex spectra which are composed of many electronic transitions, since these spectra cannot be calculated with MMM. Since FFM is based on different assumptions than MMM, it does not focus on the preservation of the second moment. This is sometimes seen as an disadvantage of the model. However, FFM can reproduce line shapes obtained from MD simulations [57]. Furthermore, it can be implemented easily, see Appendix A.8.

The reformulation of the FFM [57] assumes that a line profile has been calculated and area-normalized in the quasi-static approximation $I_\mathrm{s}(\omega)$, i.e. in our case based on Eq. (1.96). Then, the ion-dynamics can simply be taken into account in the following way

$$I_\mathrm{FFM}(\omega) = \frac{r^2}{\pi}\mathrm{Re}\frac{Q(\omega,\gamma)}{1-\gamma\,Q(\omega,\gamma)}, \qquad \text{with} \qquad Q(\omega,\gamma) = \int_0^\infty \frac{I_\mathrm{s}(\omega')\mathrm{d}\omega'}{\gamma + \imath(\omega-\omega')}. \quad (1.100)$$

Here, the inverse state lifetime γ is defined as $\gamma = v_\mathrm{therm}/d_i$, where the thermal velocity $v_\mathrm{therm} = \sqrt{8k_\mathrm{B}T/\pi m_i}$ as well as the inter-particle distance d_i of the ions are known from the plasma parameters. n_i and m_i are density and mass of the perturbing ions, respectively. The intensity is proportional to $r^2 = \sum_k a_k$, where a_k are the intensities of the different Stark components that contribute to the line. The static approximation, Eq. (1.96), is recovered in the limit $v_\mathrm{therm} \to 0$, i.e. $\gamma \to 0$.

Comparison: We could show in [14], that the choice of the specific ion-dynamics model can have a huge influence on the line shape. For H Lyman-α, differences in the width of up to $\pm 30\%$ have been found between calculations with FFM and MMM. So far, it is not possible to pick one of the models to be more precise or more reliable then the other. For the application in plasma diagnostics, one has to be aware of this fact. Further comparisons, especially with measured spectra are desirable. First attempts in this direction are presented in [15].

1.3.3. Effects due to free electrons

To determine the effects on the emitter states due to electron-emitter collisions, we compare two approaches both based on a quantum-statistical treatment. First, we discuss a perturbative approach. Namely a dynamically screened Born approximation which can take the dynamical screening of weak collisions correctly into account. However, the effects of strong electron-emitter collisions are overestimated [54] and have to be cutoff. The cutoff has previously been adjusted for hydrogen to advanced T-matrix calculations [5, 89]. We apply the approach for Li^{2+} with a Z^2 scaled cutoff. Secondly, we use an effective two-particle T-matrix approach. This approach is based on scattering amplitudes. For H, static (Debye) screening is implemented. For Li^{2+}, the effects of screening are estimated based on the results for H, see Appendix B in Ref. [15].

Dynamically screened Born approximation

The self-energy in Born approximation is given by [3]

$$\Sigma_\nu^{\mathrm{e}}(\Delta\omega) = -\sum_\alpha \int \frac{d^3k}{(2\pi)^3} \frac{Z_{\mathrm{i}} e^2}{\varepsilon_0 k^2} |M^0_{\nu\alpha}(\mathbf{k})|^2 \int_{-\infty}^{\infty} \frac{d\omega}{\pi} \frac{\left(1 + g\left(\frac{\hbar\omega}{k_{\mathrm{B}}T}\right)\right) \operatorname{Im}\, \varepsilon^{-1}(\mathbf{k}, \omega + \imath\,\delta)}{\Delta\omega + \omega_{\nu\alpha} - (\omega + \imath\,\delta)} \,. \tag{1.101}$$

Here, the dielectric function $\varepsilon(\mathbf{k}, \omega + \imath\,\delta)$ is approximated by the dielectric function in random phase approximation (RPA). Again, we imply limit $\delta \to 0+$. For H and Li^{2+}, we restrict the virtual transitions to state α in the following way: The main quantum number n_α runs from $n_\nu - 1$ to $n_\nu + 2$ for the real part of $\Sigma_\nu^{\mathrm{el}}(\Delta\omega)$, and for the imaginary part, we use the no-quenching approximation $n_\alpha = n_\nu$. Thereby, we take the main contributions to the self-energy into account. For the evaluation of Eq. (1.101) we consider the frequency-independent case $\Delta\omega = 0$ which corresponds to the binary collision approximation. Details on the applicability of this approximation can be found in Appendix A.1.

The coupling contribution – also called vertex term – is given in a similar way

$$\Gamma_{ii'ff'} = -2\imath \int \frac{\mathrm{d}^3k}{(2\pi)^3} M^0_{i'i}(-\mathbf{k}) M^0_{f'f}(\mathbf{k}) \frac{Z_{\mathrm{i}} e^2}{\varepsilon_0 k^2} \int_{-\infty}^{\infty} \mathrm{d}\omega \left(1 + g\left(\frac{\hbar\omega}{k_{\mathrm{B}}T}\right)\right) \operatorname{Im}\, \varepsilon^{-1}(\mathbf{k}, \omega + \imath\,\delta) \delta(\omega) \,. \tag{1.102}$$

The correct dynamical screening of weak collisions is included in Eqs. (1.101) and (1.102) by the imaginary part of the inverse dielectric function. However, the Born

approximation overestimates strong collisions. This can be rectified to some extend by a cut-off $k_{\max} = 1/\rho_{\min}$. For the case of H, $k_{\max,\mathrm{H}}$ has been adjusted in such a way, that the self-energies of an advanced T-matrix approach are recovered, see Ref [5, 89]. For Li^{2+}, we use a cut-off scaled by the square of the atomic number $Z = 3$, i.e.

$$k_{\max,\mathrm{Z}} = Z^2 k_{\max,\mathrm{H}}\,, \tag{1.103}$$

since $\rho_{\min} \sim \langle\psi_n^Z|r|\psi_n^Z\rangle^2 = \frac{1}{Z^2}\langle\psi_n^H|r|\psi_n^H\rangle^2$. Further details about the evaluation of Eqs. (1.101) and (1.102) can be found in Appendix A.9 and in Refs. [3, 6, 7, 54].

Effective two-particle T-matrix approximation

The effective T-matrix approach is a reduced version of the T-matrix approach presented in [5, 89]. It can describe weak and strong collisions equally well, but does so far only include static[25] screening [11–13]. For a non-degenerate plasma, the electronic self-energy, again evaluated at $\Delta\omega = 0$, is then given by

$$\Sigma_\nu^{\mathrm{e}} = -\frac{2}{\pi} n_e \Lambda_{\mathrm{th}}^3 \int_0^\infty \mathrm{d}k\; \frac{\hbar^2 k^2}{2m_e} e^{-\hbar^2 k^2/2m_e k_B T} f_\nu(0,k)\,, \tag{1.104}$$

where $\hbar k$ is the momentum of the scattered electron. Plasma properties enter via the electron density n_e and the thermal wavelength $\Lambda_{\mathrm{th}} = \hbar\sqrt{2\pi/m_e k_{\mathrm{B}} T}$ as well as the forward scattering amplitude $f_{i,f}(0,k)$ for elastic electron scattering at the Debye screened emitter in state i and f, respectively. A similar expression, Eq. (1.104), was also found by Baranger in [48]. He uses the impact approximation and treats the perturbing electrons quantum-mechanically. Fluctuating interactions are replaced by a constant effective one-perturber-atom interaction. In Ref. [48], a level coupling term is derived as well, which is given by

$$\Gamma_{if} = \frac{2\imath}{\pi} n_e \Lambda_{\mathrm{th}}^3 \int_0^\infty \mathrm{d}k\; \frac{\hbar^2 k^3}{2m_e} e^{-\hbar^2 k^2/2m_e k_B T} \int_0^\pi \mathrm{d}\theta\; \sin(\theta) f_f(\theta,k) f_i^*(\theta,k)\,. \tag{1.105}$$

Here, θ is the scattering angle and the dependence of the scattering amplitudes on θ has to be known, too.

To obtain the scattering amplitudes $f_n(k,\theta)$ that enter in Eqs. (1.104) and (1.105), we have to consider the three body problem for H and H-like emitters. The time-independent Schrödinger equation for singlet and triple channel ($\pm$)

$$H\Psi^{\pm}(\mathbf{r}_0,\mathbf{r}_1) = E\Psi^{\pm}(\mathbf{r}_0,\mathbf{r}_1)\,, \tag{1.106}$$

[25] In contrast to the dynamically screened Born approximation, Eq. (1.101).

depends on the positions of both electrons ($\mathbf{r_0}, \mathbf{r_1}$). The Hamiltonian has the form

$$H = -\frac{\hbar^2}{2m_e} \bigtriangledown_{r_0}^2 - \frac{Ze^2}{4\pi\epsilon_0 r_0} - \frac{\hbar^2}{2m_e} \bigtriangledown_{r_1}^2 - \frac{Ze^2}{4\pi\epsilon_0 r_1} + \frac{e^2}{4\pi\epsilon_0 r_{01}} \,. \tag{1.107}$$

Using the fact, that eigenenergies E_n and eigenstates $\phi_n(\mathbf{r})$ of the hydrogen problem are known, the wave function is expanded in these eigenstates [90]

$$\Psi^{\pm}(\mathbf{r}_0, \mathbf{r}_1) = \sum\!\!\!\!\!\!\int_a \left[F_a^{\pm}(\mathbf{r}_0)\Phi_a(\mathbf{r}_1) \pm F_a^{\pm}(\mathbf{r}_1)\Phi_a(\mathbf{r}_0)\right] \,, \tag{1.108}$$

where exchange is already considered. A sum over the bound part is necessary and an integral over the scattering part. Then, the Schrödinger equation can be transformed into coupled integro-differential equations [90]

$$(\bigtriangledown^2 + k_a^2)F_a^{\pm}(\mathbf{r}) = \frac{4m_e}{\hbar^2} \sum\!\!\!\!\!\!\int_b (V_{ab} + W_{ab}^{\pm} + X_{ab}^{\pm})F_b^{\pm}(\mathbf{r}) \,, \tag{1.109}$$

with the direct potential

$$V_{ab}(\mathbf{r}) = \frac{e^2}{4\pi\epsilon_0} \int \phi_a^*(\mathbf{r}')[-\frac{Z}{r} + \frac{1}{|\mathbf{r} - \mathbf{r}'|}]\phi_b(\mathbf{r}')\mathrm{d}\mathbf{r}' \,, \tag{1.110}$$

the non-local exchange potential

$$W_{ab}^{\pm}F_b^{\pm}(\mathbf{r}) = \pm \int \phi_a^*(\mathbf{r}')[\frac{e^2}{4\pi\epsilon_0|\mathbf{r} - \mathbf{r}'|} + E_a + E_b - E]\phi_b(\mathbf{r})F_b^{\pm}(\mathbf{r}')\mathrm{d}\mathbf{r}' \,, \tag{1.111}$$

and the non-local correlation potential $X_{ab}^{\pm}$ (Coupling continuous and bound states). The calculation is carried out with the help of a partial wave decomposition for the potentials depending on $\frac{1}{|\mathbf{r}-\mathbf{r}'|}$.

One-channel calculation and optical potential: The simplest solution strategy is to reduce the set of eigenstates. As an example a single channel calculation has been carried out in Ref. [11]. There, only the ground state of H is considered in the expansion, Eq. (1.108). Then, the problem can be reduced to a two particle problem with an optical potential $V_{\nu\pm}^{opt}(\mathbf{r}, z)$, which is an energy($z$)-dependent effective electron-atom potential with the atom in state ν. The optical potential is spin-dependent ($\pm$) and constructed from several parts,

$$V_{\nu,\pm}^{\mathrm{opt}}(r, z) = \left(V_{\nu}^{\mathrm{stat}}(r) + V_{\nu}^{\mathrm{pol}}(r) + V_{\nu,\pm}^{\mathrm{ex}}(r, z) + V_{\nu}^{\mathrm{vr}}(r, z)\right) e^{-\frac{r}{\lambda_{\mathrm{D}}}} \,, \tag{1.112}$$

where Debye screening is taken into account artificially by the factor $e^{-r/\lambda_{\mathrm{D}}}$.

Many-channel calculation – Convergent-close coupling: Since one channel calculations are not sufficient to describe scattering on an emitter with several states[26], a multi-channel method has to be used to calculate the scattering amplitudes. Besides R-matrix methods, e.g. [91], convergent close-coupling methods (CCC) are capable to solve this problem. As input for Eqs. (1.104) and (1.105), CCC calculations have been carried out by our collaborators at Curtin University (Perth, Australia) [92–94]. They used two different codes for H and Li^{2+}, respectively. For the neutral emitter H, the code is modified to include Debye screening in the interaction potentials [95]. The modification is also available for He [96]. For the charged emitter (Li^{2+}), this modification was not immediately possible. Thus, we give an estimate on the error which we make by neglecting the screening, see Appendix B of Ref. [15].

For H and Li^{2+}, 54 (Sturmian) Laguerre functions are used as a basis for bound and continuous emitter states. With this choice, the emitter states up to 4f are reproduced with the correct energies. The electron-electron interaction is treated within a partial wave decomposition, where the first partial waves (up to 70) are considered directly. For larger numbers of partial waves, scattering amplitudes are extrapolated following O'Malley's approach [97]. The coupled equations are solved in momentum space and lead to the scattering amplitude. The method gives separate results for singlet and triplet scattering channels as well as for scattering at the emitter with initial and final states $n_i, l_i, m_i \to n_f, l_f, m_f$. Here, we consider only elastic scattering $n_i, l_i, m_i \to n_i, l_i, m_i$ to calculate the self-energies and level coupling term, since we make the assumption that the electronic self-energy is diagonal, see Eq. (1.91). Scattering amplitudes from CCC calculations have been used in Refs. [12, 13, 15] for the calculation of Lyman lines of H and Li^{2+}.

1.4. Overview over published results

1.4.1. Paper 1 - Li^{2+} Lyman lines in Born approximation without ion-dynamics

Ref. [10] is focused on Li^{2+} Lyman lines and laser produced plasmas. General density dependence of FWHM and line shift are given for the first three Lyman lines. A

[26] Especially, if the emitter is in an excited state.

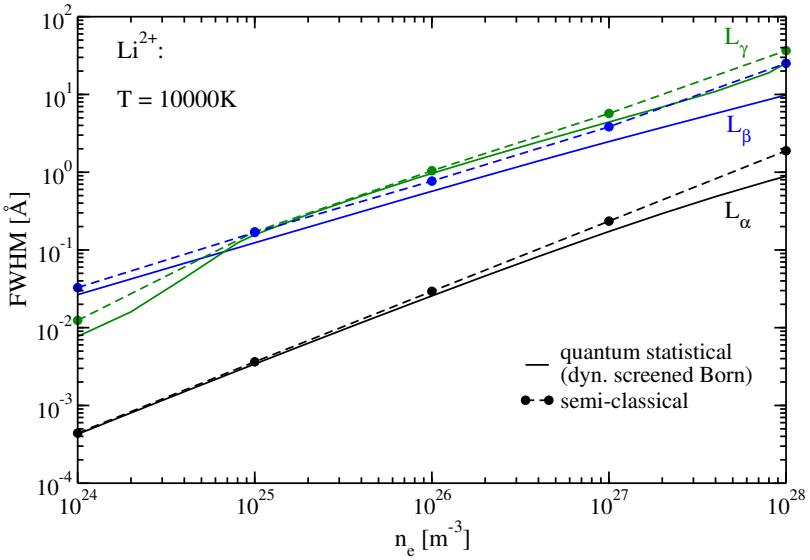

Figure 1.7.: Comparison of FWHM of Li^{2+} Lyman lines based on Born approach and on semi-classical theory for charged radiators after Kepple [45]. The linear behavior of our semi-classical calculation is better than in Fig.1 of Ref. [10] because we detected an error in our implementation.

semi-classical theory based on hyperbolic trajectories [45] was adjusted for Li^{2+} and used for a comparison, see Fig. 1.7. While the agreement is good for low densities and Lyman-α, stronger deviations between both approaches occur for higher densities and lines. Temperature dependence for Lyman-α and the dominance of Doppler broadening up to $n_e = 5 \cdot 10^{25}$ m^{-3} are discussed. Then, we use the quantum-statistical method to analyze two different emission spectra from laser-produced lithium plasmas [20, 21]. Ions are treated static but the influence of ion-dynamics is estimated to be low for the considered plasma parameters of the experiments.

1.4.2. Paper 2, 3, 4 - testing an effective two-particle T-matrix approach for H Lyman-α

These papers are solely concerned with the electronic part of the self energy Σ^e and a simplified way to treat strong electron emitter collisions correctly. In Ref. [11][27], the connection between the dynamical screened T-matrix approach of Könies and

[27] This paper was written and handed in in 2009, but has been published in 2011.

Günter [5] and the effective two-particle T-matrix approach has been presented. The latter uses scattering amplitudes as input. For the ground state of hydrogen, one channel test calculations with an artificially Debye screened optical potential are carried out to obtain scattering amplitudes and are compared to the Born approximation. The subsequent papers [12] and [13], both proceedings to the International Conference on Spectral Line Shapes, present calculations for the H(2p) level and the H Lyman-α, respectively. These calculations are based on scattering amplitudes from close-coupling calculations. Here, we test the convergence of the partial wave expansion. The resulting widths are compared to the Born approach and the T-matrix approach of Könies and Günter [5, 54], and to close-coupling calculations of Unnikrishnan and Callaway [98]. The capability to resolve the dependence on the magnetic quantum number m and on the spin scattering channel (singlet or triplet) distinguished our T-matrix approach from the other two. The results encouraged us to carry on and to apply the method for Li^{2+}, were it had not been used before.

1.4.3. Paper 5 - Comparing two ion-dynamics models for H Lyman-α and Lyman-β

Since ion-dynamics had been treated poorly in the previous papers and a new simple method to implement ion-dynamics had been brought to my attention. Ref. [14] presents a comparison of two methods to go beyond the quasi-static treatment of perturbing ions for a broad region of plasma parameters. Electrons are treated within the Born approximation. While ion-dynamics is always crucial for Lyman-α, it is less important for Lyman-β. However, the choice of the ion-dynamics model can have an notable effect on the line shape as well. For Lyman-β, not only the width is affected but the shape, i.e. the depth of the dip, is changed, too.

1.4.4. Paper 6 - Applying the effective two-particle T-matrix approach with static screening to H, He and Li^{2+}

This work [15] combines the methods of the previous ones and applies the methods to H, Li^{2+} and He. For H, the importance of the plasma screening for the scattering process and the dependence on the magnetic quantum number m for electronic width and shift is discussed. We find that the dependence on the spin scattering channel is rather weak and can be neglected. The comparison with the measurement of

Grützmacher and Wende [17] favors MMM over FFM, when electronic effects are calculated with the CCC-based T-matrix approach. For Li^{2+}, using FFM ion-dynamics and our T-matrix approach with estimated plasma screening does not change the line shape significantly when self-absorption and instrumental broadening are considered for the parameters of the measurement of Schriever et al. [21]. Thus, our analysis from Ref. [10] has been confirmed. In order to distinguish between different theoretical approaches for the electronic self-energy measurements with higher resolution are needed. A broad comparison to theoretical results and measurements is presented for the He 3889 Å line, where the He line shape calculations have been performed by Banaz Omar.

1.5. Outlook

Due to the used approximations, the presented theory is not applicable for all plasma parameters. Some extensions can be considered. Since all our calculations in this thesis are within the weakly coupled regime, the no-coupling approximation is so far applicable. However, it would be a valuable extension of our quantum-statistical approach to include electron-ion coupling and the back-reaction of the emitter on the perturbers in the future. It might be possible to develop our theory further with similar methods to the ones used in the generalized theory [61].

The correct treatment of strong collisions is one of the foci of this thesis. However, in our T-matrix approach, we stick to a static screened interaction. The extension to dynamical screening would be useful, but cannot be implemented in the close-coupling calculations easily. If the interaction is ω-dependent, the resulting scattering amplitudes would depend on ω, too, and the number of necessary CCC calculations for one line would increase drastically. However, an approximation might be derived with an ω-dependent correction factor for the scattering amplitudes, to keep the number of CCC calculations small.

For diagnostic purposes, the discussion of ion-dynamics models is important and should be extended. Our comparison for H showed, that different models can lead to the derivation of different plasma parameters in the analysis of measured spectra. Thus, it might be valuable to compare the FFM with the MMM-based model for charged particles, namely BID[28] [99], or other models in order to get a deeper

[28] named after its inventors: D. Boercker, C. Iglesias and J. Dufty

insight into the differences that are produced by different ion-dynamics models for H-like emitters. Although the comparison with the Grützmacher-Wende measurement in [15] favors MMM over FFM, further studies are necessary to single one theory out. For this purpose, measurements of highly resolved H and H-like spectral lines at well determined, dense plasma conditions are needed.

As has briefly been discussed in Ref. [10], the transient nature of laser-produced plasmas, has to be taken into account for the diagnostics of such plasmas. Under the assumption of local thermal equilibrium, our approach can be combined with a hydrodynamics simulation that produces time- and space dependent temperature and density distributions. These can then be used as input for the line shape calculations as has been demonstrated in [100]. To go beyond the assumption of (local) thermal equilibrium can be achieved within a microscopical quantum-master equation [101], which leads to transition rates, i.e. life-times of energy levels, and hence spectral line width.

Although our approach is given analytically to a large extend for H and H-like emitters due to the analytical wave functions. There is a need, to extend the theory for many-electron emitters and for inner shell transitions using numerical wave functions as an input. A first step in this direction was the extension to He-like emitters [7, 102]. A theoretical basis for the line width has not been developed for K-lines[29] so far and an extension of the presented theory in this direction would be a valuable contribution to plasma diagnostics.

As one can see from the last paragraphs, a long list of further questions remains which have to be answered in order to use spectral line shapes as a reliable and precise tool for diagnostics of dense plasmas. Some steps towards this goal have already been taken and presented in this thesis.

[29] Here, an empirical value is assumed [8].

2. Publications

2.1. List of own contributions in the publications

1. Sonja Lorenzen, August Wierling, Heidi Reinholz, and Gerd Röpke, *Pressure Broadening of Lyman-Lines in Dense Li^{2+} Plasmas*, Contributions to Plasma Physics, **48**, 657-669 (2008)

my work: All calculations, figures, and the first version of the text of the manuscript.

co-authors: Wierling: Direct Supervision: detailed instructions, discussion of results, correction of the text.
Reinholz, Röpke: Supervision and proofreading, project management.

2. Sonja Lorenzen, August Wierling, Heidi Reinholz, and Gerd Röpke, *Improved Self-Energy Calculations for Pressure Broadening of Spectral Lines in dense Plasmas*, Contributions to Plasma Physics, **51**, 349-354, (2011) (submitted 2009, Proceedings PNP13)

my work: Assembling of information about different theories. Test calculations for H(1s) with an optical potential. First manuscript draft.

co-authors: Wierling: Direct Supervision: instructions, discussion and testing of different T-matrix methods, discussion of results, correction of the text.
Reinholz, Röpke: Supervision and proofreading, project management

3. Sonja Lorenzen, August Wierling, Heidi Reinholz, Gerd Röpke, Mark C. Zammit, Dmitry V. Fursa, and Igor Bray, *Quantum-statistical T-matrix approach to line broadening of hydrogen in dense plasmas*, AIP Conference Proceedings **1290**, 99 (2010) (Proceedings ICSLS 20)

my work: Preparation of the figures and calculation of H(2p) self-energies in Born approximation and with effective T-matrix method. All text besides the section "CCC with Debye screening".

co-authors: Wierling: Supervision and proofreading
Reinholz, Röpke: Supervision and project management
Zammit, Fursa, Bray: Implementation of screening modifications in close-coupling

code, calculation of scattering amplitudes as input for self-energy calculations, and text in section "CCC with Debye Screening".

4. Sonja Lorenzen, August Wierling, Heidi Reinholz, Gerd Röpke, Mark C. Zammit, Dmitry V. Fursa, and Igor Bray, *Quantum-statistical line shape calculation for Lyman-α lines in dense H plasmas*, Journal of Physics: Conference Series **397**, 012021 (2012) (Proceedings ICSLS 21)

my work: Preparation of the figures, all calculations, and all text.

co-authors: Wierling: Supervision and proofreading.
Reinholz, Röpke: Supervision and project management.
Zammit, Fursa, Bray: Calculation of scattering amplitudes as input for self-energy calculations of H(2p), H(2s) and H(1s).

5. Sonja Lorenzen, *Comparative study on ion-dynamics for broadening of Lyman lines in dense hydrogen plasmas*, Contributions to Plasma Physics, **53**, 368-374, (2013) (Proceedings PNP14)

6. Sonja Lorenzen, Banaz Omar, Mark C. Zammit, Dmitry V. Fursa, and Igor Bray, *Plasma pressure broadening for few-electron emitters including strong electron collisions within a quantum-statistical theory*, Physical Review E, **89**, 023106 (2014)

my work: All text besides Section "V. He", all figures besides Figs. 7 and 8, development of the estimated correction for charged emitters, all calculations for H and Li^{2+}, management of the collaboration.

co-authors: Omar: Calculations, figures and text for He, discussion and proofreading.
Zammit, Fursa, Bray: Calculations of scattering amplitudes as input for H and He with screening modifications as well as for Li^{2+} without screening modifications.

2.2. Peer-reviewed publications

Contrib. Plasma Phys. **48**, No. 9-10, 657 – 669 (2008) / **DOI** 10.1002/ctpp.200810097

Pressure Broadening of Lyman-Lines in Dense Li^{2+} Plasmas

S. Lorenzen[*1], **A. Wierling**[1], **H. Reinholz**[1,2], and **G. Röpke**[1]

[1] Universität Rostock, 18051 Rostock, Germany
[2] University of Western Australia, Nedlands, WA 6009, Australia

Received 10 October 2008, accepted 3 November 2008
Published online 12 December 2008

Key words Pressure broadening, lithium, laser-produced plasmas.
PACS 52.25.Os,52.27.Gr

Pressure broadening of Lyman-lines of hydrogen-like lithium is studied using a quantum statistical approach to the line shape in dense plasmas. We report line widths (FWHM) and shifts for L_α, L_β, and L_γ in a wide range of densities and temperatures relevant for laser-produced lithium plasmas. We estimate the influence of ion dynamics and strong collisions. The results are applied to measured spectra of lithium irradiated by a nanosecond laser pulse of moderate intensities ($I \approx 10^{11} - 10^{13}$ W/cm^2), see G. Schriever et al. [1, 2]. By matching synthetic spectra to the experimental ones, density and temperature conditions are inferred assuming the model of a one-dimensional uniform plasma slab. This allows for a more precise estimate of the density compared to the results reported earlier. Self-absorption is accounted for and found to be important for L_α.

1 Introduction

The search of next-generation light sources for EUV lithography has also triggered interest in Lyman-α emission of hydrogen-like lithium being located at the desired wavelength of 13.5 nm [3, 4]. To be economically feasible, a conversion efficiency (CE) of 4 % is targeted but not yet achieved. Promising methods to generate EUV are laser-produced and gas-discharge-produced plasmas, the former being more advantageous due to compactness, intensity, power scalability, high repetition rate, small source size, and energy stability [5]. Maximizing the CE is a main goal and can be attained e.g. by laser pulse shaping and target design. Recently, a CE of 2.3 % has been reported [6, 7] due to the use of a tamper on the lithium target. Earlier, even higher values have been claimed [8]. For a recent description of a lithium-based discharge-produced plasma source, see Ref. [9]. Besides lithium, tin is studied as a possible candidate [5, 10], but its use requires more sophisticated debris control. Also, from a theoretical point of view, the spectral emission of Li^{2+} is much easier to describe since the radiator is hydrogen-like.

Irradiating lithium with a high-intensity laser (typically $I > 10^{10}$ W/cm^2) creates a hot and dense plasma. Under these conditions, strong modifications of spectral line features as compared to isolated lines are observed [11]. Also, time-resolved measurements show large alterations of the spectrum due to the transient character of the expanding plasma. Stark broadening as well as Doppler shift and broadening play an important role. On the other hand, due to the sensitivity of these spectral line features on density, temperature, and composition, optical spectroscopy serves as a powerful diagnostic tool for these plasmas [12–14] once a detailed theoretical understanding of medium modifications has been achieved.

Since the classical description of broadening of absorption lines by collisions with surrounding atoms in 1906 by Lorentz [15], the calculation of pressure broadening has evolved drastically [14]. Several microscopic approaches have been advanced. The most widely used approach is due to Griem [16] and utilizes an impact approximation together with a semi-classical description of the perturber-radiator interaction. Treatments beyond perturbation theory have been given by the unified theory [17, 18] and by a close-coupling method [19]. We also mention the frequency fluctuation method [20]. Recently, computer simulation techniques have been found quite successful in treating medium modifications of spectral line shapes [21].

*Corresponding author: e-mail: sonja.lorenzen@uni-rostock.de, Phone: +49 381 4986946, Fax: +49 381 4986942

In this communication, we use a quantum-statistical approach based on thermodynamic Green's functions [22]. This approach has been successfully applied to diagnose experimental plasmas of hydrogen [23] and of hydrogen-like carbon [24]. The approach was recently extended to the calculation of spectral lines of neutral helium [25].

The paper is organized as follows. We give a short review of the quantum-statistical approach to the spectral line shape in plasmas in Sec. 2. Results for the shift and broadening of the L_α, L_β, and L_γ lines are presented in Sec. 3 for the case of a homogeneous plasma in thermal equilibrium. There, the results for the broadening are compared to calculations within a semi-classical approach adapted from studies for ionized helium by Griem et al. [26,27]. To complete our study, we use our approach in Sec. 4 to analyze experimental spectra, obtained from laser-heated lithium. The Lyman series, especially L_α, have been experimentally observed by several groups [1, 2,5,11,28–32]. Detailed spectra were published by G. Schriever et al. [1,2] and recently by S. George et al. [5,32] and P. Nica et al. [31]. As laser-produced plasmas vary in time and space, for plasma diagnostics time- and space-resolved spectra would be preferable. Space-resolved measurements of L_α have been done by P. Nica et al. [31]. However, full spectra have not been given. The calibration of [5, 32] has to be reconsidered [33]. Therefore, we use the data of G. Schriever et al. [1, 2] to demonstrate the determination of the mean free electron density, the mean temperature, and the thickness l of the plasma layer.

2 Theory of line broadening

Pressure broadening comprises all shift and broadening effects caused by the medium that surrounds the emitting ion. Here, we outline a microscopic approach to include the most important ones. To this end, let us consider a plasma in thermal equilibrium at a given temperature T and electron density n_e. We consider a radiator with nuclear charge $Z_N = 3$. For simplicity, we restrict our presentation to one ion species with charge $Z_{\rm ion} = 2$ in the medium. Extensions to more species can be readily made. Due to the different masses of ions and electrons, the broadening caused by ions is calculated in quasi-static approximation whereas the broadening of the electrons is considered in binary collision approximation [16]. The validity of these approximations in the considered density region is discussed in Sec. 3.2.

With these approximations, the pressure-broadened line profile $I^{\rm pr}(\Delta\omega)$ is given by [34, 35]

$$\begin{aligned} I^{\rm pr}(\Delta\omega) &= \frac{(\omega_0)^4}{8\pi^3 c^3} \exp\left[-\frac{\hbar\omega_0}{k_{\rm B}T}\right] \left(1+\frac{\Delta\omega}{\omega_0}\right)^4 \exp\left[-\frac{\hbar\Delta\omega}{k_{\rm B}T}\right] \\ &\times \sum_{i,i',f,f'} \left\{ \langle i|\vec{r}|f\rangle\langle f'|\vec{r}|i'\rangle \int_0^\infty dE\, W(E) \langle i|\langle f|L^{-1}(\Delta\omega,E)|f'\rangle|i'\rangle \right\}, \end{aligned} \tag{1}$$

where $\Delta\omega = \omega - \omega_0$ is the difference between the considered frequency ω and the frequency of the unperturbed electronic transition ω_0. $W(E)$ is the ionic microfield distribution, i.e. the probability distribution to find the electric field strength E at the site of the emitting ion due to the surrounding ions, see Sec. 2.3. Medium modifications enter also into the line profile operator

$$L(\Delta\omega,E) = \hbar\Delta\omega - {\rm Re}\left[\Sigma_i(\omega,E) - \Sigma_f(\omega,E)\right] - {\rm i}\,{\rm Im}\left[\Sigma_i(\omega,E) + \Sigma_f(\omega,E)\right] + i\Gamma^{\rm V}_{if}, \tag{2}$$

via the self-energies $\Sigma_n(\omega,E)$ of initial ($n=i$) and final states ($n=f=$ ground state). The vertex correction $\Gamma^{\rm V}_{if}$ containes the coupling between the upper and the lower state and vanishes for the Lyman series [35]. Following the argument above, we approximate the self-energy by an electronic part which is independent of the ionic microfield and a frequency-independent ionic part

$$\Sigma_n(\omega,E) = \Sigma^{\rm el}_n(\omega) + \Sigma^{\rm ion}_n(E). \tag{3}$$

Furthermore, the thermal motion of the ions leads to Doppler broadening and is accounted for by a convolution of the pressure broadened profile, Eq. (1), with a Maxwellian velocity distribution

$$I(\Delta\omega) = \frac{c}{\omega_0}\sqrt{\frac{m_{\rm ion}}{2\pi k_{\rm B}T}} \int_{-\infty}^{\infty} {\rm d}\Delta\omega'\, I^{\rm pr}(\Delta\omega') \exp\left[-\frac{m_{\rm ion}c^2}{2k_{\rm B}T}\left(\frac{\Delta\omega-\Delta\omega'}{\omega_0+\Delta\omega'}\right)^2\right]. \tag{4}$$

Contrib. Plasma Phys. **48**, No. 9-10 (2008) / www.cpp-journal.org 659

Here, $m_{\rm ion}$ is the mass of the emitting ion. Finally, we define the normalized line profile by

$$P(\Delta\omega) = \frac{I(\Delta\omega)}{\int I(\Delta\omega)\mathrm{d}\Delta\omega} \quad . \tag{5}$$

2.1 Electronic self-energy $\Sigma_n^{\rm el}(\omega)$

The self-energy of the electrons has been derived within a quantum-statistical many-particle approach using thermodynamic Green's functions [22–24]. Accounting for dynamical screening, the emitter-electron interaction reads

$$V^s(q,\omega_\mu) = V(q)\left(1+\int_{-\infty}^{\infty}\frac{\mathrm{d}\omega}{\pi}\frac{\mathrm{Im}\epsilon^{-1}(q,\omega+i\delta)}{\omega-\omega_\mu}\right), \tag{6}$$

depending on the bosonic Matsubara frequency ω_μ and the wave vector q. The electronic self-energy can be evaluated in Born approximation as

$$\Sigma_n^{\rm el}(\Delta\omega) = -\int\frac{d^3q}{(2\pi)^3}V(q)\sum_\alpha|M^0_{n\alpha}(q)|^2\int_{-\infty}^{\infty}\frac{d\omega}{\pi}(1+n_B(\omega))\frac{\mathrm{Im}\epsilon^{-1}(\vec{q},\omega+i\delta)}{\Delta\omega+\omega_{n\alpha}-(\omega+i\delta)}. \tag{7}$$

Here, we have neglected the first term (Fock exchange) in Eq. (6).

For the evaluation of Eq. (7) we consider the frequency-independent case $\Delta\omega = 0$. The dielectric function ϵ is approximated by the dielectric function in random phase approximation (RPA). $M^0_{n\alpha}(q)$ is the vertex contribution for virtual transitions from n to α. $V(q) = Z_{\rm ion}e^2/\epsilon_0 q^2$ is the Fourier transformed Coulomb potential and $n_{\rm B}(\omega) = (\exp[\hbar\omega/(k_{\rm B}T)]-1)^{-1}$ is the Bose function. Further details can be found in the references given above.

We are aware of the fact that this Born approximation of the electronic self-energy might not suffice in the case of dense plasmas, where multiple and strong collisions become important. This is further discussed in Sec. 3.2.

2.2 Ionic self-energy $\Sigma_n^{\rm ion}(E)$

Assuming a quasi-static approximation, the ionic contribution to the self-energy of the ions is given by level perturbations due to the electric field of the ions (Stark effect) and due to the field gradients (quadrupole effect) [24]. For hydrogen and hydrogen-like ions with charge $Z_{\rm ion}$, the Stark effect can be evaluated in perturbation theory. The first and second order are [36]

$$\Sigma^{{\rm ion},(1)}_{n_1n_2m}(E) = \frac{3}{2}\frac{n(n_1-n_2)ea_{\rm B}}{Z_{\rm ion}+1}E, \tag{8}$$

$$\Sigma^{{\rm ion},(2)}_{n_1n_2m}(E) = -\left(17n^2-3(n_1-n_2)^2-9m^2+19\right)\frac{4\pi\epsilon_0a_B^3}{16(Z_{\rm ion}+1)^4}n^4\,E^2, \tag{9}$$

where parabolic quantum numbers n_1, n_2 and m are used. The principal quantum number is given by $n = n_1+n_2+|m|+1$.

For the quadrupole effect, we have used the expression of Halenka [37]

$$\Sigma^{{\rm ion},(q)}_{nn'}(E) = -\frac{5}{2\sqrt{32\pi}}\frac{eE_0}{R_0}B_\rho\left(\frac{E}{E_0}\right)\langle n|3z^2-r^2|n'\rangle, \tag{10}$$

where n stands for the quantum numbers n_1, n_2 and m. The function $B_\rho(x)$ corresponds to the average field gradient for a given field strength in units of the Holtsmark field $E_0 = Z_{\rm ion}e/(4\pi\epsilon_0R_0^2)$ with the next-neighbor distance R_0. The parameter $\rho = R_0/r_D$ is the screening parameter with the Debye screening length $r_D = \left[\epsilon_0k_{\rm B}T/(n_ee^2)\right]^{1/2}$. Further details can be found in [24, 37].

In total, the self-energy of the ions is given by

$$\Sigma^{\rm ion}_{nn'}(E) = \delta_{n,n'}\left(\Sigma^{{\rm ion},(1)}_n(E)+\Sigma^{{\rm ion},(2)}_n(E)\right)+\Sigma^{{\rm ion},(q)}_{nn'}(E). \tag{11}$$

2.3 Static microfield distribution $W(E)$

There are several approaches to the ionic microfield distribution function $W(E)$ in a plasma, see e.g. [38–41]. For ionic radiators, the adjustable parameter exponential approximation (APEX) has been worked out by Iglesias and coworkers [40,42]. Good agreement of this approach with Monte Carlo results has been observed [43]. Since we expect rather moderate values of the coupling parameter, a simplified version is used in the actual calculation, see Ref. [40]. Assuming an isotropic field distribution, the microfield distribution can be calculated with the help of a sine-transformation

$$W(E) = \frac{2E}{\pi}\int_0^\infty T(k)\sin(kE)k\,\mathrm{d}k, \tag{12}$$

$$T(k) = e^{-L(k)}. \tag{13}$$

As a special example, we give $L(k)$ using a Debye-Hückel pair correlation function

$$L(k) = -\frac{4\pi\epsilon_0 k_\mathrm{B} T r_\mathrm{D}}{Z_\mathrm{ion}^2 e^2}\int_0^\infty \mathrm{d}x\,\frac{x^2 e^x}{1+x}\exp\left[-\frac{Z_\mathrm{ion}^2 e^2}{4\pi\epsilon_0 k_\mathrm{B} T r_\mathrm{D} x}e^{-x}\right]\left(\frac{\sin(kb(x))}{kb(x)}-1\right) \tag{14}$$

with

$$b(x) = \frac{Z_\mathrm{ion} e}{4\pi\epsilon_0 r_\mathrm{D}^2}\frac{e^{-x}(1+x)}{x^2}, \quad x=\frac{r}{r_\mathrm{D}}. \tag{15}$$

This expression can be improved by using better approximations for the pair distribution functions, e.g. from the hypernetted-chain approximation, thus leading to a direct account for strong coupling effects. Alternatively, pair distribution results from molecular dynamics simulations can be taken into account, see the paper of Nersisyan, Toepffer, and Zwicknagel [44].

In this communication, detailed numerical comparison has been performed for $L(k)$ given by Eq. (14) and the Hooper microfield distribution [39]. Variances up to 4 % are found for the line width at $T = 10^5$ K and $n_e = 10^{24}$ to 10^{28} m^{-3}.

The existing approach has been extended to include dynamic ionic microfields [45], e.g. within the scope of the model microfield method (MMM) [46, 47]. As will been shown below, the account of dynamic ionic microfields is not necessary for the conditions considered in this paper.

2.4 Radiative transfer in 1d monolayer

Being high in density, self absorption is likely to occur in laser-produced plasmas. Indeed, experimental evidence for self-absorption has been found in a number of experiments [24, 48]. In general, the consideration of radiative transfer in dense plasmas is involved, as shown in [49]. Here, we use a simple, one-dimensional monolayer model to estimate the effect of self-absorption in the calculation of the line profile. This model has already been successfully applied in [24]. We consider a homogeneous plasma of thickness l, temperature T, and free electron density n_e. For this model, the transfer equation can be solved resulting in an intensity $I^s(\omega)$ emitted by the layer [50]

$$I^\mathrm{s}(\omega) = \left[1-\exp(-a_{if}P(\omega)d)\right]S_\omega(\omega)\ , \tag{16}$$

where $S_\omega(\omega)$ is the source function and a_{if} is given by

$$a_{if} = f_{fi} n_f \frac{e^2}{4\epsilon_0 m_e c}, \tag{17}$$

i.e. by the oscillator strength f_{fi}, taken from [51], and the density of the emitting ions that are in the lower energy level n_f. The line profile $P(\omega)$ is taken from Eq. (5), the source function is the spectral power density of the Planck distribution function

$$S_\omega(\omega) = \frac{\hbar\omega^3}{8\pi^2 c^2}\left[\exp(\hbar\omega/k_B T)-1\right]^{-1}\ . \tag{18}$$

The density n_f is calculated with the help of a Saha equation [52] assuming a Boltzmann distribution for the occupation of energy levels of a given ion species. Finally, the observed intensity $I^\mathrm{obs}(\omega)$ is obtained from Eq. (16) by convolution with the detector profile.

Note, that this model assumes (local) thermal equilibrium, an assumption, which will be discussed in Sec. 4.2.

Contrib. Plasma Phys. **48**, No. 9-10 (2008) / www.cpp-journal.org 661

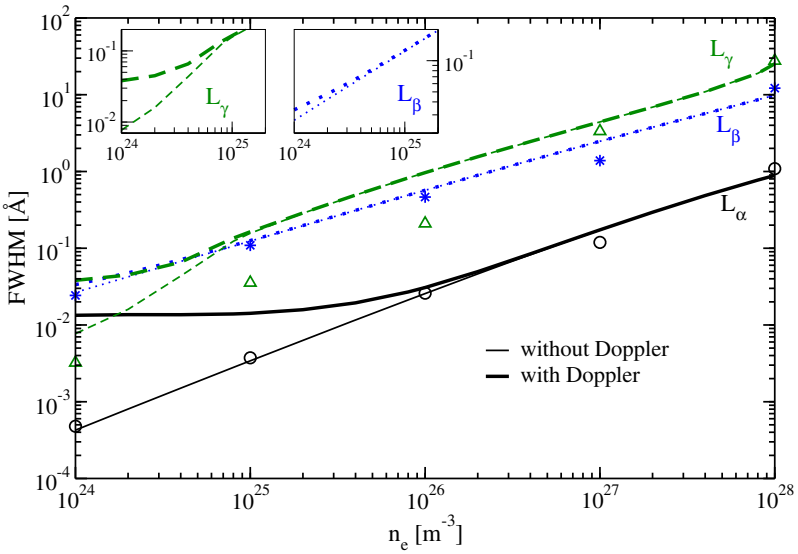

Fig. 1 Density dependence of FWHM of Lyman lines at $T = 10^5$ K. For clarity, the insets show the low density region of L_β ($\star$) and L_γ ($\triangle$). Symbols mark semi-classical calculations adapted from [26, 27]. (Online colour:www.cpp-journal.org).

3 FWHM and shifts for L_α, L_β, and L_γ

In a first step, we characterize the modifications of spectral line shapes in a plasma of given electron density n_e and temperature T by reporting the full width at half maximum (FWHM) and the shift of the maximum (L_α,L_γ) or the shift of the dip (L_β). Details such as asymmetries are not discussed. We postpone showing full spectra to the comparison with experimental data. Also, we assume the plasma to be optically thin accounting only for pressure and Doppler broadening. Self-absorption is discussed in Sec. 4.

3.1 Density and temperature dependence

In Fig. 1 and Fig. 2, the results for FWHM and shifts are given for $T = 10^5$ K and free electron densities between $n_e = 10^{24}$ m^{-3} and $n_e = 10^{28}$ m^{-3}. At densities where the pressure broadening dominates the line profile, FWHM and shift vary strongly with the density. Thus, they can be used to determine the density in emission experiments.

For FWHM, the Doppler effect can be neglected at densities above $n_e = 10^{26}$ m^{-3} in the case of L_α, below, it dominates the broadening. For L_β and L_γ, the influence of the Doppler broadening is less pronounced, but still visible at low densities.

The FWHM is compared with a semi-classical theory, which we have evaluated for Li^{2+} adapting the calculations that were done by Griem and Kepple [26, 27] for He^+. Whereas FWHM of L_α and L_β match well, semi-classical FWHM of L_γ deviate considerably from the quantum statistical results. We have used the same level of approximation for the ionic self-energies in both calculations. Thus, the differences are caused by the different approach to the electronic self-energies. The shift increases with the density and from L_α to L_γ, see Fig. 2. Semi-classical results for the shift are not available.

Fig. 3 and Fig. 4 show the temperature dependence of FWHM and maximum shift of L_α of Li^{2+}, respectively. The dependence on the temperature is only weak, thus FWHM and maximum shift are not preferred means to infer the temperature of a plasma. The Doppler broadened lines tend to be blue-shifted at low densities as the line profile is asymmetric.

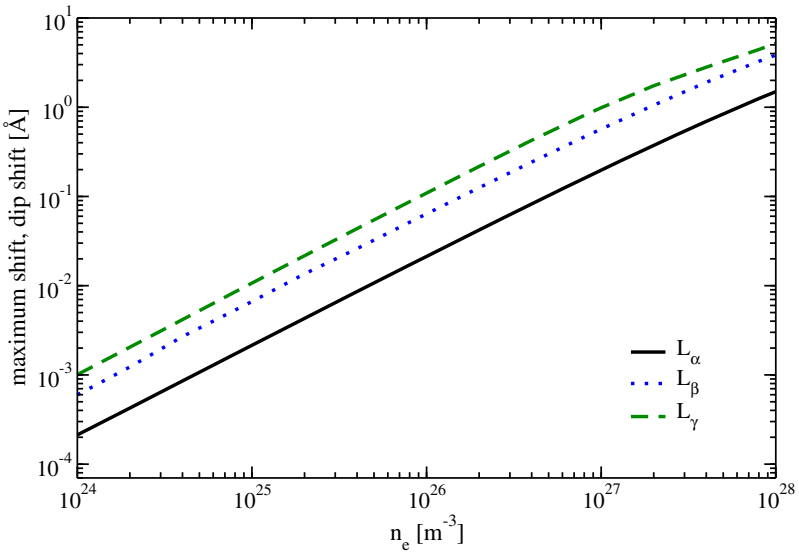

Fig. 2 Density dependence of the shift of Doppler broadened Lyman lines at $T = 10^5$ K. Maximum shift is shown for L_α and L_γ, dip shift for L_β.

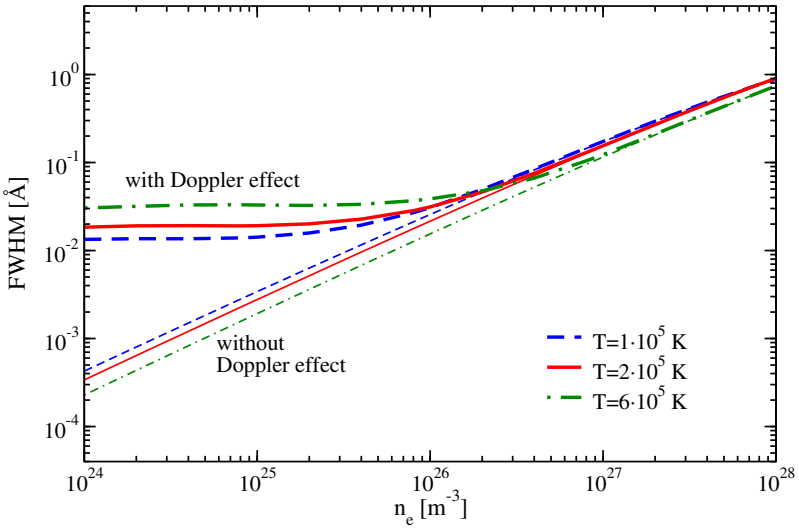

Fig. 3 Density dependence of FWHM of L_α for different temperatures. Bold lines correspond to calculations including the Doppler effect. Doppler broadening dominates the L_α-line width in the low density regime. (Online colour:www.cpp-journal.org).

3.2 Validity domain of approximations

In order to assess the validity of the approximations made above, we have to estimate the importance of ion dynamics and the relevance of strong collisions with the perturbing electron. Both effects have not been taken into account yet.

Contrib. Plasma Phys. **48**, No. 9-10 (2008) / www.cpp-journal.org 663

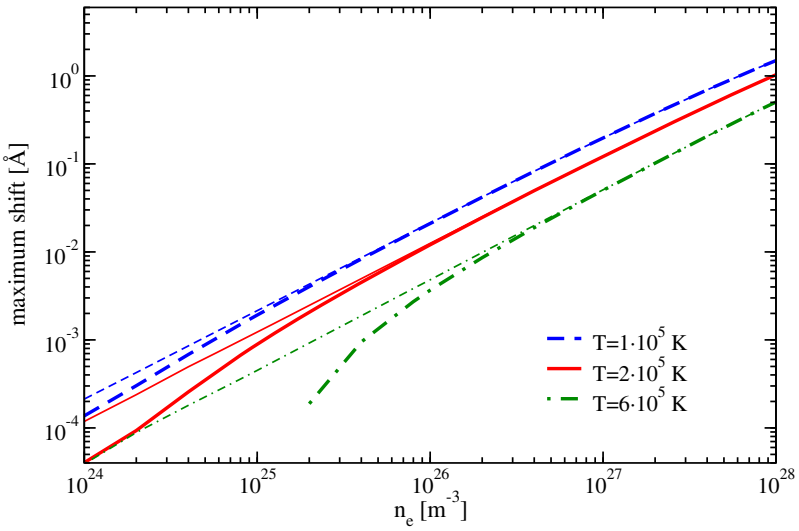

Fig. 4 Density dependence of maximum shift of L_α for different temperatures. Bold lines correspond to calculations including the Doppler effect. Due to asymmetries in the line profile, Doppler broadened lines are blue shifted. (Online colour:www.cpp-journal.org).

Table 1 The quasi-static approximation can be used if $\Delta\lambda_c/\Delta\lambda_{\mathrm{HWHM}} \ll 1$. This table gives the comparison for $T = 10^5$ K. $\Delta\lambda_c$ and $\Delta\lambda_{\mathrm{HWHM}}$ are given in Å, the electron density n_e is given in m^{-3}.

	L_α:			L_β:			L_γ:		
n_e	$\Delta\lambda_c$	$\Delta\lambda_{\mathrm{HWHM}}$	$\frac{\Delta\lambda_c}{\Delta\lambda_{\mathrm{HWHM}}}$	$\Delta\lambda_c$	$\Delta\lambda_{\mathrm{HWHM}}$	$\frac{\Delta\lambda_c}{\Delta\lambda_{\mathrm{HWHM}}}$	$\Delta\lambda_c$	$\Delta\lambda_{\mathrm{HWHM}}$	$\frac{\Delta\lambda_c}{\Delta\lambda_{\mathrm{HWHM}}}$
10^{24}	0.0015	0.0002	$8 \cdot 10^{0}$	0.0011	0.013	$2 \cdot 10^{-1}$	0.0010	0.0039	$3 \cdot 10^{-1}$
10^{25}	0.0033	0.0017	$2 \cdot 10^{0}$	0.0023	0.062	$4 \cdot 10^{-2}$	0.0021	0.0783	$3 \cdot 10^{-2}$
10^{26}	0.0070	0.0125	$6 \cdot 10^{-1}$	0.0050	0.284	$2 \cdot 10^{-2}$	0.0045	0.4825	$9 \cdot 10^{-3}$
10^{27}	0.0152	0.0862	$2 \cdot 10^{-1}$	0.0108	1.237	$9 \cdot 10^{-3}$	0.0097	2.2107	$4 \cdot 10^{-3}$

3.2.1 Ion dynamics

As a rule of thumb, the quasi-static approximation can be used as long as the collision time, which can be approximated by $t_c = n_{\mathrm{ion}}^{1/3}/\left(2k_{\mathrm{B}}T/m_{\mathrm{ion}}\right)^{1/2}$, is long compared to the emission time $\tau = (\Delta\omega)^{-1}$ [16], i.e. $t_c \gg \tau$. Thus, it is sufficient for long collision times corresponding to high densities or low temperatures. The innermost part of the line center is always affected by the ion dynamics due to the relationship $\tau = (\Delta\omega)^{-1}$. As long as this part is small, i.e. $\Delta\lambda_c/\Delta\lambda_{\mathrm{HWHM}} \ll 1$, the quasistatic approximation is justified. Here, $\Delta\lambda_c$ is the wavelength where $t_c = \tau$ for a given temperature and density, i.e. the border between quasi-static and collision approximation.

A comparison of $\Delta\lambda_c$ and our calculated line width $\Delta\lambda_{\mathrm{HWHM}}$ is given in Table 1 for a fixed temperature $T = 10^5$ K and various electron densities. As can be seen, ion dynamics only need to be included in calculations up to $n_e = 10^{26}$ m^{-3} for $T = 10^5$ K in the case of L_α. However, in this region, the line broadening is dominated by the Doppler effect anyway. Therefore, further studies of the ion dynamics are omitted. As for L_β and L_γ, the quasi-static approximation is valid for all conditions considered here.

3.2.2 Strong collisions

Next, we will estimate the influence of strong collisions. So far, our treatment was restricted to a Born approximation taking into account only weak collisions. Within our quantum-statistical approach, a T-matrix approximation has been developed [53] to take account of strong collisions. Doing calculations for a large number of density and

temperature conditions is computationally quite expensive. We can give two arguments to neglect these extended calculations for strong collisions.

We compare the classical impact parameter [26] that leads to 90° scattering of a thermal electron

$$\rho = \frac{Z_{\rm ion} e^2}{4\pi\epsilon_0 m_e v_{\rm therm}^2} \tag{19}$$

to the mean electron distance d_e. At $T = 10^5$ K and $n_e = 10^{26}$ m^{-3}, ρ is about 9 % of d_e, thus strong collisions are expected to be rare. Even at $n_e = 10^{28}$ m^{-3}, ρ is still below 50 % of d_e. At higher temperatures these values are even lower.

Although the influence of strong collisions is thus expected to be small, we use the semi-classical theory of Griem and Kepple [26, 27] to give a more quantitative estimate. In their approach, strong collisions are approximated by an additional term ($\pi v n_e \rho_{\rm min}^2$) with the minimal impact parameter $\rho_{\rm min} \approx \hbar/(m_e v)$ which depends on the electron velocity v. For L_α, this additional term changes the line width by up to 2 % at $T = 10^5$ K and $n_e = 10^{24} - 10^{28}$ m^{-3}.

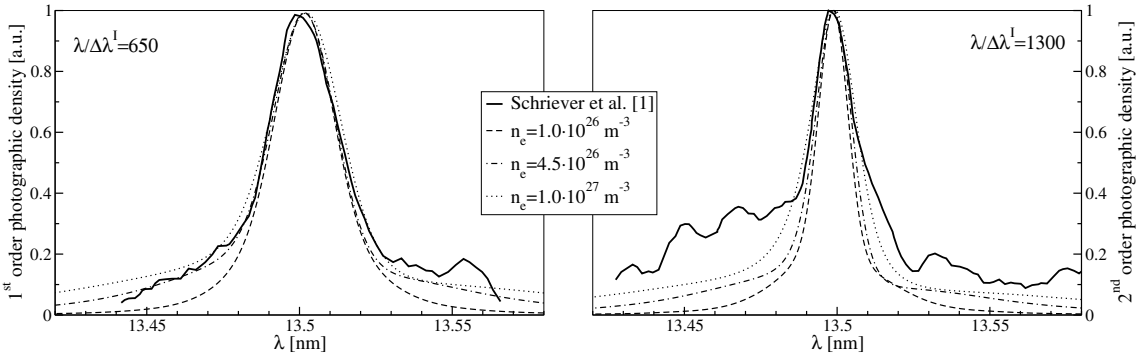

Fig. 5 L_α of Li^{2+}: Experimental data [1] can be reproduced with a free electron density between $n_e = 10^{26}$ m^{-3} and $n_e = 10^{27}$ m^{-3} without considering radiative transport effects. These conditions correspond to ionic coupling parameters $\Gamma_{ii} = 0.30$, 0.48 and 0.62, respectively.

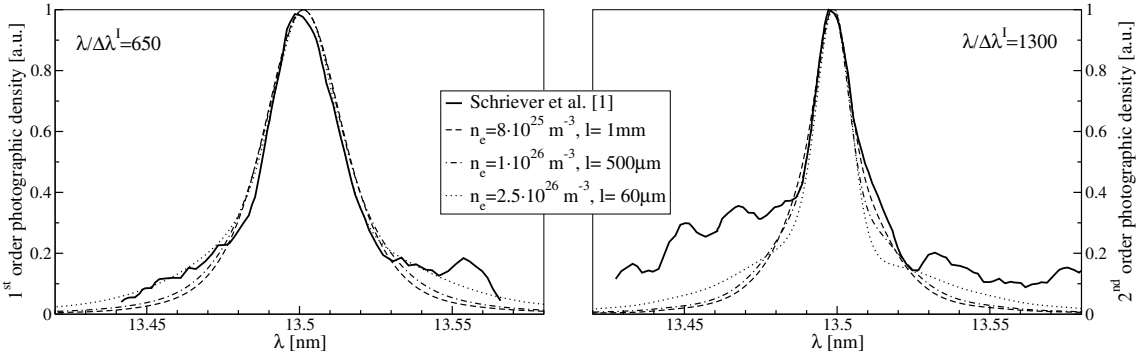

Fig. 6 L_α of Li^{2+}: Considering radiative transport through a plasma layer of thickness l, experimental data [1] can be reproduced at lower densities compared to Fig. 5. These conditions correspond to ionic coupling parameters $\Gamma_{ii} = 0.28$, 0.30 and 0.40, respectively.

4 Comparison with measurements from laser-produced plasmas

So far, we have considered line emission for fixed temperature and density conditions. Now, we want to use our approach to analyze transient plasmas created by intense laser radiation. We use the experimental data of

Contrib. Plasma Phys. **48**, No. 9-10 (2008) / www.cpp-journal.org 665

Schriever et al. [1, 2]. In their experimental setup, a pulsed laser beam of a Nd:YAG laser (wavelength $\lambda = 1064$ nm) with a maximum energy of 1300 mJ per pulse was focused on the surface of a lithium target. Finding a spot size of 30 μm, intensities between 10^{10} and $1.1 \cdot 10^{13}$ W/cm^2 were realized by attenuating the laser beam. The pulse length was 13 ns. The emitted light has been detected in single pulse experiments at an angle of 45°. The resulting spectra are time- and space-integrated. The emission time was measured to be as long as the laser pulse (13 ns).

4.1 Lyman-α

In [1], the line width of L_α is determined in first and second diffraction order. The line profile is measured with a Rowland circle grazing-incidence spectrograph with the spectral resolution $\lambda/\Delta\lambda^{\mathrm{I}} = 650$ in first order and $\lambda/\Delta\lambda^{\mathrm{I}} = 1300$ in second order. With an intensity of $I_{\mathrm{L}} = 5.5 \cdot 10^{11}$ W/cm^2 of the laser, the plasma is assumed to have an average electron temperature of $k_{\mathrm{B}}T_e = 47$ eV. The electron density is expected to be above $n_e = 1 \cdot 10^{25}$ m^{-3} [1].

Using a temperature of $k_{\mathrm{B}}T = 47$ eV, as stated in [1], we calculate the line profile for different densities. The calculated and measured profiles are compared in Fig. 5. The instrumental broadening is taken to be of Gaussian form. Due to the huge influence of the instrumental broadening, the line profiles can be reproduced sufficiently well with densities between $n_e = 10^{26}$ m^{-3} and $n_e = 10^{27}$ m^{-3}.

Next, we consider radiative transport within the 1d monolayer model. Thus, we neglect the fact that the experimental spectrum is time and space integrated and use an average temperature and density as fixed values. Having an additional broadening mechanism, the line profile can be matched with lower densities provided the plasma layer is taken to be thick enough. In Fig. 6, line profiles are shown for three different sets of free electron density n_e and thickness of plasma layer l. A layer of several micrometer seems reasonable for a laser-produced plasma leading to our preferred estimate: $n_e = 2.5 \cdot 10^{26}$ m^{-3}, $l = 60$ μm. For these conditions a red shift of $\Delta\lambda_S = +1.1 \cdot 10^{-3}$ nm is calculated. According to [1], the line shift was deduced in the second diffraction order to be $\Delta\lambda_S = -1 \cdot 10^{-3}$ nm. This contradiction might be due to neglecting the Doppler shift caused by the directed motion of the radiator $\Delta\lambda_{\mathrm{D}} = c_{\mathrm{ion}}\lambda/c$ in our calculations. As an estimate $\Delta\lambda_D = -1.6 \cdot 10^{-3}$ nm is obtained by using the ionic speed of sound $c_{\mathrm{ion}} = (Z_{\mathrm{ion}}k_{\mathrm{B}}T/m_{\mathrm{ion}})^{1/2}$ as an approximation.

4.2 Lyman-spectrum

The Lyman-spectrum has been measured in [2] with a spectral resolution of $\lambda/\Delta\lambda^{\mathrm{I}} = 300$. A laser intensity of $I_{\mathrm{L}} = 1.1 \cdot 10^{13}$ W/cm^2 was used to generate the plasma. The higher intensity leads to an electron temperature of $k_{\mathrm{B}}T_e > 100$ eV. Within the assumption of complete local thermodynamic equilibrium (LTE), the Li^{2+}-fraction reduces to less than 0.1 % at these temperatures. In the comparison, we apply a linear rescaling of the wavelength axis by 1.1 % centered at 13.5 nm, thus shifting the measured L_β and L_γ to their unperturbed positions. Due to the rescaling, we do not consider the line shift in this part of our work.

To generate the full Lyman spectrum, we use the relative intensity of L_β to L_γ to deduce the temperature from the experiment. Assuming thermodynamic equilibrium and neglecting radiative transport effects in a first step, the temperature is evaluated to $T = 3 \cdot 10^5$ K. The electron density is fitted to the line width of L_γ as shown in Fig. 7. In contrast to the situation discussed before, Stark broadening is much stronger, leading to a clear discrimination between different densities. Here, an electron density $n_e = 4 \cdot 10^{25}$ m^{-3} gives the best fit.

With these parameters, L_α and L_β are calculated accounting for radiative transport. Also, L_γ is recalculated including self-absorption effects. By adjusting the plasma layer thickness, the correct ratio between L_α- and L_γ-peak values can be obtained. Fig. 8 shows the full spectrum using a plasma layer of thickness $l = 180$ μm. For comparison, the spectrum without self-absorption effects is given, too. Note that radiative transport reduces the height of L_α considerably. L_β is much less affected by radiation transfer, while L_γ shows almost no influence at all. Our synthetic spectrum reproduces the experimental line width and peak values (relative to L_γ). However, the line wings are considerably underestimated. One reason for this might be the simple description of the microfield we use. Furthermore, the self-energy of the electrons should be improved, taking strong collisions into account. Both topics have been discussed above outlining possible improvements. For the parameters inferred here, estimations indicate, that these improvements are unlikely to rectify the discrepancy in the line wings.

Last but not least we have to emphasize, that our approach neglects the transient nature of the plasma and only considers mean values for temperature and density, which is questionable for laser-produced plasmas.

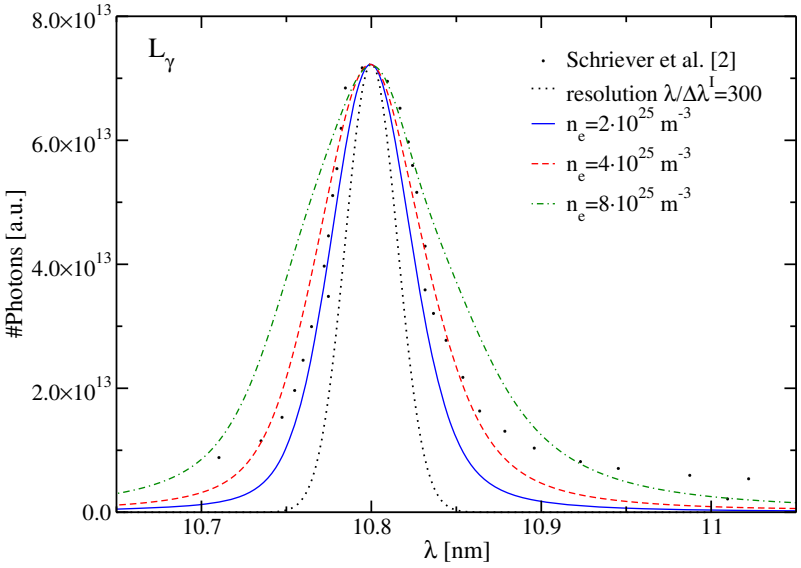

Fig. 7 At $T = 3 \cdot 10^5$ K and assuming a resolution of $\lambda/\Delta\lambda^{\mathrm{I}} = 300$, the line width of L_γ is reproduced best with an electron density of $n_e = 4 \cdot 10^{25}$ m^{-3}. (Online colour:www.cpp-journal.org).

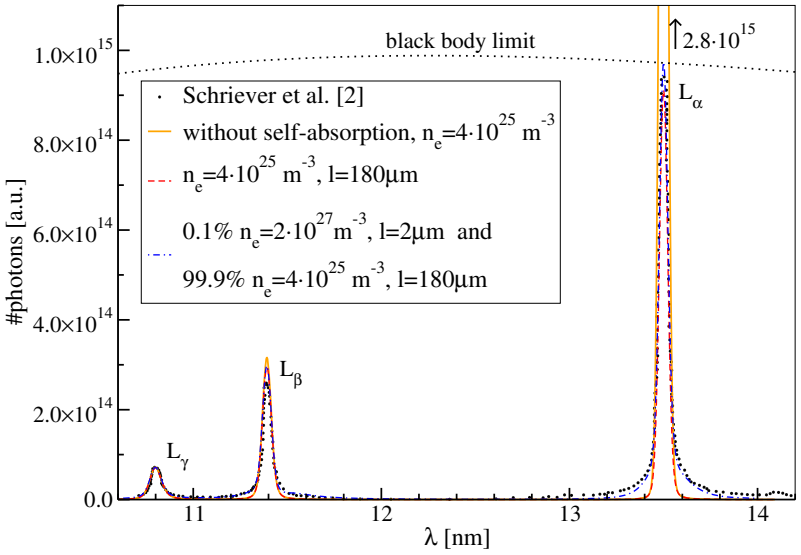

Fig. 8 Comparison of experimental data [2] with a synthetic Li^{2+}-Lyman spectrum at $T = 3 \cdot 10^5$ K and $n_e = 4 \cdot 10^{25}$ m^{-3} with and without radiative transport through $l = 180$ μm, respectively. This corresponds to an ionic coupling parameter $\Gamma_{ii} = 0.37$. The dash-dotted line corresponds to a spectrum synthesized from two plasma regions. Instrumental broadening $\lambda/\Delta\lambda^{\mathrm{I}} = 300$ is taken into account. (Online colour:www.cpp-journal.org).

We present an exploratory calculation by estimating the time evolution of the plasma. Adding the line emission of an estimated earlier stage of the plasma, with $n_e = 2 \cdot 10^{27}$ m^{-3} and $l = 2$ μm, and assuming that these conditions prevail only 0.1 % of the time, the line wings can be synthezised, too. This is also shown in Fig. 8.

Contrib. Plasma Phys. **48**, No. 9-10 (2008) / www.cpp-journal.org 667

A further crucial approximation is the assumption of LTE. A detailed study for hydrogen-like ions has been carried out by Fujimoto and McWhirter [54, 55] solving the collisional-radiative equations. Following their parametrization, LTE is established for hydrogen-like atoms with atomic number Z as long as

$$n_e/\mathrm{m}^{-3} \geq 1.5 \cdot 10^{24} Z^7 \left(\frac{T/\mathrm{K}}{Z^2 \cdot 10^6} \right)^{0.55-(0.49/Z)^{1.5}} . \tag{20}$$

Using the temperature $T_e = 3 \cdot 10^5$ K, we obtain $n_{e,\mathrm{cr}} = 6.3 \cdot 10^{26}$ m^{-3} for the critical density beyond which LTE is established, i.e. roughly one order of magnitude above the density inferred in the previous paragraph. However, this criteria has to be substantially relaxed for optically thick plasmas [54]. It is expected, that LTE conditions are indeed established for the densities found here. For a detailed answer to this question, collisional-radiative equation and radiation transport have to be solved at the same time [54]. This can be achieved extending the studies of Stapleton et al. [56] on equilibrium conditions in a laser ablation plume of lithium.

5 Conclusions

Using a microscopic quantum statistical approach, the line profiles of Lyman lines for hydrogen-like lithium plasmas were studied. FWHM and shifts were generated showing the importance of Stark broadening in the considered density and temperature region. Clearly, a quasi-static treatment of the ionic microfields is sufficient for the conditions of laser-produced plasmas at moderate and high intensities.

We were able to reproduce the gross features of experimental Lyman spectra within a simple model of a one-dimensional uniform layer. For the L_α profile reported in [1], we infer from the line profile a plasma layer thickness $l = 60$ μm and an electron density $n_e = 2.5 \cdot 10^{26}$ m^{-3} which is in accordance with the lower limit of $n_e > 10^{25}$ m^{-3} claimed in Ref. [1]. Note however, that the dominance of instrumental broadening impedes a clear discrimination of different density conditions.

In case of the Lyman spectrum measured in [2] , the relative height and the FWHM of L_α, L_β, and L_γ can be matched by a synthetic emission spectrum from a plasma layer with temperature $T = 3 \cdot 10^5$ K, electron density $n_e = 4 \cdot 10^{25}$ m^{-3} and layer thickness $l = 180$ μm. However, there are clear discrepancies when comparing the line wings. As explained, improvements to the microfield and/or the account of strong collisions seem not to rectify this shortcoming. It appears more likely to be connected to the transient nature of laser-produced plasmas showing a strong time dependence in density and ionization. A detailed account using the 1d hydrocode MEDUSA [57] is work in progress. It is expected that this will lead to a more sound picture of emission sites and emission times.

Clearly, a more precise record of the time-evolution of the plasma would be possible by applying the above diagnostics to time- and spatial resolved measurements. Also, an independent estimate of the temperature could be considered having the continuum part of the spectrum at our disposal.

Acknowledgements This article was supported by the Deutsche Forschungsgemeinschaft within the Sonderforschungsbereich 652 ' Starke Korrelationen und kollektive Phänomene im Strahlungsfeld: Coulombsysteme, Cluster und Partikel.'

References

[1] G. Schriever, S. Mager, A. Naweed, A. Engel, K. Bergmann, and R. Lebert, Applied Optics **37**, 1243 (1998).

[2] G. Schriever, K. Bergmann, and R. Lebert, J. Appl. Phys. **83**, 4566 (1998).

[3] V. Banine and R. Moors, J. Phys. D **37**, 3207–3212 (2004).

[4] J. Jonkers, Plasma Sources Sci. Technol. **15**, S8–S16 (2006).

[5] S. A. George, W. T. Silfvast, K. Takenoshita, R. T. Bernath, C. S. Koay, G. Shimkaveg, and M. C. Richardson, Optics Letters **32**, 997–999 (2007).

[6] A. Nagano, T. Inoue, P. E. Nica, S. Amano, S. Miyamoto, and T. Mochizuki, Appl. Phys. Lett. **90**, 151502 (2007).

[7] A. Nagano, T. Mochizuki, S. Miyamoto, and S. Amano, Appl. Phys. Lett. **93**, 091502 (2008).

[8] I. V. Fomenkov, W. N. Partlo, N. R. Böwering, A. I. Ershov, C. L. Rettig, R. M. Ness, I. R. Oliver, S. T. Melnychuk, O. V. Khodykin, J. R. Hoffman, V. B. Fleurov, J. M. Algots, J. W. Viatella, B. A. M. Hansson, O. Hemberg, A. N. Bykanov, E. A. Lopez, P. C. Oh, T. D. Steiger, and D. W. Myers, Progress in development of a high power source for EUV lithography, 2004, presented at the Symposium on EUVL (Miyasaki, Japan).

[9] M. Masnavi, M. Nakajima, E. Hotta, and K. Horioka, J. Appl. Phys. **103**, 013303 (2008).

[10] K. Nishihara and al., Phys. Plasmas **15**, 056708 (2008).

[11] G. Jamelot, P. Jaegle, P. Lemaire, and A. Carillon, J. Quant. Spectrosc. Radiat. Transfer **44**, 71 (1990).

[12] W. Lochte-Holtgreven, Plasma diagnostics (AIP Press, New York, 1995), originally published in 1968.

[13] I. H. Hutchinson, Principles of plasma diagnostics (Cambridge University Press, Cambridge, 1987).

[14] H. R. Griem, Principles of Plasma Spectroscopy (Cambridge University Press, Cambridge, 1997).

[15] H. A. Lorentz, Proc. R. Acad. Sci. **8**, 591 (1906).

[16] H. R. Griem, Spectral Line Broadening by Plasmas (Academic Press, London, 1974).

[17] D. Voslamber, Phys. Lett **40A**, 266 (1972).

[18] C. Vidal, J. Cooper, and E. Smith, Astrophys. J. Suppl. Ser. **25**, 37 (1973).

[19] K. Unnikrishan and J. Callaway, Phys. Rev. A **44**, 3001 (1991).

[20] B. Talin, A. Calisti, L. Godbert, R. Stamm, R. Lee, and L. Klein, Phys. Rev. A **51**, 1918–1928 (1995).

[21] M. Gigosos and V. Cardeñoso, J. Phys. B: At. Mol. Opt. Phys. **29**, 4795–4838 (1996).

[22] W. D. Kraeft, D. Kremp, W. Ebeling, and G. Röpke, Quantum Statistics of Charged Particle Systems (Akademie-Verlag Berlin, Berlin, 1986).

[23] S. Günter, Optische Eigenschaften dichter Plasmen, habilitation thesis at Rostock University, 1995.

[24] S. Sorge, A. Wierling, G. Röpke, W. Theobald, R. Sauerbrey, and T. Wilhein, J. Phys. B: At. Mol. Opt. Phys. **33**, 2983–3000 (2000).

[25] B. Omar, A. Wierling, S. Günter, and G. Röpke, J. Phys. Conf. Series **11**, 147 (2005).

[26] H. R. Griem and K. Y. Shen, Phys. Rev. **122**, 1490–1496 (1961).

[27] P. C. Kepple, Phys. Rev. A **6**, 1–9 (1972).

[28] W. Theobald, C. Wülker, J. Jasny et al., Optics Communications **149**, 289 (1998).

[29] C. Rajyaguru, T. Higashiguchi et al., Appl. Phys. B **80**, 409 (2005).

[30] P. E. Nica, S. Miyamoto, S. Amano, T. Inoue, A. Shimoura, K. Kaku, and T. Mochizuki, Appl. Phys. Lett. **89**, 41501 (2006).

[31] P. Nica, S. Miyamoto, S. Amano, T. Inoue, A. Shimoura, and T. Mochizuki, Phys. Lett. A **370**, 154–157 (2007).

[32] S. A. George, W. Silfvast, K. Takenoshita, R. Bernath, C. S. Koay, G. Shimkaveg, and M. Richardson, Proc. SPIE. **6151**, 615143 (2006).

[33] S. A. George (2008), private communication.

[34] S. Günter, L. Hitzschke, and G. Röpke, Phys. Rev. A **44**, 6834–6844 (1991).

[35] A. Könies and S. Günter, J. Quant. Spectrosc. Radiat. Transfer **52**, 825 (1994).

[36] L. D. Landau and E. M. Lifschitz, Quantum mechanics : non-relativistic theory (Pergamon Press, Oxford, 1977).

[37] J. Halenka, Z. Phys. D **16**, 1 (1990).

[38] M. Baranger and B. Mozer, Phys. Rev. **115**, 521–525 (1959).

[39] C. F. Hooper, Jr., Phys. Rev. **149**, 77–91 (1966).

[40] C. A. Iglesias, Phys. Rev. A **27**, 2705–2709 (1983).

[41] X. Z. Yan and S. Ichimaru, Phys. Rev. A **34**, 2167 (1986).

[42] C. A. Iglesias, J. L. Lebowitz, and D. MacGowan, Phys. Rev. A **28**, 1667–1672 (1983).

[43] C. Iglesias, H. DeWitt, J. Lebowitz, D. MacGowan, and W. Hubbard, Phys. Rev. A **31**, 1698–1702 (1985).

[44] H. Nersisyan, C. Toepffer, and G. Zwicknagel, Phys. Rev. E **72**, 036403 (2005).

[45] A. Könies, S. Günter, and G. Röpke, J. Phys. B: At. Mol. Opt. Phys. **29**, 6091–6101 (1996).

[46] A. Brissaud and U. Frisch, J. Quant. Spectrosc. Radiat. Transfer **11**, 1767 (1971).

[47] J. Seidel, Z. Naturf. **32a**, 1195 (1977).

[48] Y. Leng, J. Goldhar, H. Griem, and R. Lee, Phys. Rev. E **52**, 4328–4337 (1995).

[49] J. P. Apruzese, J. Davis, K. G. Whitney, J. W. Thornhill, P. C. Kepple, and R. W. Clark, Phys. Plasmas **9**, 2411 (2002).

[50] G. B. Rybicki and A. P. Lightman, Radiative Processes in Astrophysics (John Wiley and Sons, New York, 1979).
[51] D. A. Verner, E. M. Verner, and G. J. Ferland, Atomic Data and Nuclear Data Tables **64**, 1–180 (1996).
[52] M. R. Zaghloul, M. A. Bourham, and J. M. Doster, J. Phys. D: Appl. Phys. **33**, 977–984 (2000).
[53] A. Könies and S. Günter, Phys. Rev. E **52**, 6658–6663 (1995).
[54] T. Fujimoto and R. McWhirter, Phys. Rev. A **42**, 6588–6601 (1990).
[55] T. Fujimoto, Plasma Spectroscopy (Oxford University Press, Oxford, 2004).
[56] M. W. Stapleton, A. P. McKiernan, and J. P. Mosnier, J. Appl. Phys. **97**, 64904 (2005).
[57] J. Christiansen, D. Ashby, and K. Roberts, Comp. Phys. Commun. **7**, 271 (1974).

Contrib. Plasma Phys. **51**, No. 4, 349 – 354 (2011) / **DOI** 10.1002/ctpp.201010104

Improved Self-Energy Calculations for Pressure Broadening of Spectral Lines in Dense Plasmas

S. Lorenzen[*1], **A. Wierling**[1], **H. Reinholz**[1,2], and **G. Röpke**[1]

[1] Universität Rostock, 18051 Rostock, Germany
[2] University of Western Australia, Nedlands, WA 6009, Australia

Received 16 October 2009, accepted 24 November 2009
Published online 4 May 2010

Key words Pressure broadening, self-energy, strong collisions, T-matrix.

Pressure broadening of Lyman-lines of hydrogen-like lithium (Li^{2+}) has been studied using a quantum statistical approach to the line shape in dense plasmas, for details see [1]. In this communication, we concentrate on the electronic self-energy, which is a basic input to the theory of spectral line profiles. We discuss the effect of strong, i.e. close, collisions which have been neglected so far for Li^{2+} plasmas, but play generally an important role in dense plasmas, as has been shown in [2]. We present a method to calculate an improved electronic self-energy including strong collisions based on a two-body T-matrix and an effective optical potential. The method is tested for level broadening of the ground state of hydrogen.

1 Introduction

Spectral line profiles can be used as a diagnostic tool in experiments due to the dependence of the line shape on plasma parameters such as density and temperature, see [3, 4]. Several microscopic approaches to line broadening are available, e.g. the semi-classical treatment [2], and the unified theory [5–7]. Computer simulation techniques [8] and close-coupling based methods [9] have also been used successfully. In Rostock, a quantum-statistical approach to full line profiles has been developed based on thermodynamic Green's functions [10]. It has been applied to hydrogen, helium and hydrogen-like ions, e.g. the analysis of C^{5+} in a laser-produced carbon plasma [11]. Most recently, we presented results for hydrogen-like lithium (Li^{2+}) Lyman lines emitted from a laser-produced Li plasma in Ref. [1].

Within the quantum-statistical formalism, the self-energy of the bound state enters as a basic input quantity. Performing a cluster-decomposition, the leading term of the self-energy is due to perturbations by the free plasma electrons. Thus, the three-particle self-energy has to be considered. Typically, it is evaluated in Born approximation. However, this perturbative approach neglects strong collisions, although they might be of importance in dense plasmas. To include strong collisions, an in-medium three-body T-matrix T_3 has to be evaluated, i.e. a Faddeev-Merkuriev integral-equation has to be solved [12]. For an isolated hydrogen atom this has been done in Ref. [13]. As this is numerically involved, simplifications are desired.

In the semi-classical theory [2], a cut-off at a minimum collision parameter $\varrho_{\min}$ ensures convergence, and strong collisions are estimated by a term proportional to $\varrho_{\min}^2$. However, this involves a certain arbitrariness. A more recent semi-classical approach, the classical path all-order model [14], avoids this arbitrariness by using a Deutsch potential [15]. In the quantum-statistical theory, strong collisions have only been included systematically for hydrogen in Ref. [16], i.e. for a neutral radiator. There, the T-Matrix was obtained from a partial summation of ladder diagrams. This is correct up to the third order in the interaction potential V. As we are interested in a quantum-statistical approach for a charged radiator (Li^{2+}), the potential between electron and radiator is no longer weak and long ranged. Thus, this approximation is not well justified. Instead, we make a different approximation, known from atomic scattering theory. Namely, we reduce the three-body T-matrix to a two-body T-matrix with an appropriately constructed optical potential. This approach is discussed in Sec. 3. As an

* Corresponding author: E-mail: sonja.lorenzen@uni-rostock.de, Phone: +49 381 4986946, Fax: +49 381 4986942

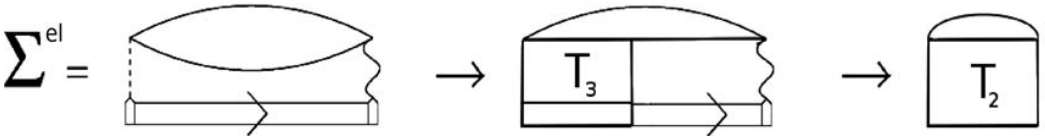

Fig. 1 Electronic part of the self-energy: dynamically screend Born approximation (see [1]), with full three-particle T-matrix (see Ref. [16]), and two particle T-matrix with effective potential as an approximation (considered here).

example, the self-energy of the ground state of hydrogen is calculated in Sec. 4. There, it is compared to the Born approximation and the implications for our line-profile calculations are discussed.

2 Improved electronic self-energy

Due to different interaction time scales, the influence of surrounding electrons and ions on the emitter is considered seperately. Binary collision approximation is applied for the dynamic electrons, whereas the surrounding ions are treated as quasi-static perturbers. The details of this approach have been presented in [1] and are reviewed here. The full line profile $I^{\rm pr}(\Delta\omega)$ can be calculated. It is proportional to [17]

$$I^{\rm pr}(\Delta\omega) \quad \sim \quad \sum_{ii'ff'} \left\{ \langle i|\vec{r}|f\rangle\langle f'|\vec{r}|i'\rangle \int_0^\infty {\rm d}E\; W(E)\langle i|\langle f|L^{-1}(\Delta\omega,E)|f'\rangle|i'\rangle \right\}, \tag{1}$$

where the sum contains all terms of degenerate initial and final states i, i' and f, f' weighted with dipole moments $\langle i|\vec{r}|f\rangle$. As we consider the influence due to the surrounding ions in quasi-static approximation, we integrate over the ionic microfield distribution $W(E)$. We take $W(E)$ in the APEX approximation of Iglesias [18].

The medium modifications are contained in the line profile operator that is given by

$$L(\Delta\omega,E) = \hbar\Delta\omega - {\rm Re}\left[\Sigma_i(\omega,E) - \Sigma_f(\omega,E)\right] - {\rm i}\,{\rm Im}\left[\Sigma_i(\omega,E) + \Sigma_f(\omega,E)\right] + i\Gamma^{\rm V}_{if}\,, \tag{2}$$

where the real and imaginary part of $\Sigma_{i,f}$ correspond to the shift and broadening of the initial and final energy level due to the surrounding medium, respectively. The coupling between initial and final state, the so called vertex correction $\Gamma^{\rm V}_{if}$, is given by

$$\Gamma^{\rm V}_{if} = -4\pi \int \frac{{\rm d}^3q{\rm d}^3p}{(2\pi)^6} f_{\rm e}(E_p) V^2(q) M_{ii'}(\vec{q}) M_{ff'}(-\vec{q}) \delta(\frac{\vec{p}\cdot\vec{q}}{m_{\rm e}}). \tag{3}$$

It can be neglected for Lyman lines [19], as the vertex contribution $M_{ff'}(\vec{q})$ is small for the ground state.

The broadening and shift due to the surrounding electrons, the so called electronic self-energy $\Sigma^{\rm el}$, plays an important rôle in our approach. The real and imaginary part of $\Sigma^{\rm el}_{i,f}$ correspond to the shift and broadening of the initial and final energy level, respectively.

In Fig. 1, we give diagrammatic representations of various approximations to the self-energy $\Sigma^{\rm el}_\nu$ of the bound state with quantum numbers $\nu = (n_\nu, l_\nu, m_\nu)$. The first diagram is the self-energy used so far, i.e. a dynamically screened Born approximation without exchange, given by

$$\Sigma^{\rm el}_\nu(\Delta\omega) = -\int \frac{{\rm d}^3q}{(2\pi)^3} V(q) \sum_{\nu'} |M^0_{\nu\nu'}(q)|^2 \int_{-\infty}^{\infty} \frac{{\rm d}\omega}{\pi} (1+n_{\rm B}(\omega)) \times \frac{{\rm Im}\varepsilon^{-1}(\vec{q},\omega+i\delta)}{\Delta\omega + \omega_{\nu\nu'} - (\omega+i\delta)}\,, \tag{4}$$

with the vertices $|M^0_{\nu\nu'}(q)|^2 \sim q^2\langle\nu|\vec{r}|\nu'\rangle + O(q^3)$, the Bose distribution $n_{\rm B}(\omega)$, and the dielectric function $\varepsilon(\vec{q},\omega+i\delta)$. We evaluate the self-energy at $\Delta\omega = 0$, i.e. the frequency of the unperturbed transition.

In the second diagram of Fig. 1, the first interaction line is replaced by a static three-particle T-matrix. By this generalization, we include strong collisions. Ignoring dynamical screening, we arrive at

$$\Sigma^{\rm el}_\nu \quad = \quad \frac{i}{e} \int \frac{{\rm d}^3q{\rm d}^3p}{(2\pi)^6} V(q) \sum_{\nu'} M_{\nu\nu'}(\vec{q}) f_{\rm e}(E_p) \times \frac{T^{\rm eb}_3(\nu,\nu',\vec{p},\vec{q}-\vec{q},E_\nu+E_p)}{E_{\nu'} - E_\nu + E_{\vec{p}-\vec{q}} - E_p}\,, \tag{5}$$

Contrib. Plasma Phys. **51**, No. 4 (2011) / www.cpp-journal.org 351

where $T_3^{\rm eb}$ is defined by a ladder summation, for details see Ref. [16].

The full three-particle T-matrix has to be evaluated, which can be done by solving the Faddeev equation with a static screened interaction. However, as a huge number of open channels has to be considered for weak screening, it is a very challenging task.

3 Optical potential approach

The last diagram approximates the second by including a two-particle T-matrix with an effective potential between scattered electron and emitter, thus simplifying the calculation enormously. A general approach to the effective potential is given by the projector operator technique of Feshbach [20] which leads to a coupled set of Lippmann-Schwinger equations [21]. Here, we consider a local equivalent potential, where non-local effects are described by a local optical potential, i.e. a complex and energy dependent potential. This approach has been applied successfully in scattering theory. In the following, atomic Rydberg units are used ($m_e = 1/2$, $e^2 = 2$, $\hbar = 1$, $\epsilon_0 = 1/4\pi$). The last diagram in Fig. 1 evaluates to

$$\Sigma_\nu^{\rm el} = \frac{1}{\pi^2}\int_0^\infty {\rm d}p\, p^2 f_{\rm e}(p^2) T^{\rm eb}(p,p,p^2+E_\nu), \tag{6}$$

where $f_{\rm e}(p^2) = (e^{(p^2-\mu)/kT}+1)^{-1}$ is the Fermi distribution, and E_ν is the energy of the emitter in state ν. Now, the off-shell transition matrix $T^{\rm eb}(p,p,p^2+E_\nu)$ has to be calculated from the Lippmann-Schwinger equation

$$T^{\rm eb}(\vec{p},\vec{k},z) = V^{\rm eb}(\vec{p},\vec{k},z) + \frac{1}{8\pi^3}\int {\rm d}^3q\, V^{\rm eb}(\vec{p},\vec{q},z) G_2^{0,\nu}(\vec{q},z) T^{\rm eb}(\vec{q},\vec{k},z), \tag{7}$$

where $G_2^{0,\nu}(\vec{q},z) = 1/(z-q^2-E_\nu)$ is the free two particle propagator with binding energy E_ν. The momenta $\vec{p}$ and $\vec{k}$ are the incoming and outgoing momenta of the scattered electron relative to the emitter.

In the following, we restrict the derivation to a radial symmetric potential, but it can easily be extended for angular dependend potentials. An angular momentum expansion for $T^{\rm eb}$ and $V^{\rm eb}$ is carried out

$$T^{\rm eb}(\vec{p},\vec{q},z) = \sum_{l=0}^\infty (2l+1) T_l^{\rm eb}(p,q,z) P_l(\cos\theta), \tag{8}$$

$$V^{\rm eb}(\vec{p},\vec{q},z) = \sum_{l=0}^\infty (2l+1) V_l^{\rm eb}(p,q,z) P_l(\cos\theta), \tag{9}$$

where $P_l(x)$ are Legendre polynomials and $\theta = \sphericalangle(\vec{p},\vec{q})$. Thus, the Lippmann-Schwinger equation of channel l reads in atomic Rydberg units

$$T_l^{\rm eb}(p,k,z) = V_l^{\rm eb}(p,k,z) + \frac{1}{2\pi^2}\int_0^\infty {\rm d}q\, q^2 \frac{V_l^{\rm eb}(p,q,z) T_l^{\rm eb}(q,k,z)}{z-q^2-E_\nu}. \tag{10}$$

The Nyström method is used to solve the Lippmann-Schwinger equation (10). As the integral has a singular kernel for $z > E_\nu$, we follow the method of Sasakawa [22] and Kowalski [23] to handle the pole.

The interaction potential between the emitter in state ν and the scattered electron in the Lippmann-Schwinger equation is taken as a local optical potential $V^{\rm opt}(r)$. This potential consists of several parts: a direct static potential that depends on the hydrogen-like wavefunctions $\Psi_\nu(\vec{r}) = R_{n_\nu l_\nu}(r) Y_{l_\nu m_\nu}(\Omega)$

$$V_\nu^{\rm stat}(r) = -\frac{2Z}{r} + \int {\rm d}^3 r_1 \Psi_\nu^*(\vec{r}_1) \frac{2}{|\vec{r}-\vec{r}_1|} \Psi_\nu(\vec{r}_1), \tag{11}$$

and a Norcross polarization potential [24]

$$V_\nu^{\rm pol}(r) = -\frac{\alpha_\nu}{r^4}\left(1 - e^{-(r/r_\nu)^6}\right), \tag{12}$$

with the static dipole polarizability α_ν and a cut-off parameter r_ν. Following Ref. [25], a local energy dependent exchange potential

$$V^{\rm ex}_{\nu,\pm}(r,z) = \pm\frac{1}{2}\left(z - E_\nu - V^{\rm stat}_\nu(r) - \sqrt{\left[z - E_\nu - V^{\rm stat}_\nu(r)\right]^2 + 8R^2_{n_\nu l_\nu}(r)}\right) \tag{13}$$

is added with $+/-$ for the triplet/singlet state. To include virtual and real excitations, we again follow [25] and use

$$V^{\rm vr}_\nu(r,z) = \left(w_1(z) + i\,w_2(z)\right) R^2_{n_\nu l_\nu}(r) \frac{(z-E_\nu)^2}{4\left(z - E_\nu - V^{\rm stat}_\nu(r)\right)^2} \tag{14}$$

as the excitation potential. The energy-dependent parameters w_1 and w_2 have to be adjusted to reproduce experimental scattering phases and cross sections of the isolated radiator, see [25]. To consider the screening effect of the surrounding medium, a factor $e^{-\kappa r}$ is multiplied with $\kappa = \sqrt{8\pi n_{\rm e}/kT}$. This would be correct for a Coulomb potential, and should give a satisfactory result for our application. Thus, the total potential for scattering of an electron with energy p^2 at the emitter in state ν is given by

$$V^{\rm opt}_{\nu,\pm}(r,z) = \left(V^{\rm stat}_\nu(r) + V^{\rm pol}_\nu(r) + V^{\rm ex}_{\nu,\pm}(r,z) + V^{\rm vr}_\nu(r,z)\right) e^{-\kappa r}, \tag{15}$$

where $z = p^2 + E_\nu$ is the total energy of the three-body system. Now, the angular momentum expanded potential $V^{\rm eb}_l(k,q,z)$ can be obtained from the radial optical potential $V^{\rm opt}(r,z)$ as

$$V^{\rm eb}_l(k,q,z) = 4\pi \int_0^\infty {\rm d}r\, r^2 j_l(qr) j_l(kr) V^{\rm opt}(r,z), \tag{16}$$

which has to be evaluated numerically. With this potential, the T-matrix can be calculated from Eq. (10) and (8). Then, the improved electronic self-energy $\Sigma^{\rm el}$ can be obtained from Eq. (6) including strong collisions. In the next section, we give results for the 1s level of hydrogen as an example.

4 Explorative calculations

Here, we calculate the self-energy of the ground state of hydrogen $\Sigma^{\rm el}_{1s}$. Although the broadening of the ground state is often negligible, it can serve as a testbed for the method outlined in the previous section. For the hydrogen 1s state, the static polarizability is known as $\alpha_{1s} = 4.5$. Following Ref. [26], the cut-off is set to $r_{1s} = 2$. We neglect real excitations, setting $w_2(z) = 0$. The parameter for virtual excitations $w_1(z) = 0.065$ Ryd is taken from the 30 eV-scattering fit of Ref. [25]. For the isolated scattering process the phase shift $\delta_0(k)$ is reproduced well with this choice of parameters for the triplet case. We restrict the partial wave expansion to $l \leq 4$ and $l \leq 12$ for low and high temperatures, respectively. This is sufficient for the ground state of hydrogen at the conditions given in Tab. 1. The shift can be calculated as well (real part of $\Sigma^{\rm el}_{1s}$), but results are not presented here.

In Tab. 1, the results are given for the imaginary part of the self-energy (level broadening). They are compared to self-energies in Born approximation. The Born approximation corresponds to Eq. (4), where the dielectric function is taken in RPA approximation and the sum over ν' is terminated at $n_{\nu'} = 2$. In this approximation, strong collisions are entirely neglected. To include strong collisions approximatively, the Born approximation is combined with a cut-off procedure and a correction term following Griem's standard theory [2]. The cut-off is implemented at $q_{\rm max} = 1/\varrho_{\rm min}$ with the minimum impact parameter $\varrho_{\rm min}$. Furthermore, a correction term $\pi n_{\rm e} v_{\rm th} \varrho^2_{\rm min}$ is added, where $v_{\rm th} = \sqrt{3kT/m_{\rm e}}$ is the thermal velocity.

For the given densities and low temperatures ($T_e = 1$, 3, and 5 eV), the scattering T-matrix calculations exceed the broadening in the Born approximation up to one order of magnitude. This is due to the fact, that the Born approximation is not valid at low temperatures. However, the Born approximation is expected to give accurate results at high temperatures. We have confirmed this for $T_e = 100$ eV, where we found good agreement between the results of Born approximation and scattering theory, see Tab. 1.

At low temperatures, the estimate via the cut-off procedure after Griem agrees within 15% to the results obtained from scattering theory. This agreement is due to the correction term, as the Born result is an order of

Table 1 Comparison of imaginary part of the electronic self-energy $\Sigma^{\rm el}_{1s}$ for hydrogen at $n_e = 10^{23}$, 10^{25}, and 10^{27} m^{-3}. The scattering T-matrix approach (ST) from Sec. 3 is compared to results from Born approximation (B), Eq. (4), where strong collisions are neglected, and to results, where the effect of strong collisions is taken into account by a cut-off procedure and a correction term $\pi n_e v_{\rm th} \varrho^2_{\rm min}$ (BC). The self-energy is given in Rydberg. Only the triplet exchange interaction is considered.

n_e [m^{-3}]:	10^{23}			10^{25}			10^{27}		
T_e [eV]	ST	B	BC	ST	B	BC	ST	B	B C
1	3.00e-7	4.72e-8	3.20e-7	2.94e-5	4.62e-6	3.19e-5	3.35e-3	2.53e-4	3.04e-3
3	4.35e-7	6.67e-8	4.02e-7	4.23e-5	6.64e-6	4.02e-5	3.61e-3	5.67e-4	3.96e-3
5	4.40e-7	8.24e-8	4.19e-7	4.30e-5	8.22e-6	4.19e-5	3.63e-3	7.56e-4	4.15e-3
100	1.21e-7	1.30e-7	2.48e-7	1.17e-5	1.30e-5	2.48e-5	1.15e-3	1.29e-3	2.46e-3

magnitude smaller. Thus, the correction term gives a good estimate on the strong collisions for the densities considered here. For $T = 100$ eV, the broadening is overestimated, since the Born approximation and the correction term equal approximately the results from scattering theory, respectively.

Realistic line profile calculations require self-energy calculations for the excited states, too. As a consequence, the optical potential has to be evaluated for e.g. the 2p state. Lacking experimental results for the phase shifts of electron scattering at hydrogen in the 2p state, the adjustment of the parameters $w_{1,2}(E)$ is an open question. We hope, to overcome this problem in future, e.g. by adjusting the parameters to theoretical phase shift results for excited atoms, e.g. from close-coupling calculations.

5 Conclusions

In this communication, we have presented a new method to calculate the self-energy for pressure broadening of spectral lines in dense plasmas beyond the perturbative Born approximation. In order to improve the electronic-self energy, which is a basic input quantity in quantum-statistical pressure broadening calculations, we have constructed an optical potential for electron scattering at hydrogen analogous to atomic scattering theory. With this potential, a two particle T-matrix has been obtained as a solution of the Lippmann-Schwinger equation in a partial wave expansion. The method has been tested for the level broadening of the hydrogen ground state. For line profile calculations, broadening of excited states has to be calculated as well. Experimental data of electron scattering at excited atoms are not available, but are needed to adjust the energy dependent parameters. Hence, the parameters have to be adjusted with the help of theoretical results, e.g. from close-coupling calculations. This and the weighting of singlet and triplet contributions have not yet been incorporated. As soon as these modifications are included, we expect, that it is possible to give a better estimate of the influence of strong collisions on spectral line broadening and shift, without solving the three-particle Faddeev equation.

Acknowledgements This article was supported by the Deutsche Forschungsgemeinschaft within the Sonderforschungsbereich 652 'Strong correlations and collective effects in radiation fields: Coulomb systeme, clusters and particles.'

References

[1] S. Lorenzen, A. Wierling, H. Reinholz, and G. Röpke, Contrib. Plasma Phys. **48**, 657 (2008).
[2] H. R. Griem, Spectral Line Broadening by Plasmas (Academic Press, London, 1974).
[3] H. R. Griem, Principles of Plasma Spectroscopy (Cambridge University Press, Cambridge, 1997).
[4] I. H. Hutchinson, Principles of plasma diagnostics (Cambridge University Press, Cambridge, 1987).
[5] D. Voslamber, Phys. Lett **40A**, 266 (1972).
[6] C. Vidal, J. Cooper, and E. Smith, Astrophys. J. Suppl. Ser. **25**, 37 (1973).
[7] R. L. Greene, J. Cooper, and E. W. Smith, J. Quant. Spectrosc. Radiat. Transfer **15**, 1025–1036 (1975).
[8] M. Gigosos and V. Cardeñoso, J. Phys. B: At. Mol. Opt. Phys. **29**, 4795–4838 (1996).
[9] K. Unnikrishan and J. Callaway, Phys. Rev. A **44**, 3001 (1991).
[10] W. D. Kraeft, D. Kremp, W. Ebeling, and G. Röpke, Quantum Statistics of Charged Particle Systems (Akademie-Verlag Berlin, Berlin, 1986).
[11] S. Sorge, A. Wierling, G. Röpke, W. Theobald, R. Sauerbrey, and T. Wilhein, J. Phys. B: At. Mol. Opt. Phys. **33**, 2983–3000 (2000).

[12] M. Beyer, G. Röpke, and A. Sedrakian, Phys. Lett. B **376**, 7 (1996).
[13] Z. Papp and C. Y. Hu, Phys. Rev. A **66**, 052714 (2002).
[14] M. A. Gunderson, G. C. Junkel-Vives, and C. F. Hooper Jr., J. Quant. Spectrosc. Radiat. Transfer **71**, 373–382 (2001).
[15] H. Minoo, M. M. Gombert, and C. Deutsch, Phys. Rev. A **23**, 924–943 (1981).
[16] S. Günter, Phys. Rev. E **48**, 500–505 (1993).
[17] S. Günter, L. Hitzschke, and G. Röpke, Phys. Rev. A **44**(Nov), 6834–6844 (1991).
[18] C. A. Iglesias, Phys. Rev. A **27**, 2705–2709 (1983).
[19] A. Könies and S. Günter, J. Quant. Spectrosc. Radiat. Transfer **52**, 825 (1994).
[20] H. Feshbach, Ann. Phys. New York **5**, 357 (1958).
[21] I. E. McCarthy and A. T. Stelbovics, Phys. Rev. A **28**, 2693 (1983).
[22] T. Sasakawa, Proc. Theor. Phys. Suppl. **27**, 1 (1963).
[23] K. L. Kowalski, Phys. Rev. Lett. **15**, 798 (1965).
[24] D. W. Norcross, Phys. Rev. Let. **32**, 192 (1974).
[25] J. B. Furness and I. E. McCarthy, J. Phys. B **6**, 2280 (1973).
[26] K. Bartschat, Computational atomic physics : electron and positron collisions with atoms and ions (Springer, Berlin, 1996).

http://dx.doi.org/10.1063/1.3517588

Quantum-statistical T-matrix approach to line broadening of hydrogen in dense plasmas

Sonja Lorenzen*, August Wierling*, Heidi Reinholz†,*, Gerd Röpke*, Mark C. Zammit**, Dmitry V. Fursa** and Igor Bray**

*Institute of Physics, University of Rostock, 18051 Rostock, Germany
†Institute for Theoretical Physics, Johannes Kepler University Linz, 4040 Linz, Austria
**Institute of Theoretical Physics, Curtin University of Technology, Perth WA 6845, Australia

Abstract. The electronic self-energy Σ^e is an important input in a quantum-statistical theory for spectral line profile calculations. It describes the influence of plasma electrons on bound state properties. In dense plasmas, the effect of strong, i.e. close, electron-emitter collisions can be considered by three-particle T-matrix diagrams. These digrams are approximated with the help of an effective two-particle T-matrix, which is obtained from convergent close-coupling calculations with Debye screening. A comparison with other theories is carried out for the 2p level of hydrogen at $k_BT = 1$ eV and $n_e = 2 \cdot 10^{23}$ m^{-3}, and results are given for $n_e = 1 \cdot 10^{25}$ m^{-3}.

Keywords: hydrogen, pressure broadening, strong electron collisions
PACS: 52.20.Fs, 52.25.Os, 52.27.Gr

Spectral lines emitted in a dense plasma are modified by several effects [1, 2]. The thermal motion leads to a Gaussian broadening due to the Doppler effect. Reabsorption and -emission can result in broader lines and line inversion. In this communication, we concentrate on pressure broadening. Based on the Stark effect, it describes the influence of the surrounding particles on the energy levels of the emitter, which leads to broadening and shift of a spectral line. Within our quantum-statistical approach, that is represented by thermodynamic Green's functions, pressure broadening can be described with the help of the self-energy Σ of the emitter. So far, the electronic self-energy Σ^e has been evaluated in Born approximation, e.g. in [3]a), where Lyman-lines of H-like Lithium were obtained. While a calculation with the perturbative Born approach is appropriate for low densities, strong, i.e. close, collisions have to be taken into account at high densities, as has already been shown in [1]. The inclusion of strong electron-emitter collisions into the quantum-statistical approach has recently been outlined in [3]b). Although a Green's functions description for strong collisions is available, based on partial summation of ladder diagrams [4], we use a different approach here: The results of convergent close-coupling calculations (CCC) [5], which take plasma screening into account, are used to calculate the electronic self-energy within an effective two-particle description. In order to compare with other theories, we restrict our calculations to hydrogen at the moment, but aim at H-like ions in the future, which is not possible within the partial summation method. Note, that a close-coupling approach to spectral line shapes has also been advanced by Unnikrishnan and Callaway [6]. However, plasma screening effects have not been taken into account there.

CP1290, 20th International Conference on Spectral Line Shapes
edited by J. K. C. Lewis and A. Predoi-Cross

QUANTUM-STATISTICAL APPROACH TO SPECTRAL LINES

Throughout the paper, atomic Rydberg units are used. The spectral intensity due to pressure broadening is proportional to

$$I^{\rm pr}(\omega) \sim {\rm Im}\left[\sum_{ii'ff'}\left\{\langle i|\vec{r}|f\rangle\langle f'|\vec{r}|i'\rangle\int_0^\infty {\rm d}E\, W(E)\langle i|\langle f|L^{-1}(\omega,E)|f'\rangle|i'\rangle\right\}\right], \quad (1)$$

where the sum over initial and final states i,i' and f,f', respectively, is due to degeneracies. The terms are weighted with the dipole moments $\langle i|\vec{r}|f\rangle$ corresponding to the transition from i to f. We integrate over the ionic microfield distribution $W(E)$ taking Hooper's low frequency tables for hydrogen [7]. Near the unperturbed frequency ω_0, the line profile operator is given by

$$L(\omega,E) = \omega - \omega_0 - {\rm Re}\left[\Sigma_i(\omega,E) - \Sigma_f(\omega,E)\right] - {\rm i\,Im}\left[\Sigma_i(\omega,E) + \Sigma_f(\omega,E)\right] + i\Gamma^{\rm V}_{if}, \quad (2)$$

where the real and imaginary part of the self-energy $\Sigma_{i,f}$ correspond to the shift and broadening of the energy levels due to the surrounding medium, respectively. The coupling between initial and final states is described by the vertex correction $\Gamma^{\rm V}_{if}$, which gives a negligible contribution for Lyman lines.

We split the influence of the plasma into an ionic and an electronic part $\Sigma = \Sigma^e + \Sigma^i$. As we consider the influence of surrounding ions in quasi-static approximation, the ionic self-energy $\Sigma^{\rm i}$ is given by the linear and quadratic Stark effect and a term that includes the effect of the field gradient, details can be found in [8].

We aim at including strong collisions into the electronic self-energy $\Sigma^{\rm e}$. Within a diagrammatic description, this corresponds to a summation of ladder-like diagrams for the electron-emitter propagator. For H-like ions, we approximate the resulting three-particle propagator by an effective two-body T-matrix $T^{\rm e}_\nu$ with an effective interaction between electron and emitter in state ν. Details can be found in [3]b). To first order, the ionic microfield does not influence $\Sigma^{\rm e}$, furthermore $\Sigma^{\rm e}$ varies slowly with the frequency. Thus, the electronic self-energy $\Sigma^{\rm e}_\nu$ of the emitter at ω_0 and $E=0$ is given by

$$\Sigma^{\rm e}_\nu(\omega_0,0) = \frac{2}{\pi}\int_0^\infty {\rm d}k\, k^2 f_{\rm e}(E_k) f^{\rm e}_\nu(0,k), \quad (3)$$

exploiting the connection of the T-matrix elements for $\mathbf{k}=\mathbf{k}'$ to the forward scattering amplitude $f^{\rm e}_\nu(0,k)$. The forward scattering amplitude is obtained from convergent close-coupling calculations including Debye screening, see next section. In Eq. (3), $f_{\rm e}(E_k)$ is the Fermi distribution at the energy $E_k = k^2$.

CONVERGENT CLOSE COUPLING WITH DEBYE SCREENING

Hot, dense, weakly-coupled (Debye) plasmas exhibit Coulomb screened interactions, which is a collective, many-particle effect. In the approximation of pair-wise correlations, this interaction reduces to the Debye-Hückel potential

$$V(r) = -2Z/r\, \exp(-r/\lambda_D). \quad (4)$$

We utilize the Sturmian (Laguerre) basis to diagonalize the hydrogen atom Hamiltonian under Debye screening

$$H_T = -\nabla_1^2 - \frac{2}{r_1}\exp\left(-\frac{r_1}{\lambda_D}\right). \tag{5}$$

This results in set of N positive and negative-energy square-integrable pseudostates $\phi_n^{(N)}(r;\lambda_D)$

$$\langle\phi_f^{(N)}(r;\lambda_D)|H_T|\phi_i^{(N)}(r;\lambda_D)\rangle = \varepsilon_f^{(N)}\delta_{fi}. \tag{6}$$

With increasing N, the negative-energy pseudostates converge to true eigenstates and the positive-energy states provide an increasingly dense discretization of the continuum. These pseudostates are then used to perform an expansion of the total wavefunction for the electron-hydrogen scattering system and formulate a set of close-coupling equations for the T-matrix [9]. The CCC method solves the close-coupling equations in momentum space and uses the T-matrix to determine cross sections and other observables of interest.

The CCC method requires minor modifications (from the pure Coulomb case) for electron-hydrogen scattering in Debye plasmas. The electron-hydrogen Hamiltonian under Debye screening has the form:

$$H = -\nabla_1^2 - \frac{2}{r_1}\exp\left(-\frac{r_1}{\lambda_D}\right) - \nabla_2^2 - \frac{2}{r_2}\exp\left(-\frac{r_2}{\lambda_D}\right) + \frac{2}{|r_1 - r_2|}\exp\left(-\frac{|r_1 - r_2|}{\lambda_D}\right). \tag{7}$$

The electron-electron potential V_{12} is represented in partial wave form

$$V_{12} = \frac{2}{|r_1 - r_2|}\exp\left(-\frac{|r_1 - r_2|}{\lambda_D}\right) = -\frac{2}{\lambda_D}\sum_{l=0}^{\infty}(2l+1)j_l\left(\frac{ir_<}{\lambda_D}\right)h_l^{(1)}\left(\frac{ir_>}{\lambda_D}\right)P_l\cos(\theta). \tag{8}$$

RESULTS FOR THE 2P LEVEL OF HYDROGEN

There exist results from other approaches [4, 6] for the 2p level of hydrogen at $k_BT = 1$ eV and a free electron density of $n_e = 2 \cdot 10^{23}$ m^{-3}. Thus, we study the upper level of the Lyman-α line of hydrogen at these conditions, which leads to a Debye length $\lambda_D = 314$ a$_0$. As the importance of strong collisions is increasing with density, we give results for $n_e = 1 \cdot 10^{25}$ m^{-3} and $k_BT = 1$ eV as well, i.e. $\lambda_D = 44$ a$_0$.

The scattering calculations are carried out in partial wave expansion, see Eq. (8), thus the convergence of the numerical results with the number of partial waves has to be checked. As shown in [6], the imaginary part diverges logarithmically in the case of electron-isolated hydrogen scattering. However, the screened potentials, used in the CCC code here, are of short range, and the sum over partial waves is convergent.

In Fig. 1, the real and imaginary part of $f_{2p}^{e}(0,k)$ are given for **a)** the singlet and **b)** the triplet scattering channel for scattering at hydrogen in the 2p level with magnetic quantum number $m = \pm 1$, i.e. H(2p, $m = \pm 1$), for $\lambda_D = 314$ a$_0$. The real part converges faster than the imaginary part. The main contribution to the self-energy, see Eq. (3),

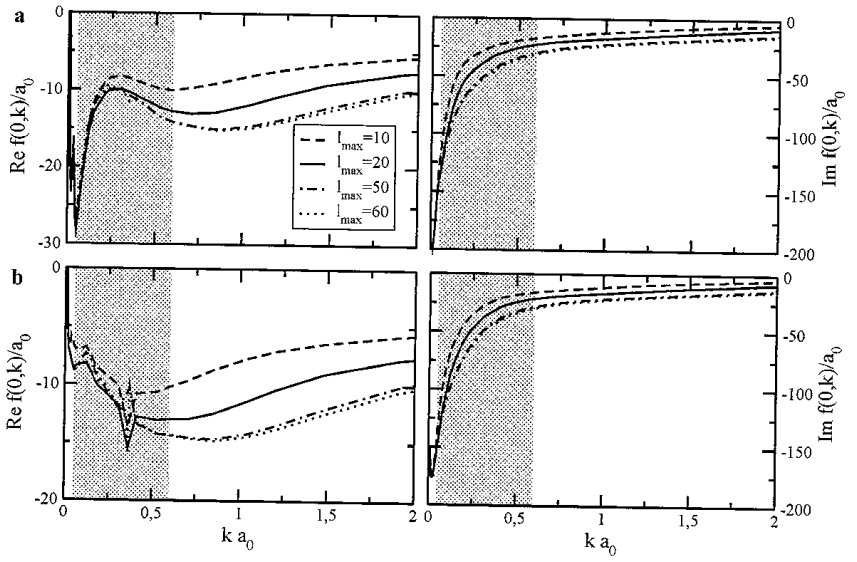

FIGURE 1. The real and imaginary part of the forward scattering amplitude $f^{e}_{2p}(0,k)$, for scattering of an electron in the singlet (**a**) and triplet (**b**) channel at hydrogen in the 2p level ($m = \pm 1$) for $\lambda_D = 314$ a_0. Different line styles refer to different numbers of included partial waves l_{max}.

comes from the shaded area. There, the result of 60 partial waves coincides nicely with the one of 50 partial waves. For higher energies, a larger number of partial waves is needed. The convergence behaviour differs slightly for scattering at H(2p, $m = 0$) and also for $\lambda_D = 44$ a_0. In the latter case, the imaginary part converges much faster.

In Tab. 1 **a)**, the integrated results for the self-energy due to the surrounding electrons, i.e. shift and broadening of the level 2p with magnetic quantum numbers $m = \pm 1, 0$, are compared to the results from other approaches. The quantum statistical Born approximation used so far and described, e.g. in Eq. (4) of Ref. [3]b), is indicated by Born. This approach gives a result independent of the magnetic quantum number m. Compared to our results, the Born approximation overestimates the influence of strong collisions. This can also be seen in Tab. 1 **b)**, where the results for the higher density are presented. Furthermore, we compare in Tab. 1 **a)** with the results of [6], where a close-coupling description for the line modification was used and the partial-wave sum was terminated at $l_{max} = k_B T/(2\pi n_e)^{1/2} = 170$, based on a Debye screening argument. Our result is 7% larger for the real part and 26% smaller for the imaginary part than the one from [6]. In [4], the $m = 1$ result including strong collisions was obtained within the Green's function theory by a partial summation of ladder diagrams. In comparison to [4], our result is 1.3% smaller for the real part and 22% larger for the imaginary part.

The large deviations of the results can have multiple reasons. First of all, as we use screened potentials, the results differ from the ones obtained in the previous close-coupling calculation [6] with unscreened potentials. However, we have to be careful, since our results have not yet fully converged and the contribution of the resonances (see Fig. 1 **b)**, has not yet been evaluated to a sufficient extend. Thus, our results are preliminary and further studies are needed.

TABLE 1. Comparison with other theories for shift $\mathrm{Re}\Sigma^e(\omega_0,0)$ and broadening $\mathrm{Im}\Sigma^e(\omega_0,0)$ of the H 2p-level at $k_BT = 1$ eV and **a)** $n_e = 2\cdot10^{23}$ m^{-3}, and **b)** $n_e = 1\cdot10^{25}$ m^{-3}.

a) $\lambda_D = 314\ a_0$ $l_{max} = 60$	**this work*** $m=0$	**this work*** $m=\pm1$	**[4]** $m=1$	**this work*** $m=\pm1,0$	**[6]** $m=\pm1,0$	**Born** $m=\pm1,0$
$\mathrm{Re}\Sigma(\omega_0,0)/10^{-5}$Ry	0.261	0.731	0.740	0.574	0.537	1.85
$\mathrm{Im}\Sigma(\omega_0,0)/10^{-5}$Ry	1.29	3.73	3.08	2.92	3.95	4.01

b) $\lambda_D = 44\ a_0$ $l_{max} = 50$	**singlet** $m=\pm1$	**triplet** $m=\pm1$	**singlet** $m=0$	**triplet** $m=0$	**weighted average**	**Born**
$\mathrm{Re}\Sigma(\omega_0,0)/10^{-4}$Ry	1.15	1.22	-0.68	0.26	0.81	8.35
$\mathrm{Im}\Sigma(\omega_0,0)/10^{-4}$Ry	8.50	9.24	4.09	4.25	7.44	11.38

* weighted average of singlet and triplet scattering results

CONCLUSIONS

Results from convergent close-coupling theory with a proper inclusion of Debye screening can be used to calculate broadening and shift of spectral lines within a quantum-statistical approach in density regions, where strong collisions have to be considered. We give an example for electron scattering at H(2p), where the different magnetic quantum numbers and the different spin scattering channels are considered. In a comparison with other approaches at $k_BT = 1$ eV and $n_e = 2\cdot10^{23}$ m^{-3}, our results deviate slightly for the real part (shift) and to a larger extend for the imaginary part (broadening). At a higher density $n_e = 1\cdot10^{25}$ m^{-3}, a faster convergence of the imaginary part is observed.

ACKNOWLEDGMENTS

This work was supported by the German Research Foundation DFG within SFB 652 'Strong correlations and collective effects in radiation fields: Coulomb systems, clusters and particles.'

REFERENCES

1. H. R. GRIEM, Spectral Line Broadening by Plasmas (Academic Press, London, 1974).
2. I. H. HUTCHINSON, Principles of plasma diagnostics (Cambridge University Press, Cambridge, 1987).
3. S. LORENZEN, A. WIERLING, H. REINHOLZ, and G. RÖPKE, a) *Contrib. Plasma Phys.* **48**, 657 (2008); b) *Contrib. Plasma Phys.* (2010), DOI: 10.1002/ctpp.201010104.
4. S. GÜNTER, *Phys. Rev. E* **48**, 500 (1993); Optische Eigenschaften dichter Plasmen (Habilitation at University of Rostock, Germany, 1995) .
5. M. C. ZAMMIT, D. V. FURSA, and I. BRAY, not yet published.
6. K. UNNIKRISHNAN, and J. CALLAWAY, *Phys. Rev. A* **43**, 3619 (1991).
7. C. F. HOOPER, JR., *Phys. Rev.* **165**, 215 (1968) and *Phys. Rev.* **169**, 193 (1968).
8. S. SORGE, A. WIERLING, G. RÖPKE, W. THEOBALD, R. SAUERBREY, and T. WILHEIN, *J. Phys. B: At. Mol. Opt. Phys.* **33**, 2983 (2000).
9. I. BRAY, and A. T. STELBOVICS, *Phys. Rev. A* **46**, 6995 (1992).

XXI International Conference on Spectral Line Shapes (ICSLS 2012) IOP Publishing
Journal of Physics: Conference Series **397** (2012) 012021 doi:10.1088/1742-6596/397/1/012021

Quantum-statistical line shape calculation for Lyman-α lines in dense H plasmas

S Lorenzen[1], A Wierling[1], H Reinholz[1], G Röpke[1], M C Zammit[2], D V Fursa[2], I Bray[2]

[1]Institute of Physics, University of Rostock, 18051 Rostock, Germany
[2]Institute of Theoretical Physics, Curtin University, Perth WA 6845, Australia

E-mail: Sonja.L@renzen.de

Abstract. We present results for the Lyman-α line of hydrogen in dense plasmas. Full line profiles are calculated within a quantum-statistical method, based on thermodynamic Green's functions. The contributions of plasma ions and electrons are considered separately. Linear and quadratic Stark effect as well as quadrupole effects are taken into account for ions. The model microfield method is used to include ion dynamics. The focus of this work lies on the contribution to broadening and shift by free electrons beyond the Born approximation. The effect of strong collisions can be identified as ladder-like diagrams of the electron-emitter propagator. In an effective two-particle approximation, the electronic self-energy is given in terms of scattering amplitudes, analogous to Baranger's expressions [Baranger, M 1958 *Phys. Rev.* **112** 855]. We obtained scattering amplitudes from convergent close-coupling calculations including medium effects via Debye screening. Additionally, the electronic coupling between initial and final states is taken care of by a vertex correction. In our examples, the free electron density ranges between 10^{23} and 10^{25} m^{-3} at a plasma temperature of 1 and 2 eV, respectively.

1. Introduction

Details of spectral lines like width, shift, and asymmetries can be used to determine plasma properties from an electro-magnetic spectrum [1]. The plasma can either be part of an astrophysical object or be created in arc discharges or by laser impact in the laboratory. A sound theory to calculate line profiles is needed in order to obtain accurate information about plasma parameters such as composition, temperature, and density. There exist many approaches to calculate the spectrum of bound-bound electron transitions, emitted from or absorbed by a plasma. No matter, if they use pure quantum mechanics [2], involve a semi-classical view on the perturbers, e.g. [3, 4], or depend on MD simulations, e.g. [5], they are based on the calculation of the dipole-dipole correlation. In our case, the dipole-dipole correlation – namely, the polarization function – is calculated within a many-body theory using thermodynamic Green's functions. The theory is briefly described in Sec. 2. The focus of this paper is twofold. At first, we want to improve the perturbative Born approach used so far for the perturbing electrons. It has the shortcoming to overestimate strong electron collisions. Hence, we implement an effective two-particle T-matrix approach, which accounts for strong collisions. This is done at the cost of neglecting dynamical screening for weak collisions. Instead, static screening is used in the calculation of the T-matrix in a convergent close-coupling scheme. The second focus is on the limit of the quasi-static approximation used for ion contributions so far. In this short

XXI International Conference on Spectral Line Shapes (ICSLS 2012) IOP Publishing
Journal of Physics: Conference Series **397** (2012) 012021 doi:10.1088/1742-6596/397/1/012021

communication, we restrict ourselves to theoretical results for the Lyman-α line of hydrogen, see Sec. 3. Lyman lines of hydrogen-like lithium and the application in plasma diagnostics will be discussed in a forthcoming paper.

2. Quantum-statistical approach to line profiles

The quantum-statistical theory for pressure broadening has been described in detail in [6–8]. Here, we give only the key formulas in atomic Rydberg units, i.e $\hbar = 2m_e = e^2/2 = 1$. These units are used throughout this paper. The emitted spectral intensity $I(\Delta\omega)$ at $\Delta\omega = \omega - \omega_0$ near the unperturbed transition frequency ω_0 is given by

$$I(\Delta\omega) = \frac{(\omega_0+\Delta\omega)^4}{8\pi^4 c^3} e^{-\frac{\omega_0+\Delta\omega}{k_B T}} \operatorname{Im}\left[\sum_{ii'ff'} \left\{\langle i|\vec{r}|f\rangle\langle f'|\vec{r}|i'\rangle\langle i|\langle f| < U(\Delta\omega) >_{\mathrm{KP}} |f'\rangle|i'\rangle\right\}\right]. \quad (1)$$

The sum runs over all initial i and final f emitter states. The double sum is due to degeneracy. The contributions to the line profile are weighted with the transition probability, which is given by the dipole matrix elements $\langle i|\vec{r}|f\rangle$. In order to include ion dynamics in the theory, the model microfield method (MMM) based on a kangoroo process (KP) [9, 10] is adapted. Here, the time evolution operator $< U(\Delta\omega) >_{\mathrm{KP}}$ depends on the jump frequency $\Omega(E)$ and is given by

$$< U(\Delta\omega) >_{\mathrm{KP}} =< U(\Delta\omega|\vec{E}) >_{\mathrm{s}} + \frac{< \Omega(E) U(\Delta\omega|\vec{E}) >_{\mathrm{s}}^2}{< \Omega(E) >_{\mathrm{s}} - < \Omega^2(E) U(\Delta\omega|\vec{E}) >_{\mathrm{s}}}, \quad (2)$$

where the average $< \cdots >_{\mathrm{s}}$ is over the static ion microfield with the distribution function $W(E)$. For hydrogen, we use Hooper's low frequency tables [11] to determine $W(E)$. In our theory, the time evolution operator is constructed in the following way to include electron contributions

$$U(\Delta\omega|\vec{E}) = \{\Delta\omega - \operatorname{Re}[\Sigma_i(\Delta\omega) - \Sigma_f(\Delta\omega)] + i\Omega(E) + i\operatorname{Im}[\Sigma_i(\Delta\omega) + \Sigma_f(\Delta\omega)] + \Gamma_{if}(\Delta\omega)\}^{-1}. \quad (3)$$

Here, Σ_i and Σ_f are the self-energies, i.e. broadening and shift, of energy level i and f due to the surrounding plasma, respectively, and Γ_{if} is the upper-lower level coupling term. Due to different interaction time scales, the self-energy can be split into an E-field-dependent ionic part and a frequency-dependent electronic part

$$\Sigma_{i,f}(E, \Delta\omega) = \Sigma^{\mathrm{i}}_{i,f}(E) + \Sigma^{\mathrm{e}}_{i,f}(\Delta\omega). \quad (4)$$

The perturbation of the emitter by the plasma ions is mainly given by the linear and quadratic Stark effect. Furthermore, quadrupole contributions are taken into account from [12]. In the quasi-static limit, i.e. with $\Omega(E) \to 0$, the second term of Eq. (2) vanishes.

2.1. Contribution of electron-emitter collisions

Two approaches have been developed to account for the contribution by free electrons. They are either considered within a dynamically screened Born approximation (1st order) or within an effective two particle T-matrix approach. While the former includes the dynamical screening of weak collisions, it overestimates strong collisions. This can be rectified to some extend by a cut-off procedure introduced by Griem [3]. The effective T-matrix approach is a simplified version of the T-matrix approach presented in [13]. It can describe weak and strong collisions equally well, but does so far only include static screening [14]. For a non-degenerate plasma, the electronic self-energy, evaluated at $\Delta\omega = 0$, is then given by

$$\Sigma^{\mathrm{e}}_{i,f} = -\frac{2}{\pi} n_e \Lambda^3_{\mathrm{th}} \int_0^\infty \mathrm{d}k\; k^2 e^{-k^2/k_B T} f_{i,f}(0,k). \quad (5)$$

XXI International Conference on Spectral Line Shapes (ICSLS 2012) IOP Publishing
Journal of Physics: Conference Series **397** (2012) 012021 doi:10.1088/1742-6596/397/1/012021

Plasma properties enter via the electron density n_e and the thermal wavelength $\Lambda_{\rm th} = \sqrt{4\pi/k_{\rm B}T}$ as well as the forward scattering amplitude $f_{i,f}(0,k)$ for elastic electron scattering at the emitter in state i and f, respectively. This expression was also found by Baranger in [2]. There, a level coupling term is derived, which is given by

$$\Gamma_{if} = \frac{2i}{\pi} n_e \Lambda_{\rm th}^3 \int_0^\infty {\rm d}k\; k^3 e^{-k^2/k_B T} \int_0^\pi {\rm d}\theta \sin(\theta) f_f(\theta,k) f_i^*(\theta,k). \tag{6}$$

2.2. Scattering amplitudes from Debye screened convergent close-coupling
The scattering amplitudes, which enter Eqs. (5) and (6), are obtained from a convergent close-coupling calculation (CCC). It is modified to include Debye screening in the interaction potentials. Details of the CCC method and its modification can be found in [15] and [16], respectively. Here, we use 54 (Sturmian) Laguerre functions as a basis for bound and continuous emitter states. With this choice, the emitter states up to 4f are reproduced with the correct energies. The electron-electron potential is expanded in partial waves, where the first partial waves (up to 70) are considered directly, for larger numbers of partial waves extrapolation formulas are used. The coupled equations are solved in momentum space and lead to the scattering amplitude. Our method gives separate results for singlet and triplet scattering channels as well as for scattering at the emitter with initial and final states $n_i, l_i, m_i \to n_f, l_f, m_f$. Here, we consider only elastic scattering $n_i, l_i, m_i \to n_i, l_i, m_i$ for the self-energies.

3. Lyman-α line of H

To illustrate the T-matrix approach, we consider the simplest line of hydrogen, namely Lyman-α. As the lower level 1s gives a small contribution, we focus on shift and broadening of the 2p level due to electrons in the discussion. In Fig. 1, the convergence with the number of partial waves is presented for $k_{\rm B}T = 1$ eV and $n_{\rm e} = 2 \cdot 10^{23}$ m^{-3}, and $n_{\rm e} = 1 \cdot 10^{25}$ m^{-3}, respectively. The self-energies are given for different magnetic quantum numbers m of the emitter. Singlet and triplet scattering results are averaged.

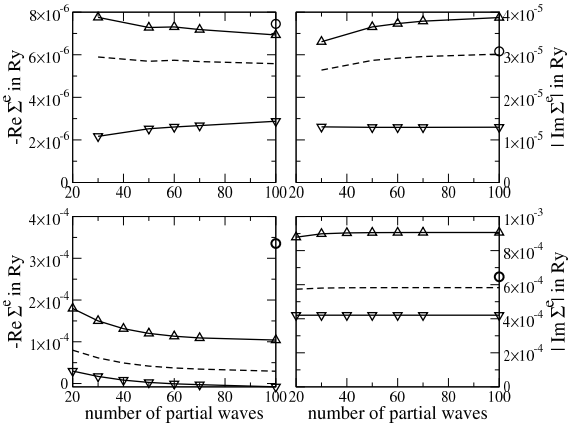

Figure 1. Convergence of the electronic contribution to the self-energy of the hydrogen 2p level with the number of partial waves. Left: real part, right: imaginary part. Dependence on the magnetic quantum number is indicated by symbols: $m = \pm 1$ ($\triangle$) and $m = 0$ ($\triangledown$), the average is (- - - -). The results are given for $k_{\rm B}T = 1$ eV and $n_{\rm e} = 2{\cdot}10^{23}$ m^{-3} in the upper and $n_{\rm e} = 1 \cdot 10^{25}$ m^{-3} in the lower panel. For comparison, the result from the Born approximation with a cut-off procedure is given at the right ordinate axis ($\bigcirc$).

The convergence is faster for the imaginary part and at the higher density, where the screening is stronger. The plasma conditions correspond to a Debye length of 314 a_0 and 44 a_0, respectively, where a_0 is the Bohr radius. Assuming our T-matrix results as benchmark, the cut-off Born approximation overestimates the shift (real part), especially for the higher density of $n_{\rm e} = 1 \cdot 10^{25}$ m^{-3}. The width (imaginary part) agrees within 10% with the average

XXI International Conference on Spectral Line Shapes (ICSLS 2012) IOP Publishing
Journal of Physics: Conference Series **397** (2012) 012021 doi:10.1088/1742-6596/397/1/012021

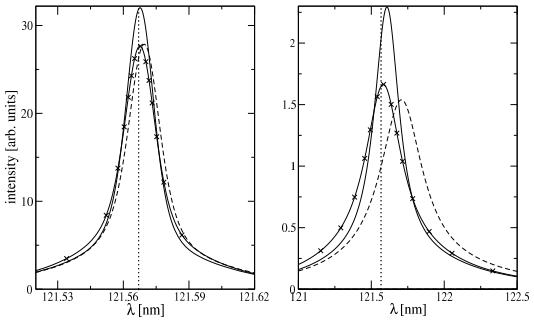

Figure 2. Hydrogen Lyman-α line calculated for quasi-static ions and electrons in either Born approximation (- - - -), Born approximation supplemented with a cut-off procedure (——) or with T-matrix approach (×——×). For $k_{\mathrm{B}}T = 1$ eV and $n_{\mathrm{e}} = 2 \cdot 10^{23}$ m^{-3} (left) and $n_{\mathrm{e}} = 1 \cdot 10^{25}$ m^{-3} (right). All profiles are area normalized.

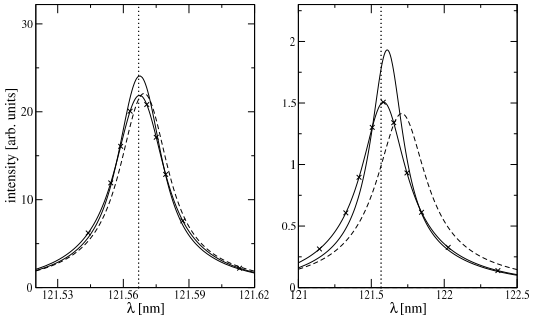

Figure 3. Same as Fig. 2 but with ion dynamics considered within the model microfield method, the scale is identical to Fig. 2.

over m. However, as the central component of the Lyman-α line is given by the transition $2\mathrm{p}_{m=\pm1} \rightarrow 1\mathrm{s}$, the line width is dominated by the width of the $2\mathrm{p}_{m=\pm1}$ level. Thus, in Fig. 2, the Born approximation with cut-off underestimates the width by up to 35% compared to the T-matrix approach. There, ions are only considered quasi-statically. In Fig. 3, the lines are further broadenend by up to 50% for the lower density, and up to 30% for the higher density due to the ion dynamics (MMM). The importance of ion dynamics for H Lyman-α has been known from measurements [17] since 1977. Our full line profiles include Stark broadening by the plasma surroundings and are convoluted with a Gaussian to account for Doppler broadening.

In Tab. 1, we compare the width and shift due to electron collisions with an older close-coupling calculation [18]. There, Debye screening is included by restricting the calculation of isolated e-H scattering to a certain number of partial waves. When we average the self-energy and vertex term of different line components, our results agree within few percent with [18]. However, when we calculate the full line profile without ion effects and Doppler broadening, the line is 50% narrower and up to 40% less shifted. Thus, it is not appropriate to average width and shift over different scattering channels in line shape calculations.

Table 1. Width and shift of H Lyman-α from electron collisions compared with results from [18] for two plasmas with the same Debye length $\lambda_D = 314$ a$_0$. Conditions are 1) $k_{\mathrm{B}}T = 1$ eV, $n_e = 2 \cdot 10^{23}$ m^{-3} and 2) $k_{\mathrm{B}}T = 2$ eV and $n_e = 4 \cdot 10^{23}$ m^{-3}. All values are given in Å.

	shift:	averaged	full line	[18]	HWHM:	averaged	full line	[18]
1)		0.0087	0.0051	0.0087		0.062	0.031	0.064
2)		0.021	0.014	0.021		0.098	0.048	0.099

XXI International Conference on Spectral Line Shapes (ICSLS 2012) IOP Publishing
Journal of Physics: Conference Series **397** (2012) 012021 doi:10.1088/1742-6596/397/1/012021

4. Conclusions

Full Lyman-α line profiles have been calculated for H plasmas within a quantum-statistical theory using a perturbative Born approximation as well as an effective two particle T-matrix approach for the electronic contributions. The latter needs scattering amplitudes as an input. They are obtained from convergent close-coupling calculations with Debye screening. The T-matrix approach can intrinsically treat strong electron-emitter collisions, whereas the Born approximation compensates the overestimation of strong collision contributions by an artificial cut-off procedure.

We show, that for a density of $n_e = 1 \cdot 10^{25}$ m^{-3} and a temperature of $k_B T = 1$ eV, the Born approach overestimates the shift even after cut-off by a factor of three, whereas the width agrees to the average obtained in the T-matrix approach within 10%. However, the line shape is significantly different between both approaches, because the self-energy is strongly dependent on the magnetic quantum number. This feature cannot be reproduced within the Born approximation. Ion contributions have been taken into account quasi-statically, and dynamically within the model microfield method. The ion dynamics leads to further line broadening.

Results for hydrogen Lyman-α were presented as a test case in comparison to older results. The method can be applied for other lines of hydrogen and hydrogen-like ions, as well.

5. Acknowledgement

This work was supported by the German Research Foundation DFG within SFB 652. The support of the Australian Research Council, the Australian National Computational Infrastructure Facility and its Western Australian node iVEC, are gratefully acknowledged.

References

[1] Griem H R 1997 *Principles of Plasma Spectroscopy* (Cambridge University Press, Cambridge)
[2] Baranger M 1958 *Phys. Rev.* **112** 855
[3] Griem H R 1974 *Spectral Line Broadening by Plasmas* (Academic Press, London)
[4] Sahal-Brechot S 1969 *Astron. Astrophys.* **1** 91
Sahal-Brechot S 1969 *Astron. Astrophys.* **2** 322
[5] Stamm R and Voslamber D 1979 *J. Quant. Spectros. Radiat. Transfer* **22** 599
[6] Hitzschke L, Röpke G, Seifert T and Zimmermann R 1986 *J. Phys. B* **19** 2443
[7] Günter S 1995 habilitation thesis at Rostock University, Germany
[8] Sorge S, Wierling A, Röpke G, Theobald W, Sauerbrey R and Wilhein T 2000 *J. Phys. B* **33** 2983
[9] Brissaud A and Frisch U 1971 *J. Quant. Spectros. Radiat. Transfer* **11** 1767
[10] Seidel J 1977 *Z. Naturf.* **32a** 1195
Seidel J 1980 *Z. Naturf.* **35a** 679
[11] Hooper, Jr C F 1968 *Phys. Rev.* **165** 215
Hooper, Jr C F 1968 *Phys. Rev.* **169** 193
[12] Halenka J 1990 *Z. Phys. D* **16** 1
[13] Günter S 1993 *Phys. Rev. E* **48** 500
[14] Lorenzen S, Wierling A, Reinholz H and Röpke G 2011 *Contrib. Plasma Phys.* **51** 349
Lorenzen S, Wierling A, Reinholz H, Röpke G, Zammit M, Fursa D and Bray I 2010 *AIP Conference Proceedings* vol 1290 pp 99–103 20th International Conference on Spectral Line Shapes, 6-11 June 2010, St. John's, NF, Canada
[15] Bray I and Stelbovics A T 1992 *Phys. Rev. A* **46** 6995
[16] Zammit M C, Fursa D V and Bray I 2010 *Phys. Rev. A* **82** 52705
[17] Grützmacher K and Wende B 1977 *Phys. Rev. A* **16** 243–246
[18] Unnikrishnan K and Callaway J 1991 *Phys. Rev. A* **43** 3619

Contrib. Plasma Phys. **53**, No. 4-5, 368 – 374 (2013) / **DOI** 10.1002/ctpp.201200118

Comparative Study on Ion-Dynamics for Broadening of Lyman Lines in Dense Hydrogen Plasmas

S. Lorenzen*

Universität Rostock, 18051 Rostock, Germany

Received 07 December 2012, revised 10 January 2013, accepted 10 January 2013
Published online 13 May 2013

Key words spectral line shapes, pressure broadening, ion-dynamics, model microfield method, frequency fluctuation model, hydrogen.

Broadening of spectral lines by a plasma surrounding can be used for plasma diagnostics. Full hydrogen Lyman line profiles are calculated with a quantum-statistical approach. The effects of plasma electrons and ions on the emitter states are considered separately. The influence of electrons is considered in a dynamically screened Born approximation (collision approximation). For the ions, we apply the quasi-static approximation and two different approaches to account for ion-dynamics, namely, the model microfield method (MMM) and the frequency fluctuation model (FFM). We compare resulting widths of Lyman lines in the temperature range $T = 10^4$ to 10^7 K and the free electron density range $n_e = 10^{23}$ to 10^{26} m^{-3}. For L_α, the error made by neglecting ion-dynamics increases with increasing temperature and decreasing density, and is at least -15%. Due to the double peaked structure of L_β the situation is less systematic. However, a large region exists, where ion-dynamics does not affect the line shape of L_β.

1 Introduction

In plasma diagnostics, precise tools are needed to determine temperature, electron density, and composition of laboratory and astrophysical plasmas. One such tool is given by spectral line profiles due to the dependence of the line shape on plasma parameters, see Refs. [1, 2]. Besides Doppler broadening, pressure broadening has a high influence on the line shape. There exist several microscopic approaches to plasma pressure broadening. They use either quantum mechanics [3] or view the perturbers semi-classically [4, 5]. Computer simulation techniques [6, 7] are also successful in predicting plasma parameters. All these approaches are based on the determination of the dipole-dipole correlation. In the quantum-statistical approach, the dipole-dipole correlation (polarization function) is calculated within a many-body theory based on thermodynamic Green's functions [8]. So far, it has been applied to hydrogen [9], helium [10] and hydrogen-like ions, e.g. the analysis of C^{5+} [11] and Li^{2+} [12] in laser-produced plasmas.

The focus of this communication is on the role of ion-dynamics. Due to the different time-scales of ion- and electron-emitter collisions, ions and electrons are considered separately. Often, the quasi-static approximation is used for ions, i.e. the motion of perturbing ions is completely neglected, see Sec. 2. There, the emitter states are shifted by the electric field of the surrounding ions due to the (static) Stark effect. Then, the probability to have a certain electric field at the site of the emitter is given by the microfield distribution, e.g. the Holtsmark [13] distribution for uncorrelated or Hooper's distributions [14] for weakly correlated plasmas.

To include ion-dynamics in our calculation of spectral lines, we consider the model microfield method (MMM), where the change of the electric field is considered as a stochastic process [15, 16], see Sec. 3.1. To compare different approaches to ion-dynamics, we apply also the reformulated frequency fluctuation model (FFM) [17], see Sec. 3.2. Full line shapes and line widths from quasi-static and dynamic calculations are compared in Sec. 4. As has been known since the 1970s [18, 19], the ion-dynamics leads to a drastic broadening of the L_α line. For L_β, broadening or narrowing – analogously to Dicke narrowing – occurs as has been discussed in Refs. [17, 20]. How much the line is affected by ion-dynamics depends strongly on plasma temperature and density.

* Corresponding author. E-mail: Sonja.L@renzen.de, Phone: +49 381 4986945, Fax: +49 381 4986942

Contrib. Plasma Phys. **53**, No. 4-5 (2013) / www.cpp-journal.org 369

2 Plasma pressure broadening with quasi-static ions

The influence of surrounding electrons and ions on the emitter is considered separately within the quantum-statistical approach to plasma pressure broadening. Binary collision approximation is applied for the free electrons, whereas the surrounding ions are treated as quasi-static perturbers. The details of this approach have been presented in [9] and are briefly summarized here. The unperturbed transition from initial state i to final state f of the emitter has the angular frequency ω_0. The intensity due to pressure broadening at angular frequency $\Delta\omega = \omega - \omega_0$ is proportional to

$$I_{\rm s}^{\rm pr}(\Delta\omega) \quad \sim \quad \sum_{ii'ff'} \left\{ \langle i|\vec{r}|f\rangle\langle f'|\vec{r}|i'\rangle \int_0^\infty {\rm d}E\; W(E)\langle i|\langle f|L^{-1}(\Delta\omega, E)|f'\rangle|i'\rangle \right\}, \tag{1}$$

where the double sums account for the degeneracy of the hydrogen states. The different contributions are weighted by the dipole moments $\langle i|\vec{r}|f\rangle$. To consider the influence of the surrounding ions in quasi-static approximation, hence the index s, we have to integrate over the ionic microfield distribution $W(E)$. We interpolate between the tabulated values of Hooper [14], to obtain $W(E)$ for the different plasma conditions. Outside the validity range of Hooper's distributions, i.e. in the low temperature, high density regime, we apply the fit formula of Potekhin et al. [21] based on Monte Carlo simulations for the microfield distribution for H L_α. We use only the fit formula from Ref. [21] for H L_β.

The modifications due to the surrounding plasma particles are contained in the line profile operator, given by

$$L(\Delta\omega, E) = \hbar\Delta\omega - {\rm Re}\left[\Sigma_{ii'}(\Delta\omega, E) - \Sigma_{ff'}(\Delta\omega, E)\right] - {\rm i}\,{\rm Im}\left[\Sigma_{ii'}(\Delta\omega, E) + \Sigma_{ff'}(\Delta\omega, E)\right] + i\Gamma^{\rm V}_{ii'ff'}\,. \tag{2}$$

Here, the real and imaginary part of the self-energies $\Sigma_{ii',ff'}$ correspond to the shift and broadening of the initial and final energy levels due to the medium, respectively. $\Gamma^{\rm V}_{ii'ff'}$ is the coupling between initial and final states. It plays a negligible role for hydrogen Lyman lines [22].

The medium effects, i.e. the self-energies $\Sigma_{\nu\nu'}$ of the bound state with quantum number $\nu = i, f$, are split into a frequency dependent diagonal electronic and an ionic part depending only on the electric field strength E

$$\Sigma_{\nu\nu'}(\Delta\omega, E) = \Sigma^{\rm e}_{\nu}(\Delta\omega)\delta_{\nu\nu'} + \Sigma^{\rm i}_{\nu\nu'}(E). \tag{3}$$

The electronic self-energy is calculated in Born approximation with dynamically screening as

$$\Sigma^{\rm e}_{\nu}(\Delta\omega) = -\int \frac{{\rm d}^3q}{(2\pi)^3 e^2} V(q) \sum_{\nu'} |M^0_{\nu\nu'}(q)|^2 \int_{-\infty}^{\infty} \frac{{\rm d}\omega}{\pi} (1 + n_{\rm B}(\omega)) \times \frac{{\rm Im}\varepsilon^{-1}(\vec{q}, \omega + i\delta)}{\Delta\omega + \omega_{\nu\nu'} - (\omega + i\delta)}\,, \tag{4}$$

with the vertices $|M^0_{\nu\nu'}(q)|^2 \sim q^2\langle\nu|\vec{r}|\nu'\rangle + O(q^3)$, the Bose distribution $n_{\rm B}(\omega)$, and the dielectric function $\varepsilon(\vec{q}, \omega + i\delta)$. To simplify the calculation, we evaluate the self-energy only at $\Delta\omega = 0$, i.e. the angular frequency of the unperturbed transition and use the dielectric function in random phase approximation. To avoid overestimation of strong collisions, the integration over the transfer momentum q is cut off at $q_{\rm max}$ following Griem's standard theory [4]. Although we focused on a more systematical treatment of strong electron-emitter collisions via T-matrix calculations in previous publications [23, 24], we use the Born approximation of Eq. (4), as we are mainly interested in ion-dynamics.

The ionic self-energy $\Sigma^{\rm i}_{\nu\nu'}(E)$ is given by the linear and quadratic Stark effect, which is diagonal and given analytically for hydrogen in parabolic coordinates [25]. Furthermore, we consider a non-diagonal quadrupole contribution [26], which is proportional to the mean field gradient.

In this quasi-static approach, we calculate full pressure broadened line profiles $I_s^{\rm pr}(\Delta\omega; n_e; T)$ for L_α and L_β of hydrogen. To include Doppler broadening, a convolution with a Gaussian of full width $\gamma_D = \frac{2\omega_0}{c}\sqrt{\frac{2\ln 2 k_{\rm B} T}{M}}$ has to be carried out, where c is the speed of light, $k_{\rm B}$ is the Boltzmann constant and M is the mass of the emitter.

3 Ion-dynamics

Now, we want to consider the effect of ion-dynamics. Qualitatively, line wings can be treated statically and the line center is affected by ion-dynamics. This can be seen from the fact that the inverse of the excited emitter

state lifetime τ is of the same order as the resulting line shift $\Delta\omega$, $\tau \sim \Delta\omega^{-1}$. Hence, in the center, $\tau \gg t_{\text{coll}}$, where t_{coll} is the duration of perturber-emitter collisions. Thus, perturber and emitter can complete a full collision during the emission time. Here, dynamics are important and the collision approximation does apply. In the line wings, the opposite is true, $\tau \ll t_{\text{coll}}$, i.e. the perturber is almost static during the emission time. Then, the quasi-static approximation is well justified. Depending on the plasma parameters, either of the approximations can be dominant for the line profile. Both regimes can be bridged by the unified theory [27, 28]. However, as the unified theory implies binary collisions, it can only be applied for ions in low density plasmas, see e.g. [29]. Thus, we follow two other ideas to include ion-dynamics into the line profile calculation, namely the model microfield method [15, 16] and the reformulation of the frequency fluctuation model [17]. They are both closely connected to the static approximation based on microfield distributions.

3.1 Model microfield method (MMM)

The MMM considers the microfield dynamics as a stochastic process, where the electric field at the site of the emitter changes with a certain jump-frequency $\nu_{\text{jump}}(E)$ from one constant value E_1 to another random constant value E_2 and so on. Thus, the change of the electric field models the movement of the surrounding ions. In this process, E_2 does not depend on E_1 and the system has no memory. The time dependence can be worked out analytically [15, 16], if the jumps in the electric field are described by a kangoroo process. Then, the jump-frequency is chosen to preserve the second moment of the static microfield distribution [30].

To include the MMM into the line profile calculation, Eq. (1) has to be changed to [31]

$$I^{\text{pr}}_{\text{MMM}}(\Delta\omega) \sim \text{Im}\left[\sum_{ii'ff'} \left\{\langle i|\vec{r}|f\rangle\langle f'|\vec{r}|i'\rangle\langle i|\langle f|U(\Delta\omega)|f'\rangle|i'\rangle\right\}\right], \tag{5}$$

with the time evolution operator

$$U(\Delta\omega) = < L^{-1}_{\text{MMM}}(\Delta\omega, E) >_{\text{s}} + \frac{< \Omega(E) L^{-1}_{\text{MMM}}(\Delta\omega, E) >^2_{\text{s}}}{< \Omega(E) >_{\text{s}} - < \Omega^2(E) L^{-1}_{\text{MMM}}(\Delta\omega, E)) >_{\text{s}}}, \tag{6}$$

and the extended line profile operator based on Eq. (2)

$$L_{\text{MMM}}(\Delta\omega, E) = L(\Delta\omega, E) + i\Omega(E), \tag{7}$$

where $\Omega(E) = 2\pi\hbar\nu_{\text{jump}}(E)$.

In Eq. (6), the average $< \cdots >_{\text{s}}$ is over the static ion microfield distribution function $W(E)$. In the limit $\Omega(E) \to 0$, the second terms on the right hand sides of Eqs. (6) and (7) vanish and the quasi-static approximation from Eq. (1) is recovered.

3.2 Frequency fluctuation model (FFM)

The reformulation of the FFM [17] assumes that a line profile has been calculated and area-normalized in the quasi-static approximation $I_{\text{s}}(\omega)$, i.e. in our case based on Eq. (1). Then, the ion-dynamics can simply be taken into account in the following way

$$I_{\text{FFM}}(\omega) = \frac{r^2}{\pi}\text{Re}\frac{Q(\omega,\gamma)}{1-\gamma\, Q(\omega,\gamma)}, \qquad \text{with} \qquad Q(\omega,\gamma) = \int_0^\infty \frac{I_{\text{s}}(\omega')\text{d}\omega'}{\gamma + i(\omega-\omega')}. \tag{8}$$

Here, the inverse state lifetime γ is defined as $\gamma = v_{\text{therm}}/d$, where the thermal velocity $v_{\text{therm}} = \sqrt{8k_{\text{B}}T/\pi m}$ as well as the interparticle distance $d = (3/4\pi n)^{-3}$ of the ions are known from the plasma parameters. n and m are density and mass of the perturbing ions, respectively. The intensity is proportional to $r^2 = \sum_k a_k$, where a_k are the intensities of the different Stark components that contribute to the line.

The main ideas behind the FFM are that microfield-fluctuations produce frequency fluctuations and that the emitting system perturbed by the microfield can be described by a set of dressed two level transitions each with a certain frequency, amplitude and width [20]. The FFM can reproduce line shapes obtained from MD simulations [17] and is easily implemented.

Contrib. Plasma Phys. **53**, No. 4-5 (2013) / www.cpp-journal.org 371

4 Comparison of the different approaches

We have calculated the H Lyman-α and Lyman-β lines for a broad range of plasma parameters in quasi-static approximation, Eq. (1), and with ion-dynamics in both MMM, Eq. (5), and FFM, Eq. (8), 144 times each.

In Fig. 1, we give three examples for full L_α lines for a plasma at $n_e = 8 \cdot 10^{25}$ m^{-3} and $T = 10^4, 4 \cdot 10^5$ and $8 \cdot 10^6$ K, respectively. For higher temperatures, ion-dynamics becomes more important. Furthermore, the difference in shapes of the lines calculated with the different approaches to ion-dynamics can be seen in Fig. 1.

In Fig. 2, examples for full L_β line shapes are given. To include a case where ion-dynamics leads to narrowing of the line, we keep the temperature in these examples constant at $T = 8 \cdot 10^6$ K and go from the lowest density to the highest density. At $n_e = 10^{23}$ m^{-3}, L_β is symmetric and narrowed by ion-dynamics. The dip is less pronounced with MMM compared to the static line shape and fully supressed by FFM, i.e. the fast fluctuation limit (Lorentzian shape) is reached due to the large value of γ.

At the highest density considered here, L_β is highly asymmetric due to the difference in electronic self-energies entering into the Stark shifted line components. Again, the dip is more supressed by FFM than MMM. As only the blue peak contributes to the full width at half maximum (FWHM) in the quasi-static case, but both peaks are taken into account when FFM ion-dynamics is included, the line is strongly broadened by ion-dynamics.

In the following, we only compare the FWHM, Γ, as a characteristic parameter of the line profile, bearing in mind that it does not include any information about the symmetry of the line.

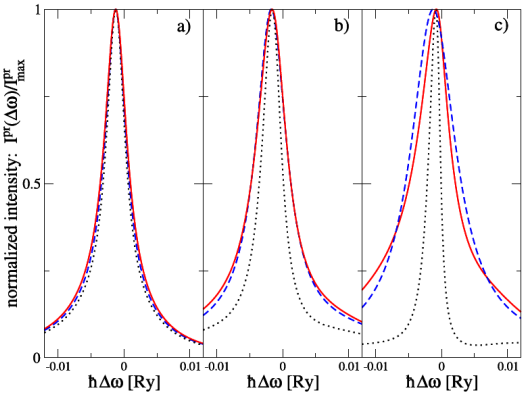

Fig. 1 Line shape of H L_α. Dotted line: Eq. (1) with quasi-static ions, full line: Eq. (5) with ion-dynamics in MMM, broken line: Eq. (8) with ion-dynamics in FFM. Plasma conditions are $n_e = 8 \cdot 10^{25}$ m^{-3} and **a)** $T = 10^4$ K, **b)** $T = 4 \cdot 10^5$ K, and **c)** $T = 8 \cdot 10^6$ K.

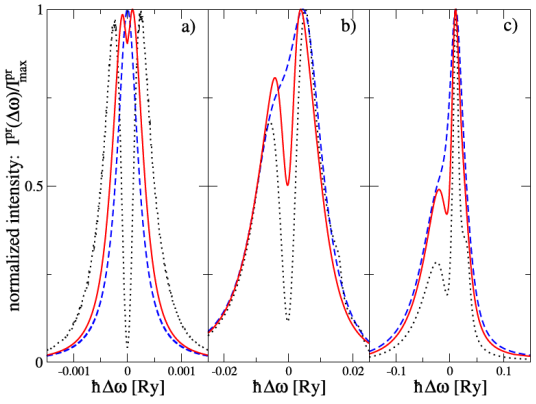

Fig. 2 Line shape of H L_β. Legend as in Fig. 1. Plasma conditions are $T = 8 \cdot 10^6$ K and **a)** $n_e = 10^{23}$ m^{-3}, **b)** $n_e = 10^{25}$ m^{-3}, and **c)** $n_e = 8 \cdot 10^{25}$ m^{-3}.

4.1 Quasi-static versus dynamic ions (MMM)

To assess the effect of ion-dynamics for Lyman lines, we compare the line-width without and with ion-dynamics for a broad range of plasma parameters. In Fig. 3, we give the ratio x_s of the width in quasi-static approximation to the width with ion-dynamics in MMM,

$$x_s = \frac{\Gamma_s}{\Gamma_{MMM}}. \tag{9}$$

We can see, that the error made by neglecting ion-dynamics increases with increasing temperature and decreasing density. It is for the L_α profiles calculated here at least -15%, i.e. the quasi-static width is only 85% of the width with ion-dynamics. In the worst case, the quasi-static width of L_α is only 6% of the one with MMM ion-dynamics.

The analogous comparison for L_β is shown in Fig. 4. In general, L_β is less affected by ion-dynamics, as can be seen by the huge area where the width does only change by $\pm 3\%$ when ion-dynamics is included. However, due to the asymmetric double-peak structure of L_β, the line can be up to 51% too broad in the low-density, high

temperature region or up to 73% too narrow in the high temperature, high density regime when ion-dynamics is neglected.

For this comparison, we did not include Doppler broadening. However, in Figs. 3 and 4, we give contour lines (dotted) for the ratio x_D of the width with Doppler broadening to the one without Doppler broadening, both with ion-dynamics in MMM, too. For L_α, the width of pressure and Doppler broadenend profiles exceeds the width of pressure broadenend profiles drastically in the low density and high temperature range, i.e. in the region, where the quasi-static approximation is not sufficient at all. There, the width of any measured L_α profile is dominated by Doppler broadening. Doppler broadening is less important for L_β as the pressure broadened linewidth of L_β is greater than the one of L_α.

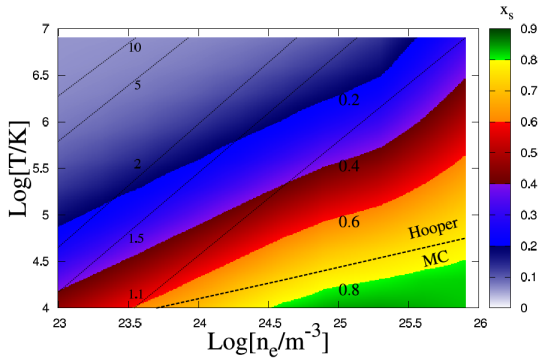

Fig. 3 Influence of ion-dynamics for L_α: x_s from Eq. (9) The dashed line indicates the border between used microfield distributions (Hooper [14], MC [21]). Dotted lines with small numbers refer to the ratio x_D of pressure and Doppler broadened to only pressure broadened MMM line width.

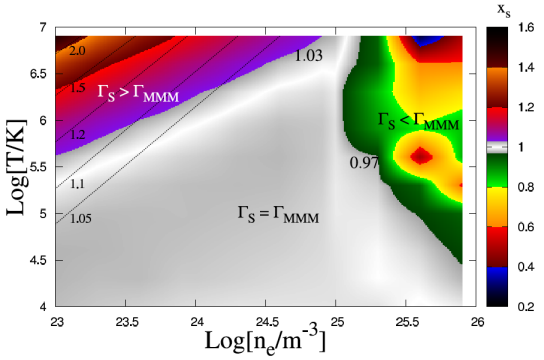

Fig. 4 Influence of ion-dynamics for L_β: The ratio x_s of the width in quasi-static approximation to the width with ion-dynamics in MMM using the MC based microfield distribution [21]. Ion-dynamics is negligible in the grey area (1±3%). Dotted lines refer to Doppler broadening as in Fig. 3.

4.2 FFM versus MMM

The different approaches to include ion-dynamics are compared in Figs. 5 and 6. Again, we give the ratio x_{FFM} of the width with ion-dynamics in FFM to the width with ion-dynamics in MMM. Thus, the numerator of Eq. (9) is replaced by Γ_{FMM}. There is a region where both approaches lead to the same width. As L_β is less affected by ion-dynamics, see Fig. 4, this region is larger for L_β. For L_α, differences up to -15% occur in the low temperature, low density region. For high temperatures and low densities, Γ_{FFM} exceeds Γ_{MMM} by up to +28%.

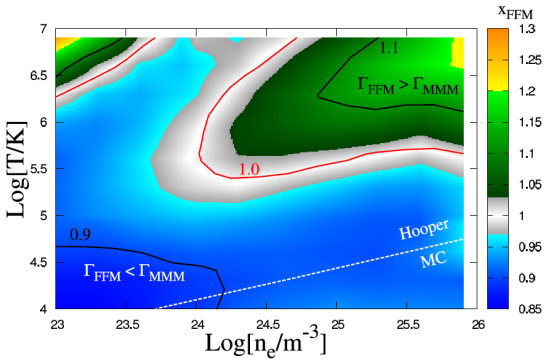

Fig. 5 Different approaches to include ion-dynamics for H L_α: The ratio x_{FFM} of the width with ion-dynamics in FFM to the width with ion-dynamics in MMM. Dashed line as in Fig. 3.

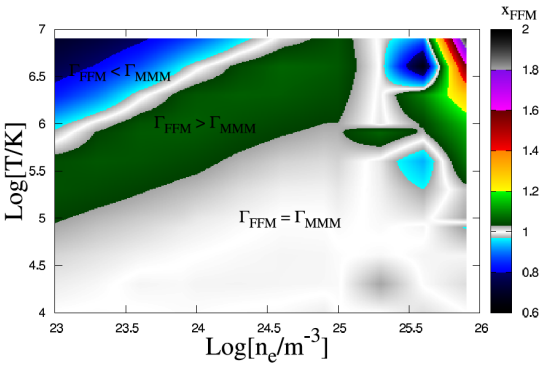

Fig. 6 Different approaches to include ion-dynamics for H L_β: The ratio x_{FFM} of the width with ion-dynamics in FFM to the width with ion-dynamics in MMM.

Contrib. Plasma Phys. **53**, No. 4-5 (2013) / www.cpp-journal.org 373

For L_β, the effect of ion-dynamics in the different approaches depends strongly on the underlying quasi-static line shape, i.e. the electronic self-energy. Thus, the asymmetric peak structure can produce either $x_{\mathrm{FFM}} = 0.7$, when the double peak is transformed to a Lorentzian, or $x_{\mathrm{FFM}} = 1.94$), when only one peak contributes to the FWHM in MMM but both do in FFM.

5 Conclusions

We studied the influence of ion-dynamics on pressure broadening of spectral lines in hydrogen plasmas. As the focus of this work is on the ions, we treated broadening due to plasma electrons only in a second Born approximation, however, in previous publications [23, 24], we focused on the self-energy due to the surrounding electrons to treat strong electron-emitter collisions systematically (T-matrix). Our quantum-statistical approach provides full line profiles, but we used mainly ratios of the width in our comparison. The ion-dynamics was considered with two methods that are closely related to the quasi-static approximation. The model microfield method (MMM) reaches the quasi-static approximation as a limit and the frequency fluctuation model (FFM) depends on it as an input. In our study, we found that FWHM of L_α is always too thin when ion-dynamics is neglected. In general, ion-dynamic gets more and more important for increasing temperature and decreasing density. The different approaches to ion-dynamics, MMM and FFM, give comparable results for the width with deviations up to -15% and +28% in the considered density and temperature region. However, the shapes of the lines differ slightly. Under experimental conditions, the small differences might be covered by Doppler broadening and instrumental broadening. For L_β, ion-dynamics is in general less important. However, it can lead to narrowing or broadening of the line. Especially, for high temperatures, the situation is less systematic due to the partly asymmetric double peak structure. A comparison with measurements – if there exist any at these high temperatures – could give valuable insight and distinguish between the different models for ion-dynamics. A similar comparison with the measurement exists already for He II Balmer-α lines [32].

Acknowledgements The author would like to thank Heidi Reinholz and Gerd Röpke for advice and helpful discussions. This article was supported by the German Research Foundation within SFB 652 'Strong correlations and collective effects in radiation fields: Coulomb systems, clusters und particles.'

References

[1] H. R. Griem, Principles of Plasma Spectroscopy (Cambridge University Press, Cambridge, 1997).
[2] I. H. Hutchinson, Principles of Plasma Diagnostics (Cambridge University Press, Cambridge, 1987).
[3] M. Baranger, Phys. Rev. **112**, 855 (1958).
[4] H. R. Griem, Spectral Line Broadening by Plasmas (Academic Press, London, 1974).
[5] S. Sahal-Brechot, Astron. Astrophys. **1**, 9 (1969); Astron. Astrophys. **2**, 322 (1969).
[6] R. Stamm and D. Voslamber, J. Quant. Spectros. Radiat. Transfer **22**, 599 (1979).
[7] M. Gigosos and V. Cardeñoso, J. Phys. B: At. Mol. Opt. Phys. **29**, 4795 (1996).
[8] W. D. Kraeft, D. Kremp, W. Ebeling, and G. Röpke, Quantum Statistics of Charged Particle Systems (Akademie-Verlag Berlin, Berlin, 1986).
[9] S. Günter, L. Hitzschke, and G. Röpke, Phys. Rev. A **44**, 6834 (1991).
[10] B. Omar, S. Günter, A. Wierling, and G. Röpke, Phys. Rev. E **73**, 056405 (2006).
[11] S. Sorge, A. Wierling, G. Röpke, W. Theobald, R. Sauerbrey, and T. Wilhein, J. Phys. B: At. Mol. Opt. Phys. **33**, 2983 (2000).
[12] S. Lorenzen, A. Wierling, H. Reinholz, and G. Röpke, Contrib. Plasma Phys. **48**, 657 (2008).
[13] J. Holtsmark, Phys. Z. **20**, 162 (1919).
[14] C. F. Hooper, Jr., Phys. Rev. **165**, 215 (1968); Phys. Rev. **169**, 193 (1968).
[15] A. Brissaud and U. Frisch, J. Quant. Spectros. Radiat. Transfer **11**, 1767 (1971).
[16] J. Seidel, Z. Naturf. **32a**, 1195 (1977); Z. Naturf. **35a**, 679 (1980).
[17] A. Calisti, C. Mossé, S. Ferri, B. Talin, F. Rosmej, L. A. Bureyeva, and V. S. Lisitsa, Phys. Rev. E **81**, 016406 (2010).
[18] K. Grützmacher and B. Wende, Phys. Rev. A **16**, 243 (1977).
[19] R. W. Lee, Journal of Physics B: Atomic and Molecular Physics **11**, L167 (1978).
[20] S. Ferri, A. Calisti, C. Mossé, B. Talin, and V. Lisitsa, AIP Conf. Proc. **1290**, 53 (2010).
[21] A. Potekhin, G. Chabrier, and D. Gilles, Phys. Rev. E **65**, 036412 (2002).
[22] A. Könies and S. Günter, J. Quant. Spectros. Radiat. Transfer **52**, 825 (1994).
[23] S. Lorenzen, A. Wierling, H. Reinholz, and G. Röpke, Contrib. Plasma Phys. **51**, 349 (2011).

[24] S. Lorenzen, A. Wierling, H. Reinholz, G. Röpke, M. C. Zammit, D. V. Fursa, and I. Bray, AIP Conf. Proc. **1290**, 99 (2010); J. Phys.: Conf. Series **397**, 012021 (2012).
[25] L. D. Landau and E. M. Lifschitz, Quantum mechanics: non-relativistic theory (Pergamon Press, Oxford, 1977).
[26] J. Halenka, Z. Phys. D **16**, 1 (1990).
[27] E. Smith, J. Cooper, and C. Vidal, Phys. Rev. **185**, 140 (1969).
[28] D. Voslamber, Phys. Lett **40A**, 266 (1972).
[29] J. Cooper, E. Smith, and C. Vidal, J. Phys. B: At. Mol. Opt. Phys. **7**, L101 (1974).
[30] A. Brissaud, C. Goldbach, J. Leorat, A. Mazure, and G. Nollez, J. Phys. B: At. Mol. Opt. Phys. **9**, 1129 (1976).
[31] S. Günter, Optische Eigenschaften dichter Plasmen, habilitation thesis at University of Rostock, 1995.
[32] Th. Wrubel, S. Büscher, H.-J. Kunze, and S. Ferri, J. Phys. B: At. Mol. Opt. Phys. **34**, 461 (2001).

PHYSICAL REVIEW E **89**, 023106 (2014)

Plasma pressure broadening for few-electron emitters including strong electron collisions within a quantum-statistical theory

Sonja Lorenzen* and Banaz Omar
Institute of Physics, University of Rostock, D-18051 Rostock, Germany

Mark C. Zammit, Dmitry V. Fursa, and Igor Bray
Institute of Theoretical Physics, Curtin University, Perth, Western Australia 6845, Australia

(Received 15 May 2013; revised manuscript received 18 December 2013; published 21 February 2014)

To apply spectroscopy as a diagnostic tool for dense plasmas, a theoretical approach to pressure broadening is indispensable. Here, a quantum-statistical theory is used to calculate spectral line shapes of few-electron atoms. Ionic perturbers are treated quasistatically as well as dynamically via a frequency fluctuation model. Electronic perturbers are treated in the impact approximation. Strong electron-emitter collisions are consistently taken into account with an effective two-particle T-matrix approach. Convergent close-coupling calculations give scattering amplitudes including Debye screening for neutral emitters. For charged emitters, the effect of plasma screening is estimated. The electron densities considered reach up to $n_e = 10^{27}$ m^{-3}. Temperatures are between $T = 10^4$ and 10^5 K. The results are compared with a dynamically screened Born approximation for Lyman lines of H and H-like Li as well as for the He 3889 Å line. For the last, a comprehensive comparison to simulations and experiments is given. For the H Lyman-α line, the width and shift are drastically reduced by the Debye screening. In the T-matrix approach, the line shape is notably changed due to the dependence on the magnetic quantum number of the emitter, whereas the difference between spin-scattering channels is negligible.

DOI: 10.1103/PhysRevE.89.023106 PACS number(s): 52.25.Os, 32.70.Jz, 34.80.Bm

I. INTRODUCTION

Plasma pressure broadening (PPB), i.e., broadening and shift of spectral lines due to the plasma surroundings, has been studied for a long time. In particular, it can be used for plasma diagnostics, as reviewed, e.g., in [1]. The charged plasma particles affect the atomic states of the emitting atom or ion. The mechanisms are the same, no matter if the plasma is part of an astrophysical object or created in the laboratory, e.g., in arc discharges or by laser impact. A sound theory to calculate line profiles is needed in order to obtain accurate information about plasma parameters such as composition, temperature, and density from the measured line spectrum. Several approaches are applied to calculate the spectrum of bound-bound electron transitions, emitted from or absorbed by a plasma. Some use pure quantum mechanics [2], others involve a semiclassical view of the perturbers, e.g., the standard theory [3,4], or they depend on molecular dynamics (MD) simulations, e.g., [5].

All theories are based on the calculation of the dipole-dipole correlation function, which describes the emission or absorption of radiation from charged particles. Within our quantum-statistical theory, the dipole-dipole correlation, i.e., the polarization function, is calculated with the help of thermodynamic Green's functions; see [6–8]. For dense plasmas, strong electron-emitter collisions are important and perturbative methods are no longer applicable. One way to include strong collisions in the framework of the standard theory has been discussed in Ref. [9], allowing for penetrating collisions.

The aim of this work is to treat strong electron-emitter collisions consistently within quantum-statistical theory. For this reason, we combine sophisticated scattering theory with our line shape formalism; thus, we go beyond the perturbative Born approximation. We show that plasma screening has to be included in the scattering process, otherwise the line shift and width are overestimated. Furthermore, we discuss the resulting line shapes, when different spin-scattering channels and emitter states with different magnetic quantum numbers are considered separately.

The theory is briefly reviewed in Sec. II with a focus on the treatment of strong electron-emitter collisions. They can be included by ladderlike diagrams in our theory. Neglecting the dynamical screening, an effective two-particle T-matrix approach can be derived; see [10]. Then, the electronic contribution to PPB is given by the electron-emitter scattering amplitude. It is obtained from convergent close-coupling (CCC) calculations for electron scattering on a Debye-screened neutral emitter; see [11,12]. Hence, we go beyond the close-coupling approach presented by Unnikrishnan and Callaway [13] which does not include screening. In our theory, electron scattering on charged emitters in a plasma surrounding is approximated by isolated electron-emitter scattering [14–16]. We show in Appendix A that the divergent Coulomb part of the scattering amplitudes can be removed. We estimate the error made by neglecting the screening in Appendix B. PPB by perturbing ions is treated quasistatically or dynamically using the renewed formulation of the frequency fluctuation model (FFM) [17].

Our first example is the H Lyman-α (L_α) line in Sec. III. Its simplicity makes it an ideal test case; however, its shape has recently been discussed controversially at the spectral line shapes in plasmas code comparison workshop [18]. For H L_α, we compare the PPB of electrons in the effective T-matrix approach with and without Debye screening to a dynamically screened Born approximation for $n_e = 10^{25}$ m^{-3} at $T =$ 11 604 K. Furthermore, we give a comparison to the measured H L_α profiles of Grützmacher and Wende [19]. In Sec. IV, we apply the effective T-matrix approach to a charged H-like emitter. Full Lyman line profiles of Li^{2+} are calculated for the free-electron densities of $n_e = 4 \times 10^{25}$ m^{-3} and

*Sonja.L@renzen.de

4×10^{26} m^{-3} at a temperature of $T = 3 \times 10^5$ K. Here, the asymmetry of L_β and L_γ lines is drastically changed when applying the T-matrix approach without screening. Screening corrections are estimated and lead to a better agreement between the two approaches. A comparison of the linewidth from the two approaches is carried out for $n_e = 10^{25}$–10^{27} m^{-3}. The last example on the He 3889 Å line is given in Sec. V. There, results for the linewidth and shift of the T-matrix approach are compared to experimental data, results of computer simulations, and other theories for the density range $n_e = 10^{22}$–10^{24} m^{-3} and $T \sim 10^4$ K

II. QUANTUM-STATISTICAL APPROACH TO PLASMA PRESSURE BROADENING

The quantum-statistical theory for pressure broadening has been described in detail in [6–8]. Here, we give only the key formulas in atomic Rydberg units, i.e., $\hbar = 2m_e = e^2/2 = 1$. These units are used throughout this paper. In the case of local thermodynamic equilibrium, the emitted spectral intensity $I(\Delta\omega)$ at $\Delta\omega = \omega - \omega_0$ near the frequency ω_0 of the unperturbed transition is given by

$$I(\Delta\omega) = \frac{(\omega_0+\Delta\omega)^4}{8\pi^4 c^3} e^{-(\omega_0+\Delta\omega)/k_B T} \times \mathrm{Im}\left[\sum_{ii'ff'} \{\langle i|\vec{r}|f\rangle\langle f'|\vec{r}|i'\rangle\langle i|\langle f|U(\Delta\omega)|f'\rangle|i'\rangle\}\right] \quad (1)$$

with the speed of light c and the Boltzmann constant k_B. The sum runs over all initial i and final f emitter states. The double sum is not necessary for isolated lines. The contributions to the line profile are weighted with the transition probability, which is given by the dipole matrix elements $\langle i|\vec{r}|f\rangle$. The time evolution operator $U(\Delta\omega)$ can be taken in different approximations. For the quasistatic approximation, it is given by

$$U(\Delta\omega)_{\mathrm{static}} = \langle L(\Delta\omega, E)^{-1}\rangle_s = \int_0^\infty dE\, W(E) L(\Delta\omega, E)^{-1}, \quad (2)$$

where $\langle\cdots\rangle_s$ stands for the average over the static ion microfield with the microfield distribution function $W(E)$. For neutral emitters, i.e., hydrogen and helium, we use Hooper's low-frequency tables [20] to determine $W(E)$ for weakly coupled plasmas. Outside the validity range of Hooper's approach, we use the fit formula of Potekhin *et al.* [21]. The fit formula is based on Monte Carlo simulations and is appropriate for strongly coupled plasmas as well. For the charged H-like emitter Li^{2+}, we use APEX [22] to calculate $W(E)$ with Debye-Hückel pair correlation functions.

The line profile operator $L(\Delta\omega, E)$ contains the width and shift of atomic energy levels caused by the plasma surroundings according to

$$L(\Delta\omega, E) = \Delta\omega - \mathrm{Re}[\Sigma_{ii'}(\Delta\omega) - \Sigma_{ff'}(\Delta\omega)] + \imath\, \mathrm{Im}[\Sigma_{ii'}(\Delta\omega) + \Sigma_{ff'}(\Delta\omega)] + \Gamma_{ii'ff'}(\Delta\omega). \quad (3)$$

Here, $\Sigma_{ii'}$ and $\Sigma_{ff'}$ are the self-energies, i.e., the shift (real part) and broadening (imaginary part), of energy levels i and f due to the surrounding plasma, respectively, and $\Gamma_{ii'ff'}$ is the upper-lower level coupling term. Due to different interaction time scales, the self-energy can be split into a nondiagonal E-field-dependent ionic part and a diagonal frequency-dependent electronic part,

$$\Sigma_{\nu\nu'}(E, \Delta\omega) = \Sigma^i_{\nu\nu'}(E) + \Sigma^e_\nu(\Delta\omega)\delta_{\nu\nu'}, \quad (4)$$

with $\nu = i, f$. Now, we discuss the details of the self-energy calculation for ions and electrons separately.

A. Perturbing ions

The perturbation of the emitter by the plasma ions is mainly caused by the linear and quadratic Stark effects. The linear Stark effect is nonzero for H and H-like emitters and given analytically in parabolic coordinates [23]. For He, the quadratic Stark effect gives the first nonvanishing contribution. The wave functions enter into the calculation for He. As they are not given analytically, we approximate their spherical part by a linear combination of H-like wave functions. The radial part is calculated by the Coulomb approximation after Bates and Damgaard [24]; for more details see [25]. Furthermore, the inhomogeneity of the ionic microfield is treated by the quadrupole Stark effect after Halenka [26], leading to a nondiagonal term in the ionic self-energy $\Sigma^i_{\nu\nu'}(E)$.

For high densities and low temperatures, the ions' movement during the time of emission is negligible and the quasistatic limit can be applied. Then, the time evolution operator is given by Eq. (2). In the opposite regime, ion dynamics has to be treated seriously. There exist several methods to include ion dynamics; for an overview see Refs. [1,27]. In particular, molecular dynamics simulations are a useful tool to treat the dynamics of the system. However, we want to keep the line shape calculations analytic. Recently, a comparison of two analytic methods—the model microfield method (MMM) [28,29] and the FFM [17]—was presented for a broad range of plasma parameters for H Lyman lines [30]. For H L_α, differences between the two approaches up to ±30% were observed for the full width at half maximum (FWHM). As the focus of this communication is on the contribution of strong electron collisions, we present only the FFM briefly here and use it throughout the paper. However, since the use of the MMM leads to a better agreement with the Grützmacher-Wende experiment, we give results for MMM ion dynamics there, too. Details of our implementation of MMM can be found in [30].

The FFM connects microfield fluctuations with frequency fluctuations. It assumes that the emitting system can be described by a set of dressed two-level transitions each with a certain frequency, amplitude, and width [17]. Starting from the area-normalized line profile $I_s(\omega)$ calculated in the quasistatic limit, e.g., with Eqs. (1) and (2), the dynamic profile is given by

$$I_{\mathrm{FFM}}(\omega) \sim \mathrm{Re}\frac{Q(\omega,\gamma)}{1-\gamma\, Q(\omega,\gamma)} \quad (5)$$

with

$$Q(\omega,\gamma) = \int_0^\infty \frac{I_s(\omega')d\omega'}{\gamma + \imath(\omega - \omega')}. \quad (6)$$

Here, γ is the inverse state lifetime

$$\gamma = \frac{v_{\text{therm}}}{d_{\text{i}}}. \quad (7)$$

It depends on the thermal velocity of ions $v_{\text{therm}} = \sqrt{8k_BT/(\pi m_i)}$ and the mean ion distance $d_i = [3/(4\pi n_i)]^{1/3}$, where m_i and n_i are the mass and density of the perturbing ions, respectively. For large γ, the high-frequency limit is reproduced and a Lorentzian line shape is obtained. Although the FFM does not reproduce the second moment of the microfield distribution correctly, the resulting line profiles compare well to simulated line shapes [17].

B. Perturbing electrons

In contrast to the ions, the electron dynamics plays a crucial role, and thus the quasistatic approximation is not applicable. Furthermore, multiple electron-emitter collisions occur and have to be treated. Within our quantum-statistical view of spectral line shapes, two approaches have been developed to account for the contribution by free electrons. Perturbing electrons are considered either within a dynamically screened Born approximation (first order) or within an effective two-particle T-matrix approach which can so far take only static (Debye) screening into account.

1. Dynamically screened Born approximation

The self-energy in the Born approximation is given by [6]

$$\Sigma_\nu^e(\Delta\omega) = -\int \frac{d^3q}{(2\pi)^3} V(q) \sum_\alpha \left|M_{\nu\alpha}^0(q)\right|^2 \times \int_{-\infty}^\infty \frac{d\omega}{\pi}[1 + n_B(\omega)] \frac{\text{Im}\,\varepsilon^{-1}(\vec{q},\omega + \imath\,\delta)}{\Delta\omega + \omega_{\nu\alpha} - (\omega + \imath\delta)}. \quad (8)$$

The dielectric function $\varepsilon(\vec{q},\omega + \imath\delta)$ is approximated by the dielectric function in the random phase approximation. $M_{\nu\alpha}^0(q)$ is the vertex contribution for virtual transitions from ν to α. For H and Li^{2+}, we restrict the main quantum number n_α to run from $n_\nu - 1$ to $n_\nu + 2$ for the real part of $\Sigma_\nu^e(\Delta\omega)$. For the imaginary part, we use the no-quenching approximation $n_\alpha = n_\nu$, since it gives the main contribution to the line broadening. For He, n_α runs always from $n_\nu - 2$ to $n_\nu + 2$. $V(q) = Z_{\text{ion}}e^2/\varepsilon_0 q^2$ is the Fourier-transformed Coulomb potential and $n_B(\omega) = \{\exp[\hbar\omega/(k_BT)] - 1\}^{-1}$ is the Bose function. For the evaluation of Eq. (8) we consider the frequency-independent case $\Delta\omega = 0$ which corresponds to the binary collision approximation. This alters the line profile negligibly, e.g., for H L_α at $T = 11\,604$ K and $n_e = 1 \times 10^{25}$ m^{-3}, the resulting FWHM is 1% smaller in test calculations with full $\Delta\omega$ dependence in Eq. (8). For all considered lines, we followed the method in Refs. [31,32] and checked that correlated collisions can be neglected for our plasma parameters.

The coupling contribution—also called the vertex term—is given in a similar way:

$$\Gamma_{ii'ff'} = -\imath \int \frac{d^3q}{(2\pi)^3} M_{i'i}^0(-\vec{q}) M_{f'f}^0(\vec{q}) V(q) \times \int_{-\infty}^\infty d\omega[1 + n_B(\omega)]\text{Im}\,\varepsilon^{-1}(\vec{q},\omega + \imath\delta)\delta(\omega). \quad (9)$$

The correct dynamical screening of weak collisions is included in Eqs. (8) and (9) by the imaginary part of the inverse dielectric function. However, the Born approximation overestimates strong collisions. This can be rectified to some extent by a cutoff $q_{\max} = 1/\rho_{\min}$. For the case of H, $q_{\max,\text{H}}$ has been adjusted in such a way that the self-energies of an advanced T-matrix approach are recovered; see Ref. [33]. For Li^{2+}, we use a cutoff scaled by the square of the atomic number $Z = 3$, i.e.,

$$q_{\max,Z} = Z^2 q_{\max,\text{H}}. \quad (10)$$

Since there are no advanced T-matrix calculations available for He, we follow the cutoff procedure introduced by Griem *et al.* [3,34]. There, the minimum impact parameter $\rho_{\min}$ is calculated under the assumption of straight electron trajectories in order to assure the unitarity of the scattering matrix. Then a strong collision term for the width is added [34],

$$\Delta\Sigma_{\text{strong}}^e \approx 1.21\imath n_e v_{\text{therm}} \pi q_{\max}^{-2}, \quad (11)$$

depending on the free-electron density n_e and the thermal velocity v_{therm} of the electrons. Further details about the evaluation of Eqs. (8) and (9) can be found in Refs. [6–8,25].

2. Effective two-particle T-matrix approximation

The effective T-matrix approach is a reduced version of the T-matrix approach presented in [33]. It can describe weak and strong collisions equally well, but so far only includes static screening [10,35]. For a nondegenerate plasma, the electronic self-energy, again evaluated at $\Delta\omega = 0$, is then given by

$$\Sigma_\nu^e = -\frac{2}{\pi} n_e \Lambda_{\text{th}}^3 \int_0^\infty dk\, k^2 e^{-k^2/k_BT} f_\nu(0,k). \quad (12)$$

Plasma properties enter via the electron density n_e and the thermal wavelength $\Lambda_{\text{th}} = \sqrt{4\pi/k_BT}$ as well as the forward scattering amplitude $f_{i,f}(0,k)$ for elastic electron scattering at the Debye-screened emitter in state i and f, respectively. This expression, Eq. (12), was also found by Baranger in [2]. He uses the impact approximation and treats the perturbing electrons quantum-mechanically. Fluctuating interactions are replaced by a constant effective one-perturber-atom interaction. In Ref. [2], a level coupling term is derived as well, which is given by

$$\Gamma_{if} = \frac{2\imath}{\pi} n_e \Lambda_{\text{th}}^3 \int_0^\infty dk\, k^3 e^{-k^2/k_BT} \times \int_0^\pi d\theta\, \sin(\theta) f_f(\theta,k) f_i^*(\theta,k). \quad (13)$$

Here, θ is the scattering angle and the dependence of the scattering amplitudes on θ has to be known, too.

The scattering amplitudes, which enter Eqs. (12) and (13), are obtained from a convergent close-coupling calculation.

For the neutral emitters (H, He), it is modified to include Debye screening in the interaction potentials. For the charged emitter (Li^{2+}), we neglect screening and estimate the error thus made. Details of the CCC method and its modification can be found in [14–16] and [11,12], respectively. For H and Li^{2+}, we use 54 (Sturmian) Laguerre functions as a basis for bound and continuous emitter states. With this choice, the emitter states up to $4f$ are reproduced with the correct energies. 153 pseudostates are used to describe electron-He scattering; all details can be found in Ref. [12].

The electron-electron interaction is treated within a partial wave decomposition, where the first partial waves (up to 70) are considered directly. For larger numbers of partial waves, scattering amplitudes are extrapolated following O'Malley *et al.*'s approach [36]. The coupled equations are solved in momentum space and lead to the scattering amplitude. Our method gives separate results for singlet and triplet scattering channels as well as for scattering at the emitter with initial and final states $n_i,l_i,m_i \to n_f,l_f,m_f$. Here, we consider only elastic scattering $n_i,l_i,m_i \to n_i,l_i,m_i$ to calculate the self-energies and level coupling term.

III. HYDROGEN

The L_α line of hydrogen serves as a testbed. It is emitted in the electron transition from $n = 2$ to the ground state $1s$. First, we study the contributions of the electrons for the example of a plasma with Debye screening length $D = \sqrt{k_B T/8\pi n_e} = 44a_0$. This corresponds, e.g., to plasma conditions $T = 11\,604$ K and $n_e = 1 \times 10^{25}$ m^{-3}, where strong electron collisions are relevant due to the high electron density. Then, we reconsider the measured L_α spectra of Grützmacher and Wende [19] with larger screening length $D \sim 300a_0$.

A. Strong collisions and Debye screening

We investigate the influence of screening in the convergent coupling calculation. This has been done in detail for the cross sections σ in [11]. Now, we are explicitly interested in real and imaginary part of the forward scattering amplitude $f(\theta = 0,k)$, as they enter in Eq. (12) and lead to shift (real part) and broadening (imaginary part) of the line. We concentrate on the upper $2p$ states, as the contribution of the lower level $1s$ is small. The effect of screening can be seen in Fig. 1 for the forward scattering amplitude of e-H($2p,m = \pm 1$) scattering. The scattering amplitudes are reduced by screening. Thus, the resulting self-energies are reduced, too. As the different spin-scattering channels lead only to slightly different scattering amplitudes in the low-energy region $k < 0.7a_0$, averaging over spin-scattering channels has been carried out. The results for Σ^e_{2p} and $\Gamma_{2p;1s}$ can be found in Table I together with the ones obtained from the dynamically screened Born approximation from Eqs. (8) and (9). The Born approximation gives the same results for different magnetic quantum numbers m. The shift ($\mathrm{Re}[\Sigma^e_{2p}]$) is still overestimated by a factor of 3 even after the cutoff has been applied to account for strong collisions. The width ($\mathrm{Im}[\Sigma^e_{2p}]$) is sufficiently reduced by the cutoff procedure. The width from the Born approximation

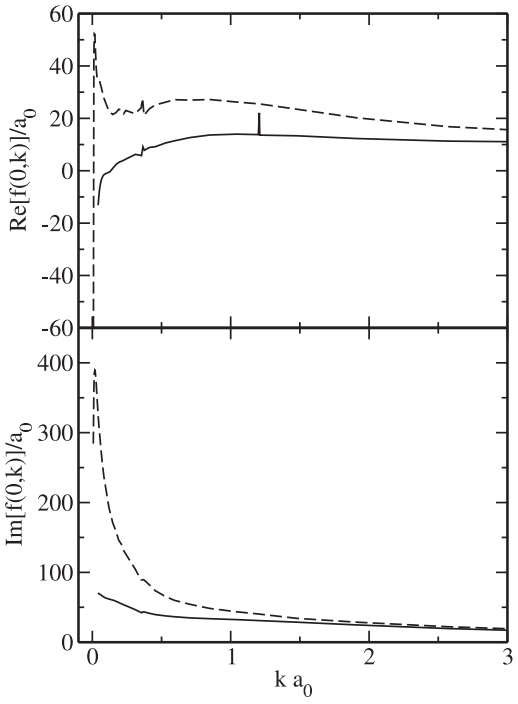

FIG. 1. Forward scattering amplitude for scattering of an electron with momentum k on a H atom in state $2p$ ($m = \pm 1$) without screening (broken line) and with Debye screening for $D = 44a_0$ (full line). Spikes are due to resonances.

TABLE I. Self-energy Σ^e_{2p} from Eqs. (8) and (12) and coupling term $\Gamma_{2p;1s}$ from Eqs. (9) and (13) in different approximations in units of 10^{-4}Ry: The spin-averaged, m-dependent T-matrix approach is given without screening and with Debye screening ($D = 44a_0$) and compared to the m-independent dynamically screened Born approximation with full integration and cutoff at $q_{\max}$, respectively. The considered hydrogen plasma has $n_e = 10^{25}$ m^{-3} at $T = 11\,604$ K.

	T matrix						Born approximation	
	$m = \pm 1$		$m = 0$		m average		$m = 0, \pm 1$	
	Unscreened	$D = 44a_0$	Unscreened	$D = 44a_0$	Unscreened	$D = 44a_0$	Without cutoff	With cutoff
$\mathrm{Re}[\Sigma^e_{2p}]$	− 4.38	− 1.03	− 1.51	0.083	− 3.42	− 0.66	− 9.61	− 3.36
$\mathrm{Im}[\Sigma^e_{2p}]$	− 21.8	− 9.07	− 6.76	− 4.22	− 16.8	− 7.46	− 11.0	− 6.46
$\mathrm{Re}[\Gamma_{2p;1s}]$	0.09	0.11	− 0.05	− 0.05	0.04	0.06	0.0	0.0
$\mathrm{Im}[\Gamma_{2p;1s}]$	0.13	0.13	0.48	0.43	0.25	0.23	0.63	0.24

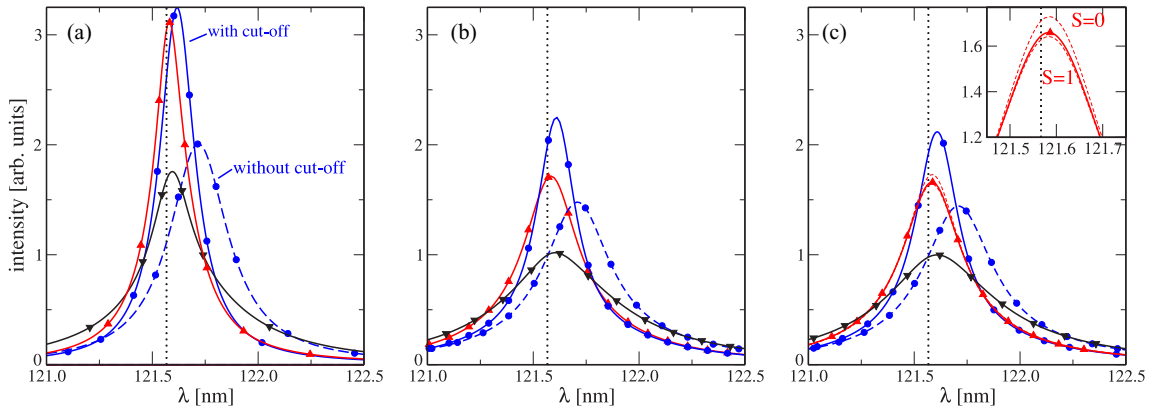

FIG. 2. (Color online) Full H L_α profile calculated in different approximations for $T = 11\,604$ K and $n_e = 10^{25}$ m^{-3}. (a) Only electronic contributions in (●) the dynamically screened Born approximation, (▼) the T-matrix results without screening, and (▲) the T-matrix approach with screening ($D = 44a_0$). (b) Electronic contributions and static ions and (c) electronic contributions and ion dynamics in the FFM. Inset: Different line shapes for pure singlet ($S = 0$) and triplet ($S = 1$) electron-emitter scattering channels (red broken lines). Doppler broadening is included and all profiles are area normalized.

is between the two m-dependent T-matrix results, only 14% below their average.

The resulting L_α line profile of hydrogen is shown in Fig. 2. As long as only electrons are considered [Fig. 2(a)], the widths from the T-matrix approach and in the Born approximation with cutoff are similar, i.e., the cutoff procedure gives a reasonable correction. Nevertheless, the line with ionic Stark splitting [Fig. 2(b)] is broader for the m-dependent T-matrix calculation compared to the m-independent Born approach. This is because the central components ($m = \pm 1$) are broader in the T-matrix approach than the shifted components ($m = 0$, i.e., $2p$ with $2s$ superposed). The approach which can resolve the dependence on the magnetic quantum number m represents the physics of the line emission process better.

In Fig. 2(c), the full treatment including FFM ion dynamics is shown. The ion dynamics lead to further broadening of the line. There, singlet ($S = 0$) and triplet ($S = 1$) electron-emitter scattering channels are considered separately, too. In the inset, this is shown in more detail. Although the line is narrower for $S = 0$ and broader for $S = 1$, their average coincides with the one calculated with spin-averaged electronic self-energies. Hence, it is justified to average over the spin-scattering channels when Eqs. (12) and (13) are evaluated.

B. Grützmacher-Wende experiment reconsidered

In the experiment of Grützmacher and Wende [19], a wall-stabilized argon arc source was used to create dense equilibrium plasmas with $n_e \sim 10^{23}$ m^{-3} at $T \sim 10^4$ K. Under these conditions, pressure broadening by electrons and Ar^+ ions dominates over the Doppler broadening of the L_α line of H. With a hydrogen density of $n_H < 10^{19}$ m^{-3}, the plasma was optically thin and reabsorption could be avoided. The spectrometer bandwidth was stated to be better than $\lambda/\Delta\lambda = 30\,390$. The measured line profiles were already compared to the results of the unified theory in [19], and the remaining discrepancy was resolved by Lee [37] with a perturbative method taking ion dynamics into account. Here, the importance of ion dynamics for L_α was emphasized.

We use the data of Grützmacher and Wende for a comparison, as we are not aware of a better measurement of H L_α under dense plasma conditions. Our theoretical results use singly charged argon ions as perturbers with FFM ion dynamics. To emphasize the importance of ion dynamics, results with MMM ion dynamics are discussed as well. The electronic medium effects are calculated with Eqs. (12) and (13) using scattering amplitudes from unscreened and Debye-screened interactions. We average over the spin-scattering channels and apply a Gaussian instrumental broadening ($\lambda/\Delta\lambda = 30\,390$). The use of the effective T-matrix approach leads to a better agreement with the experimental data than the use of the Born approximation from Eqs. (8) and (9); see Table II. For $n_e = (2,3) \times 10^{23}$ m^{-3}, both the unscreened and screened T-matrix approaches with the MMM agree with the experiment. For the lowest density, only the FWHM without screening lies within the confidence interval of the experiment, in contrast to the highest density, where the screening has to be taken into account to reproduce the experimental FWHM. As has been shown in an earlier paper [30], the FFM leads to narrower lines than the MMM in the considered density and temperature region. Thus, it does not reproduce the experimental linewidth within the framework of our theory. Furthermore, we give the results of Halenka and Olchawa [38] in Table II, who used computer simulations to calculate the L_α lines in full agreement with the experiment.

For $n_e = 2 \times 10^{23}$ m^{-3} and $T = 13\,200$ K, the full Lyman-α line profile is considered,; see Fig. 3. The main contribution to the linewidth is caused by ion dynamics. It is crucial for this experiment, as was already shown in [37]. Nevertheless, the effective T-matrix approach gives a better agreement with the measurement than the Born approach with cutoff procedure. As has been discussed above, the additional broadening is mainly caused by the m dependence of the electronic self-energy in the effective T-matrix approach.

TABLE II. FWHM of H L_α in Å for the experimental conditions of Grützmacher and Wende [19]: Comparison of the m-dependent T-matrix approach (averaged over spin-scattering channels) without and with Debye screening to the m-independent dynamically screened Born approximation with cutoff using two different ion-dynamics models. The theoretical values include Gaussian instrumental broadening of $\lambda/\Delta\lambda = 30\,390$.

			FWHM (Å)				
n_e (10^{23} m^{-3})	T (10^4 K)	D (a_0)	Expt. [19]	Born FFM/MMM	T matrix[a] FFM/MMM	T matrix[b] FFM/MMM	Simulation [38]
1	1.27	456	0.23 ± 0.02	0.16/0.19	0.17/0.21	0.17/0.20	0.22
2	1.32	335	0.30 ± 0.02	0.19/0.25	0.23/0.29	0.22/0.28	0.29
3	1.32	273	0.36 ± 0.02	0.23/0.29	0.30/0.37	0.28/0.35	0.36
4	1.40	243	0.42 ± 0.02	0.26/0.34	0.37/0.45	0.34/0.42	0.43

[a]Without Debye screening.
[b]With Debye screening for mean $D = 314a_0$.

IV. HYDROGENLIKE LITHIUM

For Li^{2+}, the Lyman series is studied for $T = 3 \times 10^5$ K and free-electron density $n_e = 4 \times 10^{25}$ m^{-3}, following the experimental conditions obtained in a laser-induced plasma experiment by Schriever *et al.* [39] and its analysis via synthetic spectral lines [40]. The corresponding Debye length is $D = 113a_0$. As the effect of strong collisions is more prominent for high densities, we consider the line profiles for a higher density $n_e = 4 \times 10^{26}$ m^{-3} as well.

The T-matrix approach is used without implementing the screening into the CCC code for the charged emitter Li^{2+}. Instead, we use scattering amplitudes from electron scattering on an isolated Li^{2+} ion. Since the long-range Coulomb potential gives rise to a divergent forward scattering amplitude, we skip the Coulomb part of the scattering amplitude. This does not affect the line profile operator because divergent terms in the self-energies are canceled by divergent terms in the coupling term; see Appendix A. An estimation of the necessary correction due to screening in the scattering process is given in Appendix B. The scattering amplitudes were calculated for $l = 60$ partial waves with an extrapolation to $l_{\max} = 125$.

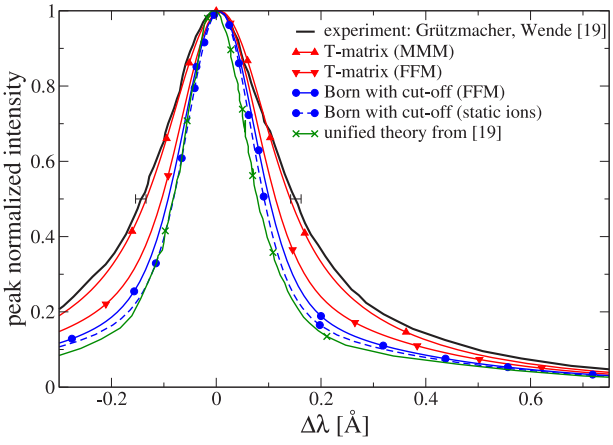

FIG. 3. (Color online) Comparison of measured and theoretical full H L_α profiles. Experimental data and unified theory are from Ref. [19] for plasma conditions $n_e = 2 \times 10^{23}$ m^{-3} and $T = 13\,200$ K. In the quantum-statistical theory, electrons are treated either in Born approximation with cutoff or within our T-matrix approach for $D = 314a_0$.

In Fig. 4, the Lyman lines are shown in Born approximation using Eqs. (8) and (9) with cutoff according to Eq. (10), and in the effective T-matrix approach Eqs. (12) and (13). We show the results averaged over the spin-scattering channels, as the differences in the resulting lines for the singlet and triplet channels are small. To focus on the effect of the different treatment of electrons, we neglect self-absorption and instrumental broadening in our comparison.

At the lower density (upper panel of Fig. 4), the screening correction for the T-matrix approach does not affect the line shape. In contrast to the comparison for H L_α, Fig. 2, the Li^{2+} L_α line is slightly redshifted when the T-matrix approach is used. For L_β and L_γ, the line shape is changed more drastically compared to the Born approximation result, leading to different asymmetric line features. The difference in the asymmetry is partly due to the different values for the self-energies in the two approximations. However, the main effect is again caused by the dependence on the magnetic quantum number m which is present only in the T-matrix approach. When Gaussian instrumental broadening with $\lambda/\Delta\lambda = 300$ [39] is applied, the prominent differences between the two approaches disappear. Thus, the analysis of the experiment would give the same results as previously presented in [40] and is not repeated here. It would be useful to have measurements with a better resolution for Li^{2+} to distinguish between the different theories.

At the higher density (lower panel of Fig. 4), the T-matrix approach gives a larger width compared to the Born approach. For L_α, the difference in the shift is equally pronounced and cannot be corrected by our simple screening correction. For L_β and even more for L_γ, the difference between the two approaches can be corrected to a large extent by the screening correction.

After these examples of full line profiles, we further study the influence of the screening correction in the T-matrix approach. For this reason, we give a comparison of the density dependence of the FWHM of L_α and L_β in Figs. 5 and 6 for a density range $n_e = 10^{25}$–2×10^{27} m^{-3} at $T = 3 \times 10^5$ K. For Li^{2+} L_α, the width is dominated by Doppler broadening up to $n_e = 10^{26}$ m^{-3}. For higher densities, the T-matrix approach gives a larger width even after applying

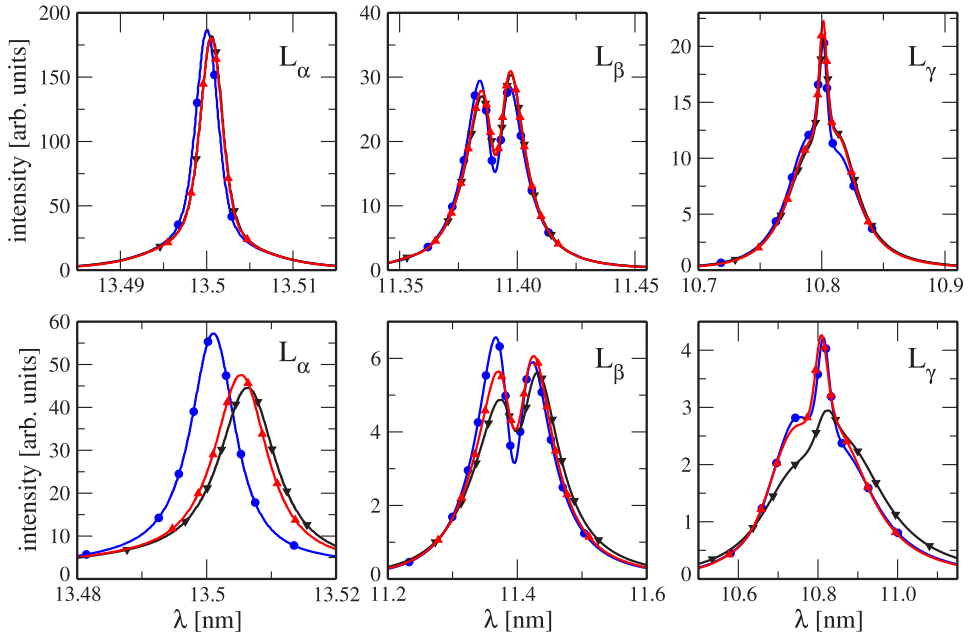

FIG. 4. (Color online) Area-normalized Lyman lines of Li^{2+} for $T = 3 \times 10^5$ K and $n_e = 4 \times 10^{25}$ m^{-3} (upper panel) and $n_e = 4 \times 10^{26}$ m^{-3} (lower panel), respectively. Electronic effects are treated in the dynamically screened Born approximation with cutoff (●) and with the T-matrix approach without screening (▼) and with an estimated screening correction (▲), according to Appendix B. Ion dynamics is considered within the FFM. Doppler broadening is included.

the screening correction. This might be due to the dependence on the magnetic quantum number m as discussed for H L_α in Sec. III A. For L_β, the screening correction leads to agreement of the FWHM from the T-matrix approach and that from the Born approach with cutoff.

For both considered one-electron emitters (H and Li^{2+}), the results of the perturbative Born approximation with adjusted cutoff are confirmed by our T-matrix approach for lower densities; see Figs. 3 and 4 (upper panel). There, the effect of strong collisions is expected to be small. For higher densities, and hence more strong collisions, differences between boththe two approaches are more pronounced; see Figs. 2 and 4 (lower panel). For the charged emitter Li^{2+}, plasma screening has not been implemented so far; however, our estimated correction leads to similar line shapes for both approaches. Remaining differences are caused by the different treatment of the dependence on the magnetic quantum number m. The screening of the charged emitter should be taken into account in the calculation of scattering amplitudes in the future.

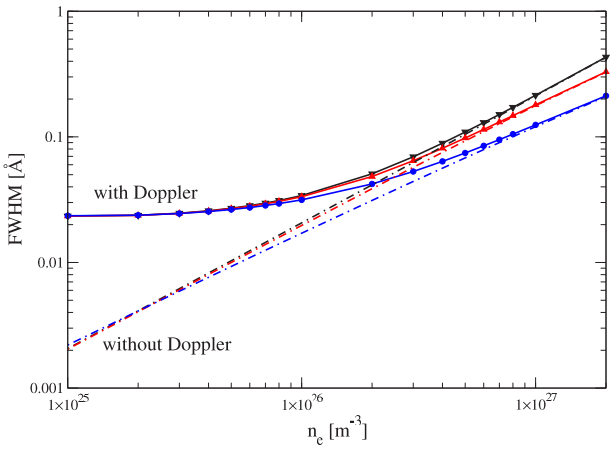

FIG. 5. (Color online) FWHM of Li^{2+} L_α line at $T = 3 \times 10^5$ K without ion dynamics. Electronic effects are treated in the dynamically screened Born approximation with cutoff (●) and in the T-matrix approach without screening (▼) and with an estimated screening correction (▲), according to Appendix B.

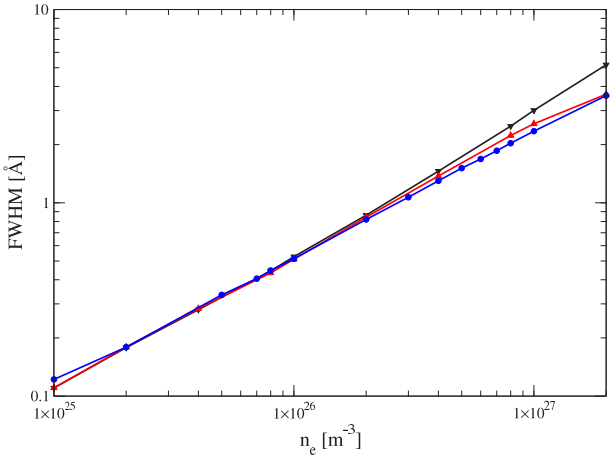

FIG. 6. (Color online) FWHM of Li^{2+} L_β line at $T = 3 \times 10^5$ K without ion dynamics. Legends are the same as in Fig. 5. Doppler broadening is included.

V. HELIUM 2 ^3S–3 ^3P

The quantum-statistical theory, originally developed for one-electron emitters, has also been extended to treat two-electron emitters; see Refs. [25,41,42]. There, an extensive comparison of the theory with measured data and results of other approaches has been given for several visible He lines. In this paper, we focus on the particular transition $2\,^3S$–$3\,^3P$, i.e., the He 3889 Å line. So far [41], the electronic self-energy had been considered only in the Born approximation within the cutoff procedure. In our calculations, we apply the effective two-particle T-matrix approach, Eq. (12), and consider strong collisions consistently. Furthermore, we take ion dynamics into account and apply the FFM from Eq. (5).

In Fig. 7, the theoretical FWHM and peak shifts of the He 3889 Å line are given as functions of the free-electron density. The results from our approach calculated in various approximations are compared to other theoretical data. In the T-matrix approach, ions are treated either quasistatically or dynamically within the FFM. Within the Born approach from Eq. (8), the inverse dielectric function consistently takes dynamical screening into account. The binary approximation ($\mathrm{Im}\,\varepsilon^{-1} \approx -\mathrm{Im}\,\varepsilon$) is also considered. Furthermore, nonquenching results are given, i.e., the sum in Eq. (8) includes only states of the same principal quantum number ($n_\alpha = n_\nu$). The different approximations were discussed in an earlier paper [41]. Our results are compared with molecular dynamics simulations [43,44] and Griem's standard theory [3]. The values for the latter are taken from Ref. [45].

The MD simulations of Gigosos *et al.* [43,44] were performed in density and temperature ranges of $n_e = (0.25\text{–}50) \times 10^{22}$ m^{-3} and $T = (2\text{–}6) \times 10^4$ K, respectively, in the nonquenching approximation for independent and interacting particles, respectively. Considering independent particles, they move along straight line trajectories at a constant speed. The correlation between the particles is considered only through the Debye-screened Coulomb interaction with the emitter. For interacting particles, all charge-charge coupling is considered. An ion-electron regularized Coulomb potential is chosen to account for quantum diffraction mechanisms in close collisions via the electron de Broglie wavelength. The correlation between perturbers tends to decrease the line broadening parameters at high electron densities [44]; see Fig. 7.

The width calculated in the T-matrix approach shows good agreement with the other theories, especially with the MD simulation data of Gigosos *et al.* [43] at high densities. The ion dynamics changes the linewidth only a little.

Compared to the MD simulation [43], the shift from the effective T-matrix approach is drastically reduced at lower densities. At $n_e = 9.8 \times 10^{22}$ m^{-3}, the shift agrees with Ref. [43]; see Fig. 7. At the highest densities, the line with the T-matrix approach is more shifted than the simulated one and reaches the nonquenching results of the Born approximation. The shift is generally overestimated in the Born approximation compared to our present results and the MD simulations. In contrast to the width, the shift is affected by the ion dynamics. Within the FFM, the shift is increased at lower densities compared to the quasistatic treatment.

In Fig. 8, we present the density dependence of the FWHM and peak shifts of the He 3889 Å line in comparison with measurements [45–52]. The Stark broadening parameters of this line are obtained by using the T-matrix approach with quasistatic ions and ion dynamics in the FFM, respectively. Furthermore, Doppler broadening is taken into account as well in Fig. 8.

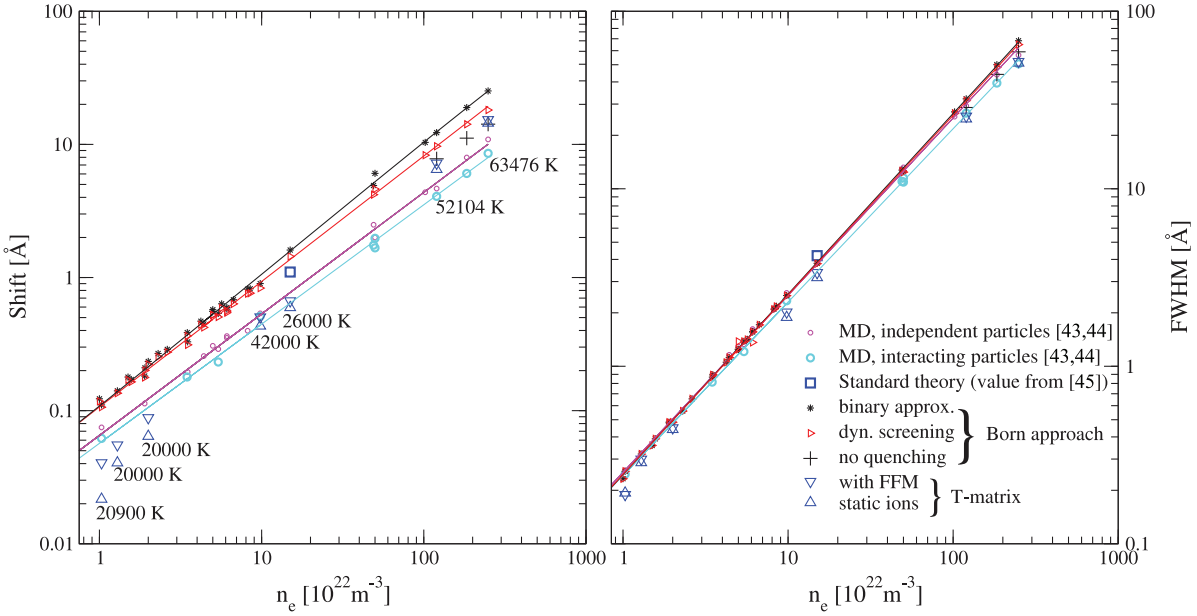

FIG. 7. (Color online) Shift and width of neutral He line 3889 Å vs electron density. The T-matrix approach with quasistatic ions and with ion dynamics in the FFM is compared to the Born approach in different approximations and to results from MD simulations [43,44] and from Griem's standard theory [3,45]. The electron temperature is given for the T-matrix data points (left).

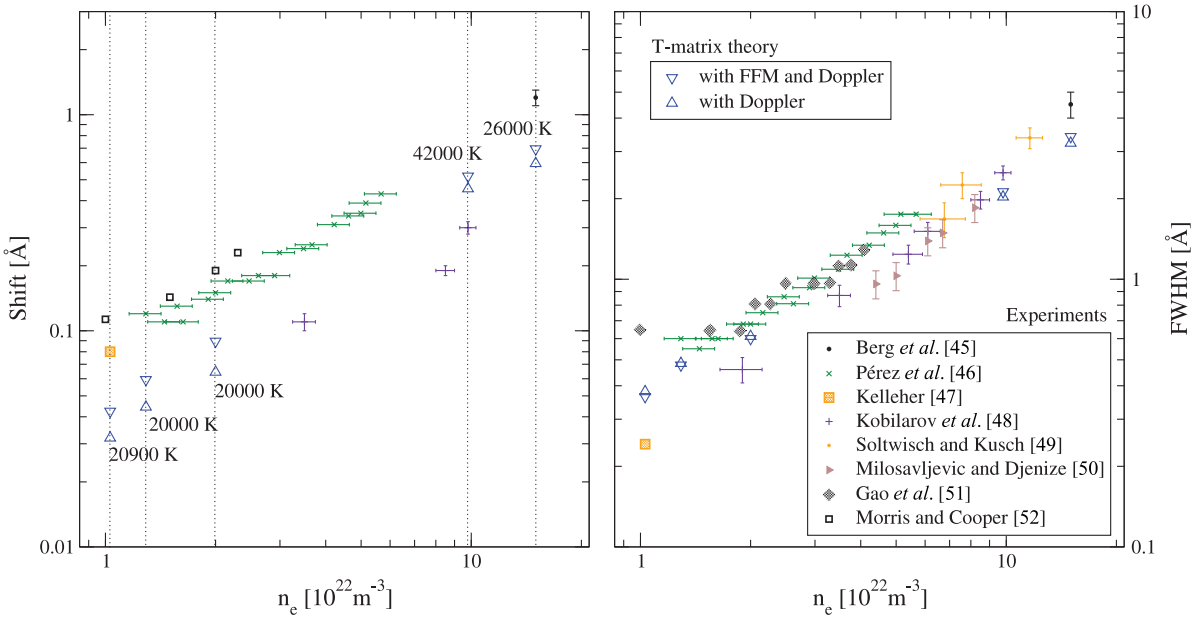

FIG. 8. (Color online) Shift and FWHM of neutral He line at 3889 Å vs electron density. The T-matrix approach with quasistatic ions and with ion dynamics in the FFM including Doppler broadening is compared to measured data [45–52].

The following experiments are included in Fig. 8: The measurement by Pérez *et al.* [46] was made in a plasma of a low-pressure pulsed arc, within the plasma density range of $n_e = (1\text{–}6) \times 10^{22}$ m^{-3} and temperature interval of $T = (0.8\text{–}3) \times 10^4$ K with a mean value of 2×10^4 K. The error bar of n_e was $\pm 10\%$, and the uncertainty in the temperature evaluation was about 20%. The experimental result of Kelleher [47] was obtained in a helium plasma generated in a wall-stabilized arc, with $n_e = 1.03 \times 10^{22}$ m^{-3} and $T_e = 2.09 \times 10^4$ K. Recently, the FWHM of the same transition line was measured by Gao *et al.* [51] from a helium arc for the density range $n_e = (0.5\text{–}4) \times 10^{22}$ m^{-3} at $T = 2.3 \times 10^4$ K. Values reported by Kobilarov *et al.* [48] from a pulsed low-pressure arc at $n_e = (2\text{–}10) \times 10^{22}$ m^{-3} and $T = (3.1\text{–}4.2) \times 10^4$ K are included. Note that the shift at the half-width is given in this case. Furthermore, values for the shift measured by Morris and Cooper [52] within the density range $n_e = (0.6\text{–}2.3) \times 10^{22}$ m^{-3} and temperature $T = (1\text{–}1.6) \times 10^4$ K are shown. The Stark parameters of this line were also measured by Berg *et al.* [45] at $n_e = 1.5 \times 10^{22}$ m^{-3} and $T = 2.6 \times 10^4$ K. The measured values by Milosavljević and Djeniže [50] at $n_e = (4.4\text{–}8.2) \times 10^{22}$ m^{-3} and at $T = (1.8\text{–}3.3) \times 10^4$ K by using a linear low-pressure pulsed arc are given as well.

In Table III, a numerical comparison of the FWHM from the T-matrix approach to the corresponding experimental data [45–48] is given. Ion dynamics (FFM) and Doppler broadening are included in the T-matrix results. Furthermore, the FWHM results from the Born approximation with dynamical screening are included as well as the result of MD simulations for interacting particles [43]. Since the ion dynamics affect the width only slightly (see Fig. 7), we can directly compare the width in the Born approximation within quasistatic ion motion with the one from our T-matrix approach. As shown in Fig. 7, the T-matrix approach always gives a smaller FWHM than the Born approximation. This trend leads to a better agreement with the experiment at the lowest density, i.e., for the FWHM of Kelleher [47]. For the data of Pérez *et al.* [46], the calculated width in the T-matrix approach with and without Doppler broadening agrees very well with the result of the Born approximation. However, the measured FWHM is higher than the calculated one; this may be due to self-absorption, as mentioned in Ref. [46]. At $n_e = 9.8 \times 10^{22}$ m^{-3}, our results in the Born approximation show a very good agreement with both measurement and MD simulation data. However, the T-matrix

TABLE III. Theoretical calculations of the FWHM of the He 3889 Å line from the T-matrix approach and the Born approximation are compared with measurements and MD simulations [43]. The FWHM is given in Å.

n_e	T_e	FWHM (Å)			
(10^{22} m^{-3})	(10^4 K)	Expt.	[43][a]	T matrix[b]	Born[c]
1.03 ± 0.12	2.1 ± 0.2	0.24[d]	0.25	0.30/0.19	0.34/0.25
1.29 ± 0.10	2.0 ± 0.2	0.6[e]		0.40/0.30	0.41/0.31
2.00 ± 0.10	2.0 ± 0.2	0.68[e]		0.53/0.45	0.55/0.47
9.8 ± 0.5	4.2	2.5 ± 0.15[f]	2.34	2.06/2.02	2.48/2.45
15.0 ± 0.8	2.6 ± 0.2	4.5 ± 0.5[g]		3.39/3.37	3.76/3.75

[a]Molecular dynamics simulations with interacting particles, without Doppler broadening.
[b]T-matrix approach (FFM ion dynamics, with/without Doppler broadening).
[c]Dynamical screening, with/without Doppler broadening.
[d]Kelleher [47].
[e]Pérez *et al.* [46].
[f]Kobilarov *et al.* [48].
[g]Berg *et al.* [45].

approach gives a lower value outside the validity range given in the experiment. At the highest measured density, the FWHM of both theories is below that of Berg *et al*. [45]. Note that the contribution of Doppler broadening to the linewidth is reduced with increasing density, i.e., with increasing Stark broadening.

VI. CONCLUSION

We use a quantum-statistical approach to calculate full line profiles of neutral emitters (H, He) and a charged H-like emitter (Li^{2+}). To go beyond the Born approximation, we apply a T-matrix approach based on scattering amplitudes for plasma pressure broadening caused by electrons. Thus, strong electron-emitter collisions are included implicitly. Scattering amplitudes are calculated within a sophisticated close-coupling scheme, taking static plasma screening into account for neutral emitters.

For H L_α, we analyze the effect of screening on the scattering amplitudes. They are reduced by screening, thus leading to narrower and less shifted lines. For the linewidth, we could verify the validity of the cutoff procedure, which is implemented in the Born approximation to compensate the overestimation of strong collisions. However, the shift is still overestimated when using the cutoff procedure adjusted to an advanced T-matrix calculation [33]. Furthermore, the line shape differs due to the dependence on the magnetic quantum number m in the effective two-particle T-matrix approach. Finally, we reconsidered the experiment of Grützmacher and Wende [19]. There, the T-matrix approach leads to a satisfying agreement with the experiment. However, the resulting linewidth depends strongly on the ion-dynamics theory considered.

For Li^{2+}, the Lyman lines were calculated for the experimental conditions of Schriever *et al*. [39]. Small differences in the details of the line shape can be found between the Born and the T-matrix approaches. However, they disappear as soon as Gaussian instrumental broadening is applied. Thus, our calculation confirms the previous analysis of Ref. [40], which was based only on the Born approach. The density dependence of the width was here studied in more detail, taking into account an estimated screening correction. The unscreened T-matrix approach generally leads to broader linewidths than the Born approach with a cutoff. The screening correction reduces the difference in the width drastically.

For the He I line at 3889 Å, the FWHM and shift are compared with results of other theories and several experiments for a broad range of densities. The shift is overestimated in the Born approximation even after adopting the cutoff procedure to account for strong electron-emitter collisions. On the other hand, underestimation can be seen for the T-matrix approach compared to the MD simulation data. However, the FWHM values from both theoretical approaches are in good agreement with each other and with the MD simulation data. Further, the effect of ion dynamics is pronounced at lower electron densities, especially for the shift of the line. The discrepancy between the measured and calculated line broadening is partially related to self-absorption [51].

Thus, we showed that the effective two-particle T-matrix approach gives the possibility to treat strong electron-emitter collisions in a consistent way. Plasma screening was treated with static Debye theory in the case of neutral emitters, and approximated in the case of charged emitters. It would be important to extend the approach to include dynamic screening. Thus, the proper treatment of the plasma screening has to be investigated in the future.

Ion dynamics has not been discussed in detail in this work. Since we have not implemented the model microfield method for He and Li^{2+} yet, we were restricted to the use of the frequency-fluctuation model. However, we note that our calculations for H in comparison to the Grützmacher-Wende profiles suggest the MMM as the better choice for ion-dynamics calculations. Hence, further investigations of ion dynamics are necessary. Furthermore, for the analysis of laser-produced plasmas, like the one presented in [39], an extension to nonequilibrium physics is crucial.

ACKNOWLEDGMENTS

We would like to thank Heidi Reinholz and Gerd Röpke for their advice, Sandrine Ferri for suggesting use of the FFM, and Joël Rosato for the discussion of correlated collisions. This work was supported by the German Research Foundation DFG within SFB 652. The support of the Australian Research Council, the Australian National Computational Infrastructure Facility, and its Western Australian node iVEC are gratefully acknowledged.

APPENDIX A: SPLITTING OF INTERNAL AND EXTERNAL PARTS OF THE SCATTERING AMPLITUDE

To handle the divergent Coulomb part of the scattering amplitude, we split the total scattering phases

$$\delta_l^{C+\mathrm{in}} = \delta_l^C + \delta_l^{\mathrm{in}}, \tag{A1}$$

into an inner part δ_l^{in} which depends on the excitation state and the atomic structure of the emitter and an outer part δ_l^C which is independent of the emitter state. For the Li^{2+} example, δ_l^C is due to the long-ranging Coulomb potential with $Z = 2$.

The scattering amplitudes for electron scattering at the initial and final emitter states are given by

$$f_i(\theta,k) = \frac{1}{2\imath k}\sum_{l=0}^{\infty}(2l+1)\left(e^{2\imath(\delta_l^C+\delta_{l,i}^{\mathrm{in}})}-1\right)P_l[\cos(\theta)], \tag{A2}$$

$$f_f(\theta,k) = \frac{1}{2\imath k}\sum_{l=0}^{\infty}(2l+1)\left(e^{2\imath(\delta_l^C+\delta_{l,f}^{\mathrm{in}})}-1\right)P_l[\cos(\theta)], \tag{A3}$$

with the Legendre polonomials $P_l[x]$.

For the forward scattering, the scattering amplitude can be constructed from its parts. Here, we neglect the k dependence for the sake of clarity. We start with the following expression:

$$\begin{aligned}\int_0^\pi d\theta\,\sin(\theta) f^C(\theta) f^{\mathrm{in}}(\theta) &= \sum_{ll'}(2l+1)(2l'+1)\left(\frac{1}{2\imath k}\right)^2\left\{\left(e^{2\imath\delta_l^C}-1\right)\left(e^{2\imath\delta_{l'}^{\mathrm{in}}}-1\right)\right\}\\ &\quad\times\int_0^\pi d\theta\,\sin(\theta)P_l[\cos(\theta)]P_{l'}[\cos(\theta)].\end{aligned} \tag{A4}$$

With two simplifications

$$\int_0^\pi d\theta \sin(\theta) P_l[\cos(\theta)] P_{l'}[\cos(\theta)] = \frac{2}{2l+1}\delta_{ll'}, \quad \text{(A5)}$$

$$\{\cdots\} = e^{2\imath(\delta_l^C+\delta_l^{\rm in})} - e^{2\imath\delta_l^C} - e^{2\imath\delta_l^{\rm in}} + 1 + (1-1)$$
$$= \left(e^{2\imath(\delta_l^C+\delta_l^{\rm in})} - 1\right) - \left(e^{2\imath\delta_l^C} - 1\right) - \left(e^{2\imath\delta_l^{\rm in}} - 1\right), \quad \text{(A6)}$$

we obtain

$$\int_0^\pi d\theta \sin(\theta) f^C(\theta) f^{\rm in}(\theta) = \frac{1}{\imath k}\{f^{\rm C+in}(0) - f^{\rm C}(0) - f^{\rm in}(0)\}. \quad \text{(A7)}$$

And thus,

$$f^{C+\rm in}(0) = f^C(0) + f^{\rm in}(0) + \imath k \int_0^\pi d\theta \sin(\theta) f^C(\theta) f^{\rm in}(\theta), \quad \text{(A8)}$$

and analogously, for the complex conjugate

$$f^{C+\rm in*}(0) = f^{C*}(0) + f^{\rm in*}(0) - \imath k \int_0^\pi d\theta \sin(\theta) f^{C^*}(\theta) f^{\rm in*}(\theta). \quad \text{(A9)}$$

However, for the coupling term, we need the full θ dependence of $f_i(\theta,k)$ and $f_f(\theta,k)$. In the vertex term, we have (again dropping the k dependence)

$$\imath \int_0^\pi d\theta \sin(\theta) f_i^*(\theta) f_f(\theta) = \imath \int_0^\pi d\theta \sin(\theta) \left\{ \frac{-1}{2\imath k} \sum_{l=0}^\infty (2l+1)\left(e^{-2\imath(\delta_l^C+\delta_{l,i}^{\rm in})} - 1\right) P_l[\cos(\theta)] \right.$$
$$\left. \times \frac{1}{2\imath k} \sum_{l'=0}^\infty (2l'+1)\left(e^{2\imath(\delta_{l'}^C+\delta_{l',f}^{\rm in})} - 1\right) P_{l'}[\cos(\theta)] \right\}. \quad \text{(A10)}$$

Using again the orthogonality of Legendre polynomials, we obtain

$$\imath \int_0^\pi d\theta \sin(\theta) f_i^*(\theta) f_f(\theta) = \frac{\imath}{2k^2} \sum_{l=0}^\infty (2l+1)\left\{\left(e^{-2\imath(\delta_l^C+\delta_{l,i}^{\rm in})} - 1\right)\left(e^{2\imath(\delta_l^C+\delta_{l,f}^{\rm in})} - 1\right)\right\}. \quad \text{(A11)}$$

The coupling term of the inner structure alone is given by

$$\imath \int_0^\pi d\theta \sin(\theta) f_i^{\rm in*}(\theta) f_f^{\rm in}(\theta) = \imath \int_0^\pi d\theta \sin(\theta) \left\{ \frac{-1}{2\imath k} \sum_{l=0}^\infty (2l+1)\left(e^{-2\imath(\delta_{l,i}^{\rm in})} - 1\right) P_l[\cos(\theta)] \right.$$
$$\left. \times \frac{1}{2\imath k} \sum_{l'=0}^\infty (2l'+1)\left(e^{2\imath(\delta_{l',f}^{\rm in})} - 1\right) P_{l'}[\cos(\theta)] \right\} \quad \text{(A12)}$$

$$= \frac{\imath}{2k^2} \sum_{l=0}^\infty (2l+1)\left\{e^{2\imath(\delta_{l,f}^{\rm in}-\delta_{l,i}^{\rm in})} - e^{2\imath\delta_{l,f}^{\rm in}} - e^{-2\imath\delta_{l,i}^{\rm in}} + 1\right\}. \quad \text{(A13)}$$

Expanding the term in the braces in Eq. (A11) and adding missing terms to obtain the inner coupling term, we obtain for the full coupling term

$$\imath \int_0^\pi d\theta \sin(\theta) f_i^*(\theta) f_f(\theta) = \imath \int_0^\pi d\theta \sin(\theta) f_i^{\rm in*}(\theta) f_f^{\rm in}(\theta) + \frac{\imath}{2k^2} \sum_{l=0}^\infty (2l+1)\left\{ - e^{2\imath(-\delta_l^C-\delta_{l,i}^{\rm in})} - e^{2\imath(\delta_l^C+\delta_{l,f}^{\rm in})} + e^{2\imath\delta_{l,f}^{\rm in}} + e^{-2\imath\delta_{l,f}^{\rm in}} \right\}. \quad \text{(A14)}$$

The first term is the vertex term for the inner structure alone, the second term can be rearranged as

$$\frac{\imath}{2k^2} \sum_{l=0}^\infty (2l+1)\left\{ - e^{2\imath(-\delta_l^C-\delta_{l,i}^{\rm in})} - e^{2\imath(\delta_l^C+\delta_{l,f}^{\rm in})} - e^{2\imath\delta_{l,f}^{\rm in}} - e^{-2\imath\delta_{l,f}^{\rm in}} \right\} \quad \text{(A15)}$$

$$= -\frac{\imath}{2k^2} \sum_{l=0}^\infty (2l+1)\left\{\left(e^{2\imath\delta_{l,f}^{\rm in}} - 1 + 1\right)\left(e^{2\imath(\delta_l^C)} - 1\right) + \left(e^{-2\imath\delta_{l,f}^{\rm in}} - 1 + 1\right)\left(e^{-2\imath(\delta_l^C)} - 1\right)\right\} \quad \text{(A16)}$$

$$= \frac{\imath}{4\imath^2k^2} \sum_{ll'} (2l+1)(2l'+1)\left\{\left(e^{2\imath\delta_{l',f}^{\rm in}} - 1\right)\left(e^{2\imath(\delta_l^C)} - 1\right) + \left(e^{-2\imath\delta_{l',f}^{\rm in}} - 1\right)\left(e^{-2\imath(\delta_l^C)} - 1\right)\right\}$$
$$\times \int_0^\pi d\theta \sin(\theta) P_l[\cos(\theta)] P_{l'}[\cos(\theta)] + \frac{1}{k} f^C(0) - \frac{1}{k} f^{C*}(0) \quad \text{(A17)}$$

$$= \imath \int_0^\pi d\theta \sin(\theta)\left\{f_f^{\rm in}(\theta) f^C(\theta) + f_i^{\rm in*}(\theta) f^{C*}(\theta)\right\} + \frac{1}{k} f^C(0) - \frac{1}{k} f^{C*}(0). \quad \text{(A18)}$$

With this expression, we can consider the full line profile operator as in Eq. (3). With the electronic contributions to the self-energy Eq. (12) and the coupling term Eq. (13) we have

$$L(\Delta\omega,E) = \Delta\omega - \mathrm{Re}[\Sigma_i - \Sigma_f] + \imath\,\mathrm{Im}[\Sigma_i + \Sigma_f] + \Gamma_{ii'ff'} \tag{A19}$$

$$= \Delta\omega + \Sigma_f - \Sigma_i^* + \Gamma_{ii'ff'} \tag{A20}$$

$$= \Delta\omega + A\Bigg(f_f^{C+\mathrm{in}}(0,k) - f_i^{C+\mathrm{in}*}(0,k) - \imath k\int_0^\pi d\theta\,\sin(\theta) f_i^{C+\mathrm{in}*}(\theta) f_f^{C+\mathrm{in}}(\theta)\Bigg). \tag{A21}$$

Here, the function $A(x(k))$ was introduced consisting of the prefactor and the k integration,

$$A(x(k)) = -\frac{2}{\pi} n_e \Lambda_{\mathrm{th}}^3 \int_0^\infty dk\, k^2 e^{-k^2/k_B T} x(k). \tag{A22}$$

The argument of this function is

$$x(k) = f_f^{C+\mathrm{in}}(0,k) - f_i^{C+\mathrm{in}*}(0,k) - \imath k\int_0^\pi d\theta\,\sin(\theta) f_i^{C+\mathrm{in}*}(\theta) f_f^{C+\mathrm{in}}(\theta). \tag{A23}$$

Using Eqs. (A8), (A9), and (A18), we obtain

$$x(k) = f_f^{\mathrm{in}}(0) - f_i^{\mathrm{in}*}(0) - \imath k\int_0^\pi d\theta\,\sin(\theta) f_f^{\mathrm{in}}(\theta) f_i^{\mathrm{in}*}(\theta). \tag{A24}$$

This is exactly the result one would obtain by neglecting δ_C. Thus, the divergent Coulomb terms in the self-energies are canceled by the ones in the coupling term and it is legitimate to neglect them in the calculation.

APPENDIX B: ESTIMATION OF ERROR MADE BY NEGLECTING SCREENING IN e-Li^{2+} SCATTERING

Following the reasoning in Appendix A, the fact that the long-range ($Z = 2$) potential is screened does not change the line shape when considering binary collisions. However, the screening within the atom and the resulting change of the inner structure do affect the scattering process and, thus, the line shape. To obtain a measure for the change of the inner structure, we consider first the Debye shift [53] relative to the energy of a level with quantum number n,

$$X(D,n,Z) = \frac{\Delta E}{E_n} = \frac{\frac{2Z}{D}}{\frac{Z^2}{n^2}} = \frac{2n^2}{ZD}. \tag{B1}$$

TABLE IV. Relative change in % of electronic width and shift from the unscreened to the screened calculation of H($2p$, $m = \pm1$) with coupling to H($1s$) for different temperatures.

	$D = 314a_0$, $X = 2.55\%$					$D = 44a_0$, $X = 18.2\%$				
k_BT (eV)	1	2	10	20	26	1	2	10	20	26
Width	−11	−9.3	−5.5	−3.7	−3.0	−58	−52	−35	−28	−25
Shift	−22	−16	−5.8	−3.9	−3.5	−63	−62	−47	−41	−40

TABLE V. Relative Debye shift X and relative error estimates in % for the electronic contribution to the shift and width of the Lyman lines of Li^{2+} at $T = 3\times10^5$ K, as shown in Fig. 4.

	$D = 113a_0$			$D = 35a_0$		
	L_α	L_β	L_γ	L_α	L_β	L_γ
X (%)	2.4	5.3	9.4	7.6	17.1	30.5
Width	−3	−7	−13	−10	−24	−42
Shift	−4	−10	−20	−15	−37	−67

This gives us a connection between our hydrogen calculations ($Z = 1$) and any H-like emitter. We calculated the H L_α line with unscreened and screened scattering amplitudes ($D = \infty$, $D = 314a_0$, $D = 44a_0$). In Table IV, we compare the relative change of width and shift of the central component of the L_α line for several temperatures. It can be seen that the effect decreases with temperature. This can be understood from Fig. 1, which shows that screening changes the scattering amplitudes especially for small k values. Higher temperatures shift the Boltzmann distribution in Eqs. (12) and (13) to higher k values and thus to regions which are less affected by the screening. We include the values for $T = 3\times10^5$ K, i.e., for 26 eV as this is the temperature in our Li^{2+} example.

For $D = 314a_0$ and $D = 44a_0$, the relative Debye shifts of the $n = 2$ level are $X(314,2,1) = 2.55\%$ and $X(44,2,1) = 18.2\%$, respectively. The X values for the Li^{2+} Lyman lines from Fig. 4 are given in Table V together with an estimate of the relative correction due to screening in the scattering process. The estimate is based on the assumption that the effect on the electronic part of the line shape is similar for the same value of X for different emitters at a certain temperature, using an interpolation linear in X.

In Fig. 9, the screening correction is shown for Li^{2+} L_α, L_β, and L_γ lines for a broad density range.

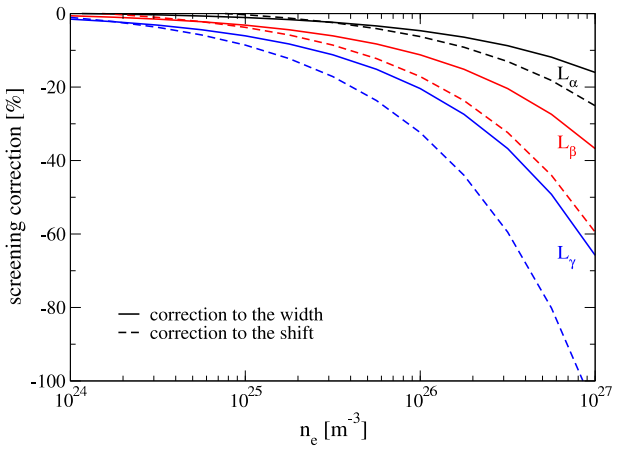

FIG. 9. (Color online) Relative correction to the electronic width and shift of Lyman lines of Li^{2+} due to screening. Calculated for $T = 3\times10^5$ K.

[1] H. R. Griem, *Principles of Plasma Spectroscopy* (Cambridge University Press, Cambridge, 1997).
[2] M. Baranger, Phys. Rev. **112**, 855 (1958).
[3] H. R. Griem, *Spectral Line Broadening by Plasmas* (Academic Press, London, 1974).
[4] S. Sahal-Brechot, Astron. Astrophys. **1**, 91 (1969); **2**, 322 (1969).
[5] R. Stamm and D. Voslamber, J. Quant. Spectrosc. Radiat. Transfer **22**, 599 (1979).
[6] L. Hitzschke, G. Röpke, T. Seifert, and R. Zimmermann, J. Phys. B **19**, 2443 (1986).
[7] S. Günter, Habilitation thesis, Rostock University, Germany, 1995.
[8] S. Sorge, A. Wierling, G. Röpke, W. Theobald, R. Sauerbrey, and T. Wilhein, J. Phys. B **33**, 2983 (2000).
[9] S. Alexiou and A. Poquerusse, Phys. Rev. E **72**, 046404 (2005).
[10] S. Lorenzen, A. Wierling, H. Reinholz, and G. Röpke, Contrib. Plasma Phys. **51**, 349 (2011).
[11] M. C. Zammit, D. V. Fursa, and I. Bray, Phys. Rev. A **82**, 052705 (2010).
[12] M. C. Zammit, D. V. Fursa, I. Bray, and R. K. Janev, Phys. Rev. A **84**, 052705 (2011).
[13] K. Unnikrishnan and J. Callaway, Phys. Rev. A **43**, 3619 (1991).
[14] I. Bray and A. T. Stelbovics, Phys. Rev. A **46**, 6995 (1992).
[15] I. Bray and D. V. Fursa, J. Phys. B **44**, 061001 (2011).
[16] I. Bray, D. V. Fursa, A. S. Kadyrov, A. T. Stelbovics, A. S. Kheifets, and A. M. Mukhamedzhanov, Phys. Rep. **520**, 135 (2012).
[17] A. Calisti, C. Mossé, S. Ferri, B. Talin, F. Rosmej, L. A. Bureyeva, and V. S. Lisitsa, Phys. Rev. E **81**, 016406 (2010).
[18] E. Stambulchik, High Energy Density Phys. **9**, 528 (2013).
[19] K. Grützmacher and B. Wende, Phys. Rev. A **16**, 243 (1977).
[20] C. F. Hooper, Jr., Phys. Rev. **165**, 215 (1968); **169**, 193 (1968).
[21] A. Y. Potekhin, G. Chabrier, and D. Gilles, Phys. Rev. E **65**, 036412 (2002).
[22] C. A. Iglesias, Phys. Rev. A **27**, 2705 (1983).
[23] L. D. Landau and E. M. Lifschitz, *Quantum Mechanics: Non-Relativistic Theory* (Pergamon Press, Oxford, 1977).
[24] D. R. Bates and A. Damgaard, Philos. Trans. R. Soc., A **242**, 101 (1949).
[25] B. Omar, S. Günter, A. Wierling, and G. Röpke, Phys. Rev. E **73**, 056405 (2006).
[26] J. Halenka, Z. Phys. D **16**, 1 (1990).
[27] A. V. Demura, Int. J. Spectrosc **2010**, 671073 (2010).
[28] A. Brissaud and U. Frisch, J. Quant. Spectrosc. Radiat. Transfer **11**, 1767 (1971).
[29] J. Seidel, Z. Naturforsch. **32a**, 1195 (1977); **35a**, 679 (1980).
[30] S. Lorenzen, Contrib. Plasma Phys. **53**, 368 (2013).
[31] J. Rosato, H. Capes, and R. Stamm, Phys. Rev. E **86**, 046407 (2012).
[32] J. Rosato, H. Capes, and R. Stamm, High Energy Density Phys. **9**, 484 (2013).
[33] S. Günter, Phys. Rev. E **48**, 500 (1993).
[34] H. R. Griem, M. Baranger, A. C. Kolb, and G. Oertel, Phys. Rev. **125**, 177 (1962).
[35] S. Lorenzen, A. Wierling, H. Reinholz, G. Röpke, M. C. Zammit, D. V. Fursa, and I. Bray, in *Proceedings of the 20th International Conference on Spectral Line Shapes*, edited by J. Lewis and A. Predoi-Cross, AIP Conf. Proc. No. 1290 (AIP, New York, 2010), p. 99; J. Phys.: Conf. Ser. **397**, 012021 (2012).
[36] T. O'Malley, L. Spruch, and L. Rosenberg, J. Math. Phys. **2**, 491 (1961).
[37] R. W. Lee, J. Phys. B **11**, L167 (1978).
[38] J. Halenka and W. Olchawa, J. Quant. Spectrosc. Radiat. Transfer **56**, 17 (1996).
[39] G. Schriever, K. Bergmann, and R. Lebert, J. Appl. Phys. **83**, 4566 (1998).
[40] S. Lorenzen, A. Wierling, H. Reinholz, and G. Röpke, Contrib. Plasma Phys. **48**, 657 (2008).
[41] B. Omar, Int. J. Spectrosc. **2010**, 983578 (2010).
[42] B. Omar, A. Wierling, H. Reinholz, and G. Röpke, Phys. Rev. Res. Int. **3**, 218 (2013).
[43] M. A. Gigosos, M. A. Gonzalez, V. Talin, and A. Calisiti (unpublished).
[44] M. A. Gigosos, M. A. Gonzalez, V. Talin, and A. Calisiti, in *Proceedings of the 17th International Conference on Spectral Line Shapes*, edited by E. Dalimier (Frontier Group, Paris, 2004), p. 451.
[45] H. F. Berg, A. W. Ali, R. Lincke, and H. R. Griem, Phys. Rev. **125**, 199 (1962).
[46] C. Pérez, R. Santamarta, M. I. de la Rosa, and S. Mar, Eur. Phys. J. D **27**, 73 (2003).
[47] D. E. Kelleher, J. Quant. Spectrosc. Radiat. Transfer **25**, 191 (1981).
[48] R. Kobilarov, N. Konjević, and M. V. Popović, Phys. Rev. A **40**, 3871 (1989).
[49] H. Soltwisch and H. J. Kusch, Z. Naturforsch. **34a**, 300 (1979).
[50] V. Milosavljević and S. Djeniže, New Astron. **7**, 543 (2002).
[51] H. M. Gao, S. L. Ma, C. M. Xu, and L. Wu, Eur. Phys. J. D **47**, 191 (2008).
[52] R. N. Morris and J. Cooper, Can. J. Phys. **51**, 1746 (1973).
[53] H. R. Griem, Phys. Rev. **128**, 997 (1962).

A. Appendix

A.1. About binary and correlated collisions

In the evaluation of the self-energy due to electronic perturbers in Sec. 1.3.3, we assume $\Delta\omega = 0$. This corresponds to the binary collision approximation, i.e. multiple simultaneous collisions are neglected [54]. However, since we include static screening, our approximation does not correspond to the "usual" binary collision approximation. Rosato *et al.* [59, 60] discussed the importance of correlated, i.e. non-binary, collisions to extend the unified theory (UTPP). There, an approximation to the validity range of the binary approximation is derived which can be applied for our calculations as well. As long as the dimensionless parameter

$$h = n_e b_{\mathrm{W}}^2 \lambda_{\mathrm{D}} \ln\left(\frac{\lambda_{\mathrm{D}}}{b_{\mathrm{W}}}\right) , \tag{A.1}$$

is smaller than 0.2, correlated collisions are rare. For a hydrogen-like emitter in state n, the Weisskopf radius b_{W} can be approximated by [103]

$$b_{\mathrm{W}} = \frac{\hbar n^2}{m_e v_{\mathrm{therm}}} . \tag{A.2}$$

Furthermore, the importance of simultaneous strong collisions is estimated with the dimensionless parameter $g = n_e b_{\mathrm{W}}^3$ for details see again [59, 60]. In Fig. A.1, the density-temperature plane is divided into regions, where our approximation can either be applied ($h < 0.2$, $g < 0.2$) or not for different main quantum numbers of the upper level, i.e. for the different spectral lines. All Lyman-α lines discussed in this thesis fall within the region, where correlated collisions can be neglected, i.e. the assumption $\Delta\omega = 0$ is justified. After the publication of paper 1 [10], we realized the importance of correlated collisions for Lyman-β and Lyman-γ. Thus, the considered parameter range was adjusted for paper 6 [15], since the binary approximation can so far not be avoided within our T-matrix approach. For the Born approximation, the full ω-dependence can be evaluated, see the following example.

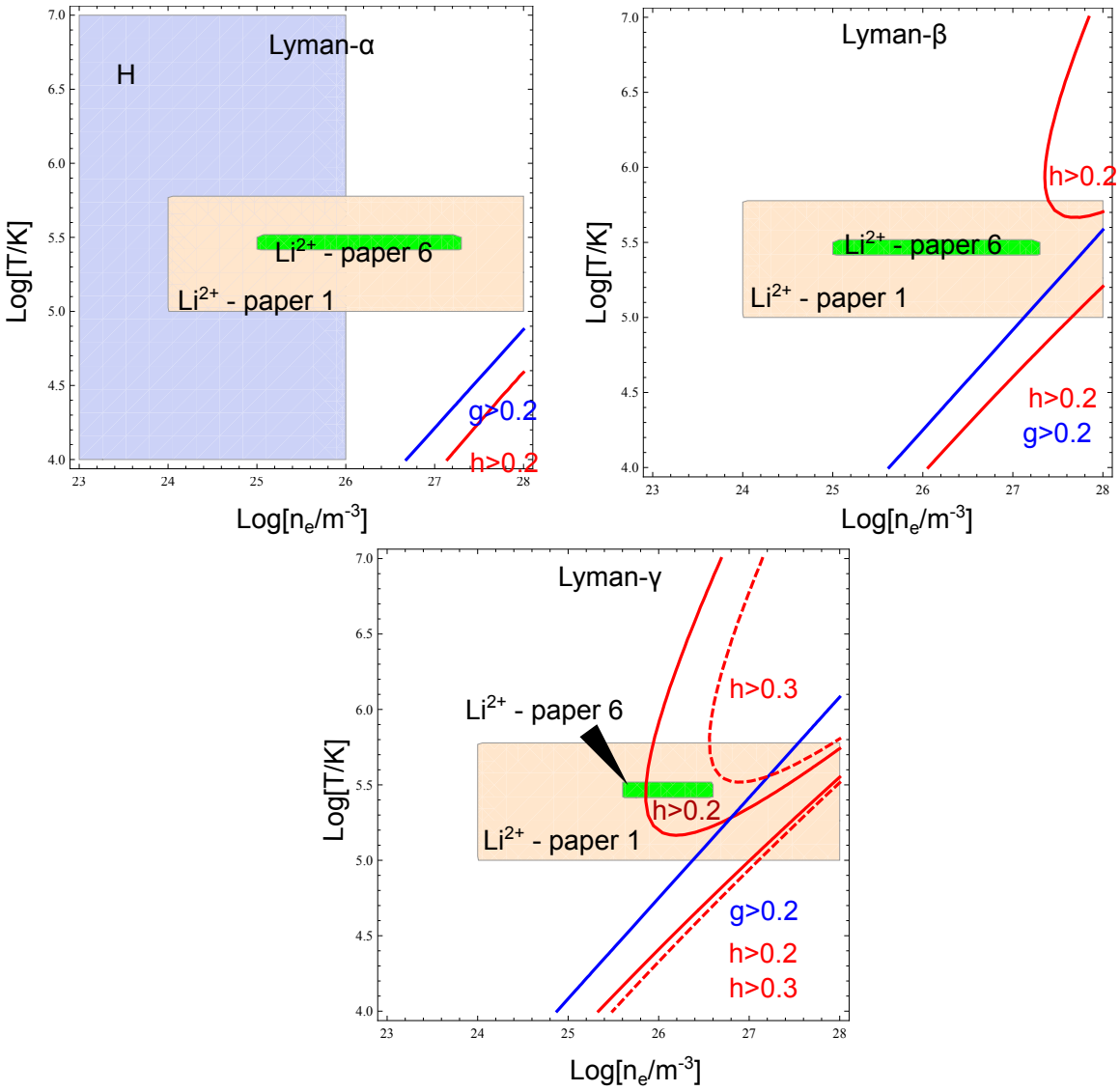

Figure A.1.: Validity range of the binary collision approximation for electronic perturbers via the parameters h for correlated collisions and g for strong simultaneous collisions. While correlated collisions are unproblematic for Lyman-α-lines, their influence on the line shape is expected to get more important for Lyman-β and Lyman-γ.

If we now consider a model system, where perturbing electrons are not interacting with each other but only with the emitter, we have a system where correlated collisions become important because weak collisions are not screened but take place simultaneously (non-binary collisions). This has been discussed as a test case on

SLSP2[1] in connection with the necessary box-size for MD simulations for H Lyman-α, see [104]. The box-size dependence is transfered into a lower-momentum cut-off $k_{\min} = 1/R$ in the quantum-statistical Born approximation. Hence, weak, i.e. distant collisions are neglected. Since the cut-off of strong collisions $k_{\max}$ has been adjusted for the case with Debye screening [89]. Since $k_{\max}$ is not adjusted for the unscreened calculation, we use it as a free parameter there.

In Fig. A.2, the box-size dependence is shown for electron broadening of H Lyman-α at $k_{\mathrm{B}}T = 100\ eV$ and $n_e = 10^{23}\ \mathrm{m}^{-3}$. While the line width from the calculation with screening converges for a box-size with radius R_0, the unscreened version does not converge at all when correlated collisions are neglected ($\Delta\omega = 0$). As soon as we include the ω-dependence, the transfer momentum integration converges for $R = 2^{10}R_0$, which is in accordance with the UTPP calculation [104].

In Fig. A.2, we compare furthermore results that are based on a pure dipole approximation with those that use the more general definition of the matrix element $M(\mathbf{k})$, Eq. (1.62). As the dipole-approximation is justified for small k-values, see Appendix A.5, this only leads to a difference when the integration in Eq. (1.101) includes large k-values, i.e. for large $k_{\max}$.

A.2. Formal connection between dipole-dipole and current-current correlation functions

The dipole moment of the emitter with eigenstates ψ_a and ψ_b is given by

$$\mathbf{d}_{ab} = \langle\psi_a|\mathbf{d}|\psi_b\rangle = -e\langle\psi_a|\mathbf{r}|\psi_b\rangle\,. \tag{A.3}$$

With the help of the time-independent Schrödinger equation

$$H_0|\psi_a\rangle = E_a|\psi_a\rangle\,, \tag{A.4}$$

where $H_0 = \frac{\hbar^2\mathbf{p}^2}{2m_e} + V(\mathbf{r})$ and the commutator

$$\langle\psi_a|\,[H_0, \mathbf{r}]\,|\psi_b\rangle = \langle\psi_a|H_0\mathbf{r} - \mathbf{r}H_0|\psi_b\rangle \tag{A.5}$$

$$= (E_a - E_b)\langle\psi_a|\mathbf{r}|\psi_b\rangle\,, \tag{A.6}$$

[1] Spectral line shapes in plasmas code comparison workshop 2, Vienna 2013

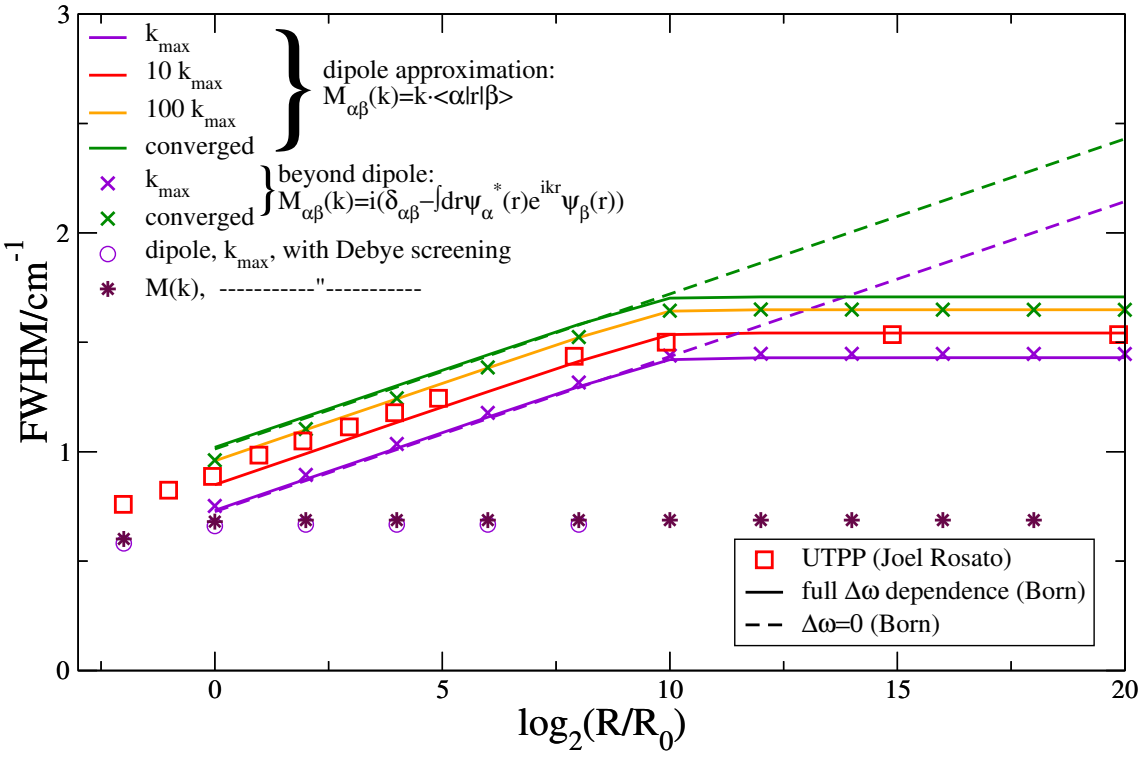

Figure A.2.: Estimation of the box-size dependence for electron broadening of H Lyman-α at $k_\mathrm{B}T = 100\ eV$ and $n_e = 10^{23}\ \mathrm{m}^{-3}$: R_0 corresponds to a spherical MD simulation with 8000 particles. The radius R corresponds to a cut-off of weak collisions $k_\mathrm{min} = 1/R$. Only virtual $\Delta n = 0$ transitions are taken into account in the Born approximation. Given is a comparison of UTPP [104] and our Born approximation with and without correlated collisions ($\Delta\omega = 0$), with and without Debye screening. The cut-off for strong collisions k_max has been adjusted for the screened Born calculation. In the calculation without screening, it is used as a free parameter. Note, FWHM is given in the wavenumber domain here, i.e. in cm^{-1}.

we obtain the relation

$$\langle\psi_a|\mathbf{r}|\psi_b\rangle = \frac{1}{E_a - E_b}\langle\psi_a|\left[H_0, \mathbf{r}\right]|\psi_b\rangle\,. \tag{A.7}$$

Since $V(\mathbf{r})$ commutes with $\mathbf{r}$, we have only to consider

$$\langle\psi_a|\left[\hbar^2\mathbf{p}^2, \mathbf{r}\right]|\psi_b\rangle\,. \tag{A.8}$$

Since $\mathbf{p} = -\imath\hbar\nabla_r$, we have

$$\langle\psi_a|\left[\hbar^2\mathbf{p}^2, \mathbf{r}\right]|\psi_b\rangle = -\hbar^2\langle\psi_a|\left[\nabla_r^2, \mathbf{r}\right]|\psi_b\rangle \tag{A.9}$$

$$= -\hbar^2\langle\psi_a|\,\nabla_r^2\,\mathbf{r} - \mathbf{r}\,\nabla_r^2\,|\psi_b\rangle \tag{A.10}$$

$$= -\hbar^2\langle\psi_a|2\,\nabla_r\,|\psi_b\rangle \tag{A.11}$$

$$= \frac{2\hbar^2}{\imath}\langle\psi_a|\mathbf{p}|\psi_b\rangle\,. \tag{A.12}$$

Thus follows,

$$\langle\psi_a|\mathbf{r}|\psi_b\rangle = \frac{1}{E_a - E_b}\langle\psi_a|\left[H_0, \mathbf{r}\right]|\psi_b\rangle \tag{A.13}$$

$$= -\frac{\imath\hbar}{m_e\omega_{ab}}\langle\psi_a|\mathbf{p}|\psi_b\rangle\,, \tag{A.14}$$

where we used $\omega_{ab} = (E_a - E_b)/\hbar$. With this relation, the dipole moment can be expressed as

$$\mathbf{d}_{ab} = -e\langle\psi_a|\mathbf{r}|\psi_b\rangle \tag{A.15}$$

$$= \frac{\imath e\hbar}{m_e\omega_{ab}}\langle\psi_a|\mathbf{p}|\psi_b\rangle \tag{A.16}$$

$$= \frac{\imath e\hbar}{m_e\omega_{ab}}\mathbf{p}_{ab}\,. \tag{A.17}$$

In order to calculate the dipole-dipole correlation function, the momentum distribution n_p has to be considered as well, i.e. the probability for a certain state with momentum $\hbar\mathbf{p}$.

$$\langle\mathbf{d}_{ab};\mathbf{d}_{ab}\rangle = \langle\frac{1}{\Omega}\sum_p n_p\frac{\imath e\hbar}{m_e\omega_{ab}}\mathbf{p}_{ab};\frac{1}{\Omega}\sum_{p'} n_{p'}\frac{\imath e\hbar}{m_e\omega_{ab}}\mathbf{p'}_{ab}\rangle \tag{A.18}$$

$$= -\frac{1}{\Omega^2}\sum_{pp'}\frac{e^2\hbar^2}{m_e^2\omega_{ab^2}}\mathbf{p}_{ab}\cdot\mathbf{p}'_{ab}\langle n_p; n_{p'}\rangle\,. \tag{A.19}$$

Using the definition of the current density, Eq. (1.31), we can establish a connection between dipole-dipole correlation and the correlation of the current density

$$\langle\mathbf{d}_{ab};\mathbf{d}_{ab}\rangle = -\frac{1}{\omega_{ab}^2}\langle\mathbf{j}_{ab};\mathbf{j}_{ab}\rangle\,. \tag{A.20}$$

Here, we did so far not consider the dependence on the transfer momentum $\hbar k$, since at the end we are interested in the long wavelength limit $\mathbf{k} \to 0$.

A.3. Correlation functions via Kubo scalar products

The correlation functions are used in Sec. 1.3.1. They are given via the Kubo scalar product [65]

$$\langle A;B\rangle_z = \int_0^\infty \mathrm{d}t e^{\imath z t}(A(t);B)\,, \tag{A.21}$$

with

$$(A;B) = (A^\dagger;B^\dagger) = \frac{1}{\beta}\int_0^\beta \mathrm{d}\tau \mathrm{Tr}\left(A(-\imath\hbar\tau)B^\dagger\rho_0\right). \tag{A.22}$$

Here, A and B are operators in the Heisenberg picture and ρ_0 is the statistical operator of the system in equilibrium. These products can also be expressed by Green's functions [67, 68]

$$\langle A;B\rangle_z = \frac{\imath}{\beta}\int_{-\infty}^\infty \frac{\mathrm{d}\omega}{\pi}\frac{1}{z-\omega}\frac{1}{\omega}\mathrm{Im}\,G_{AB^\dagger}(\omega+\imath\delta)\,, \tag{A.23}$$

$$(A;B) = \frac{1}{\beta}\int_{-\infty}^\infty \frac{\mathrm{d}\omega}{\pi}\frac{1}{\omega}\mathrm{Im}\,G_{AB^\dagger}(\omega+\imath\delta)\,, \tag{A.24}$$

The thermodynamic Green's function $G_{AB^\dagger}(\omega+\imath\delta)$ can be calculated with the help of Feynman diagramms.

A.4. Matsubara summation: undressed and dressed case

The method to sum over Matsubara-frequencies is described in e.g. Ref. [69]. In the undressed case, Eq. (1.42), the summation can be carried out

$$\begin{aligned}
&\sum_{\omega_\lambda}\frac{1}{\hbar\omega_\lambda+\hbar\omega_\mu-\epsilon_{n\mathbf{P}}}\frac{1}{\hbar\omega_\lambda-\epsilon_{n'\mathbf{P}-\mathbf{k}}}\\
&\quad=\sum_{\omega_\lambda}\frac{1}{E_{n'\mathbf{P}-\mathbf{k}}-E_{n\mathbf{P}}+\hbar\omega_\mu}\left(\frac{1}{\hbar\omega_\lambda-\epsilon_{n'\mathbf{P}-\mathbf{k}}}-\frac{1}{\hbar\omega_\lambda-\epsilon_{n\mathbf{P}}+\hbar\omega_\mu}\right) &\text{(A.25)}\\
&\quad=\frac{\beta}{E_{n'\mathbf{P}-\mathbf{k}}-E_{n\mathbf{P}}+\hbar\omega_\mu}\left(g(\epsilon_{n'\mathbf{P}-\mathbf{k}})-g(\epsilon_{n\mathbf{P}}-\hbar\omega_\mu)\right) &\text{(A.26)}\\
&\quad=\frac{\beta}{E_{n'\mathbf{P}-\mathbf{k}}-E_{n\mathbf{P}}+\hbar\omega_\mu}\left(g(\epsilon_{n'\mathbf{P}-\mathbf{k}})-g(\epsilon_{n\mathbf{P}})\right)\,, &\text{(A.27)}
\end{aligned}$$

leading to Bose functions $g(x)$. The denominator depends only on $E_{n\mathbf{P}}$ instead of $\epsilon_{n\mathbf{P}}$ because the chemical potential μ_{ei} is identical in $\epsilon_{n\mathbf{P}}$ and $\epsilon_{n'\mathbf{P}-\mathbf{k}}$.

The central term in the dressed case, Eq. (1.67), is given by

$$\begin{aligned}
&\frac{1}{\beta}\sum_{\omega_\lambda} G_2(n,\mathbf{P},\omega_\mu+\omega_\lambda)G_2(n',\mathbf{P}',\omega_\lambda)\\
&\quad=\frac{\hbar^2}{\beta}\sum_{\omega_\lambda}\int_{-\infty}^{\infty}\frac{\mathrm{d}\omega_1}{2\pi}\int_{-\infty}^{\infty}\frac{\mathrm{d}\omega_2}{2\pi}\frac{A(n,\mathbf{P},\omega_1)}{\hbar(\omega_1-\omega_\mu-\omega_\lambda)}\frac{A(n',\mathbf{P}',\omega_2)}{\hbar(\omega_2-\omega_\lambda)} && \text{(A.28)}\\
&\quad=\frac{\hbar^2}{\beta}\sum_{\omega_\lambda}\int_{-\infty}^{\infty}\frac{\mathrm{d}\omega_1}{2\pi}\int_{-\infty}^{\infty}\frac{\mathrm{d}\omega_2}{2\pi}\frac{A(n,\mathbf{P},\omega_1)A(n',\mathbf{P}',\omega_2)}{\hbar(\omega_\mu-\omega_1+\omega_2)}\left(\frac{1}{\hbar(\omega_1-\omega_\mu-\omega_\lambda)}-\frac{1}{\hbar(\omega_2-\omega_\lambda)})\right) && \text{(A.29)}\\
&\quad=\hbar^2\int_{-\infty}^{\infty}\frac{\mathrm{d}\omega_1}{2\pi}\int_{-\infty}^{\infty}\frac{\mathrm{d}\omega_2}{2\pi}\frac{A(n,\mathbf{P},\omega_1)A(n',\mathbf{P}',\omega_2)}{\hbar(\omega_\mu-\omega_1+\omega_2)}\left(g(\hbar\omega_1)-g(\hbar\omega_2)\right)\,. && \text{(A.30)}
\end{aligned}$$

A.5. Matrix element $M(\mathbf{k})$

The matrix element, see Eq. (1.62), is given by

$$\begin{aligned}
M^0_{nn'}(\mathbf{k}) =& \imath\int\frac{d\mathbf{p}}{(2\pi)^3}\Big[Z\Psi^*_n(\mathbf{p}+\frac{m_e}{2M}\mathbf{k})\Psi_{n'}(\mathbf{p}-\frac{m_e}{2M}\mathbf{k})\\
&-\Psi^*_n(\mathbf{p}-\frac{m_i}{2M}\mathbf{k})\Psi_{n'}(\mathbf{p}+\frac{m_i}{2M}\mathbf{k})\Big] && \text{(A.31)}\\
=& \imath\int\frac{d\mathbf{p}}{(2\pi)^3}\Psi^*_n(\mathbf{p})\left[Z\Psi_{n'}(\mathbf{p}-\frac{m_e}{M}\mathbf{k})-\Psi_{n'}(\mathbf{p}+\frac{m_i}{M}\mathbf{k})\right]\,. && \text{(A.32)}
\end{aligned}$$

After neglecting the electron mass in comparison to the ion mass, the matrix elements are given by atomic wave functions in the following way

$$M^{(0)}_{n\alpha}(\mathbf{k}) = \imath\int\frac{d\mathbf{p}}{(2\pi)^3}\Psi^*_n(\mathbf{p})\left[Z\Psi_\alpha(\mathbf{p})-\Psi_\alpha(\mathbf{p}+\mathbf{k})\right]\,, \tag{A.33}$$

where n and α correspond to the full set of quantum numbers $n\to n_n,l_n,m_n$. In real space representation, the empty vertices are given by

$$M^{(0)}_{n\alpha}(\mathbf{k}) = \imath\left(Z\delta_{n,\alpha}-\int d\mathbf{r}\Psi^*_n(\mathbf{r})e^{\imath\mathbf{kr}}\Psi_\alpha(\mathbf{r})\right)\,. \tag{A.34}$$

The exponential function is expanded in spherical harmonics,

$$e^{\imath\mathbf{kr}} = 4\pi\sum_{l=0}^{\infty}\sum_{m=-l}^{l}\imath^l j_l(kr)Y^*_{lm}(\Omega_k)Y_{lm}(\Omega_r)\,. \tag{A.35}$$

with the spherical Bessel functions $j_l(kr)$. The first contributions are a monopole ($l = 0$), a dipole ($l = 1$) as well as a quadrupole ($l = 2$) term.

The first Bessel functions are

$$j_0(x) = \frac{\sin(x)}{x}\,, \qquad \lim_{x\to 0} j_0(x) = 1\,, \tag{A.36}$$

$$j_1(x) = \frac{\sin(x)}{x^2} - \frac{\cos(x)}{x}\,, \qquad \lim_{x\to 0} j_1(x) = \frac{x}{3}\,. \tag{A.37}$$

The first spherical harmonics are

$$Y_{00}(\Omega) = \frac{1}{\sqrt{4\pi}}\,, \quad Y_{10}(\theta,\phi) = \frac{\sqrt{3}}{\sqrt{4\pi}}\cos\theta\,, \quad Y_{1\pm1}(\theta,\phi) = \mp\frac{\sqrt{3}}{\sqrt{8\pi}}\sin\theta e^{\pm\imath\phi}\,. \tag{A.38}$$

Considering only $l = 0$ and $l = 1$ and taking the limit $k \to 0$

$$\lim_{k\to 0} e^{\imath\mathbf{kr}} = 1 + \imath kr\left(\cos\theta_r\cos\theta_k + \frac{1}{2}\sin\theta_r\sin\theta_k(e^{\imath(-\phi_k+\phi_r)} + e^{\imath(\phi_k-\phi_r)})\right) \tag{A.39}$$

$$= 1 + \imath kr\left(\cos\theta_r\cos\theta_k + \sin\theta_r\sin\theta_k\cos(\phi_k - \phi_r)\right) \tag{A.40}$$

$$= 1 + \imath kr\left(\cos\theta_r\cos\theta_k + \sin\theta_r\sin\theta_k(\cos(\phi_k)\cos(\phi_r) + \sin(\phi_k)\sin(\phi_r)\right) \tag{A.41}$$

$$= 1 + \imath\left(k_z z + k_x x + k_y y\right) \tag{A.42}$$

$$= 1 + \imath\mathbf{k}\cdot\mathbf{r}\,. \tag{A.43}$$

Thus,

$$\lim_{k\to 0} M^{(0)}_{n\alpha}(\mathbf{k}) = \lim_{k\to 0}\imath\left(Z\delta_{n,\alpha} - \delta_{n,\alpha} - i\mathbf{k}\cdot\int d\mathbf{r}\Psi^*_n(\mathbf{r})\mathbf{r}\Psi_\alpha(\mathbf{r})\right)\,. \tag{A.44}$$

For $Z = 1$ (hydrogen), the monopole is always canceled by the first term of Eq. A.34. For spectral lines, the monopole term vanishes as $n \neq \alpha$,

$$\lim_{k\to 0} M^{(0)}_{n\alpha}(\mathbf{k}) = \lim_{k\to 0}\mathbf{k}\cdot\langle n|\mathbf{r}|\alpha\rangle \quad \text{for} \quad n \neq \alpha \ \vee Z = 1\,. \tag{A.45}$$

Usually, we have to evaluate

$$M^{(0)}_{if}(\mathbf{k})\left(M^{(0)}_{i'f'}(\mathbf{k})\right)^* = k^2|\langle i|\mathbf{r}|f\rangle|\,|\langle f'|\mathbf{r}|i'\rangle| \quad \cos\theta_1\cos\theta_2\,, \tag{A.46}$$

for spectral line shape calculations. Here, θ_1 and θ_2 are the angles between $\mathbf{k}$ and the direction of the dipole moments. As the atoms are not specifically directed, averaging over the direction has to be carried out.

For the special case $i = i'$ and $f = f'$, the average over $\cos^2\theta$ is

$$\overline{\cos^2\theta} = \frac{1}{2}\int_0^\pi \mathrm{d}\theta \cos^2\theta \sin\theta = \frac{1}{3}\,. \tag{A.47}$$

For the general case, one has to remember that $\langle i|\mathbf{r}|f\rangle$ and $\langle f'|\mathbf{r}|i'\rangle$ belong to one atom, thus the angle α between the two dipole moments is constant. While θ_1 can take values from 0 to π, θ_2 is restricted to values between $|\alpha-\theta_1|$ and $\alpha+\theta_1$. Hence, the spacial average is

$$\overline{\cos\theta_1\cos\theta_2} = \frac{1}{\pi\sin\alpha}\int_0^\pi \mathrm{d}\theta_1\ \cos\theta_1\sin\theta_1 \int_{|\theta_1-\alpha|}^{\theta_1+\alpha} \mathrm{d}\theta_2\ \cos\theta_2\sin\theta_2 = \frac{\cos\alpha}{4}\,. \tag{A.48}$$

$\cos\alpha$ belongs to the scalar product of $\langle i|\mathbf{r}|f\rangle$ and $\langle f'|\mathbf{r}|i'\rangle$ which generally occurs in the line shape formulas. Thus,

$$\int \mathrm{d}\Omega_k M_{if}^{(0)}(\mathbf{k})\left(M_{i'f'}^{(0)}(\mathbf{k})\right)^* = \frac{k^2}{4}\langle i|\mathbf{r}|f\rangle\cdot\langle f'|\mathbf{r}|i'\rangle \quad \text{for} \quad i\neq i' \vee f\neq f'\,, \tag{A.49}$$

$$\int \mathrm{d}\Omega_k |M_{if}^{(0)}(\mathbf{k})|^2 = \frac{k^2}{3}|\langle i|\mathbf{r}|f\rangle|^2\,. \tag{A.50}$$

Starting from Eq. (A.34), the matrix element $M^0(\mathbf{k})$ is evaluated for H-like emitters. Here, the fine structure splitting is neglected. The wave function of the H-like emitter with atomic number Z and quantum numbers $\{n,l,m\}$ is given by

$$\Psi_{nlm}(\mathbf{r}) = R_{nl}(r)Y_{lm}(\theta,\phi)\,, \tag{A.51}$$

where $Y_{lm}(\theta,\phi)$ are spherical harmonics and the normalized radial part is given by

$$R_{nl}(r) = \frac{Z^{l+\frac{3}{2}}2^{l+1}}{n^{2+l}}\sqrt{\frac{(n-l-1)!}{(n+l)!}}r^l e^{-\frac{Z}{n}r}L_{n-l-1}^{2l+1}\left(\frac{2Z}{n}r\right)\,, \tag{A.52}$$

in atomic Rydberg units ($2m_e = e^2/2 = \hbar = 1$). Here, the modified Laguerre polynomial

$$L_n^k(x) = \sum_{j=0}^{n}(-1)^j\frac{(n+k)!}{(n-j)!(k+j)!j!}x^j\,, \tag{A.53}$$

enters. With this wavefunction, the matrix element is

$$M_{n\alpha}^{(0)}(\mathbf{k}) = \imath\left(Z\delta_{n,\alpha} - 4\pi\sum_{l=0}^{\infty}\sum_{m=-l}^{l} i^l Y_{lm}^*(\Omega_k)\int dr\ r^2 j_l(kr)R_{n_n l_n}(r)R_{n_\alpha l_\alpha}(r)\right.$$
$$\left.\times\int d\Omega_r Y_{l_\alpha m_\alpha}(\Omega_r)Y_{lm}(\Omega_r)Y_{l_n m_n}^*(\Omega_r)\right)\,. \tag{A.54}$$

The integration over the angular part Ω_r can be carried out. It leads to Clebsch Gordan coefficients [105],

$$\int d\Omega_r Y_{l_\alpha m_\alpha}(\Omega_r) Y_{lm}(\Omega_r) Y^*_{l_n m_n}(\Omega_r) = \sqrt{\frac{(2l_\alpha+1)(2l+1)}{4\pi(2l_n+1)}} \langle (l_\alpha,0),(l,0)|l_n,0\rangle \langle (l_\alpha,m_\alpha),(l,m)|l_n,m_n\rangle \,. \tag{A.55}$$

Since Clebsch Gordan coefficients are non-vanishing only, if the triangle inequality for the angular moments is fulfilled, we have $|l_\alpha - l_n| \leq l \leq l_\alpha + l_n$. For the magnetic quantum number, we have $m_\alpha + m = m_n$, and thus $m = m_n - m_\alpha$. Then, the sum from the series expansion of the exponential function, Eq. (A.35), has few non-vanishing elements. Thus, it is not necessary to restrict this sum to $l \leq 2$ as has been done previously in the discussion of the matrix element [54].

The remaining integral over r can also be treated analytically. We use the modified Rayleigh's formula [106] for the spherical Bessel's functions

$$j_l(kr) = k^l \left(-\frac{1}{k}\frac{\mathrm{d}}{\mathrm{d}k}\right)^l \frac{\sin(kr)}{kr^{l+1}} \,, \tag{A.56}$$

and obtain

$$\begin{aligned}\int \mathrm{d}r r^2 j_l(kr) R_{n_n l_n}(r) R_{n_\alpha l_\alpha}(r) &= k^l \left(-\frac{1}{k}\frac{\mathrm{d}}{\mathrm{d}k}\right)^l \int_0^\infty dr\; r^{2+l_n+l_\alpha} \frac{\sin(kr)}{kr^{l+1}} \\ &\times \frac{Z^{l_n+l_\alpha+3} 2^{l_\alpha+l_n+2}}{n_n^{2+l_n} n_\alpha^{2+l_\alpha}} \sqrt{\frac{(n_n-l_n-1)!(n_\alpha-l_\alpha-1)!}{(n_n+l_n)!(n_\alpha+l_\alpha)!}} e^{-(\frac{Z}{n_\alpha}+\frac{Z}{n_n})r} \\ &\times L^{2l_n+1}_{n_n-l_n-1}\left(\frac{2Z}{n_n}r\right) L^{2l_\alpha+1}_{n_\alpha-l_\alpha-1}\left(\frac{2Z}{n_\alpha}r\right) \,. \end{aligned} \tag{A.57}$$

When the Laguerre polynomials are replaced, we have

$$\begin{aligned}\int \mathrm{d}r\; r^2 j_l(kr) R_{n_n l_n}(r) R_{n_\alpha l_\alpha}(r) &= \\ &\sum_{j=0}^{n_n-l_n-1} \sum_{k=0}^{n_\alpha-l_\alpha-1} (-1)^{j+k} \frac{Z(2Z)^{l_n+l_\alpha+2+j+k}}{n_n^{2+l_n+j} n_\alpha^{2+l_\alpha+k}} \sqrt{\frac{(n_n-l_n-1)!(n_\alpha-l_\alpha-1)!}{(n_n+l_n)!(n_\alpha+l_\alpha)!}} \\ &\times \frac{(n_n+l_n)!(n_\alpha+l_\alpha)!}{(n_n-l_n-1-j)!(2l_n+1+j)!j!(n_\alpha-l_\alpha-1-k)!(2l_\alpha+1+k)!k!} \\ &\times k^l \left(-\frac{1}{k}\frac{\mathrm{d}}{\mathrm{d}k}\right)^l \frac{1}{k} \int_0^\infty dr\; r^{1+l_n+l_\alpha+j+k-l} \sin(kr) e^{-(\frac{Z}{n_\alpha}+\frac{Z}{n_n})r} \,. \end{aligned} \tag{A.58}$$

The integral of the last line is of the form

$$\int_0^\infty \mathrm{d}x x^a e^{-bx} \sin(kx) = \frac{\Gamma(a+1)}{(\sqrt{b^2+k^2})^{a+1}} \sin\left((a+1)\arctan\frac{k}{b}\right) , \tag{A.59}$$

with $a = 1 + l_n + l_\alpha + j + k - l$ and $b = \frac{Z}{n_\alpha} + \frac{Z}{n_n}$ and Euler's gamma function $\Gamma(x)$. For $l = 0$, the last line of Eq. (A.58) is then

$$\frac{1}{k} \frac{\Gamma(2 + l_n + l_\alpha + j + k)}{(\sqrt{(\frac{Z}{n_\alpha} + \frac{Z}{n_n})^2 + k^2})^{2+l_n+l_\alpha+j+k}} \sin\left((2 + l_n + l_\alpha + j + k)\arctan\frac{k}{\frac{Z}{n_\alpha} + \frac{Z}{n_n}}\right) . \tag{A.60}$$

For $l \geq 1$ analytic expressions can be found, because the derivative with respect to k on the right-hand side of Eq. (A.59) can be carried out analytically. Thus, the matrix element $M^0(\mathbf{k})$ can be evaluated analytically for H-like emitters.

As an example, we have for the ground state,

$$M^0_{1s1s}(\mathbf{k}) = \imath \left(Z - \frac{16Z^4}{(k^2 + 4Z^2)^2} \right) . \tag{A.61}$$

This expression vanishes only for $Z = 1$ in the limit of small k, where the integrand of the self-energy, Eq. (1.101), and coupling term, Eq. (1.102), has to be evaluated,

$$\lim_{k\to 0} M^0_{1s1s}(\mathbf{k}) = \imath(Z - 1) . \tag{A.62}$$

For H-like emitters, this term does not vanish and the usual argument[2] why the coupling term from Eq. (1.102) can be neglected in the case of Lyman lines does not hold. The non-vanishing term, Eq. (A.62), stems from $l = 0$ and is called monopole term. However, the monopole part of self-energy and coupling term are completely compensated. Thus, even for H-like emitters, it is possible to neglect the coupling term as long as the monopole part of the self-energy of the ground state is neglected, too.

A.6. Sets of variables for two-particle propagator

To come from Eq. (1.66) to Eq. (1.67), we have to express the two-particle Green's function, depending on the momenta of ion and electron p_i and p_e, via the one that

[2] $M^0_{1s1s}(\mathbf{k}) = 0$

depends on the total momentum P, the relative momentum $\mathbf{p}_{\rm rel} = \frac{m_i}{M}\mathbf{p_e} - \frac{m_e}{M}\mathbf{p_i}$ and the energy level of the bound two-particle state n. We can write

$$
\begin{aligned}
G_2^{(1)}(\mathbf{p}_e, \mathbf{p}_i; \mathbf{p}'_e, \mathbf{p}'_i; z) &= \langle \mathbf{p}_e, \mathbf{p}_i | G_2(z) | \mathbf{p}'_e, \mathbf{p}'_i \rangle && \text{(A.63)} \\
&= \sum_{n_1\mathbf{P}_1} \sum_{n_2\mathbf{P}_2} \langle \mathbf{p}_e, \mathbf{p}_i | n_1\mathbf{P}_1 \rangle \langle n_1\mathbf{P}_1 | G_2(z) | n_2\mathbf{P}_2 \rangle \langle n_2\mathbf{P}_2 | \mathbf{p}'_e, \mathbf{p}'_i \rangle && \text{(A.64)} \\
&= \sum_{n_1\mathbf{P}_1} \sum_{n_2\mathbf{P}_2} \langle \mathbf{p}_e, \mathbf{p}_i | n_1\mathbf{P}_1 \rangle G_2(n_1, \mathbf{P}_1, z) \delta_{n_1 n_2} \delta_{\mathbf{P}_1\mathbf{P}_2} \langle n_2\mathbf{P}_2 | \mathbf{p}'_e, \mathbf{p}'_i \rangle && \text{(A.65)} \\
&= \sum_{n\mathbf{P}} \langle \mathbf{p}_e, \mathbf{p}_i | n\mathbf{P} \rangle G_2(n, \mathbf{P}, z) \langle n\mathbf{P} | \mathbf{p}'_e, \mathbf{p}'_i \rangle && \text{(A.66)} \\
&= \sum_{n\mathbf{P}} \psi_{n\mathbf{P}}(\mathbf{p}_e, \mathbf{p}_i) G_2(n, \mathbf{P}, z) \psi^*_{n\mathbf{P}}(\mathbf{p}'_e, \mathbf{p}'_i) \delta_{\mathbf{P}, \mathbf{p}_e + \mathbf{p}_i} \delta_{\mathbf{P}, \mathbf{p}'_i + \mathbf{p}'_e} && \text{(A.67)} \\
&= \sum_{n\mathbf{P}} \psi_{n\mathbf{P}}(\mathbf{p}_{\rm rel}) G_2(n, \mathbf{P}, z) \psi^*_{n\mathbf{P}}(\mathbf{p}'_{\rm rel}) \delta_{\mathbf{P}, \mathbf{p}_e + \mathbf{p}_i} \delta_{\mathbf{P}, \mathbf{p}'_i + \mathbf{p}'_e} \,, && \text{(A.68)}
\end{aligned}
$$

where we used the fact that the wave-function $\psi_{n\mathbf{P}}(\mathbf{p}_e, \mathbf{p}_i)$ depends only on the relative momentum.

A.7. Details for Eq. (1.70)

$$
\begin{aligned}
&\mathrm{Im}\,(\frac{1}{\beta}\sum_{\omega_\lambda} G_2(n,\mathbf{P},\omega+\imath\delta+\omega_\lambda)G_2(n',\mathbf{P}',\omega_\lambda)) \\
&\quad= -4\hbar\pi \mathrm{Im}\,\Sigma_{n\mathbf{P}}\mathrm{Im}\,\Sigma_{n'\mathbf{P}'}\left(g(\epsilon_{n\mathbf{P}}+\mathrm{Re}\,\Sigma_{n\mathbf{P}})-g(\epsilon_{n'\mathbf{P}'}+\mathrm{Re}\,\Sigma_{n'\mathbf{P}'})\right) \\
&\qquad\times\int_{-\infty}^{\infty}\frac{\mathrm{d}\omega_1}{2\pi}\int_{-\infty}^{\infty}\frac{\mathrm{d}\omega_2}{2\pi}\delta(\omega-\omega_1+\omega_2)\frac{1}{\left(\epsilon_{n\mathbf{P}}-\hbar\omega_1+\mathrm{Re}\,\Sigma_{n\mathbf{P}}\right)^2+\left(\mathrm{Im}\,\Sigma_{n\mathbf{P}}\right)^2} \\
&\qquad\times\frac{1}{\left(\epsilon_{n'\mathbf{P}'}-\hbar\omega_2+\mathrm{Re}\,\Sigma_{n'\mathbf{P}'}\right)^2+\left(\mathrm{Im}\,\Sigma_{n'\mathbf{P}'}\right)^2} \qquad \text{(A.69)} \\
&\quad= -\frac{\hbar}{\pi}\mathrm{Im}\,\Sigma_{n\mathbf{P}}\mathrm{Im}\,\Sigma_{n'\mathbf{P}'}\left(g(\epsilon_{n\mathbf{P}}+\mathrm{Re}\,\Sigma_{n\mathbf{P}})-g(\epsilon_{n'\mathbf{P}'}+\mathrm{Re}\,\Sigma_{n'\mathbf{P}'})\right) \\
&\qquad\int_{-\infty}^{\infty}\mathrm{d}\omega_2\frac{1}{\left(\epsilon_{n\mathbf{P}}-\hbar(\omega_2+\omega)+\mathrm{Re}\,\Sigma_{n\mathbf{P}}\right)^2+\left(\mathrm{Im}\,\Sigma_{n\mathbf{P}}\right)^2} \\
&\qquad\times\frac{1}{\left(\epsilon_{n'\mathbf{P}'}-\hbar\omega_2+\mathrm{Re}\,\Sigma_{n'\mathbf{P}'}\right)^2+\left(\mathrm{Im}\,\Sigma_{n'\mathbf{P}'}\right)^2} \qquad \text{(A.70)} \\
&\quad= -\left(\left(g(\epsilon_{n\mathbf{P}}+\mathrm{Re}\,\Sigma_{n\mathbf{P}})-g(\epsilon_{n'\mathbf{P}'}+\mathrm{Re}\,\Sigma_{n'\mathbf{P}'})\right)\right. \\
&\qquad\left.\frac{\mathrm{Im}\,\Sigma_{n\mathbf{P}}+\mathrm{Im}\,\Sigma_{n'\mathbf{P}'}}{\left(\epsilon_{n\mathbf{P}}-\hbar\omega+\mathrm{Re}\,\Sigma_{n\mathbf{P}}-\epsilon_{n'\mathbf{P}'}-\mathrm{Re}\,\Sigma_{n'\mathbf{P}'}\right)^2+\left(\mathrm{Im}\,\Sigma_{n'\mathbf{P}'}+\mathrm{Im}\,\Sigma_{n\mathbf{P}}\right)^2}\right. \qquad \text{(A.71)} \\
&\quad=\mathrm{Im}\left(\frac{g(\epsilon_{n\mathbf{P}}+\mathrm{Re}\,\Sigma_{n\mathbf{P}})-g(\epsilon_{n'\mathbf{P}'}+\mathrm{Re}\,\Sigma_{n'\mathbf{P}'})}{\hbar\omega-\epsilon_{n\mathbf{P}}+\epsilon_{n'\mathbf{P}'}-\mathrm{Re}\,\Sigma_{n\mathbf{P}}+\mathrm{Re}\,\Sigma_{n'\mathbf{P}'}+\imath\left(\mathrm{Im}\,\Sigma_{n'\mathbf{P}'}+\mathrm{Im}\,\Sigma_{n\mathbf{P}}\right)}\right). \qquad \text{(A.72)}
\end{aligned}
$$

A.8. Implementation of the frequency-fluctuation model (FFM)

For a numerical calculation of Eq. (1.100), the first step is to evaluate the integral

$$
\begin{aligned}
\int\frac{I_s(\omega')\mathrm{d}\omega'}{\gamma+i(\omega-\omega')} &= \int\frac{I_s(\omega')}{\gamma+i(\omega-\omega')}\frac{\gamma-i(\omega-\omega')}{\gamma-i(\omega-\omega')}\mathrm{d}\omega' && \text{(A.73)} \\
&= \int\frac{\left[I_s(\omega')\gamma-iI_s(\omega')(\omega-\omega')\right]\mathrm{d}\omega'}{\gamma^2+(\omega-\omega')^2} && \text{(A.74)} \\
&= A(\omega)\gamma+iB(\omega)\,, && \text{(A.75)}
\end{aligned}
$$

where the real and imaginary part are defined as

$$
\begin{aligned}
A(\omega) &= \int\frac{I_s(\omega')\mathrm{d}\omega'}{\gamma^2+(\omega-\omega')^2}, && \text{(A.76)} \\
B(\omega) &= -\int\frac{I_s(\omega')(\omega-\omega')\mathrm{d}\omega'}{\gamma^2+(\omega-\omega')^2}\,. && \text{(A.77)}
\end{aligned}
$$

These quantities enter Eq. (1.100) as

$$I(\omega) = \frac{r^2}{\pi}\mathrm{Re}\frac{A(\omega)\gamma + iB(\omega)}{1-\gamma^2 A(\omega) - i\gamma B(\omega)} \tag{A.78}$$

$$= \frac{r^2}{\pi}\mathrm{Re}\left[\frac{A(\omega)\gamma + iB(\omega)}{1-\gamma^2 A(\omega) - i\gamma B(\omega)}\frac{1-\gamma^2 A(\omega) + i\gamma B(\omega)}{1-\gamma^2 A(\omega) + i\gamma B(\omega)}\right] \tag{A.79}$$

$$= \frac{r^2}{\pi}\frac{A(\omega)\gamma - \gamma^3 A^2(\omega) - \gamma B^2(\omega)}{(1-\gamma^2 A(\omega))^2 + \gamma^2 B^2(\omega)}\,. \tag{A.80}$$

Thus, a numerical programm has to

1. determine γ
2. spline $I_s(\omega)$ on an equidistant grid with stepsize $d\omega$
3. loop over ω and
   a) calculate $A(\omega)$ and $B(\omega)$ as discrete sums and
   b) calculate $I(\omega)$ from Eq. (A.80)

A.9. Self-energy calculation in Born approximation

The following expressions are given in Rydberg atomic units, i.e. $\hbar = 2m_e = e^2/2 = 1$. The detailed evaluation of Eqs. (1.101) and (1.102) has been given in Refs. [54, 55], thus, we give here only a brief summary. For the evaluation, we have to decide, which approximation we want to use to treat the screening of the interaction, i.e. to evaluate $\mathrm{Im}\,\epsilon^{-1}(\mathbf{k},\omega)$. Either the screening is treated dynamically,

$$\mathrm{Im}\,\epsilon^{-1}(\mathbf{k},\omega) = -\frac{\mathrm{Im}\,\epsilon(\mathbf{k},\omega)}{(\mathrm{Im}\,\epsilon(\mathbf{k},\omega))^2 + (\mathrm{Re}\,\epsilon(\mathbf{k},\omega))^2}\,, \tag{A.81}$$

or statically with Debye screening parameter $\kappa = 1/\lambda_\mathrm{D}$

$$\mathrm{Im}\,\epsilon^{-1}(\mathbf{k},\omega) = -\frac{\mathrm{Im}\,\epsilon(\mathbf{k},\omega)}{(1+\kappa^2/k^2)^2}\,, \tag{A.82}$$

which is justified for small ω. To neglect screening completely, we set

$$\mathrm{Im}\,\epsilon^{-1}(\mathbf{k},\omega) = -\mathrm{Im}\,\epsilon(\mathbf{k},\omega)\,, \tag{A.83}$$

this is only applicable for free electron densities $n_\mathrm{e} < 10^{24}\,\mathrm{m}^{-3}$ [54], i.e. in a regime where all collisions are binary.

Dielectric function in random phase approximation

Starting from the dielectric function in random phase approximation (RPA) [62]

$$\epsilon(\mathbf{k},\omega) = 1 - 2V(k)\int \frac{d^3p}{(2\pi)^3}\frac{f_e(E_{\mathbf{p}+\mathbf{k}}) - f_e(E_p)}{E_{\mathbf{p}+\mathbf{k}} - E_p + \omega + \imath\delta}\,, \tag{A.84}$$

and using Dirac's identity, Eq. (1.46), the imaginary part is given by

$$\mathrm{Im}\,\epsilon(\mathbf{k},\omega) = 2V(k)\int \frac{d^3p}{(2\pi)^3}(f_e(E_{\mathbf{p}+\mathbf{k}}) - f_e(E_p))\delta(E_{\mathbf{p}+\mathbf{k}} - E_p + \omega + \imath\delta)\,. \tag{A.85}$$

In the limit of low-densities, the Fermi distribution $f_e(E)$ is replaced by a Boltzmann distribution

$$f_e(E_p) \approx \frac{1}{2}n_e\Lambda_e^3 e^{-E_p/k_\mathrm{B}T}, \qquad \Lambda_e = \sqrt{\frac{4\pi}{k_\mathrm{B}T}}, \tag{A.86}$$

and the integration can be carried out by splitting $\mathbf{p}$ into a vector parallel to $\mathbf{k}$ and one orthogonal to it

$$\int \frac{d^3p}{(2\pi)^3} \quad \rightarrow \quad \frac{1}{4\pi^2}\int_0^\infty p_\perp dp_\perp \int_{-\infty}^\infty dp_\parallel. \tag{A.87}$$

Using the potential $V(k) = 8\pi/k^2$ (Rydberg atomic units), we obtain

$$\mathrm{Im}\,\epsilon(\mathbf{k},\omega) = \frac{4\pi\sqrt{\pi}n_e}{\sqrt{k_\mathrm{B}T}k^3}(e^{\omega/k_\mathrm{B}T} - 1)e^{-(\omega+k^2)^2/4k^2k_\mathrm{B}T}. \tag{A.88}$$

Electronic self-energy with static screened potential

For the static approximation, the self-energy can be calculated in the following way. Using Eq. (A.82) and Eq. (A.88), we obtain for Eq. (1.101)

$$\begin{aligned}\Sigma_\nu(\Delta\omega) = &-\frac{32\pi^2\sqrt{\pi}n_e}{\sqrt{k_\mathrm{B}T}}\int\frac{d^3k}{(2\pi)^3}\sum_\alpha |M^0_{\nu\alpha}(\mathbf{k})|^2 \\ &\times\int_{-\infty}^\infty \frac{d\omega}{\pi}\frac{1}{k(k^2+\kappa^2)^2}\frac{e^{\omega/k_\mathrm{B}T}e^{-(\omega+k^2)^2/4k^2k_\mathrm{B}T}}{\Delta\omega + \omega_{\nu\alpha} - (\omega + \imath\delta)}\,.\end{aligned} \tag{A.89}$$

We integrate over Ω_k where only $|M^0_{\nu\alpha}(\mathbf{k})|^2$ depends on these angles. This leads to angular-independent (ai) matrix elements

$$|M^{0,ai}_{\nu\alpha}(k)|^2 = \int_0^\pi \sin\theta_k d\theta_k \int_0^{2\pi} d\phi_k |M^0_{\nu\alpha}(k,\theta_k,\phi_k)|^2\,, \tag{A.90}$$

which can be calculated analytically for H-like emitters. The self-energy is then given by

$$\Sigma_\nu(\Delta\omega) = -\frac{32\pi\sqrt{\pi}n_e}{(2\pi)^3\sqrt{k_\mathrm{B}T}}\int_0^\infty dk\, k^2 \sum_\alpha |M^{0,ai}_{\nu\alpha}(k)|^2 \frac{1}{k(k^2+\kappa^2)^2} \times \int_{-\infty}^{\infty} d\omega \frac{e^{-\frac{(\omega-k^2)^2}{4k_\mathrm{B}Tk^2}}}{\Delta\omega+\omega_{\nu\alpha}-(\omega+\imath\delta)}\,. \tag{A.91}$$

Using Dirac's identity, the ω-integration can be carried out

$$\int_{-\infty}^{\infty} d\omega \frac{e^{-\frac{(\omega-k^2)^2}{4k_\mathrm{B}Tk^2}}}{\Delta\omega+\omega_{\nu\alpha}-(\omega+\imath\delta)} = 2\sqrt{\pi}F\left(\frac{\Delta\omega+\omega_{\nu\alpha}-k^2}{2k\sqrt{k_\mathrm{B}T}}\right) + \imath\pi e^{-\frac{(\Delta\omega+\omega_{\nu\alpha}-k^2)^2}{4k_\mathrm{B}Tk^2}}\,, \tag{A.92}$$

leading to the Dawson integral $F(x) = e^{x^2}\int_0^x e^{t^2}\mathrm{d}t$. Thus, we obtain for the real part, i.e. the shift of the energy level ν,

$$\mathrm{Re}\,\Sigma_\nu(\Delta\omega) = -\frac{8n_e}{\pi\sqrt{k_\mathrm{B}T}}\int_0^\infty dk \sum_\alpha |M^{0,ai}_{\nu\alpha}(k)|^2 \frac{k}{(k^2+\kappa^2)^2} F\left(\frac{\Delta\omega+\omega_{\nu\alpha}-k^2}{2k\sqrt{k_\mathrm{B}T}}\right)\,. \tag{A.93}$$

With $F(x) = \frac{1}{2}\sqrt{\pi}e^{-x^2}\mathrm{Erfi}(x)$, we can also write

$$\mathrm{Re}\,\Sigma_\nu(\Delta\omega) = -\frac{4n_e}{\sqrt{\pi k_\mathrm{B}T}}\int_0^\infty dk \sum_\alpha |M^{0,ai}_{\nu\alpha}(k)|^2 \frac{k}{(k^2+\kappa^2)^2} e^{\frac{\Delta\omega+\omega_{n\alpha}-k^2}{2k\sqrt{k_\mathrm{B}T}}} \times \mathrm{Erfi}\left(\frac{\Delta\omega+\omega_{\nu\alpha}-k^2}{2k\sqrt{k_\mathrm{B}T}}\right)\,. \tag{A.94}$$

The latter expression is evaluated by Mathematica (Version 8.0) more rapidly. Analogously, we obtain for the imaginary part, i.e. the width of the energy level ν,

$$\mathrm{Im}\,\Sigma_\nu(\Delta\omega) = -\frac{4n_e}{\sqrt{\pi k_\mathrm{B}T}}\int_0^\infty dk \sum_\alpha |M^{0,ai}_{\nu\alpha}(k)|^2 \frac{k}{(k^2+\kappa^2)^2} e^{-\frac{(\Delta\omega+\omega_{\nu\alpha}-k^2)^2}{4k_\mathrm{B}Tk^2}}\,. \tag{A.95}$$

Bibliography

[1] W. H. Wollaston, *A method of examining refractive and dispersive powers, by prismatic reflection*, Philos. Trans. Roy. Soc. London **92** (1802), 365–380.

[2] J Fraunhofer, *Bestimmung des Brechungs- und des Farbenzerstreungs-Vermögens verschiedener Glasarten, in Bezug auf die Vervollkommnung achromatischer Fernröhre*, Annalen der Physik **56** (1817), 264–313.

[3] L. Hitzschke, G. Röpke, T. Seifert, and R. Zimmermann, *Green's function approach to the electron shift and broadening of spectral lines in non-ideal plasmas*, J. Phys. B: At. Mol. Phys. **19** (1986), 2443–2456.

[4] S. Günter, L. Hitzschke, and G. Röpke, *Hydrogen spectral lines with the inclusion of dense-plasma effects*, Phys. Rev. A **44** (1991), 6834–6844.

[5] A. Könies and S. Günter, *Quantum-mechanical treatment of strong electron-atom collision contributions to the shift and width of hydrogen lines*, Phys. Rev. E **52** (1995), 6658–6663.

[6] S. Sorge, A. Wierling, G. Röpke, W. Theobald, R. Sauerbrey, and T. Wilhein, *Diagnostics of a laser-induced dense plasma by hydrogen-like carbon spectra*, J. Phys. B: At. Mol. Opt. Phys. **33** (2000), 2983–3000.

[7] B. Omar, S. Günter, A. Wierling, and G. Röpke, *Neutral helium spectral lines in dense plasmas*, Phys. Rev. E **73** (2006), 056405.

[8] A. Sengebusch, H. Reinholz, G. Röpke, U. Zastrau, T. Kämpfer, I. Uschmann, E. Förster, E. Stambulchik, E. Kroupp, and Y. Maron, *K-line emission profiles with focus on the self-consistent calculation of plasma polarization*, J. Phys. A: Math. Theo. **42** (2009), 214061.

[9] http://www.asml.com/asml/show.do?lang=EN&ctx=46772&dfp_product_id=842, Link visited at 28.2.2014.

[10] S. Lorenzen, A. Wierling, H. Reinholz, and G. Röpke, *Pressure broadening of Lyman lines in dense Li^{2+}-plasmas*, Contrib. Plasma Phys. **48** (2008), 657–669.

[11] S. Lorenzen, A. Wierling, H. Reinholz, and G. Röpke, *Improved self-energy calculations for pressure broadening of spectral lines in dense plasmas*, Contrib. Plasma Phys. **51** (2011), 349–354.

[12] S. Lorenzen, A. Wierling, H. Reinholz, G. Röpke, M. C. Zammit, D. V. Fursa, and I. Bray, *Quantum-statistical T-matrix approach to line broadening of hydrogen in dense plasmas*, AIP Conf. Proc. **1290** (2010), 99–103.

[13] S. Lorenzen, A. Wierling, H. Reinholz, G. Röpke, M. C. Zammit, D. V. Fursa, and I. Bray, *Quantum-statistical line shape calculation for Lyman-α lines in dense H plasmas*, J. Phys.: Conf. Series **397** (2012), 012021.

[14] S. Lorenzen, *Comparative study on ion-dynamics for broadening of Lyman lines in dense hydrogen plasmas*, Contrib. Plasma Phys. **53** (2013), 368–374.

[15] S. Lorenzen, B. Omar, M. C. Zammit, D. V. Fursa, and I. Bray, *Plasma pressure broadening for few-electron emitters including strong electron collisions within a quantum-statistical theory*, Phys. Rev. E **89** (2014), 023106.

[16] M. R. Zaghloul, M. A. Bourham, and J. M. Doster, *A simple formulation and solution strategy of the Saha equation for ideal and nonideal plasmas*, J. Phys. D: Appl. Phys. **33** (2000), 977–984.

[17] K. Grützmacher and B. Wende, *Discrepancies between Stark-broadening theories of hydrogen and measurements of Lyman-α Stark profiles in a dense equilibrium plasma*, Phys. Rev. A **16** (1977), 243–246.

[18] R. Radtke, K. Günther, and R. Spanke, *Study of the Balmer spectrum of hydrogen from a high-pressure arc discharge. II. Comparison of experiment and theory*, Contrib. Plasma Phys. **26** (1986), 151–158.

[19] G. Jamelot, P. Jaegle, P. Lemaire, and A. Carillon, *Experimental study of the role of plasma polarization on line shape in dense laboratory plasmas*, J. Quant. Spectrosc. Radiat. Transfer **44** (1990), 71–77.

[20] G. Schriever, S. Mager, A. Naweed, A. Engel, K. Bergmann, and R. Lebert, *Laser-produced lithium plasma as a narrow-band extended ultraviolet radiation source for photoelectron spectroscopy*, Appl. Opt. **37** (1998), 1243–1248.

[21] G. Schriever, K. Bergmann, and R. Lebert, *Narrowband laser produced extreme ultraviolet sources adapted to silicon/molybdenum multilayer optics*, J. Appl. Phys. **83** (1998), 4566–4571.

[22] W. Theobald, C. Wülker, J. Jasny, et al., *High-density lithium plasma columns generated by intense subpicosecond KrF laser pulses*, Opt. Commun. **149** (1998), 289–295.

[23] C. Rajyaguru, T. Higashiguchi, et al., *Parametric optimization of a narrow-band 13.5-nm emission from a Li-based liquid-jet target using dual nano-second laser pulses*, Appl. Phys. B **80** (2005), 409–412.

[24] P. Nica, S. Miyamoto, S. Amano, T. Inoue, A. Shimoura, K. Kaku, and T. Mochizuki, *Soft X-ray spectra from laser heated lithium targets*, Appl. Phys. Lett. **89** (2006), 41501–3.

[25] P. Nica, S. Miyamoto, S. Amano, T. Inoue, A. Shimoura, and T. Mochizuki, *Space-resolved soft X-ray emission from laser produced lithium plasma*, Phys. Lett. A **370** (2007), 154–157.

[26] S. A. George, W. Silfvast, K. Takenoshita, R. Bernath, C.-S. Koay, G. Shimkaveg, and M. Richardson, *EUV generation from lithium laser plasma for lithography*, Proc. SPIE. **6151** (2006), 615143.

[27] S. A. George, W. T. Silfvast, K. Takenoshita, R. T. Bernath, C.-S. Koay, G. Shimkaveg, and M. C. Richardson, *Comparative extreme ultraviolet emission measurements for lithium and tin laser plasmas*, Opt. Lett. **32** (2007), 997–999.

[28] W. Whitty, J. Costello, E. Kennedy, C. Moloney, and J.-P. Mosnier, *Absorption spectroscopy of an expanding laser produced lithium plasma in the extreme ultraviolet using the dual laser plasma technique*, Appl. Surf. Sci. **127-129** (1998), 686–691.

[29] D. Doria, K. D. Kavanagh, J. T. Costello, and H. Luna, *Plasma parametrization by analysis of time-resolved laser plasma image spectra*, Meas. Sci. Technol. **17** (2006), 670–674.

[30] B. A. Bushaw, W. Nörtershäuser, G. W. F. Drake, and H.-J. Kluge, *Ionization energy of* ^{6,7}*Li determined by triple-resonance laser spectroscopy*, Phys. Rev. A **75** (2007), 052503.

[31] G. W. F. Drake, *Theoretical energies for the n=1-state and 2-state of the helium isoelectronic sequence up to z=100*, Can. J. Phys. **66** (1988), 586–611.

[32] E. Stambulchik, *Review of the 1st spectral line shapes in plasmas code comparison workshop*, High Energ. Dens. Phys. **9** (2013), 528–534.

[33] R. W. Lee, *Plasma line broadening of the Lyman-α transition including ion dynamics*, J. Phys. B: At. Mol. Phys. **11** (1978), L167–L169.

[34] B. Omar, A. Wierling, H. Reinholz, and G. Röpke, *Diagnostic of laser induced LiII plasma*, Phys. Rev. Res. Int. **3** (2013), 218–227.

[35] S. A. George, 2008, private communication.

[36] C. Bahr, T. Dorfmüller, et al., *Lehrbuch der Experimentalphysik - Bergmann, Schäfer, Bd. 5*, de Gruyter, Berlin, 1992.

[37] G. B. Rybicki and A. P. Lightman, *Radiative processes in astrophysics*, John Wiley and Sons, New York, 1979.

[38] W. Lochte-Holtgreven, *Plasma diagnostics*, AIP Press, New York, 1995, originally published in 1968.

[39] *NIST: Atomic Spectra Database*, http://physics.nist.gov/PhysRefData/ASD/lines_form.html, link used 28.2.2014.

[40] H. A. Lorentz, *The absorption and emission of lines of gaseous bodies*, Proc. R. Acad. Sci. **8** (1906), 591–611.

[41] V. Weisskopf, *Zur Theorie der Kopplungsbreite und der Stoßdämpfung*, J. Phys. **75** (1932), 281–301.

[42] H. R. Griem, *Spectral line broadening by plasmas*, Academic Press, London, 1974.

[43] H. Griem, *Starkeffekt-Verbreiterung der Balmer-Linien bei großen Elektronendichten*, Z. Phys. A Hadrons Nucl. **137** (1954), 280–294.

[44] A. C. Kolb and H. Griem, *Theory of line broadening in multiplet spectra*, Phys. Rev. **111** (1958), 514–521.

[45] P. C. Kepple, *Improved Stark-profile calculation for the HeII lines at 256, 304, 1085, 1216, 1640, 3203, and 4686 Å*, Phys. Rev. A **6** (1972), 1–9.

[46] C. R. Vidal, J. Cooper, and E. W. Smith, *Hydrogen Stark broadening calculations with the unified classical path theory*, J. Quant. Spectrosc. Radiat. Transfer **10** (1970), 1011–1063.

[47] C. Vidal, J. Cooper, and E. Smith, *Hydrogen Stark-broadening tables*, Astrophys. J. Suppl. Ser. **25** (1973), 37–86.

[48] M. Baranger, *General impact theory of pressure broadening*, Phys. Rev. **112** (1958), 855–865.

[49] E. Stambulchik and Y. Maron, *A study of ion-dynamics and correlation effects for spectral line broadening in plasma: K-shell lines*, J. Quant. Spectrosc. Radiat. Transfer **99** (2006), 730–749.

[50] E. Stambulchik, D. V. Fisher, Y. Maron, H. R. Griem, and S. Alexiou, *Correlation effects and their influence on line broadening in plasmas: Application to H-alpha*, High Energ. Dens. Phys. **3** (2007), 272–277.

[51] M. A. González and M. A Gigosos, *Tables of dipolar emission and two-photon absorption Lyman-α profiles*, Astron. Astrophys. Supplement **145** (2000), 491–494.

[52] M. A. González and M. A. Gigosos, *Analysis of Stark line profiles for non-equilibrium plasma diagnosis*, Plasma Sources Sci. Technol. **18** (2009), 034001.

[53] H. R. Griem, *Principles of plasma spectroscopy*, Cambridge University Press, Cambridge, 1997.

[54] S. Günter, *Optische Eigenschaften dichter Plasmen*, habilitation thesis at Rostock University, 1995.

[55] B. Omar, *Spectral line broadening of HeI and He-like ions in dense plasmas*, Ph.D. thesis at Rostock University, 2007.

[56] B. Talin, A. Calisiti, L. Godbert, R. Stamm, R. W. Lee, and L. Klein, *Frequency-fluctuation model for line-shape calculations in plasma spectroscopy*, Phys. Rev. A **51** (1995), 1918–1928.

[57] A. Calisti, C. Mossé, S. Ferri, B. Talin, F. Rosmej, L. A. Bureyeva, and V. S. Lisitsa, *Dynamic Stark broadening as the Dicke narrowing effect*, Phys. Rev. E **81** (2010), 016406.

[58] S. Alexiou and A. Poquerusse, *Standard line broadening impact theory for hydrogen including penetrating collisions*, Phys. Rev. E **72** (2005), 046404.

[59] J. Rosato, H. Capes, and R. Stamm, *Influence of correlated collisions on Stark-broadened lines in plasmas*, Phys. Rev. E **86** (2012), 046407.

[60] ———, *Collision operators for Stark line shapes: When does the unified theory fail?*, High Energ. Dens. Phys. **9** (2013), 484–487.

[61] E. Oks, *Stark broadening of hydrogen and hydrogenlike spectral lines in plasmas*, Alphan Science International Ltd., Oxford, UK, 2006.

[62] W.-D. Kraeft, D. Kremp, W. Ebeling, and G. Röpke, *Quantum statistics of charged particle systems*, Akademie-Verlag Berlin, Berlin, 1986.

[63] G. D. Mahan, *Many-particle physics*, 2nd ed., Plenum Press, New York, 1990.

[64] L. Hitzschke, *Zur Verbreiterung und Verschiebung von Spektrallinien in dichten Plasmen und zur Berechnung dieser Effekte für ausgewählte Argon-Atomlinien im Fall eines schwach nicht-idealen Plasmas*, Ph.D. thesis, Akademie der Wissenschaften, Berlin, 1987.

[65] Heidi Reinholz, *Dielectric and optical properties of dense plasmas*, Ann. Phys. Fr. **30** (2006), 1–187.

[66] R. Kubo, *Statistical-mechanical theory of irreversible processes. I. General theory and simple applications to magnetic and conduction problems*, J. Phys. Soc. Jpn **12** (1657), 570–586.

[67] D. Zubarev, V. Morozov, and G. Röpke, *Statistical mechanics of nonequilibrium processes*, vol. 1, Akademie-Verlag, Berlin, 1996.

[68] ———, *Statistical mechanics of nonequilibrium processes*, vol. 2, Akademie-Verlag, Berlin, 1997.

[69] G. Röpke and M. Winkel, *Green's functions technique for statistical ensembles - lecture notes*, 2005, University Rostock, Germany.

[70] H. A. Bethe and E. E. Salpeter, *Quantum mechanics of one- and two-electron atoms*, Plenum Publishing Corporation, 1977, reprint from 1957.

[71] L. D. Landau and E. M. Lifschitz, *Quantum mechanics: non-relativistic theory*, Pergamon Press, Oxford, 1977.

[72] J. Halenka, *Asymmetry of hydrogen lines in plasmas utilizing a statistical description of ion-quadruple interaction in Mozer-Baranger limit*, Z. Phys. D **16** (1990), 1–8.

[73] J. Holtsmark, *Über die Verbreiterung von Spektrallinien*, Phys. Z. **20** (1919), 162–168.

[74] ———, *Über die Verbreiterung von Spektrallinien*, Ann. Phys. Leipzig **58** (1919), 577–630.

[75] C. F. Hooper, Jr., *Low-frequency component electric microfield distributions in plasmas*, Phys. Rev. **165** (1968), 215–222.

[76] ———, *Asymptotic electric microfield distributions in low-frequency component plasmas*, Phys. Rev. **169** (1968), 193–195.

[77] M. Baranger and B. Mozer, *Electric field distribution in an ionized gas*, Phys. Rev. **115** (1959), 521–525.

[78] C. A. Iglesias, *Integral-equation method for electric microfield distributions*, Phys. Rev. A **27** (1983), 2705–2709.

[79] C. A. Iglesias, J. L. Lebowitz, and D. MacGowan, *Electric microfield distributions in strongly coupled plasmas*, Phys. Rev. A **28** (1983), 1667–1672.

[80] A. Y. Potekhin, G. Chabrier, and D. Gilles, *Electric microfield distributions in electron-ion plasmas*, Phys. Rev. E **65** (2002), 036412.

[81] E. Smith, J. Cooper, and C. Vidal, *Unified classical-path treatment of Stark broadening in plasmas*, Phys. Rev. **185** (1969), 140–151.

[82] D. Voslamber, *Unified quantum statistical formulation of pressure broadening*, Phys. Lett **40A** (1972), 266–268.

[83] J. Cooper, E. W. Smith, and C. R. Vidal, *Influence of ion dynamics on Hα and Hβ at low-densities*, J. Phys. B: At. Mol. Opt. Phys. **7** (1974), L101–L105.

[84] A. Brissaud and U. Frisch, *Theory of Stark broadening–II Exact line profile with model microfield*, J. Quant. Spectrosc. Radiat. Transfer **11** (1971), 1767–1783.

[85] J. Seidel, *Hydrogen Stark broadening by model electronic microfields*, Z. Naturf. **32a** (1977), 1195–1206.

[86] A. Brissaud, C. Goldbach, J. Leorat, A. Mazure, and G. Nollez, *On the validity of the model microfield method as applied to Stark broadening of neutral lines*, J. Phys. B: At. Mol. Opt. Phys. **9** (1976), 1129–1146.

[87] D. B. Boercker, C. A. Iglesias, and J. W. Dufty, *Radiative and transport properties of ions in strongly coupled plasmas*, Phys. Rev. A **36** (1987), 2254–2264.

[88] S. Ferri, A. Calisti, C. Mosse, B. Talin, and V. Lisitsa, *Improved frequency fluctuation model for spectral line shape calculations in fusion plasmas*, AIP Conf. Proc. **1290** (2010), 53–62.

[89] S. Günter, *Contributions of strong collisions in the theory of spectral lines*, Phys. Rev. E **48** (1993), 500–505.

[90] B.H. Bransden and C. J. Joachain, *Physics of atoms and molecules*, 2 ed., Pearson Education Limited, England, 2003.

[91] K. Bartschat, *The R-matrix with pseudo-states method: Theory and applications to electron scattering and photoionization*, Comput. Phys. Commun. **114** (1998), 168–182.

[92] I. Bray and A. T. Stelbovics, *Convergent close-coupling calculations of electron-hydrogen scattering*, Phys. Rev. A **46** (1992), 6995–7011.

[93] I. Bray and D. V. Fursa, *Benchmark cross sections for electron-impact total single ionization of helium*, J. Phys. B: At. Mol. Opt. Phys. **44** (2011), 061001.

[94] I. Bray, D. V. Fursa, A. S. Kadyrov, A. T. Stelbovics, A. S. Kheifets, and A . M. Mukhamedzhanov, *Electron- and photon-impact atomic ionisation*, Physics Reports **520** (2012), 135–174.

[95] M. C. Zammit, D. V. Fursa, and I. Bray, *Convergent-close-coupling calculations for excitation and ionization processes of electron-hydrogen collisions in Debye plasmas*, Phys. Rev. A **82** (2010), 052705.

[96] M. C. Zammit, D. V. Fursa, I. Bray, and R. K. Janev, *Electron-helium scattering in Debye plasmas*, Phys. Rev. A **84** (2011), 052705.

[97] T. F. O'Malley, L. Spruch, and L. Rosenberg, *Modification of effective-range theory in presence of a long-range (r-4) potential*, J. Math. Phys. **2** (1961), 491–498.

[98] K. Unnikrishnan and J. Callaway, *Shift and width of the Lyman-alpha line of neutral hydrogen due to electron collisions*, Phys. Rev. A **43** (1991), 3619–3623.

[99] D. B. Boercker and C. A. Iglesias, *Static and dynamic shifts of spectral lines*, Phys. Rev. A **30** (1984), 2771–2774.

[100] P. Sperling, A. Wierling, G. Röpke, and M. Winkel, *Radiation hydrodynamics of laser-induced plasmas using dynamic collision frequencies*, Contrib. Plasma Phys. **49** (2009), 732–737.

[101] C. Gocke, *Dekohärenz in offenen Quantensystemen am Beispiel eines Rydbergatoms in Plasma*, Ph.D. thesis at Rostock University, 2007.

[102] B. Omar, A. Wierling, S. Günter, and G. Röpke, *Shift and broadening of neutral Helium spectral lines in dense plasmas*, J. Phys. Conf. Series **11** (2005), 147–152.

[103] H. Griem, A. C. Kolb, and K. Y. Shen, *Stark broadening of hydrogen lines in a plasma*, Phys. Rev. **116** (1959), 4–17.

[104] J. Rosato, H. Capes, and R. Stamm, *Ideal coulomb plasma approximation in line shape models: Problematic issues*, Atoms **2** (2014), 253–258.

[105] A. Clebsch and P. Gordon, *Theorie derAbelschen Funktionen*, Teubner, Leipzig, 1866.

[106] M. Abramowitz and I. A. Stegun, *Handbook of mathematical functions with formulas, graphs, and mathematical tables*, Dover, New York, 1972.

Danksagung

Ich möchte an dieser Stelle all jenen Danken, die dazu beigetragen haben, dass ich das begonnene Projekt “Promotion” nun zu Ende gebracht habe. An erster Stelle denke ich dabei an meine Familie. Winfried hat mir zuverlässig den Rücken gestärkt, wenn ich mal wieder den Eindruck hatte, fachlich auf dem Holzweg zu sein. Dabei stärkte er mich moralisch und auch durch geduldiges Zuhören und Nachfragen bis das wirkliche Fachproblem herausgekitzelt war. Die Entstehung und Entwicklung von Linus und Ina zu erleben, hat mich vom Arbeiten abgehalten, aber auch darin bestärkt, den eingeschlagenen Weg weiter zu gehen. Bestärkt wurde ich dabei auch durch meine Eltern, die trotz fortschreitender Zeit nie Zweifel äußerten, dass ich meine Promotion abschließen werde.

Für das angenehme Klima zunächst im Hauptgebäude, später in der Wismarschen Straße 44, sei allen Mitarbeitern der umliegenden AGs gedankt, insbesondere denen, die mich mit dem ein oder anderen Gespräch in der Kaffee- oder Mittagspause abwechslungsreich unterhalten haben. Über die Jahre sind das viele gewesen, ich möchte diejenigen nennen, die mir in der letzten Phase in Rostock besonders wichtig geworden sind: NUF, Thomcz und Volker aus dem Erdgeschoß, sowie Andreas, Mandy und Philipp aus dem Obergeschoß. Auch Marina Hertzfeldt möchte ich für ihre zuverlässige Sekretariatsführung und ihre von Herzen kommenden Ratschläge danken.

Zuletzt bedanke ich mich natürlich auch für die gute Zusammenarbeit mit und auch unter meinen drei Betreuern August Wierling, Gerd Röpke und Heidi Reinholz. Sie haben zu verschiedenen Zeitpunkten einzeln meine Hauptbetreuung übernommen und mich und mein Arbeitsverhalten an verschiedenen Punkten besonders geprägt. Insbesondere meine Doktormutter Heidi war die ganze Zeit nicht nur eine gute Ansprechpartnerin für fachliche Fragen, sondern auch Vorbild im Bezug auf Selbstvertrauen im Wissenschaftsbetrieb und im “alles unter einen Hut kriegen”. Danke!

Selbstständigkeitserklärung

Ich versichere hiermit an Eides statt, dass ich die vorliegende Arbeit selbstständig angefertigt und ohne fremde Hilfe verfasst habe. Dazu habe ich keine außer den von mir angegebenen Hilfsmitteln und Quellen verwendet und die den benutzten Werken inhaltlich und wörtlich entnommenen Stellen habe ich als solche kenntlich gemacht.

Bonn, den 23.7.2014

Sonja Lorenzen

Curriculum Vitae

Sonja Westermayer verh. Lorenzen, geb. 23.09.1982 in Tübingen,
zwei Kinder (*2008, *2010)

10/2002 - 02/2008	Physikstudium (Diplom) an der Universität Rostock
08/2004 - 06/2005	ERASMUS-Aufenthalt TU Luleå, Schweden
03/2008 - 03/2014	Wissenschaftliche Mitarbeiterin im SFB 652, Teilprojekt A4, AG Quantentheorie und Vielteilchensysteme, Universität Rostock
seit 04/2014	Wissenschaftliche Mitarbeiterin im Regionalen Rechenzentrum der Universität zu Köln, Abteilung Betrieb

Publikationen:

[10–15], sowie

Sandrine Ferri, Annette Calisti, Caroline Mossé, Joël Rosato, Bernard Talin, Spiros Alexiou, Marco A. Gigosos, Manuel A. Gonzalez, Diego Gonzalez, Natividad Lara, Thomas Gomez, Carlos Iglesias, Sonja Lorenzen, Roberto Mancini, and Evgeny Stambulchik, *Ion dynmaics effect on Stark broadened line shapes: A cross comparison of various models*, Atoms **2** (2014) 299-318.